



Fakultät Maschinenbau  
*fortschritt studieren*

RUHR  
UNIVERSITÄT  
BOCHUM

RUB

**Thermodynamic and microstructural stabilities at high temperatures and their effects on mechanical properties in an  $\text{AlMo}_{0.5}\text{NbTa}_{0.5}\text{TiZr}$  refractory high entropy superalloy.**

**Dissertation**

**zur**

**Erlangung des Grades**

**Doktor-Ingenieurin**

der

Fakultät für Maschinenbau  
der Ruhr-Universität Bochum

von

Patricia Suárez Ocaño  
aus Caracas, Venezuela

Bochum 2023

Dissertation eingereicht am: 29.08.2023.

Tag der mündlichen Prüfung: 27.11.2023.

Erstgutachter: Prof. Dr. Guillaume Laplanche

Zweitgutachter: Prof. Dr.-Ing. Gunther Eggeler



## Acknowledgments

This doctoral thesis and the associated research activities took place during my time as a research assistant at the department of Materials Engineering of Federal Institute for Material Research and Testing (Bundesanstalt für Materialforschung und -prüfung (BAM)). The project was developed between 2019 and 2022 as part of a grant (n° 398838389) by the German Research Foundation (Deutsche Forschungsgemeinschaft, DFG).

I am deeply grateful to all those who have contributed to the completion of this Ph.D. thesis, both directly and indirectly. Their support, guidance, and encouragement have been invaluable throughout this journey.

Firstly, I would like to express my genuine gratitude to my supervisor, Dr.- Ing. Leonardo Agudo Jácome, for his firm guidance, insightful feedback, continuous encouragement, and for the trust he placed in me by choosing me as a student. His expertise and vision have illuminated my path, inspiring me to push the boundaries of my capabilities. The opportunity to work under his guidance has been an honor, and I am truly grateful for the valuable experiences and knowledge I have gained through this project. Thank you for the tireless TEM sessions and the patience you have shown in training me how to use it.

Next, I would like to extend my appreciation to Prof. Dr. Guillaume Laplanche, my academic mentor and supervisor, for his constant support, encouragement, and academic insights, which have been instrumental in refining the academic aspect of my research. His willingness to engage in thoughtful discussions, provide constructive criticism, and offer guidance whenever needed have enriched the quality of my work immensely. His expertise and mentorship have been crucial in shaping the direction of this research.

I extend my appreciation to BAM, my colleagues, and staff from the Division 5.1, Materialography, Fractography and Ageing of Engineered Materials for providing an enriching working environment. The resources, facilities, and opportunities offered have been helpful in the successful execution of this research.

I would like to extend a special appreciation to Dr. Anna Manzoni for her exceptional support and guidance throughout the course of my doctoral research. Her expertise in data processing and her willingness to share her knowledge have been invaluable to me. Her insightful explanations have not only enhanced my understanding but also speeded up my progress in this complex aspect of my research.

I would like to thank Dr. Suzana G. Fries, whose guidance has been fundamental from the very start of my doctorate and throughout its progress. Her expertise, patience, insightful feedback and willingness to invest time and effort in my growth as a researcher have been invaluable.

Many thanks to Romeo Saliwan Neumann for the EBSD analysis and Prof. Dr. Gert Nolze for the fruitful discussions. Thanks to Dr. Axel Kranzmann for the valuable discussions and for inspiring me with all his stories. Furthermore, I would like to thank the laboratory technicians: Elke Sonnenburg, Evgenia Bajer, Gabrielle Oder, Hennig Goldbeck and René Hesse for their support and guidance through sample preparation, XRD analysis and SEM-FIB. I also acknowledge Dr. Carlos Abad, for his support on the chemical analysis. Many thanks to Dr.-Ing. Reza Darvishi Kamachali for the support with CALPHAD calculations at BAM, to Oliver Schwarze for the nanoindentation analysis, to Steffen Thärig, Christine Krimmling and Dr.-Ing. Birgit Rehmer for the microhardness tests, and to Dr.-Ing. Stefan Reinsch for the DTA analysis.

I would like to thank the collaborative partners from Karlsruher Institut für Technologie: Ing. Stephan Laube, Dr.-Ing. Alexander Kaufmann and Prof. Martin Heilmaier, for the fabrication of the alloy, and the fruitful discussions. Furthermore, many thanks to Dr.-Ing. Inmaculada López-Galilea, Dr.-Ing. Benjamin Rutttert, and Prof. Werner Theisen (Ruhr University Bochum) for the HIP treatments.

I would like to thank the collaborative partners from Bayreuth University: Dr. Christian Gadelmeier and Prof. Dr. Uwe Glatzel, for performing the creep experiments, which were crucial for this research. Many thanks to Dr.-Ing. Inmaculada Lopez Galilea, Dr.-Ing. Benjamin Rutttert and Prof. Werner Theisen for the HIP from RUB, for the HIP experiments.

Many thanks to Dr. Michael Tovar and René Schwiddessen from Helmholtz-Zentrum Berlin (HZB), for the XRD analysis.

I extend my deepest gratitude to my loving husband, René Simon Pfisterer, whose solid support has been the foundation of my journey through this project. His infinite encouragement, understanding, and patience have been my constant pillars, providing me the strength to pursue this work.

I would like to thank my best friend, Dr. Alejandra Esparza, whose friendship has been a constant source of strength throughout this academic journey. Her companionship and advice have made the toughest moments manageable.

Finally, I am deeply grateful to my family, especially my mother. I am profoundly thankful for her immeasurable love and guidance. Her endless sacrifices have covered the way for my academic achievements, as well as, her constant presence and wisdom have been my guiding light, and I am forever thankful for her unending support.

## Executive Summary

The  $\text{AlMo}_{0.5}\text{NbTa}_{0.5}\text{TiZr}$  refractory high entropy superalloy (RSA) was fabricated in different states, *i.e.*, vacuum arc melted (AC), AC + annealed (AN, 1400 °C, 24 hour), and AC + AN + hot isostatic pressed (HIPed, 1370 °C, 4 hours under 170 MPa of pressure). The purpose of the present work is threefold: 1) compare the microstructure in its three states with CALPHAD calculations and identify the transformation pathways from high to low temperature, 2) investigate the effect of cooling rate on its microstructure and examine its resulting room-temperature hardness and fracture toughness, and finally 3) assess the high-temperature tensile creep behavior and the microstructural changes linked to it. The microstructure of the AC state showed a mixture of cuboidal A2-phase precipitates (< 20 nm edge length) embedded in a B2-phase matrix within the dendritic and interdendritic regions. The grain boundaries contained a predominantly amorphous phase enriched in Al and Zr, and with  $\text{Al}_{4-x}\text{Zr}_5$  ( $x$ : 0 – 1) stoichiometry. In the AN state, the sample kept the same phase structure but with  $\approx 10 - 100$  nm cuboidal and plate-like A2 precipitates that formed coherent interfaces with the B2 matrix, whereas the  $\text{Al}_{4-x}\text{Zr}_5$  decorating the grain boundaries crystallized completely as a hexagonal (space group:  $\text{P6}_3/\text{mcm}$ ) intermetallic. CALPHAD calculations confirmed the formation of the A2/B2 substructure in the grain core through spinodal decomposition during the cooling process. Additionally, as the RSA melts at higher temperatures than Ni-based alloys (*i.e.*,  $\approx 1900$  °C), this alloy system would be attractive for usage in high-temperature structural applications. In terms of the influence of cooling rates on microstructure and properties, higher cooling rates after HIP promoted the formation of smaller and more coherent A2 precipitates with the B2 matrix, leading to a smaller lattice misfit between them. As a consequence, the nanohardness of the alloy increased, while the fracture toughness, which is comparable to that of certain B2 intermetallics, was unaffected by the cooling rate. Finally, tensile creep tests were conducted in vacuum with miniaturized specimens, in the range of 900 – 1100 °C and 30 – 160 MPa. In order to establish possible creep mechanisms, mechanical as well microstructural data of the head and gage length of the samples were analyzed. Norton exponents of  $n \approx 2.7$  for 900 and 1000 °C and  $n \approx 3.4$  for 1100 °C ( $\sigma < 90$  MPa) indicated that the deformation may be controlled by dislocation climb and viscous glide. The apparent activation energy for creep was estimated to be  $\approx 111$  kJ/mol. Microstructural changes after long-term high-temperature exposure additionally showed that the instability of the B2 phase (*i.e.*, the B2 matrix transforms into  $\text{Al}_{4-x}\text{Zr}_5$ ), and a coarsening of the A2/B2 nanostructure, influenced the creep behavior.

## Table of Contents

Acknowledgments .....	I
Executive Summary .....	III
1. Introduction .....	1
2. Fundamental background and state of the art.....	3
2.1 Context and concept of the project .....	3
2.2 Microstructure and properties of refractory CCAs, spinodally decomposed, and precipitation-strengthened alloys.....	7
2.3 The CALPHAD method .....	15
2.4 Mechanical properties and microstructure of the RSA $\text{AlMo}_{0.5}\text{NbTa}_{0.5}\text{TiZr}$ .....	17
2.5 Intrinsic properties of individual phases in RSA.....	23
3. Scientific objectives .....	37
4. Papers .....	38
4.1 Paper I.....	38
4.2 Paper II .....	59
4.3 Paper III.....	79
4.4 Paper IV.....	106
5. General conclusions and outlook .....	157
References .....	161
List of Publications.....	169
Curriculum vitae.....	170

## 1. Introduction

Currently, the constant demands of the industry continue to challenge the research and development sector to make advances in the design and properties of materials that can withstand complex environments. High entropy alloys (HEAs), with 5 or more elements at equimolar or near-equimolar concentrations have interesting properties due to the formation of single phase microstructures [1, 2]. However, compositionally complex alloys (CCAs), which can also form secondary and intermetallic phases, have caused great interest in the field of materials science in the past years, since the formation of additional phases can lead to promising properties such as high strength, toughness and high temperature phase stability [3-5]. Researchers have investigated the use of refractory elements for compositionally complex alloying to develop new alloys for components that operate at higher temperatures than existing Ni-based superalloys [6-11].

Because of its potential compression properties at high temperature *i.e.*, up to 1200 °C, a promising example is the AlMo<sub>0.5</sub>NbTa<sub>0.5</sub>TiZr refractory (r)CCA, where the subindex “0.5” represents half of the atomic ratio of Mo and Ta with respect to the other elements. The AlMo<sub>0.5</sub>NbTa<sub>0.5</sub>TiZr rCCA has been named "high entropy superalloy" (RSA) by its developers due to its remarkable morphological resemblance to Ni-based with  $\gamma/\gamma'$  microstructures, having a dual-phase structure composed by A2-structured cuboidal and plate-like precipitates embedded in a B2-structured matrix. Senkov *et al.* [12] reported a compressive yield strength between 23 and 1200 °C, which is superior to that for polycrystalline Ni-based superalloys (IN 718 [13], Mar-M247 [14] and Haynes 230 [15]). Together with its relatively low density (7.4 g/cm<sup>3</sup>), the alloy was presented as a prospect candidate for structural applications that requires high yield strength at high temperatures. The authors argued that the high volume fraction of interfaces in the RSA, retained up to 1200 °C, is responsible for its high temperature strength. However, there remain still uncertainties about the suitability of its properties for structural applications at high temperature. First, the reported mechanical properties are limited to compressive data, and considering that most structural applications at high temperatures require tensile stresses, its tensile strength remains an important question. In addition, when alloys are subjected to high temperatures for extended durations, their thermodynamic stability becomes a critical consideration. Insights if its microstructural stability has been shown already, at 800, 1000, and 1200 °C after 1000 hours of exposure under vacuum conditions [16]. Apart from their microstructural stability at high temperature, the properties under creep in conjunction with these microstructural changes must be addressed in order to establish what possible mechanisms are present in the deformation process, and how the microstructural instabilities affect the deformation process.

Therefore, this thesis focuses on exploring the thermodynamic and microstructural stabilities of the RSA at elevated temperatures. Additionally, the study investigates the alloy's mechanical properties at room and high temperatures and their correlation with the thermodynamic and microstructural stabilities, in order to assess its potential for the fabrication of high-temperature structural systems.

Thus, a cumulative thesis is prepared as follows: in Section 2, the fundamental background and state-of-the-art of the RSA and related systems is introduced, including a detailed description of the context of this study. This will give a motivation for the Section 3, which summarizes the main scientific objectives. Section 4 presents three research articles and one data article, 3 of which (the latter and two of the former) were published. The thermodynamic stabilities are addressed in the first research article through thermodynamic calculations of equilibrium and non-equilibrium pathways using the CALPHAD method, which includes a complete comparison with experimental findings. The second article, a data article, contains all relevant data analyses and processing for the first research article. The third research article is dedicated to investigating microstructural changes under three different cooling rates and their impact on lattice misfit between A2 and B2 phases and mechanical properties at room temperature. Additionally, the study explores how temperature influences the lattice misfit within the dual-phase structure. Finally, the fourth research paper, focuses on the study of the creep properties under tension of the RSA in order to establish its deformation mechanisms at high temperature. The work culminates with some general conclusions from all the performed research with some potential guidelines to follow future investigations.

## 2. Fundamental background and state of the art

### 2.1 Context and concept of the project

The energy and aerospace industry unceasingly demands improved engine efficiency, leading to the need for novel alloys that offer superior mechanical and corrosion resistance under extreme operating conditions. High-temperature materials are utilized in various industries and applications, *e.g.*, fuel cells, gas turbines, nuclear reactors, engines, and power plants [17, 18]. Materials used in gas turbine engines, for example, must exhibit strength and heat resistance over extended periods, in order to be efficient, effective, and economical [19]. In the high temperature and pressure regions of gas turbines, *i.e.*, combustion chamber and on the first row of blades (*cf.* [Figure 1a](#)), the temperatures can reach up to 1300 °C [20, 21] demanding alloys with exceptional creep behavior, and good oxidation and corrosion resistance.

Engine efficiency could further increase by incrementing the operation temperature without compromising the materials [22], *i.e.*, materials that can withstand heat without deforming due to creep. Ni-based superalloys have been used for aircraft turbines, because they have excellent heat-resistant properties, good mechanical strength up to 1100 °C, sufficient ductility to be mechanically formed, and good resistance to high-temperature oxidation [20, 23-25].

Ni-based superalloys have been developed over decades, in order to constantly improve their properties at higher temperatures. First, the development of alloys with increased tensile strength due to the dispersion of coherent intermetallic precipitates ( $\gamma'$ , Ni<sub>3</sub>(Al, Ti), L1<sub>2</sub> structure) in the continuous fcc matrix ( $\gamma$ ) with additions of Al and Ti [26, 27]. Then, the solid solution strengthening by addition of elements such as tungsten (W), niobium (Nb), and tantalum (Ta), that increases high-temperature strength while preventing precipitation of undesirable oxides and nitrides using vacuum induction melting (VIM) [27, 28]. To avoid the weakening effect of grain boundaries under stress by centrifugal forces along the blade axis, directional solidification (DS) was then enforced. Finally, the Bridgman method [29] was implemented to cast single-crystal (SX) superalloys in the 1960s [30] so as to completely eliminate creep anisotropy. An exemplary  $\gamma/\gamma'$  microstructure of a state-of-the-art Ni-based SX superalloy with fine-tuned chemistry, the LEK94, is shown in [Figure 1b](#).

Nevertheless, due to the melting temperature of these materials, they must be subjected to air cooling, which requires additional work, and brings the operating temperatures to their limits [31]. For this reason, other materials have been considered and evaluated as possible alternatives for this application. For instance, due to the high melting points, refractory metals such as molybdenum (Mo) and niobium (Nb) have been investigated as alternatives by researchers and industry [32-34].

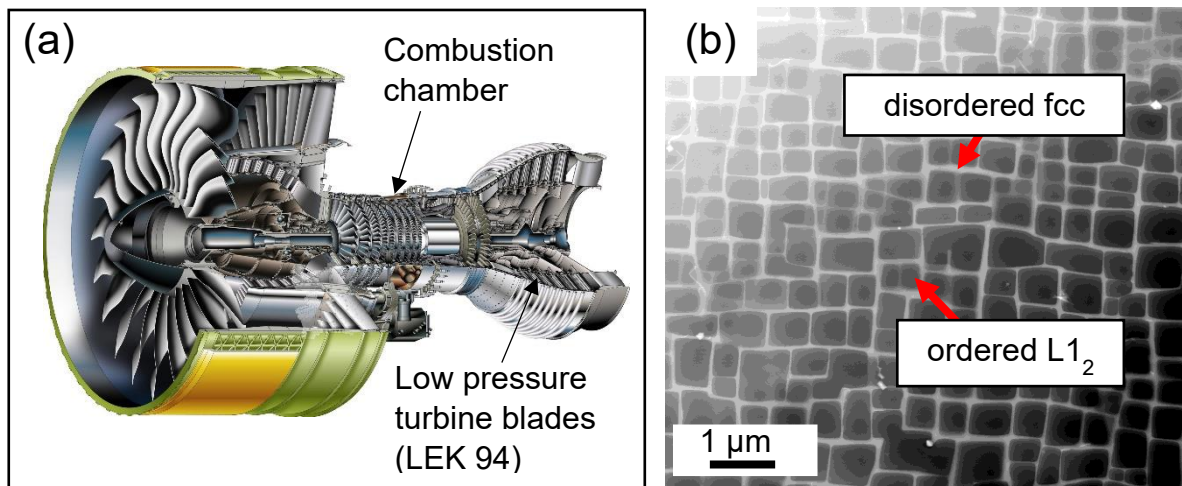


**Figure 1.** (a) Example of an aircraft turbine engine (Engine Alliance GP7000), showing the region where the single-crystal (SX) superalloy LEK 94 is used (b) Microstructure of a Ni-based SX superalloy LEK 94 [35].

However, Nb alloys tend to form an oxide powder layer of  $\text{Nb}_2\text{O}_5$  that is not protective [36], and Mo tend to form  $\text{MoO}_3$ , which is gaseous at temperatures  $> 700\text{ }^\circ\text{C}$ , which makes these refractory alloys not very resistant to oxidation and corrosion [37]. One possible solution that has been reported is the addition of alloying elements to these refractory alloys to improve their corrosion properties, although this results in degradation of the mechanical properties [38]. The Ni-based alloys have a particular structure that is composed of a fcc solid solution ( $\gamma$  phase) matrix that contains dispersed  $\text{L}_{12}$  precipitates ( $\gamma'$  phase) that are rich in Ni, Al and Ti [39] (cf. Figure 1b), thus inducing precipitation hardening [26]. Based on these alloy development limits; a key issue may be the development of new types of alloys that contain refractory elements but can also develop microstructures that meet the desired requirements.

Compared to conventional alloys, CCAs or HEAs have attracted considerable attention in the materials science community in the past 20 years, often exhibiting unexpected microstructures and properties [5, 40-42]. Yeh [1] and Cantor [2] presented the concept of multi-principal alloying, which then also adopted the name “high entropy alloys”. Under their definition, these are alloys composed of 5 or more equimolar or near-equimolar elements with 5 to 35 at % each, characteristically found to form microstructures comprising one single disordered solid solution phase by maximizing the configurational entropy. Many following studies have focused on the development of alloys with solid solution strengthening, which may be beneficial to improve processing or for transportation applications, and most of the studies have dealt with transition metals whose melting points are lower than those required for high-temperature structural applications ( $> 1000\text{ }^\circ\text{C}$ ) [43-46]. The term compositionally complex –also called “complex



concentrated”– alloys, evolved as an extension of the original definition of HEAs to allow for multiple phases, including intermetallics, which can be beneficial to some mechanical properties [47]. CCAs mainly composed by elements such as Ta, Nb and Mo, have the potential to be highly resistant to heat, making them candidates for applications in high-temperature environments. Senkov *et al.* [10] proposed an extension of this research focused on high-temperature applications in their 2010 paper “Refractory high-entropy alloys”. There, they presented two near-equiatomic alloys containing high-melting points elements (*i.e.*, Mo, Nb, Ta, V, and W).

The AlMo<sub>0.5</sub>NbTa<sub>0.5</sub>TiZr RSA, developed at the U.S. Air Force Research Lab (AFRL) in U.S.A. few years ago [48, 49], is one of the first of a specific class of CCAs that uses a combination of refractory elements and the oxidation-resisting light element Al at a specific weight ( $= 7.40 \text{ g/cm}^3$ ) that is comparable to Ni-based superalloys (*cf.* Figure 2 and Figure 1b). The scanning electron microscopy backscattered electron (SEM-BSE) image in Figure 2a shows that, after the now well-established annealing at 1400 °C for 24 h + hot isostatic press (HIP) at 1400 °C and 207 MPa for 2 h, the AlMo<sub>0.5</sub>NbTa<sub>0.5</sub>TiZr RSA is formed by equiaxed grains decorated by a secondary coarse phase along the grain boundaries, rich in Al and Zr [12]. A higher magnification using scanning transmission electron microscopy high angle annular dark field (STEM-HAADF) (Figure 2b), shows that the grain structure marked by the small red square in Figure 2a is composed by a combination of two bcc-based phases, *i.e.*, A2/B2. The microstructure of the AlMo<sub>0.5</sub>NbTa<sub>0.5</sub>TiZr RSA resembles that of Ni-based superalloys (*cf.* Figure 1b), both with a high volume fraction ( $\approx 60\%$ ) of cuboidal particles coherently embedded in continuous matrix [12] and a cube-on-cube orientation relationship. As the AlMo<sub>0.5</sub>NbTa<sub>0.5</sub>TiZr RSA was the first rCCA to show this microstructure, it was later named “refractory high entropy superalloy (RSA)” by its developers [12]. In the past years, a number of related alloys have emerged, which have also been referred to as RSAs. However, to avoid confusion, the AlMo<sub>0.5</sub>NbTa<sub>0.5</sub>TiZr alloy will be referred to as the RSA throughout this manuscript, and other related alloys will be named by its composition.

However, there are important differences between the RSA and the Ni-based alloys: 1) the Ni-based present a mixture of two fcc-based phases with one being a solid solution and the other one being L1<sub>2</sub>; 2) the Ni-based is described to be formed mostly by nucleation and growth (although under specific heat treatment conditions such as rapid-cooling, it is possible to obtain microstructures through a spinodal decomposition [50]), whereas the RSA has been described to be formed by spinodal decomposition, 3) the microstructure of the RSA is one order of magnitude smaller and it does not only show cuboidal but also plate-like precipitates. The origin of the latter is still unknown. Only limited data on relevant mechanical properties, has hitherto been reported on the RSA [12, 48, 49]. Through hardness and compression testing, the hot isostatically pressed (HIPed) and annealed material revealed an impressive yield strength of 2000 MPa at room temperature (RT), representing

the highest among refractory CCAs to date. However, it should be noted that ductility was limited, with only 10% of fracture strain (in compression) also at room temperature [12]. It has been revealed that lowering the Mo content increases the ductility at RT but reduces the strength [51]. Therefore, efforts persist to enhance the properties of the RSA through composition optimization and novel processing methods.

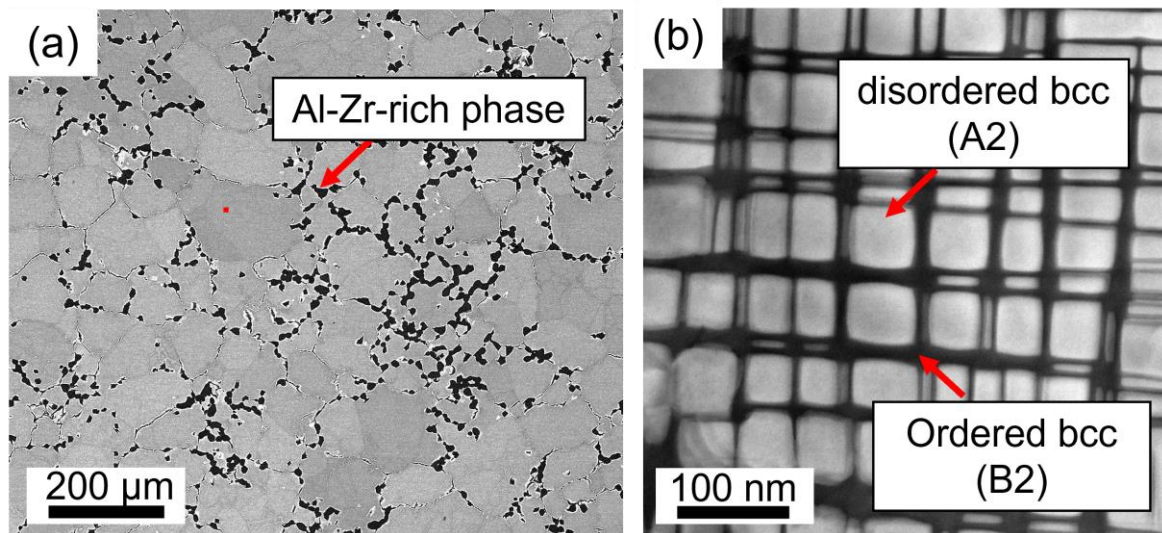


**Figure 2.** Microstructure of the RSA (a) at low magnification (SEM-BSE) and (b) at high magnification from the region marked with the red square in (a) (STEM-HAADF) [52].

For example, it has been shown that in alloys containing dual phases with embedded precipitates in a matrix, such as Ni- and Co-based alloys, controlling cooling processes is essential for modifying the microstructure and resulting mechanical properties [53-56]. Therefore, the question arises whether it is possible to improve its ductility, while keeping its high strength via such processing. Furthermore, the microstructural characteristics of the deformation mechanisms have not been verified yet, especially for loading in tension, which is relevant to the intended application. In this context, the need to elucidate the high temperature stability and properties at both room and high temperature is necessary to establish the potential of this or similar alloys for use in structural applications, *i.e.*, gas turbines. Therefore, the present work is focused on the study of the thermodynamic stability at high temperature and its effect on the room (hardness and fracture toughness) and high temperature (creep) mechanical properties of the RSA. The alloy was fabricated in the Institute for Applied Materials of Karlsruhe Institute of Technology (KIT), including vacuum arc melting followed by an annealing treatment. Hot isostatic pressing (HIP) treatment was conducted at the Institute for Materials of Ruhr Universität Bochum (RUB) under conditions comparable with the material reported in the literature. The microstructures in the as-cast and annealed states were characterized at the Bundesanstalt für Materialforschung und -prüfung

(BAM) in Berlin. Due to the limited information about the equilibrium and solidification pathways of the RSA, calculations with the CALPHAD method were developed at BAM and in collaboration with the Materials Research Department of RUB. The hardness and nanohardness tests were performed at BAM, whereas the creep tests, including the production of miniaturized creep samples, and data process were performed at the department of Metals and Alloys of the University of Bayreuth. Microstructural characterization of all was performed at BAM.

## **2.2 Microstructure and properties of refractory CCAs, spinodally decomposed, and precipitation-strengthened alloys**

The microstructure and properties of rCCAs, spinodally decomposed and coherent precipitation-strengthened alloys play a crucial role in understanding their behavior and applicability. This section explores the fundamental aspects of these alloys, the influences of some processing parameters, and the resulting properties.

### *Refractory CCAs*

Refractory compositionally complex alloys, with a reported density in the range from 5.6 to 13.8 g/cm<sup>3</sup> [57], have gathered significant attention as potential materials for high-temperature structural applications. These alloys are composed of five or more principal components, incorporating refractory elements, *i.e.*, Mo, Ta, Nb, Re and W. Additionally, non-principal components are often added to further enhance the properties of the principal elements [4].

Naka [58] was seemingly the first author to report the microstructure of two-phase refractory multi-component systems. He explored the possibilities to produce complex alloy systems in order to expand the development on intermetallic materials, which could have the potential to meet the requirements for structural applications. As multi-phase materials have higher mechanical strength than single-phase intermetallics, two-phase microstructures were generated by them in different alloy systems. It was revealed the complex Ta-based system (Ta-Ti-Zr-Al-Nb-Mo), as a “two-phase microstructure with A2 precipitates rich in Ta, embedded in a B2 phase matrix microstructure, with a small lattice misfit”. Various attempts were made, however, to reverse the two-phase A2+B2 microstructure, without success.

Years later, Senkov *et al* [10] examined two refractory CCAs, namely MoNbTaW and MoNbTaVW. These alloys were characterized as single BCC structures, retaining strengths above 400 MPa at temperatures up to 1600 °C [59]. Additionally, they exhibited Vickers hardness values of  $H_v = 4.5$  GPa and  $H_v = 5.3$  GPa, respectively. Another example of these rCCAs, is the

HfNbTaTiZr, widely studied in the past years, with BCC single phase structure, and high strength and good ductility at RT [57].

In a review article, the knowledge up to that date on yield stress for different rCCAs, was reported by Senkov *et al* [57]. The majority of the rCCAs are reported to be BCC-based, and in some cases, to have additional secondary phases, *e.g.*, HCP, Laves,  $M_5Si_3$  or  $Al_3Zr_5$  [57]. These alloys, typically prepared through conventional melting and solidification methods, have been examined under compression properties within the temperature range between 600 and 1200 °C at different states, *e.g.*, as-cast, annealed, annealed + HIPed, and thermomechanically processed [60-62]. Figure 3 shows an overview of the yield stress of reported rCCAs, as described in Ref [57].

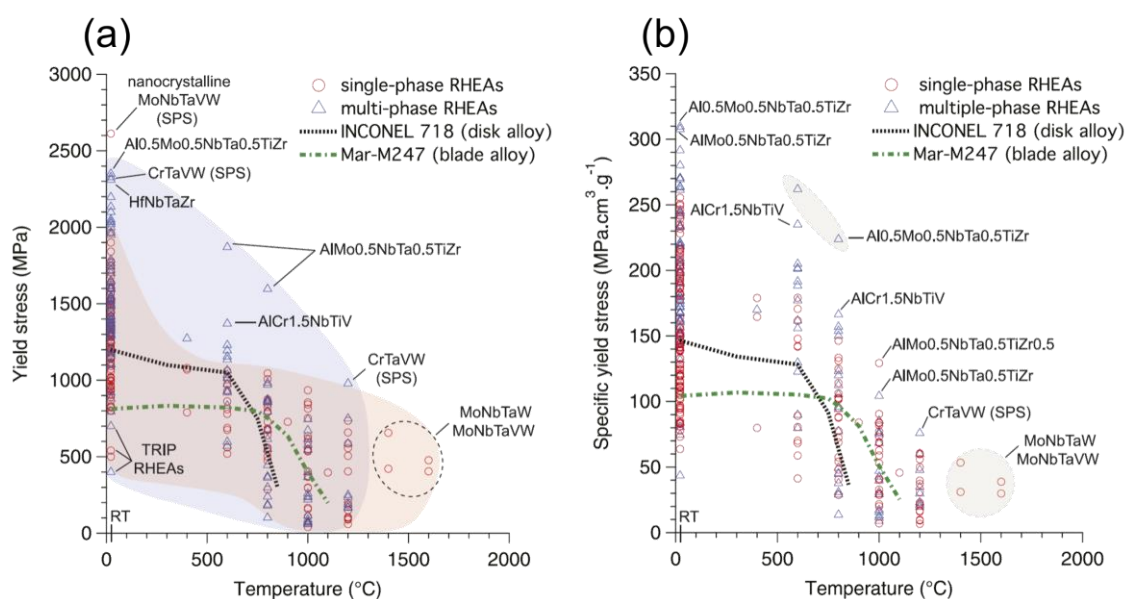


**Figure 3.** Yield stress of different rCCAs reported by Senkov *et al.* [57], where two Ni-based superalloys are also compared (a) Temperature vs. yield stress (b) Temperature vs. specific yield stress.

Some of these rCCAs, including the  $AlMo_{0.5}NbTa_{0.5}TiZr$  RSA, exhibit a microstructure in which the ordered phase constitutes the matrix. This feature reduces their ductility at room temperature. Therefore, efforts have been made to reverse this microstructure, where the disordered phase is now the matrix, and thus improve its ductility at room temperature. For example, Soni *et al.* [63] demonstrated a phase inversion phenomenon in the  $Al_{0.5}NbTa_{0.8}Ti_{1.5}V_{0.2}Zr$  alloy. Originally the alloy consisted of A2 cuboidal precipitates embedded in a B2 matrix. Phase inversion was produced by long-term annealing at 600 °C, which resulted in the formation of narrow and elongated regions of the A2 phase along specific pathways of the B2 channels, making the A2 phase continuous with containing B2 precipitates. This phase inversion was reported to be driven by the differences in elastic modulus of the two phases.

Most of the reported mechanical properties of CCAs and rCCAs are in compression [64-66]. A recent study by Kumar *et al.* [67] emphasized the significance of examining tensile properties in this type of alloys. Their investigation focused on the  $\text{Al}_{0.5}\text{Nb}_{1.25}\text{Ta}_{1.25}\text{TiZr}$  alloy, which exhibits a comparable microstructure to the RSA, *i.e.*, an A2/B2 nanostructure containing Al-Zr-rich phases along grain boundaries. Their findings revealed considerable differences in properties between compression and tensile tests. Generally, the alloy with an A2 matrix and B2 precipitates (known as HT800) exhibited plasticity in compression from RT to 1200°C. However, the alloy with a B2 matrix and A2 precipitates (referred to as HT600) did not demonstrate plasticity at RT. In both microstructural scenarios, very limited tensile ductility was observed at all temperatures, with ductility values ranging from  $\approx 0.01\%$  to 0.15%. Moreover, the presence of Al-Zr-rich precipitates along grain boundaries negatively impacted uniaxial tensile and fracture toughness properties (fracture toughness was about 77–95% lower in tension than in compression), resulting in suboptimal mechanical properties at high temperatures ( $> 800^\circ\text{C}$ ) and restricting the potential applications of these alloys [67].

Many CCAs systems composed of BCC/B2 substructures are formed by spinodal decomposition, where a supersaturated B2-structured phase spinodally decomposes upon cooling into a two-phase structure with coherent disordered BCC precipitates embedded in the B2 matrix. These include specially Al-containing alloys with  $\text{Al} > 0.9$  (molar ratio) [68], with  $\text{Al}_{1.5}\text{CoCrFeNi}$  [69], and  $\text{AlCoCrFeNiTi}_x$  ( $x \leq 1$ ) [70] as examples of these systems. However, Laube *et al.* [71] described that these reactions might instead occur by precipitation via nucleation and growth. They investigated the phase separation sequence in the 82(TaMoTi)-8Cr-10Al (at.%) rCCA, which exhibits a two-phase microstructure (BCC+B2), showing nucleation and growth as the phase separation mechanism, rather than the speculated spinodal decomposition.

### *Spinodally decomposed alloys*

In the literature, two primary phase transformation mechanisms have been identified: (1) nucleation and growth, and (2) spinodal decomposition [72].

Nucleation starts with the formation of small clusters or nuclei of the new phase within a supersaturated solution that is metastable. These nuclei serve as the starting points for the growth of the new phase, and once nuclei are formed and have reached a stable critical size, the growth process begins. During growth, atoms or molecules from the parent material are incorporated into the nuclei, increasing their size, and transforming gradually into the new phase [73]. Normally, nucleation and growth happen when the small fluctuations of chemical composition are significant enough to reduce the free energy barrier [72].

In contrast, spinodal decomposition occurs when a nearly homogeneous and thermodynamically unstable solution transforms into a mixture of two phases with compositions close to their equilibrium states, which are separated by a miscibility gap. This process does not involve a thermodynamic barrier and is diffusion-driven [74].

Figure 4 shows a schema of a coherent equilibrium phase diagram with a “miscibility gap” (solid line) and spinodal (dashed line) regions. At a given temperature  $T_1$ , the alloy is composed of a single phase ( $\alpha$ ) and the system is stable. Decreasing the temperature to  $T_2$ , the system enters in the miscibility gap region at compositions between  $x_1$  and  $x_2$  (cf. Figure 4). If the system lies outside the “spinodal” but within the miscibility gap, there are small variations in composition, which can lead to an increase in free energy and the alloy is therefore metastable. In order to reduce this free energy, nucleation and growth must occur, and at increasing times, the diffusion process will occur as shown in Figure 5a. If the system lies inside the “spinodal”, the alloy will have two regions finely dispersed and coherent, giving rise to an additional interfacial energy. In the “spinodal region”, the alloy is unstable, and the diffusion process will occur as shown in Figure 5b [73].

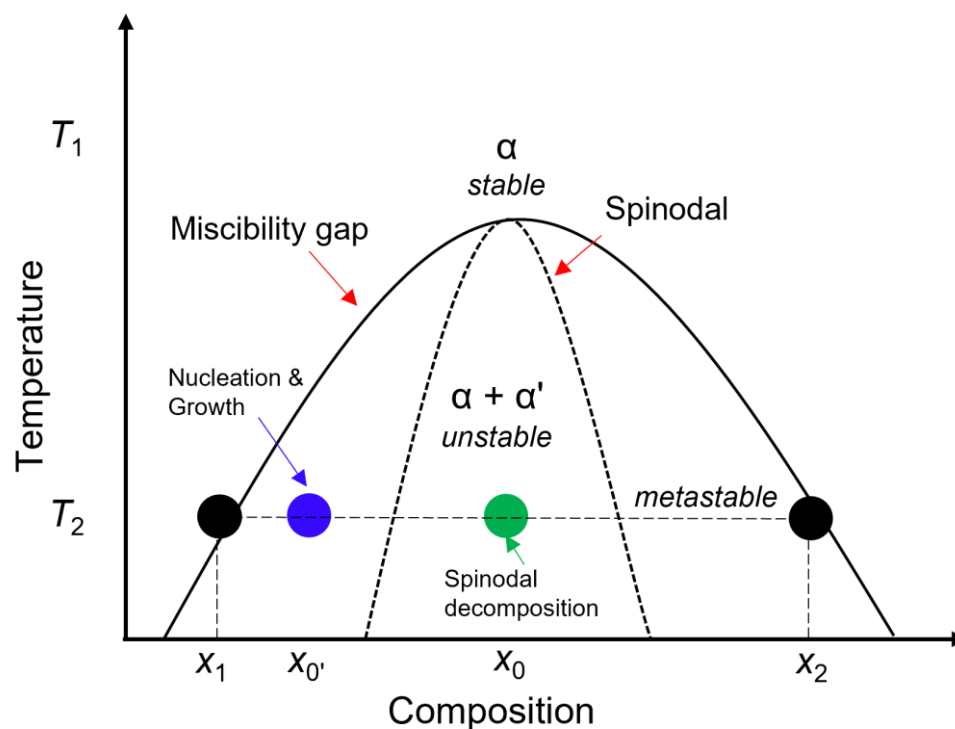


**Figure 4.** Schema of a coherent equilibrium phase diagram with a miscibility gap (solid line) and spinodal (dashed line) region. The black points  $x_1$  and  $x_2$  represent the composition boundaries of the miscibility gap region at a given temperature  $T_2$ . The green point represents the composition  $x_0$  inside the spinodal region (unstable) where spinodal decomposition occurs. The blue point represents the composition  $x_{0'}$  inside the miscibility gap, but outside the spinodal region (metastable), where nucleation and growth occur.

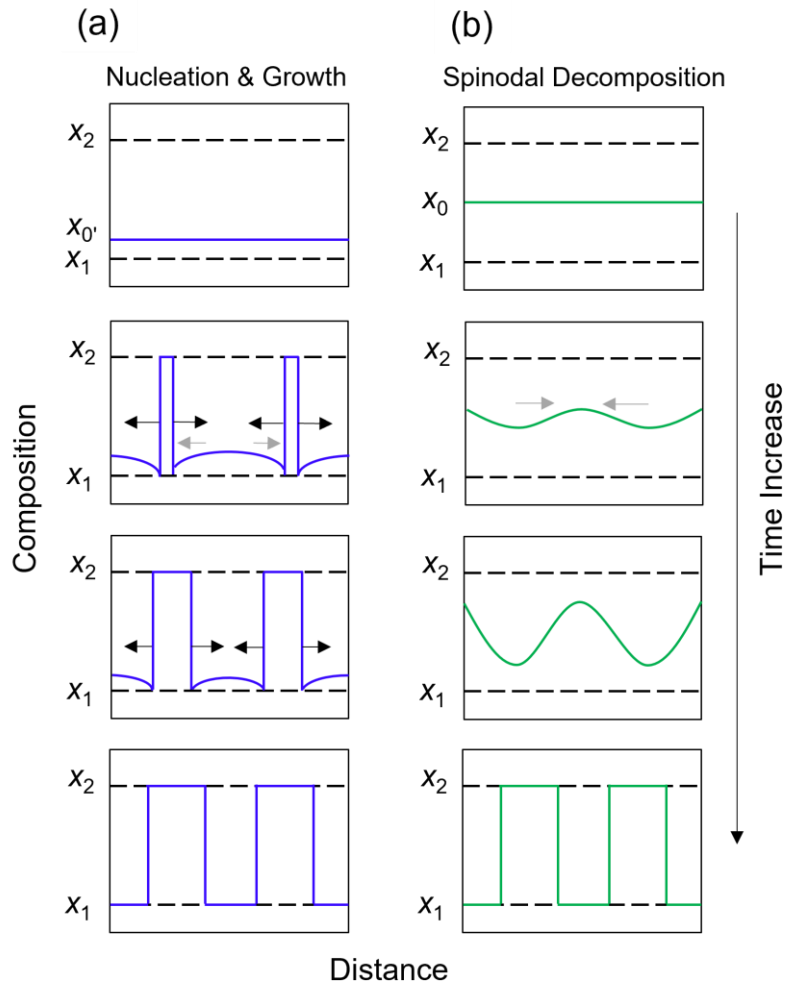


**Figure 5.** Schematic diffusion process of alloys with a miscibility gap quenched into (a) nucleation and growth and (b) spinodal decomposition regions, where the composition profiles are shown at increasing times. Grey arrows in (a) and (b) represent diffusion direction and black arrows in (a) represent growing direction.

Cahn [74] initially described the kinetics and mechanisms of spinodal decomposition in cubic crystals, in which he demonstrated that planar compositional waves depended on the elastic constants of the phases with the common orientation. The study revealed that spinodal decomposition is initiated by concentration fluctuations, which change as the temperature decreases in the "softest" directions. When habit planes are perpendicular to these softer directions, domains tend to grow along those planes.

One of the first systems described to form by spinodal decomposition is the Fe-Cr system, whose phase separation has been described by Bremmer *et al.* [75]. An initial solid solution breaks down into two highly interconnected phases with an "interwoven vein-like network." One phase is rich in Fe and the other, in Cr (known as  $\alpha_1$  and  $\alpha_2$ , respectively). The supersaturated Fe-Cr solid solution would first need to order itself to reduce its free energy before spinodal decomposition can take



place. However, this ordered state is not stable, which leads to a spinodal reaction that forms a mixture of two distinct phases before it is completed ( $\alpha_1$  and  $\alpha_2$ ). Another example is what occurs in Ni-Ti alloys [76]. At the start of the precipitation process, a metastable, coherent phase containing traces of the  $L1_2$  superstructure  $Ni_3Ti$  ( $\gamma'$ ) forms along the  $\{100\}$   $\gamma$  matrix planes. This precipitation results from spontaneous phase separation, creating solute-enriched ( $\gamma'$ ) and solute-depleted ( $\gamma$ ) regions.

### *Precipitation-strengthened alloys*

The advantage of coherent precipitation strengthening lies in its ability to enhance the mechanical properties of a material without causing significant reductions in ductility and toughness. This strengthening mechanism involves the formation of precipitate phases within the matrix of a material, where the atomic arrangement of the precipitate is compatible with that of the matrix, resulting in coherent interfaces [73]. Both must have a compatible crystallographic configuration across the coherent interface, which includes a clear orientation relative to each other. For instance, such an interface is formed between the fcc  $\gamma'$  precipitates and the  $\gamma$  matrix in Ni-based superalloys, producing the orientation relationship (OR)  $\langle 010 \rangle_\gamma \parallel \langle 010 \rangle_{\gamma'}$  and  $\{100\}_\gamma \parallel \{100\}_{\gamma'}$ , which is referred to as the cube–cube OR [26].

When there is a mismatch in atomic spacing at the interface, coherence can still be maintained by an internal elastic strain on either or both lattices (*cf.* Figure 6a). These resulting lattice deformations are referred to as “coherency strains”. This coherence ensures that the load transfer between the precipitates and the matrix is more efficient, leading to improved strength [73].

In contrast, a semi-coherent interface forms when the lattice mismatch is sufficiently high, so that it becomes more energetically advantageous to replace the coherent interface with a periodically accommodated arrangement of misfit dislocations (*cf.* Figure 6b). In this case, the strain field of the dislocations overlaps with that of the otherwise coherent interface, which causes the overall interfacial energy reduction, sometimes referred to as “relaxed strain”.

It has been shown that in precipitation-hardened alloys, controlling cooling processes is crucial for modifying microstructure and resultant mechanical properties. For example, in Ni- and Co-based superalloys, the cooling rate can impact the morphology, size and volume fraction of the  $\gamma'$  precipitates, which can in turn affect their mechanical properties [77, 78]. An investigation using differential scanning calorimetry in a Co-based alloy, showed that faster cooling rates led to increased precipitation rates of the  $\gamma'$  phase at different temperatures, and lowered the temperature of maximum precipitation. Furthermore, the cooling rate affected the  $\gamma'$  precipitate shape and size, transitioning from cuboidal to near-spherical as cooling rate increased. These shifts raised the



hardness from  $H_v = 410$  to  $H_v = 441$ , when the cooling rate was increased from  $2.5\text{ }^\circ\text{C}$  to  $40\text{ }^\circ\text{C}$  [78].

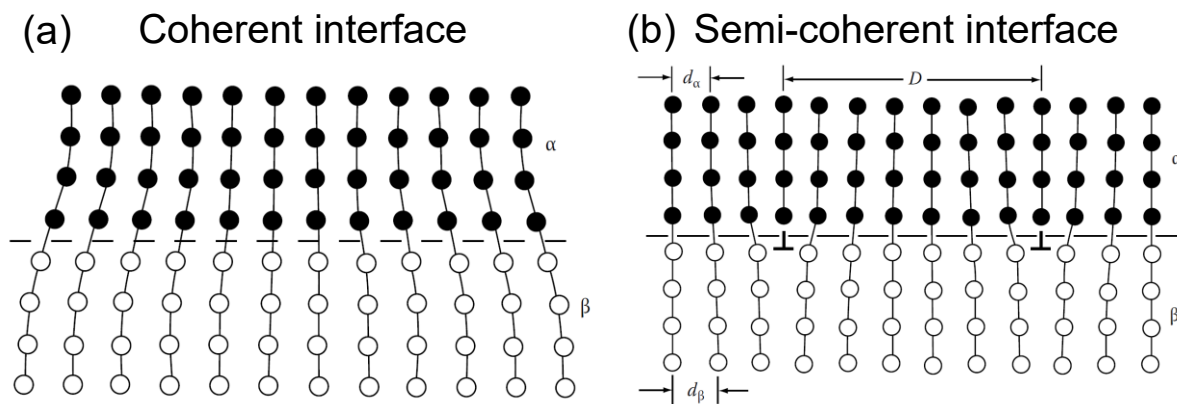


**Figure 6.** Interfaces between two phases with the same crystal structure and lattice mismatch (a) coherent with small lattice mismatch (b) semi-coherent with larger lattice mismatch [73].  $\alpha$  and  $\beta$  represent the two phases of the material, and  $d_\alpha$  and  $d_\beta$ , their interplanar distances.

In a SX Ni-based superalloy, cooling faster after HIP-solution heat treatment yielded a fine and homogeneous  $\gamma/\gamma'$  microstructure. Furthermore, the  $\gamma'$  precipitate volume fraction and size were shown to have a direct influence on the hardness of the material, *i.e.*, for a given  $\gamma'$  phase volume fraction, hardness varies inversely with  $\gamma'$  precipitate and for a given precipitate size, is directly proportional to the volume fraction of  $\gamma'$  precipitates [77].

Recent research indicates that the microstructures and resultant mechanical properties of the CCAs and rCCAs, can also be adjusted by modifying the processing methods with particular emphasis on controlling cooling rates [55, 56]. Munitz *et al.* [34] [79] established that alterations in heat treatments and cooling rates induce changes in the microstructure of the AlCrFeNiTi<sub>0.5</sub> CCA. For instance, by subjecting the alloy to a heat treatment at  $650\text{ }^\circ\text{C}$ , an increase of A2/B2 phases and decrease of the ductile fcc phase is observed, which enhanced the hardness but also reduced the ductility. In a separate study, Xiong *et al.* [80] showed similar findings, where higher cooling rates led to higher proportions of the B2 phase in the Al<sub>0.5</sub>CoCrFeNi CCA, composed of fcc, bcc, and B2 phases. Consequently, this treatment resulted in increased hardness at the expense of ductility.

### Lattice misfit

When two crystals that have slightly different lattice parameters coexist coherently or semi-coherently (*cf.* Figure 6), the mismatch between their lattice sizes, which in turn is related to the interface strain, can be defined by the so-called “lattice misfit”. The misfit ( $\delta$ ) is expressed as a

percentage or a fractional value, representing the relative change in lattice parameters between the two crystals, *e.g.*,  $a_{A2}$  and  $a_{B2}$  for the RSA, following a relationship such as:

$$\delta = \frac{2(a_{A2} - a_{B2})}{a_{A2} + a_{B2}} 100 \quad (2.1)$$

As the chemical composition of the two different phases is different, *i.e.*, the A2 phase in the RSA is rich in Mo, Nb and Ta, and the B2 phase, in Al, Ti and Zr, each phase has a different lattice parameter, with  $a_{A2} < a_{B2}$  due to the partitioning of the elements. From Equation 2.1, the misfit is thus negative, meaning that the A2 precipitates are under hydrostatic tensile stresses and the B2 matrix phase is under compressive stresses. Therefore, elastic strains are developed in the interfaces between the two phases in order to keep the coherency, *i.e.*, A2 precipitates and the B2 matrix would respectively correspond to  $\alpha$  and  $\beta$  in Figure 6a, which may also evolve to semi-coherent interfaces as in Figure 6b. Often, the misfit studied at coherent interfaces such as presented in Figure 6a is referred to as “constrained lattice misfit” [26], although it is not the misfit itself but the bonded atoms that are constrained, which are found at the interface. The distinction is made between the latter scenario and one for “unconstrained misfit”. In this case, the lattice parameters of materials are compared, which are not bonded with each other or, *e.g.*, where the additional strain fields of dislocations in Figure 6b are assumed to create a state comparable to two separate materials, (*e.g.*, [81]).

The lattice misfit of dual-phase materials, wherein precipitates are seamlessly incorporated into a matrix sharing similar structure, can influence the shape and kinetics of precipitate formation, their resistance to coarsening, and the mechanical response. In spinodally decomposed alloys, for instance, elastic strain fields can form around particles that precipitate coherently in the matrix phase due to the lattice parameter differences of the two phases. Wang *et al.* [82] described this phenomenon specifically for cubic-structured alloys, in their two-dimensional (2D) study on the kinetics of such systems. Two contributions can be responsible for the particle shape in the precipitation process, *i.e.*, interfacial and strain energies. If the total interfacial free energy is not minimized, for instance by coarsening of the precipitates, the microstructure of a two-phase alloy is always unstable. Moreover, when the strain energy is sufficiently high, which depends on lattice misfit between the phases and on their elastic constants, considering their anisotropy, concentration waves develop along elastically soft directions. For the 2D example in Wang *et al.* [82], the latter are [100] and [001], as observed in  $\gamma'$ -phase precipitates in NiAl alloys [82, 83]. Over time, however, this anisotropic growth becomes disrupted, and coarsening occurs mostly in one of the directions, *e.g.*, [100].

### 2.3 The CALPHAD method

CALculation of PHase Diagram (CALPHAD) is a method that allows to predict the thermodynamic behavior of highly-complex multicomponent materials by minimizing the total Gibbs energy of each phase in a system, extrapolating from lower-order binary and ternary systems into high-order properties [84]. Property diagrams are graphical representations that show thermodynamically distinct phases coexisting in equilibrium plotted against a thermodynamic variable (pressure, temperature, volume, etc.), while keeping fixed others [85]. [Figure 7 a](#) and [c](#) show examples of equilibrium property diagrams, the most common ones, as calculated using CALPHAD method for the RSA [16, 49], where the mole fractions of phases at equilibrium are plotted against temperature (see description below).

The validity of a CALPHAD calculation depends solely on the thermodynamic database used, which consist of optimized thermodynamic model parameters for all phases in binary and ternary systems [86]. However, many thermodynamic databases available today are designed for conventional alloys with a single principal element, as they rely on accurate available thermodynamic and kinetic data for various phases present in a material system. For conventional binary alloys, there is often extensive experimental data available for phase equilibria, which makes constructing accurate databases more straightforward. The fact that several CCAs contain more than 5 base elements brings many challenges when designing alloys with specific requirements, due to the scarce or incomplete available experimental data. For these cases, commercial software, such as Thermo-Calc [87], Pandat [88] and FactSage [89] have been further developed to design new materials and products [87, 90, 91]. Many investigations using the CALPHAD method on CCAs have employed databases originally designed for other material types, with Pandat and Thermo-Calc as the most common calculation tools [4, 90, 92-94].

If we consider the RSA composition, some related works can be mentioned, which relate to its development. For example, based on the ternary NbTiZr (equiatomic) alloy, Senkov *et al.* [90] calculated equilibrium property diagrams for ten extended CCA quaternary systems, using the PanNb2018a database. In the calculations, Al, Cr, Fe, Hf, Mo, Re, Si, Ta, V and W were added at a time with ranges from 0 to 25 at. %. The study revealed that certain compositions favored the formation of single BCC alloys at specific temperature ranges. However, the alloys containing elements with limited solubility in the BCC NbTiZr matrix exhibited the formation of additional phases [90]. Some representative alloys that showed a good agreement with CALPHAD calculations were then cast [90]. Furthermore, in a following work, Senkov *et al.* [4] calculated the property diagrams for different rCCAs beyond quaternaries using the CALPHAD approach with ThermoCalc and Pandat. They established a relationship between experimental mechanical data at

high temperature (1000 and 1200 °C) and the alloy compositions, melting point, and volume fraction of the phases contained in the rCCAs.

When some additional assumptions are made, the CALPHAD approach may also be extended to non-equilibrium systems if multi-dimensional phase diagrams are involved. Based on the assumption of homogeneous composition in the liquid, no diffusion in the solid and full thermodynamic equilibrium at the solid/liquid phase interface, the Scheil-Gulliver equation predicts the amount of solid at different temperatures or the amount of micro-segregation during solidification [95, 96]. [Figure 7b](#) shows an example of such a simulated solidification using the Scheil approach for the RSA, which will be described in detail in the following subsection.

The unexplored complexity of CCAs with respect to conventional alloys drives the special effort to understand the equilibrium and non-equilibrium phases in these alloys. Therefore, in 2017 the new thermodynamic database TCHEA1 [87] was developed by Thermo-Calc for the design of CCAs and HEAs, which consists of 105 binaries and 200 ternaries and contains all the stable solid solution and intermetallic phases in each of the assessed systems. This database enables to predict the stability of the desired multicomponent solid solutions relative to intermetallics and other solid solutions.

#### *CALPHAD analysis for the RSA*

Senkov *et al.* [48] conducted a thermodynamic calculation of the RSA using the commercial software Pandat with the PanTi database. They calculated the equilibrium property diagram and the non-equilibrium solidification through the Scheil model. In the latter, the solidification was predicted to start at 2046 K ( $\approx 1773$  °C) by the formation of a disordered bcc phase, followed by  $\approx 0.3\%$  of  $\text{Al}_2\text{Zr}_3$  at 1391K ( $\approx 1118$  °C), with T solidus ( $T_s$ ) at 1314 K ( $\approx 1041$  °C), as shown in [Figure 7b](#). The calculated property diagram also anticipated the formation of one bcc phase (enriched with Mo, Nb and Ta) in equilibrium conditions ([Figure 7a](#)). With decreasing temperature, the “BCC” phase partially transforms to the  $\text{Ti}_3\text{Al}$ -based ( $\text{Ti}_2\text{ZrAl}$ ) phase, and later additionally to the  $\text{Al}_2\text{Zr}_3$  intermetallic phase, as shown in [Figure 7a](#). The remarkable discrepancy between the experimentally observed phase compositions and the calculations was attributed to the limitations of the PanTi database, originally developed for Ti-rich alloys [48].

Many attempts of modelling phase equilibria for the RSA were later performed with several different databases by Whitfield *et al.* [16]. Their calculations suggested that the high-temperature phases were not maintained at lower temperatures. Among these attempts, the ThermoCalc SSol5 database yielded the closest match to the experimental data, particularly in predicting the formation of the  $\text{Al}_4\text{Zr}_5$  intermetallic, as shown in [Figure 7c](#). However, some differences in the solvus

temperatures still exist. The authors therefore encouraged the improvement of the current databases for more reliable predictions.

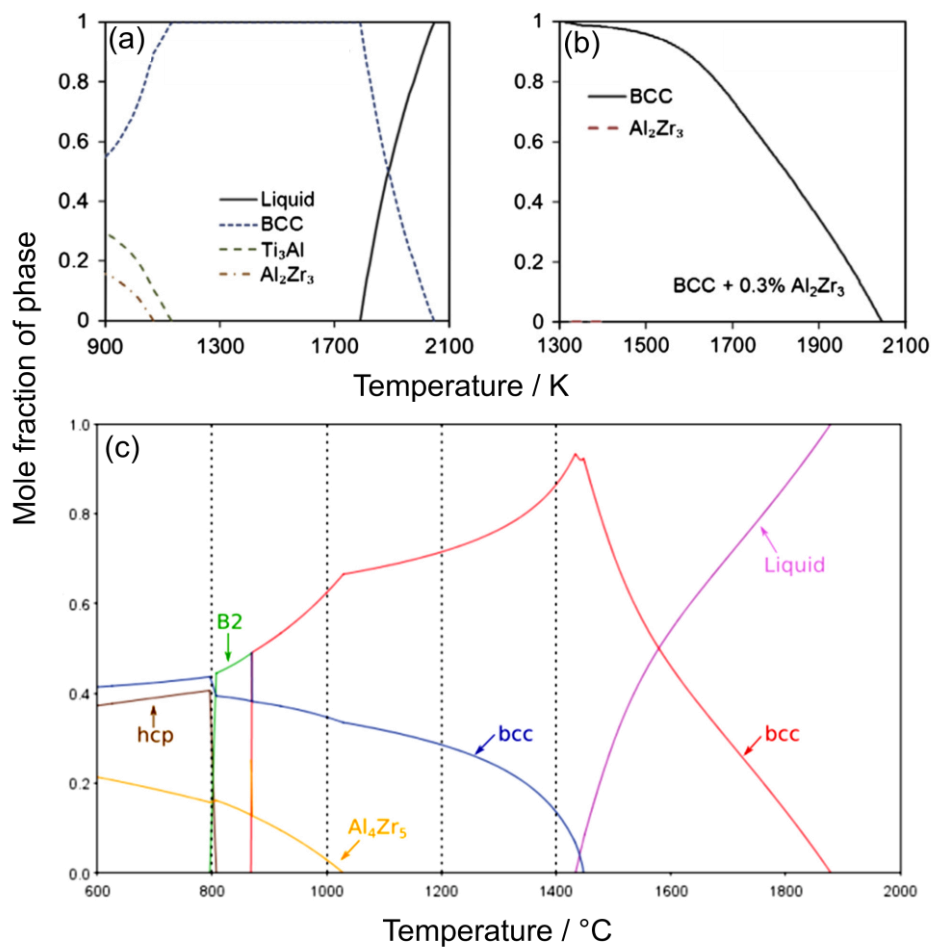


**Figure 7.** Phase fraction vs. temperature (property) diagrams calculated for the RSA by CALPHAD. (a) Equilibrium phase diagram and (b) non-equilibrium solidification (Scheil), reported in [48] (c) Simulated equilibrium phase diagram, reported in [16].

## 2.4 Mechanical properties and microstructure of the RSA $AlMo_{0.5}NbTa_{0.5}TiZr$

To date, compression tests are the only source for mechanical properties reported for the RSA  $AlMo_{0.5}NbTa_{0.5}TiZr$ . In this section, the hitherto reported compression properties, microstructural aspects and thermal stability of the RSA are presented.

### *Compression properties*

The first study on mechanical properties of RSA appeared in 2014, when Senkov *et al.* [7] reported results of compression tests carried under vacuum at room temperature, 800 and 1000 °C for several Al-containing alloys, including the RSA. There, it was described that the room temperature microhardness ( $H_v = 5.8 \pm 0.1$  GPa ( $\approx 591$  HV) [12, 48]) and strength was markedly higher than

the respective properties of the CrMo<sub>0.5</sub>NbTa<sub>0.5</sub>TiZr rCCA (9.4 % and 12.7 % higher, respectively) [7], which only compositional difference to the RSA is the complete replacement of Al with Cr. The enhanced properties were attributed to the coherent A2/B2 structure with the cube-cube OR, where they roughly estimated the lattice misfit to be as high as  $\approx -1$  %. By employing the rule-of-mixture, it was calculated that the cuboidal A2 precipitates exhibit higher stiffness than the B2 channels, with elastic moduli  $E=164$  GPa and  $E=115$  GPa, respectively [12]. Later, those same properties were complemented in 2016 with data for 600 and 1200 °C. [Table 1](#) summarizes the mechanical properties in compression of the RSA, as reported by Senkov *et al.* [12].

**Table 1.** Compression properties ( $\sigma_{0.2}$ ,  $\sigma_p$  and  $\delta$ ) of the RSA reported in [12].

Temperature (°C)	Maximum compression strength in MPa ( $\sigma_p$ )	Compression yield strength in MPa ( $\sigma_{0.2}$ )	Fracture strain in % ( $\delta$ )
23	2368	2000	10
600	2210	1870	10
800	1810	1597	11
1000	772	745	>50
1200	275	250	>50

It became evident that the RSA exhibited a higher yield strength ( $\sigma_{0.2}$ ) and specific yield strength ( $\sigma_{0.2}/\rho$ ) in compression than three common polycrystalline Ni-based superalloys in tension at all studied temperatures (*cf.* [Figure 8](#)) [48]. According to Senkov *et al.* [12], the high-temperature strength of the RSA is due to the large volume fraction of possibly coherent interface, which they assumed to be maintained at 1200 °C and to inhibit deformation transfer between phases, as it occurs in Ni-based superalloys.

Since the presence of the hexagonal intermetallic affects ductility at room temperature, the influence of compositional variations on the compression properties of the RSA were investigated in an effort to enhance its mechanical characteristics, especially at room temperature [51]. By removing Mo, the ductility improved, and the plastic flow stress at 1000 °C decreased due to the absence of the corresponding solid solution strengthening. When Mo is replaced with Ta, the strength at RT and 1000 °C is decreased by  $\approx 600$  MPa and 150–200 MPa, respectively. The alloys with Al and Mo reduction had a decrease of flow stress by  $\approx 50$  % after 20 % plastic strain (in compression at 1000 °C), attributed to the fact that for these alloys the A2 formed the continuous matrix and the B2 phase, the discontinuous precipitates (a mechanism already observed in Ni-based superalloys [97, 98]). Additionally, a lower Al content in the base alloy resulted in a lower disorder-order transformation temperature. Therefore, the Al-lean alloys (*i.e.*, Al<sub>0.5</sub>Mo<sub>0.5</sub>NbTa<sub>0.5</sub>TiZr and Al<sub>0.25</sub>NbTaTiZr) exhibited reduced strength and deformation softening at 1000°C.

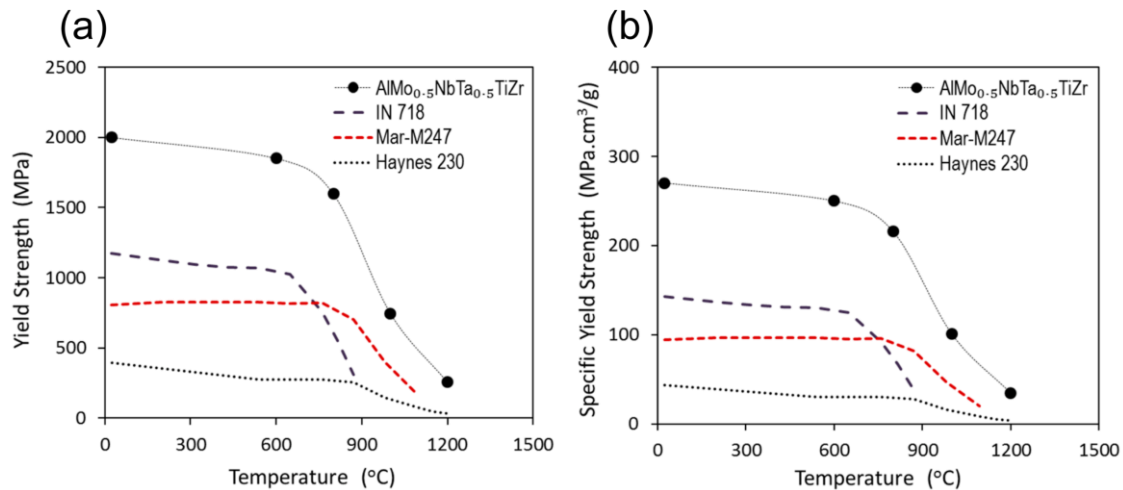


**Figure 8.** Comparison of the temperature-dependent strength for RSA and three different Ni-based alloys (a)  $\sigma_{0.2}$  and (b)  $\sigma_{0.2}/\rho$  [12].

### Microstructure

As mentioned above, the RSA was one of 6 Al-containing rCCAs studied by Senkov *et al.* [48]. The substitution of Cr by Al in the then already reported CrMo<sub>0.5</sub>NbTa<sub>0.5</sub>TiZr rCCA (with  $\rho = 8.23$  g/cm<sup>3</sup>) [7] produced several beneficial effects, among which the reduction of the density (7.40 g/cm<sup>3</sup>), and the suppression of the brittle Laves phase (which improves the ductility at room temperature) were critical. The annealed state (AN) of the RSA was achieved through HIP at 1400 °C and 207 MPa for 2 hours, followed by annealing at 1400 °C for 24 hours and cooled at a rate of 10 °C/min. The microstructure of the RSA was then characterized by equiaxed grains ( $\approx 75$   $\mu$ m), low angle grain boundaries (LGBs) and large second-phase particles at the grain boundaries. Furthermore, two distinct bcc phases were identified, each of which had different lattice parameters: one phase was rich in Ti, Al and Zr, while the other one was rich in Nb, Mo and Ta [48].

Afterwards, a deeper microstructural study of this alloy was performed by Senkov *et al.* [12]. The SEM-BSE images showed a microstructure that consisted of an Al-Zr-rich secondary coarse phase at the grain boundaries (*cf.* Figure 2a), and a basket-weave substructure within grains. Further crystal structure analysis by x-ray diffraction (XRD) together with TEM and atom probe tomography (ATP) revealed that the basket-weave substructure was formed by bcc precipitates (A2) with cuboidal and plate-like morphologies ( $\approx 10$ – $55$  nm in size) at a high-volume fraction ( $\approx 62$  %), which was embedded (coherently, they presumed) in a continuous matrix of B2 phase ( $\approx 7$  nm channel thickness). The A2/B2 substructure presented a cube-on-cube orientation along the [100] direction (OR:  $\langle 100 \rangle_{\text{bcc}} \parallel \langle 100 \rangle_{\text{B2}}$ ,  $\{001\}_{\text{bcc}} \parallel \{001\}_{\text{B2}}$  [99]). A mechanism by which the RSA can form from the disordered high temperature bcc phase by spinodal decomposition was described.



By comparing the intensities in STEM-HAADF images of the AN and a state aged at 1000 °C for 6 h, Kloenne *et al.* [100] estimated the sub-lattice occupancy of the B2 phase. They described a likely spinodal reaction among the aging or following quenching to room temperature in the aged condition. According to their proposal, the products of this spinodal decomposition could be two differing B2 phases or a mixture of bcc + B2 phases.

In a following work, Kadirvel *et al.* [101] studied the phase transformation pathway (PTP) that leads to the A2/B2 substructure via the phase-field method. The system evolution is represented in [Figure 9](#), where the current system is marked with the white squares [101]. According to their simulated PTP, a coherent ordering transformation of the initial bcc solid solution (1) is followed by the spinodal decomposition (2). During cooling, chemical modulations appear, which result in two distinct phases with the same B2-ordered structure (3 and 4). Then, a congruent disordering reaction leads to partly rafted bcc precipitates within an ordered B2 matrix from the discontinuous B2 phase (5 through 8). Although none of the steps presented in [Figure 9](#) match the microstructure of the RSA, step (8) matches the microstructure of the alloy annealed at 1000 °C for 6 hours [100, 102]. According to Jensen [102], annealing at elevated temperatures appears to cause the A2 precipitates to coalesce, resulting in a rafted structure, suggesting that only metastable structures can be formed in the AN state of the RSA.

Regarding the coarse Al-Zr-rich phase along the grain boundaries, the first and only detailed study of this phase was conducted by Jensen [102]. The structure of this Al-Zr-rich ( $\approx 37$  at. % Al and 42 at. % Zr) grain boundary phase was determined by convergent beam electron diffraction (CBD) and high-resolution STEM-HAADF images: it is an intermetallic phase with hexagonal ordered  $P6_3/mcm$  space group (lattice parameters:  $a = 8.31 \text{ \AA}$ ,  $c = 5.52 \text{ \AA}$ ), and incoherent with the A2 precipitates.

After 50% compression strain at 1000 °C, XRD revealed that the RSA contained the same phases with nearly identical lattice parameters as observed before deformation, *cf.* [Figure 10](#) [12] (325.0 pm and 332.2 pm for the two bcc-based phases they could index, one of them being the B2 phase). In [Figure 10a](#), a relief was found within the grains with elongations in the directions of the local plastic flow, as well as coarsening of the subgrain structure inside the grains ([Figure 10b](#)). The characteristic relief inside the grains is believed to be a result of local material flow through the interface boundaries of the A2/B2 substructure. Grain boundaries still contained the Al-Zr-rich as the second phase [48].



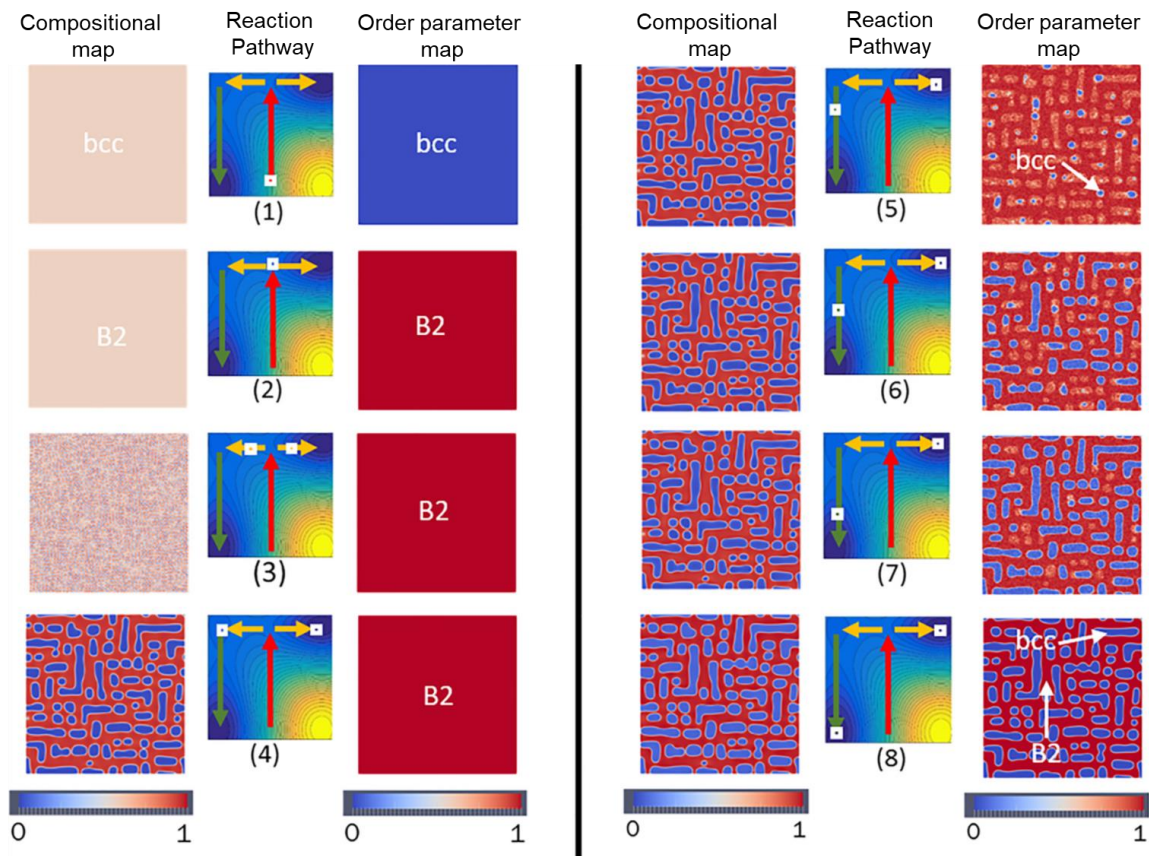


**Figure 9.** Phase-field simulations during the reaction pathway showing the composition and order parameter maps that describe the microstructure formation in the RSA. (1) before and (2) after the congruent ordering reaction (3) during and (4) after spinodal decomposition (5) nucleation of the disordered phase, (6) and (7) the final microstructure after partial congruent disordering [101].

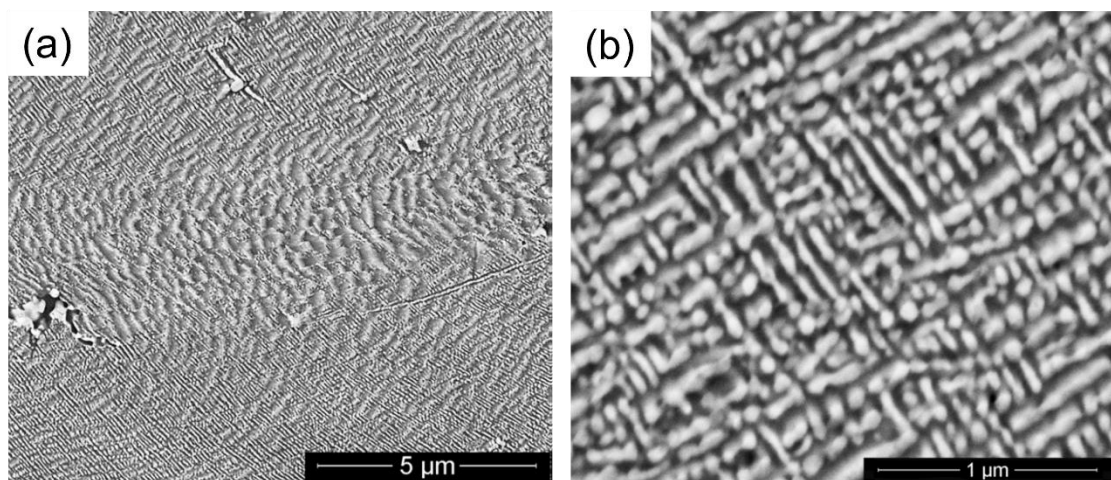


**Figure 10.** SEM-BSE images of RSA microstructure after 50 % compression strain at 1000 °C at (a) low magnification and (b) high magnification [12].

The impact of Zr reduction and Mo remotion on the microstructure of the RSA was also reported [51]. Zr reduction ( $\text{AlMo}_{0.5}\text{NbTa}_{0.5}\text{TiZr}_{0.5}$ ) does not eliminate the hexagonal phase, but it hinders

A2 phase formation, as the alloy composition is shifted beyond the miscibility gap. Consequently, the grains consist of a single B2 phase, implying that Zr plays a significant role in the formation of the two-phase nanostructure. With the additional removal of Mo ( $\text{AlNbTa}_{0.5}\text{TiZr}_{0.5}$ ), B2 single phase is also observed, and the grain boundaries still exhibit small amounts of hexagonal phase, which was attributed to the reduced solubility of Al in the B2 phase. When Mo is present, it partitions towards the Nb- and Ta-rich phase due to its complete solubility with these elements. With a reduction of Al ( $\text{Al}_{0.5}\text{Mo}_{0.5}\text{NbTa}_{0.5}\text{TiZr}$  and  $\text{Al}_{0.25}\text{NbTaTiZr}$ ), the Al-Zr-rich intermetallic is avoided, although it does not affect the formation of a B2 matrix with A2 precipitates. The Al reduction may cause a supersaturation of Zr and produce Zr-rich bristles in the microstructure [51].

### *Thermal stability*

The thermal stability of the RSA is highly important to understand long term high temperature properties, particularly in the context of creep testing. Whitfield *et al.* [16] revealed that the A2/B2 microstructure was unstable after exposure to 800, 1000, and 1200 °C for 1000 hours, as seen in [Figure 11](#). With increasing temperature, precipitation of the Al-Zr-rich phase also extended to grain interiors. At 800 and 1000 °C, the A2 and B2 phases underwent coarsening and experienced changes in morphology. This phenomenon was attributed to a reduction in surface energy and agglomeration of the cuboidal particles due to diffusion in a similar fashion to the well-known “rafting” process in Ni-based superalloys. Remarkably, at 1200 °C, the A2/B2 substructure vanished, resulting in a mixture of approximately 50-50% of A2 phase and Al-Zr-rich intermetallic, likely due to the Al reduction and refractory elements enrichment in the former B2 phase.

In their study, Kloenne *et al.* [103] investigated the microstructural evolution of the A2/B2 substructure after aging (1000 °C for 6 hours) followed by water quenching. They observed that the patterned microstructure remained unchanged, with the same volume fraction as the initial state, but with coarsened A2 precipitates along the  $\langle 100 \rangle$  directions. The authors noted that after aging, the Al content in the B2 phase decreased, as Ti segregated less strongly compared to Zr and Al.

In a follow-up study, Kloenne *et al.* [100] reported on the interface structure of the A2/B2 phase. After the 6 hours exposure at 1000 °C, the evolution involved transitioning from planar coherent interfaces along the  $\langle 100 \rangle$  to stepped interfaces with facets formed along the (110) and (100) planes at a 15° angle from the (100) plane. However, the coherency was maintained, as confirmed by full lattice registry along the new {110} and old {100} facets. The high-resolution STEM analysis revealed lattice parameters of 3.31 Å for the A2 precipitates and 3.38 Å for the B2 matrix, with which a lattice misfit of -2.1% was determined. Additionally, misfit dislocations were observed along the (110) planes, having a Burgers vector of  $1/2[111]_{\text{A2}}$ . The dislocation spacing was

estimated to be  $\approx 13.7$  nm using the Brooks equation  $\delta = |\mathbf{b}|/d$  ( $|\mathbf{b}|$ : magnitude of the Burgers vector  $d$ : dislocation spacing [104]), and later confirmed through image analysis [100].

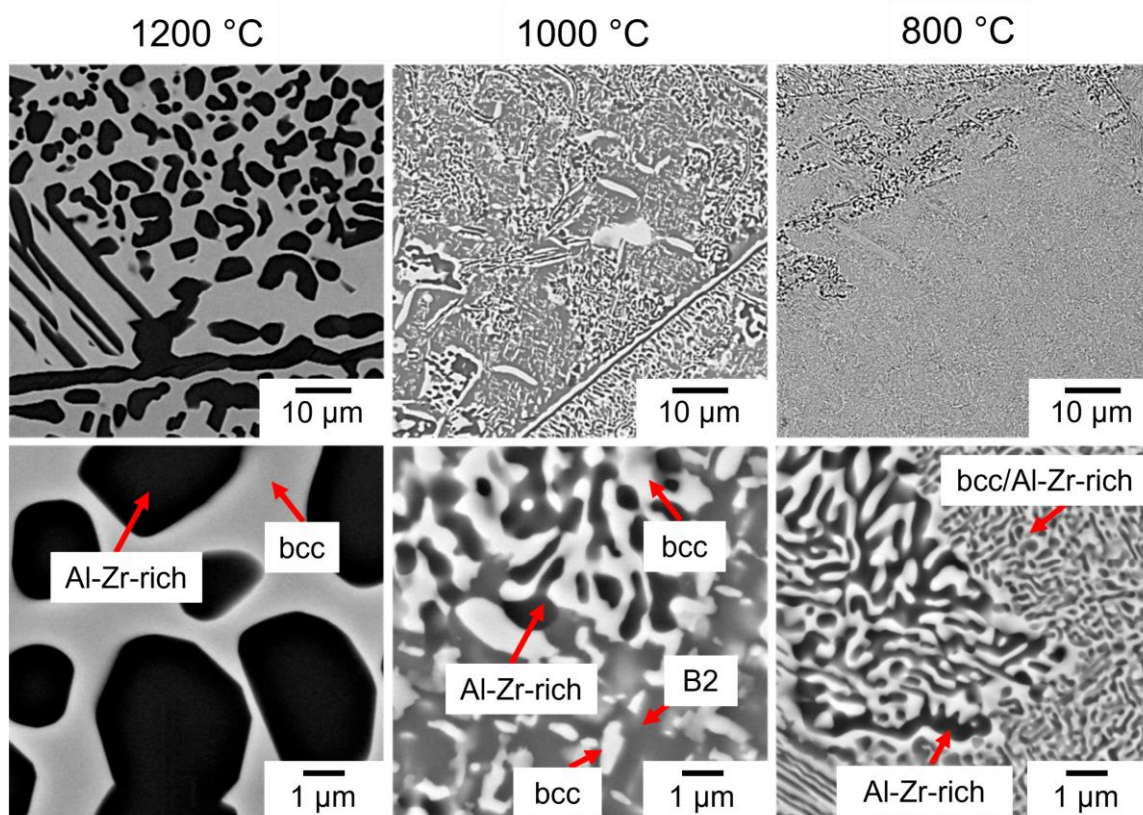


**Figure 11.** Microstructure of the RSA after exposure for 1000 h at 1200, 1000 and 800 °C [16].

## 2.5 Intrinsic properties of individual phases in RSA

An overview of the intrinsic properties of the phases observed in the RSA is provided in this section, including bcc solid solution (A2), B2 ordered phase, and the relevant intermetallics containing Al and Zr:  $\text{Al}_3\text{Zr}_5$  and  $\text{Al}_4\text{Zr}_5$ .

### *Disordered bcc (A2)*

The bcc phase is formed by a cubic unit cell with 1/4 atoms sitting at the cube corners and one atom in the center of the cube, which make a total of 2 atoms per unit cell, and a coordination number of 8 equidistant nearest neighbors (*cf.* Figure 12). The lattice cell can be described by the space group  $Im\bar{3}m$  (229), with a Pearson symbol  $cI2$  (W-prototype) and a *Strukturbericht* notation “A2” [105, 106].



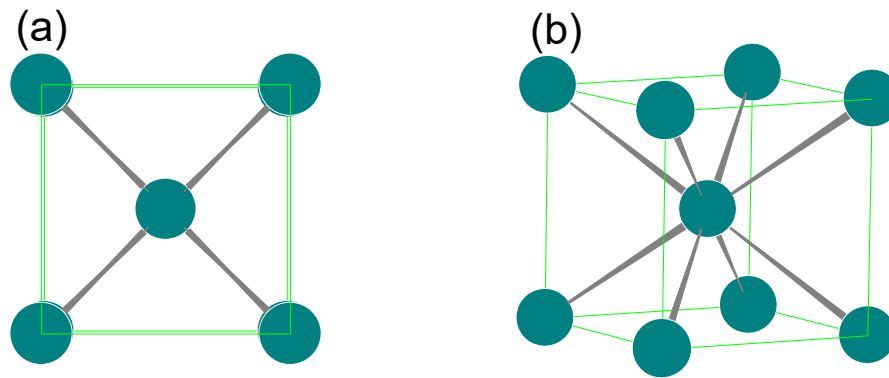


**Figure 12.** Schematic representations of an A2-structured unit cell created using the PowderCell software [107] (a) front view (b) tilted side view. The atoms are represented with the same color since all the lattice sites are randomly populated by different elements.

Most refractory metals (Mo, Nb, Ta, and W) have the A2 crystal structure. These metals share some properties, such as high melting points ( $> 2000$  °C), high density, and high  $H_v$  at RT (*cf.* Table 2) [43]. Furthermore, other metals with a lower density but also lower melting points, such as Cr, Fe, V and Zr, are A2-structured, and show also lower  $H_v$  while keeping higher ductility (Table 2).

**Table 2.** Properties of metallic elements with disordered bcc crystal structure at room temperature with the space group  $Fm\bar{3}m$  (225), and *Strukturbericht* designation “A2” [105], as reported in [43].

Element	Atomic number $Z^a$	Atomic radius (pm) <sup>a</sup>	Lattice parameters $a$ (pm) <sup>c</sup>	Density $\rho$ (g/cm <sup>3</sup> ) <sup>a</sup>	Melting temperature $T_m$ (°C) <sup>a</sup>	Young's Modulus $E$ (GPa) <sup>a</sup>	Vickers hardness (MPa) <sup>a</sup>
Cr	24	124.91	288.4	7.19	1907	279	1060
Fe	26	124.12	285.6	7.88	1538	211	608
Mo	42	136.26	315.0	10.23	2623	329	1400–2740
Nb	41	142.9	302.0	8.58	2477	105	870–1320
Ta	73	143	330.3	16.68	3017	186	873–1200
V	23	131.6	330.1	6.12	1910	128	628–640
W	74	136.7	316.5	19.41	3422	411	3430–4600

<sup>a</sup> Values taken from Ref. [43], <sup>b</sup> Values taken from Ref. [108], <sup>c</sup> Values taken from Ref. [109]

In general, alloys with single A2 structure exhibit a broad spectrum of fracture toughness ( $K_{Ic}$ ) and  $H_v$ . W and some W alloys may present  $H_v=367\text{--}389$  HV [110] and  $K_{Ic}=5.4\text{--}13.5$  MPa·m<sup>1/2</sup> [111]. Mo-based alloys, have  $H_v=230\text{--}262$  HV [112], and  $K_{Ic}=10.0\text{--}27.5$ ,  $27.8\text{--}147.32$  and  $14.6\text{--}38.5$  MPa·m<sup>1/2</sup> for TZM-Mo (Titanium-Zirconium-Molybdenum), ODS-Mo (Oxide Dispersion Strengthened), and LCAC-Mo (Low Carbon Arc Cast) alloys, respectively [113]. The majority of

reported rCCAs are single-phase A2 structures. Table 3 shows an overview of compressive mechanical properties of most relevant A2 single phase rCCAs reported in the literature, taken from Ref. [43], which include Al-containing  $\text{Al}_{0.4}\text{Hf}_{0.6}\text{NbTaTiZr}$ ,  $\text{Al}_{0.3}\text{NbTa}_{0.8}\text{Ti}_{1.4}\text{V}_{0.2}\text{Zr}_{1.3}$ , and  $\text{AlNb}_{1.5}\text{Ta}_{0.5}\text{Ti}_{1.5}\text{Zr}_{0.5}$ , as well as Al-free  $\text{HfNbTaTiZr}$ ,  $\text{NbMoTaW}$ , and  $\text{NbMoTaVW}$ . The  $\text{HfNbTaTiZr}$  rCCA exhibits better RT tensile ductility and malleability. The ductility of bcc alloys is generally lower than that of fcc-structured alloys. However, alloys formed by a single bcc phase, or at least those that contain this phase as their matrix phase, have a better RT ductility than alloys with ordered structures. In addition to the compressive tests, a limited number of tensile tests have been performed, most notably on  $\text{HfNbTaTiZr}$  rCCA at a strain rate of  $10^{-3} \text{ s}^{-1}$ . For example, the yield strength  $\sigma_y$  was reported to be  $\approx 940\text{-}958 \text{ MPa}$  (depending on the average grain size) at RT, and elongation to fracture  $\delta \approx 15\text{-}20 \%$  [114].

A separate investigation on the stability of this alloy, showed that the  $\text{HfNbTaTiZr}$  undergoes phase decomposition below  $\approx 1025 \text{ }^\circ\text{C}$ , resulting in two bcc phases, *i.e.*, HfZr-rich and NbTa-rich. Additionally, the HfZr-rich phase transforms into a hexagonal closed-packed structure (hcp) phase. The precipitates have a similar orientation to the matrix but with a slight tilt due to large lattice misfit, whereas the hcp phase follows the OR  $\{0001\}_{hcp} \parallel \{1\bar{1}0\}_{bcc}$  and  $\{2\bar{1}\bar{1}0\}_{hcp} \parallel \{111\}_{bcc}$ . This results in a strengthening mechanism by solid solution and precipitation, where the rCCA becomes stronger at lower annealing temperatures and weaker at higher annealing temperatures [115]. Generally,  $\text{Al}_{0.4}\text{Hf}_{0.6}\text{NbTaTiZr}$  [116],  $\text{AlMoNbTi}$  [117],  $\text{HfMoNbTaTiZr}$  and  $\text{HfMoTaTiZr}$  [62] also satisfy these conditions, having a metastable single A2 microstructure at RT, and after annealing at high temperature, they experience phase transformations and become multi-phase structures.

In the  $\text{AlMo}_{0.5}\text{NbTa}_{0.5}\text{TiZr}$  RSA, the bcc phase is enriched in the refractory elements, *i.e.*, Mo, Nb and Ta, which is the phase that forms the plate-like precipitates embedded in the B2-structured phase.

As rCCAs are notably desirable for high-temperature applications, evaluating their creep properties becomes exceptionally important. Consequently, understanding these properties becomes essential in assessing the suitability of rCCAs for the intended applications. Thus, the upcoming subsection will lay down the core concepts of creep and the latest developments concerning creep in rCCAs with single bcc solid solution phases.

**Table 3.** Density,  $H_v$ , and compression properties ( $E$ ,  $\sigma_y$  and  $\varepsilon$ ), at different temperatures of some relevant CCAs containing refractory elements with single phase bcc crystal structure [4]. All materials were cast before the subsequent treatments.

Alloy	Processing	Density (g/cm <sup>3</sup> )	$T$ (°C)	$E$ (GPa)	Vickers Hardness ( $H_v$ , MPa)	$\sigma_y$ (MPa)	$\varepsilon$ (%)	Reference
Al <sub>0.4</sub> Hf <sub>0.6</sub> NbTaTiZr	HIP at 1200 °C / 2 h / 207 MPa + 1200 °C / 24 h	9.05	23	78	4.9	1841	10	[49]
			800	48.8		796	>50	
			1000	23.3		298	>50	
Al <sub>0.3</sub> NbTa <sub>0.8</sub> Ti <sub>1.4</sub> V <sub>0.2</sub> Zr <sub>1.3</sub>	HIP at 1200 °C / 207 MPa / 2 h, 1200 °C / 24 h	7.78	25		4.9	1965	5	[48]
			800			678	>50	
			1000			166	>50	
AlNb <sub>1.5</sub> Ta <sub>0.5</sub> Ti <sub>1.5</sub> Zr <sub>0.5</sub>	HIP 1400 °C / 207 MPa / 2 h, 1400 °C / 24 h	6.88	25		4.0	1280	3.5	[48]
			800			728	30	
			1000			403	>50	
HfNbTaTiZr	HIP at 1200 °C / 207 MPa / 2 h, 1200 °C / 24 h	9.94	23	55	509 [118]	929	>50	[62]
			600			675	>50	
			800			535	>50	
			1000			295	>50	
			1200			92	>50	
NbMoTaVW	As-cast [119],	12.36	23		5.42 GPa	1246	1.7	[10, 119]
			600			862	13	
			800			846	17	
			1000			842	19	
			1200			735	7.5	
			1400			656	18	
			1600			477	13	
NbMoTaW		13.75	23		4.46	1058	1.5	[10, 119]
			600			561		
			800			552		
			1000			548	16	
			1200			506	12	
			1400			421	9	
1600		405	27					

### Creep

Creep is defined as the time-dependent ( $t$ ) strain ( $\varepsilon$ ) that occurs under a constant stress ( $\sigma$ ) that is lower than the yield stress, at temperatures ( $T$ ) generally higher than half of the melting temperature ( $> 0.5T_m$ ). The creep behavior is usually represented by determining a tensile or compression creep curve. Figure 13 shows the most common typical creep curves: (a) deformation vs. time “ $\varepsilon$  vs.  $t$ ”, and (b) “strain rate ( $\dot{\varepsilon}$ ) vs.  $\varepsilon$ ”. Figure 13a exhibits three distinct regions: (I) an initial stage known as *primary creep*, which shows an increase in  $\varepsilon$  due to an increase in dislocation density ( $\rho_d$ ). However, as  $t$  progresses and the  $\varepsilon$  increases, a *steady state* (*ss*) emerges where there is a balance between multiplication (strain hardening) and annihilation (recovery) of dislocations, referred to as *secondary creep* (II), and it is where the minimum creep rate occurs  $\dot{\varepsilon}_{min}$ . Since stage II has a characteristic constant creep rate or  $\dot{\varepsilon}_{ss}$ , is technically of the highest importance. Finally, when the  $\dot{\varepsilon}$  increases again after the secondary creep, further damage in terms of pores and cracks may form, resulting in a decrease in creep resistance and a connected increase in creep rate. This stage is called *tertiary creep* (III) (cf. Figure 13a). An increase in  $T$  or in  $\sigma$  has been found to promote a lower creep resistance in the same alloy as a result of an increase of  $\rho_d$ .

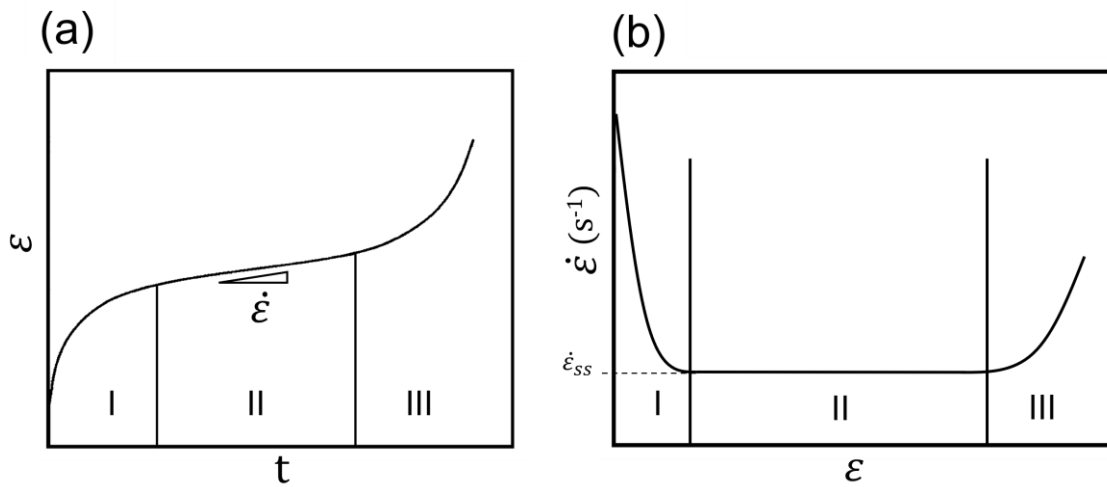


**Figure 13.** Creep curves of pure metals (a)  $\varepsilon$  vs.  $t$  showing the regions for primary (I), secondary or steady state (II, *ss*) and tertiary creep (III) (b)  $\dot{\varepsilon}$  vs.  $\varepsilon$  at constant  $T$  and  $\sigma$  [120].

A relationship between the secondary creep strain rate ( $\dot{\varepsilon}_{min}$ ) and  $\sigma$  is described by the Norton’s equation [121]:

$$\dot{\varepsilon}_{min} = A\sigma^n \exp\left(-\frac{Q_c}{RT}\right) \quad (2.2)$$

where  $A$  is a material constant,  $Q_c$  is the activation energy for creep,  $R$  is the gas constant ( $8.314 \text{ J}\cdot\text{K}^{-1}\cdot\text{mol}^{-1}$ ), and  $T$  is the absolute temperature in Kelvin. This exponential behavior is also called “power-law creep”. Using a linear fit in the  $\dot{\varepsilon}_{min}$  vs.  $\sigma$  curve, the stress or Norton exponent  $n$  can be

determined from the slope of the curves, as shown in Figure 14 for pure Al [119]. Depending on the stress exponent  $n$ , different mechanisms can be inferred in creep, the slowest ones being rate-controlling.

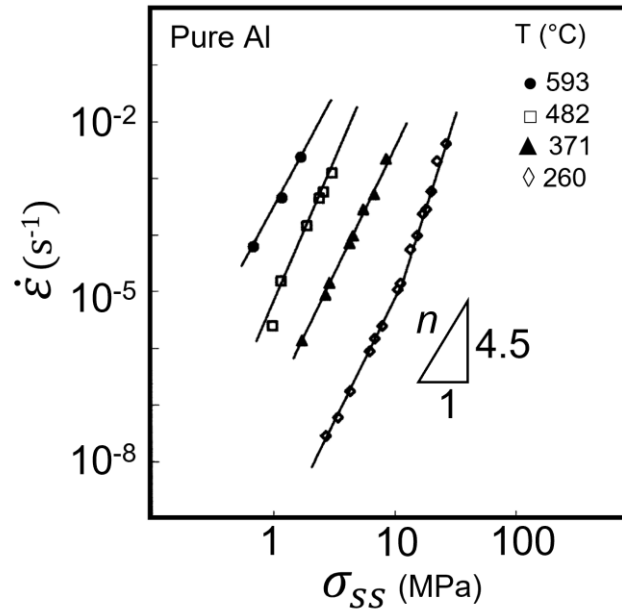


**Figure 14.**  $\sigma_{ss}$  vs.  $\dot{\epsilon}_{min}$  for high pure Al at different  $T$ , presented in [120] from Ref. [122].

With increasing  $T$ , which is usually associated with a decrease in  $\sigma$ , work-hardening typically decreases, leading to lower values of  $n$ . Conversely, at lower  $T$ ,  $n$  tends to be higher.

When  $\sigma$  is insufficient to induce dislocation creep, creep is controlled by diffusional mechanisms that are associated with  $n \approx 1$ , and which are primarily governed by stress-induced vacancy migration through grain boundaries. If  $T$  is very high, and there is an excess of vacancies, volume diffusion occurs, also known as Nabarro-Herring creep. During this process, the excess vacancies migrate from the grain boundaries aligned with the tensile direction to those that are parallel to it. Under such conditions, dislocation slip, or climb are not necessary to promote creep deformation. On the other hand, when creep predominantly occurs along the grain boundaries through diffusional processes, it is referred to as “grain boundary diffusion” or “Coble creep”. In this case, the contribution of Coble creep is greater than self-diffusion (SD) occurring within the grains [120].

When the  $\sigma$  is increased,  $n \approx 3$ , which is also known as the “three-power-law”. In this regime, the rate controlling mechanism is associated to a so-called “viscous dislocation glide”, where dislocation movement may be activated, but hindered due to an interaction with the solute atoms. This mechanism is commonly described in solid solution alloys, but dislocation-solute interactions may also occur in more complex microstructures. At a higher increase in the Norton exponent to  $n \approx 5$ , creep deformation by dislocation motion may be controlled by dislocation climb. In



dislocation-climb creep, dislocations that can leave the original slip plane by recombination of vacancies or substitutional atoms generated during previous dislocation motion can lead to recovery by extinction of dislocations with opposite signs. Once a dislocation has been annihilated, a new one with identical length and thus associated energy can form, resulting in a continuous deformation process [120, 123, 124].

The activation energy for creep ( $Q_c$ ), equivalent to self-diffusion energy ( $Q_{SD}$ ) in pure metals, holds significant importance in the equation. It describes the dependence of  $\dot{\epsilon}_{min}$  with  $T$  while maintaining a constant  $\sigma$ . The temperature-dependent behavior of creep is conventionally represented by the apparent activation energy,  $Q_c$ , which determination involves plotting Equation 2.2 as the natural logarithm of  $\dot{\epsilon}_{min}$  ( $\ln \dot{\epsilon}_{min}$ ) at a specific  $\sigma$  against  $1/T$  (in K), in an Arrhenius-type plot, where the slope of the curve becomes  $Q_c / R$ .

The first and only available study on mechanisms of tensile creep deformation up to 1250 °C of a rCCA was conducted by Liu *et al.* [125], with the bcc solid solution HfNbTaTiZr alloy. By comparing the theoretical and experimental  $\dot{\epsilon}_{min}$ , an examination of the diffusion coefficients for all elements revealed that Ta, having the lowest diffusivity, plays a predominant role in drag-dislocation control, thereby influencing the creep rate. Figure 15 shows the results described by Liu *et al.* [125], where the creep mechanism did not change within the range of tested  $T$  and  $\sigma$ , indicating a stress level not high enough to overcome this solute drag effect (glide-controlled creep). Furthermore,  $Q_c = 273 \pm 15 \text{ kJ}\cdot\text{mol}^{-1}$ , being the highest determined for this alloy (*cf.* Figure 15) [125]. Yet, as the crystal structure of this alloy is a single bcc phase, it may not be comparable with the RSA. With its continuous B2-matrix the RSA is rather expected to have a behavior comparable to alloys with B2-structure, as will be discuss in the next subsection.

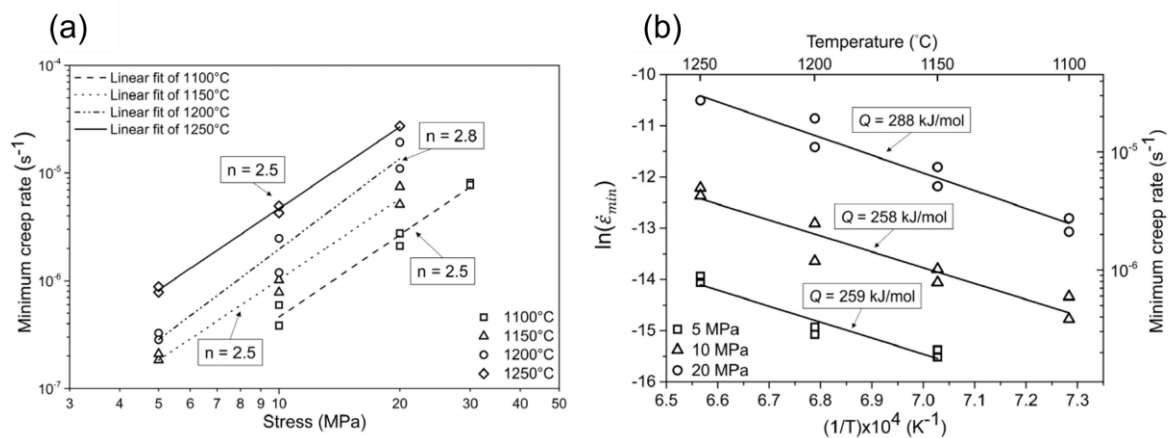


**Figure 15.** Creep behavior of the HfNbTaTiZr alloy (a)  $\dot{\epsilon}_{min}$  vs.  $\sigma$  from 1100 to 1250 °C (b)  $\dot{\epsilon}_{min}$  vs.  $(1/T)$  from 5 to 20 MPa, as reported by Liu *et al.* [125].

*Ordered bcc (B2)*

The B2 ordered crystal structure has a similar unit cell as the A2, with the difference that the atom in the center has a preferred occupation site with respect to the atoms at the corners (*cf.* Figure 16). This structure consists of two simple interpenetrating cubic sublattices and can be represented stoichiometrically as a 50:50 distribution of atoms [17]. They belong to a space group  $Pm\bar{3}m$  (221), with a structure designated with a Pearson symbol  $cP2$  (CsCl-prototype) and a *Strukturbericht* notation “B2” [105, 106].

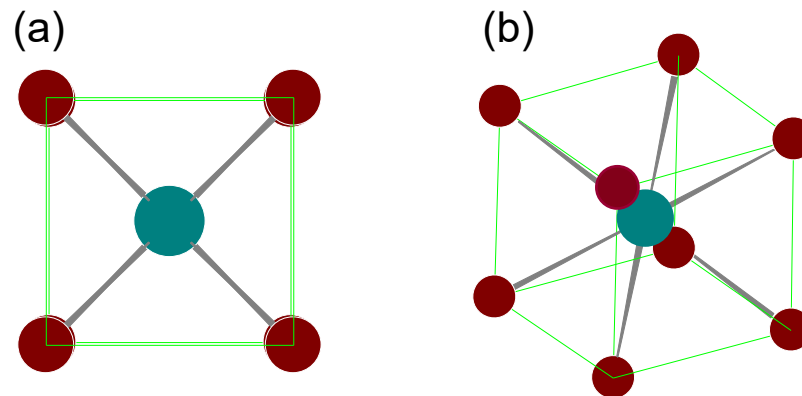


**Figure 16.** Schematic representations of a unit cell with B2 crystal structure created using PowderCell software [107] (a) frontal view (b) inclined view. The two sublattices are represented with two colors since the lattice have preferred sites to be populated by some elements.

Common intermetallic compounds of this class are NiAl, CoAl, AgMg, CuZn, NiGa, CoGa, and FeAl. Materials in this group such as NiAl and FeAl have the highest potential for structural applications. Most of the data available for the properties of binary B2 intermetallics are refer to NiAl, FeAl, and CoAl. The NiAl intermetallic, with a density of  $5.98 \text{ g/cm}^3$  and melting temperature ( $T_m$ ) of  $\approx 1638 \text{ }^\circ\text{C}$  [126], is formed by a unit cell with a Ni atom located in the center of the cube and an Al atom distributed around the corners (or viceversa) [17]. The use of NiAl alloys as structural materials, however, comes with certain limitations. These include softening at elevated temperatures, high brittle-to-ductile transition temperatures ( $\approx 400 \text{ }^\circ\text{C}$ ) [127], and relatively low creep resistance at high temperatures [128]. The FeAl intermetallic serves as another example, which retains the B2 structure when the alloy contains Al in the range between 35 at.% to 50 at.%. Fe atom are at the center of the cube and Al atoms randomly distributed in the corners (2 atoms per unit cell) [17]. Notably, it offers good oxidation and corrosion resistance and, combined with a low density ( $5.56 \text{ g/cm}^3$ ) [129], low cost compared to many other structural materials. However, Fe-Al exhibit low ductility at RT, and their creep resistance is only moderate at high temperatures [130]. For annealed and forged NiAl,  $K_{Ic}$  ranges between  $5.08 \pm 0.36$  and  $6.42 \pm 0.88 \text{ MPa}\cdot\text{m}^{1/2}$  (determined by Vickers indentation: ring on ring disk bend test). The  $H_v$  for NiAl varies from 460 to 560 HV (4.5–5.5 GPa) [131]. On the other hand, FeAl has  $K_{Ic}$  values between 11 and 55.8

MPa·m<sup>1/2</sup>, with  $H_v$  ranging from 197 to 867 HV, depending on the specific chemical composition and the determination method [132].

It has been established that in high entropy alloys, the presence of Al triggers the B2 phase formation [133]. Thus, the existence of B2 phase in the RSA suggests that sufficient Al is retained within the matrix, allowing for it to order as B2. In the particular case of the RSA, the B2 phase shows enrichment in Al, Ti, and Zr, where Ti and Zr atoms tend to occupy a different sub-lattice than the Al atoms during the ordering process [12].

#### *Creep in B2 structure alloys*

Ordered intermetallic phases exhibit significantly lower diffusion coefficients compared to disordered solid solutions. Consequently, they demonstrate higher thermal stability and lower recovery rates at comparable homologous temperatures ( $T/T_m$ ). Both factors contribute to increased resistance to creep compared to corresponding disordered solid solutions [123]. The parameters that determine the creep behavior of NiAl intermetallics vary depending on the composition, grain size, and the experimental conditions, such as loading geometry type (compression or tension),  $T$ ,  $\sigma$ , reinforcement of matrix, etc. Table 4 shows a summary of the creep parameters such as  $n$  and  $Q_c$  for the NiAl at different compositions, grain size and  $T$ , as reported in Ref. [120].  $Q_c$  values are found within 230–350 kJ·mol<sup>-1</sup>, which is in average the  $Q_{SD}$  of Ni in NiAl ( $\approx 290$  kJ mol<sup>-1</sup>). From  $n$ , dislocation climb has been described as the major creep mechanism, although both dislocation climb and viscous glide may be possible rate-controlling mechanisms depending on  $\sigma$  and  $T$  [134]. Although NiAl processing is typically simple, its mechanical properties remain unreproducible due to its high sensitivity to metallurgical factors.

**Table 4.** Summary of creep parameters for NiAl alloys found in the literature, extracted from [120].

Al, at.%	Grain size ( $\mu\text{m}$ )	T ( $^{\circ}\text{C}$ )	Norton exponent ( $n$ )	Activation energy, $Q_c$ (kJ·mol <sup>-1</sup> )	Ref.
48.25	5–9	727–1127	6.0–7.5	313	[135]
44–50.6	15–20	727–1127	5.75	314	[136]
50	$\approx 12$	927–1027	6	350	[137]
50	$\approx 450$	800–1045	10.2–4.6	283	[138]
50.4	$\approx 1000$	802–1474	7.0–3.3	230–290	[139]
50	SX	750–1055	4.0–4.5	293	[140]
49.8	$\approx 39$	727	$\approx 5$	260	[141]

Raj *et al.* [142] described the compression creep properties in polycrystalline NiAl at  $T = 1000$ – $1400$  K ( $\approx 727$ – $1127$   $^{\circ}\text{C}$ ). They reported  $n \approx 6.6$  and  $Q_c \approx 300$  kJ·mol<sup>-1</sup> at  $\sigma > 25$  MPa, whereas  $n \approx 2$  and  $Q_c \approx 95$  kJ·mol<sup>-1</sup> was observed at  $\sigma < 25$  MPa. The deformed microstructure did not show any dislocation activity in many grains, and grain boundary sliding was the dominant mechanism. A year later, the tensile creep behavior of the same alloy at 427 (100–170 MPa), 627 (40–80 MPa), and 727  $^{\circ}\text{C}$  (35–65 MPa) was reported [143]. They noted that NiAl exhibits contrasting creep

behavior in tension (with  $n \approx 13$ ) and compression, and no clear explanation was given for the  $n$  value. Particularly at low  $T$ , the NiAl alloy demonstrates significantly faster creep rates in tension compared to compression.

On the other hand, the addition of reinforcement particles in the B2 matrix has been demonstrated to optimize creep in NiAl, as in the case of the ODS NiAl-Y<sub>2</sub>O<sub>3</sub> alloy. The minimum creep rate for  $T = 1300$  K ( $T \approx 1027$  °C) and  $T = 1400$  K ( $T \approx 1127$  °C) is reported to be  $\dot{\epsilon} \approx 1.0 \times 10^{-5} \text{ s}^{-1}$  and  $8.0 \times 10^{-5} \text{ s}^{-1}$ , respectively (at  $\sigma = 30$  MPa) [144], while  $Q_c > Q_{SD}$  ( $Q_c = 576 \text{ kJ}\cdot\text{mol}^{-1}$ ), and  $n \approx 17$ , thus rendering it more resistant than the Ni-based superalloy MA956 [145, 146]. The NiAl matrix with Al<sub>2</sub>O<sub>3</sub> dispersoids showed  $n \approx 7.6\text{--}8.4$  and  $Q_c \approx 291 \text{ kJ}\cdot\text{mol}^{-1}$ , with dislocation climb as the controlling deformation mechanism.

The FeAl creep performance is notably influenced by the chemical composition of the alloy,  $T$ , and  $\sigma$ . Generally, at high  $T$  and low  $\sigma$ , diffusional creep governs, while at low  $T$  and high  $\sigma$ , dislocation climb, or viscous drag are the predominant mechanisms. Table 5 presents a summary of some reported creep data for FeAl-based alloys from previous works and Ref. [120], with the corresponding mechanisms proposed by the authors. In general, at elevated temperatures, FeAl has poor strength and creep resistance. The diffusivity of the elements is so high that it prevents the B2 lattice to form strong dislocation barriers, so the dislocations can move easier. Therefore, one of the strategies implemented to improve its creep resistance, is through precipitation hardening by the addition of alloying elements. For instance, small additions of Mo, Zr, Ti, B and C in the Fe-40Al alloy was shown to improve the creep resistance, decreasing  $\dot{\epsilon}_{\min}$  by three orders of magnitude (from  $2.5 \times 10^{-7}$  to  $2 \times 10^{-10} \text{ s}^{-1}$  at  $700$  °C and  $90$  MPa) [147]. The addition of these elements was found to precipitate titanium carbides, which blocked the dislocation sources in the samples prior to creep, thus decreasing the dislocation density in the crept samples. Furthermore, differences between compression and tensile creep have been observed in the Fe-40Al alloy with some additions of Zr and B (Fe-40Al-0.1Zr-0.4B % at.), where the minimum creep rate measured in tension was much higher due to the formation of cavities that were not seen in compression [148].

Finally, Kral *et al.* [149] conducted a study on the creep behavior of the B2-structured AlTiVNbZr<sub>0.25</sub> alloy at  $\approx 800$  °C. This alloy, composed of coarse Zr<sub>5</sub>Al<sub>3</sub> particles ( $\approx 9$  %) embedded in a B2 matrix phase, revealed the development of dislocation densities  $\rho_d \approx 2.2 \cdot 10^{13}$  and  $\approx 9.2 \cdot 10^{13} \text{ m}^{-2}$  for  $100$  and  $325$  MPa, respectively, and  $\dot{\epsilon}_{\min}$  that followed a three-power law. The authors attributed the creep mechanism to viscous glide due to “cloud drag”, typical in class-A materials, where clouds of point defects accompanying the dislocations create a viscous drag force that opposes the dislocation motion, leading to deformation under creep conditions.

**Table 5.**  $n$ ,  $Q_c$ , and deformation mechanisms from different creep studies on FeAl reported in Ref. [120]

Composition	T (°C)	$n$	$Q_c$ (kJ·mol <sup>-1</sup> )	Mechanism	Ref.
Fe-28Al-2Mo	650	1.4 (low $\sigma$ ) 6.8 (high $\sigma$ )	335	Diffusional flow Climb	[150]
Fe-28Al-1Nb-0.013Zr	650	1.8 (low $\sigma$ ) 19.0 (high $\sigma$ )	335	Diffusional flow Dispersion strengthening	
FA-180 (Fe-28Al-5Cr-0.5Nb-0.8Mo-0.025Zr-0.05C-0.005B (at.%))	593	7.9	627	Precipitation strengthening	[151]
Fe-28Al	600–675	3.4			[130]
Fe-26Al-0.1C	600–675	3.0	305		
	480–540	6.2	403		
Fe-28Al-2Cr	480–540	3.7	325	Viscous glide	
Fe-28Al-2Cr-0.04B	600–675	3.7	304		
Fe-28Al-4Mn	600–675	2.6	302		
FA-129 (Fe-28Al-5Cr-0.5Nb-0.2C)	500–610	4–5.6	380–395		[152]
FA-129	900–1200	4.81	335		[153]
Fe-39.7Al-0.05Zr-50 ppmB	500	11	260–300	Dispersion strengthening	[154]
	700	11	425–445	Climb	
Fe-27.6Al	425–625	2.7–3.4	375		[155]
Fe-28.7Al-2.5Cr	425–625	3.5–3.8	325	Viscous glide	
Fe-27.2Al-3.6Ti	425–625	3.4–3.7	375		
Fe-47.5Al (grain size = 6 $\mu$ m)	827–1127	6.3–7.2	487		[156]
Fe-47.5Al (grain size = 20 $\mu$ m)	927–1127	5.6–9.7	368		
Fe-40Al-0.2Mo-0.05Zr-0.5Ti-0.2C-0.02B	700	3–5 (high $\sigma$ ) 20 (low $\sigma$ )	300-400	Precipitation hardening	[147]

### Al-Zr-rich phases

The microstructure of the RSA has been reported to contain two bcc-based phases and a secondary phase precipitating along grain boundaries rich in Al and Zr [12, 49, 102]. Figure 17 shows the Al–Zr system, as calculated using the ThermoCalc software [87]. Based on the Al–Zr phase diagram and on the relative composition reported for the RSA, several intermetallics may be expected to form. According to the evaluation of Murray *et al.* [157], ten stable intermetallic phases are possible to form in the Al–Zr system:  $\text{Al}_3\text{Zr}$ ,  $\text{Al}_2\text{Zr}$ ,  $\text{Al}_3\text{Zr}_2$ ,  $\text{AlZr}$ ,  $\text{Al}_4\text{Zr}_5$ ,  $\text{Al}_3\text{Zr}_4$ ,  $\text{Al}_2\text{Zr}_3$ ,  $\text{Al}_3\text{Zr}_5$ ,  $\text{AlZr}_2$  and  $\text{AlZr}_3$ . However, two of them, *i.e.*,  $\text{Al}_3\text{Zr}_5$  and  $\text{Al}_4\text{Zr}_5$  (see red oval in Figure 17) are reported to be high-temperature phases [158].

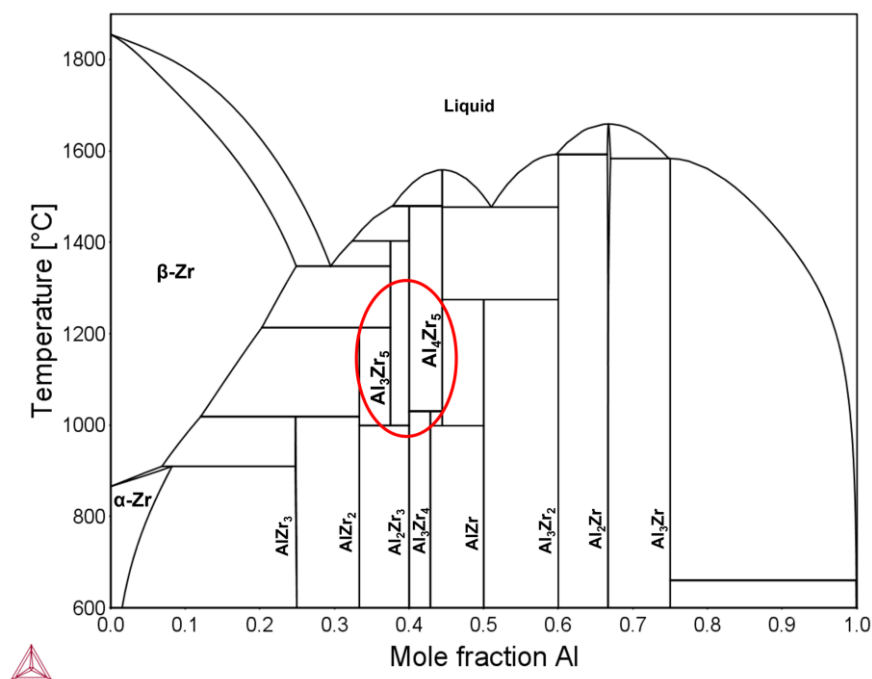


**Figure 17.** Phase diagram of the Al–Zr-system, representing the possible Al–Zr-intermetallics that can form. Common high temperature phases are enclosed in the red oval. The diagram was created using ThermoCalc software, with the TCHEA3 v1.1 database [ThermoCalc Software AB, Stockholm, Sweden/SGTE].

Furthermore, Jensen *et al.* [102] performed a more detailed characterization involving convergent beam electron diffraction. High resolution STEM-HAADF images were also analyzed in order to identify the crystal structure of the unknown intermetallic precipitate. The study revealed a complex ordered crystal structure with at least two distinct sublattice sites, belonging to the  $P6_3/mcm$  space group, with lattice parameters of the  $a = 8.31 \text{ \AA}$  and  $c = 5.52 \text{ \AA}$  [102]. Based on the experimentally determined chemical composition [102], and the space group of the phase, the two possible intermetallics that can exist in the RSA are the  $\text{Al}_3\text{Zr}_5$  and  $\text{Al}_4\text{Zr}_5$  (*cf.* Figure 18).

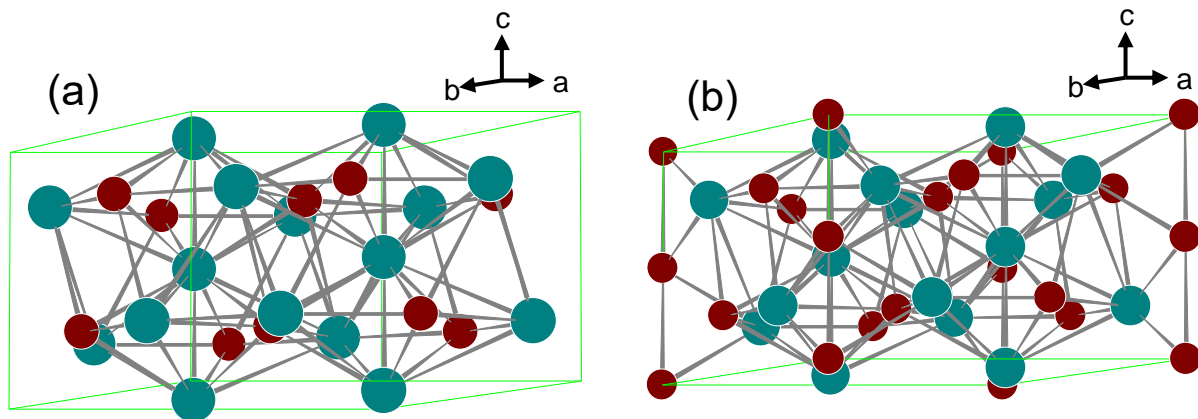


**Figure 18.** Schematic representation of the crystalline structure of hexagonal Al-Zr phase (unit-cell) with (a)  $\text{Al}_3\text{Zr}_5$  and (b)  $\text{Al}_4\text{Zr}_5$  stoichiometry. Al atoms are red and Zr atoms are green. The unit cells were created using PowderCell software [107].

#### *$\text{Al}_3\text{Zr}_5$ intermetallic*

The  $\text{Al}_3\text{Zr}_5$  intermetallic phase has a hexagonal unit cell, with Al and Zr atoms disposed as shown in [Figure 18a](#), where Al is the center atom of the cluster. Its space group is  $\text{P6}_3/\text{mcm}$  N° 193, with the Pearson symbol hP16, and  $\text{Mn}_5\text{Si}_3$  is its prototype [105]. This intermetallic has a mass density of  $5.355 \text{ g/cm}^3$ , unit cell volume of 330.74, calculated heat of formation ( $\Delta E$ ) of  $-35.816 \text{ kJ/mol}$  under normal conditions, and the lattice parameters are  $a = b = 8.184 \text{ \AA}$  and  $c = 5.702 \text{ \AA}$  [106, 159]. The mechanical properties of this intermetallic have not been experimentally assessed in the literature, and the only available data has been reported by Du *et al.* [159] through computational simulation. The calculated single-crystal elastic constants are reported to be  $C_{11} = 211.55$ ,  $C_{12} = 61.23$ ,  $C_{13} = 56.11$ ,  $C_{33} = 139.97$ , and  $C_{44} = 39.46 \text{ GPa}$ . It has a polycrystalline shear modulus ( $G$ ) of  $54.35 \text{ GPa}$ , bulk modulus ( $K$ ) of  $99.12 \text{ GPa}$ , Young's modulus ( $E$ ) of  $137.85 \text{ GPa}$ , Poisson's ratio ( $\nu$ )  $0.2682$ , and hardness ( $H$ ) of  $9.67 \text{ GPa}$  [159, 160].

#### *$\text{Al}_4\text{Zr}_5$ intermetallic*

The  $\text{Al}_4\text{Zr}_5$  intermetallic phase has also a hexagonal crystallographic structure, with Al and Zr atoms disposed as shown in [Figure 18b](#). It has a space group  $\text{P6}_3/\text{mcm}$  (193), Pearson symbol hP18, and  $\text{Ga}_4\text{Ti}_5$  prototype [105]. The mass density is  $5213 \text{ kg/m}^3$ , unit cell volume of 357.55, and experimental and calculated heat of formation ( $\Delta E$ ) of  $-52 \pm 4$  and  $-42.002 \text{ kJ/mol}$  at RT, respectively [159, 160]. The lattice parameters are slightly bigger than for the  $\text{Al}_3\text{Zr}_5$  phase with  $a = b = 8.437 \text{ \AA}$ ,  $c = 5.800 \text{ \AA}$  [106, 159]. Du *et al.* [159] reported calculated elastic constants of  $C_{11}$

= 198.59,  $C_{12} = 73.06$ ,  $C_{13} = 50.52$ ,  $C_{33} = 196.35$ , and  $C_{44} = 50.84$  GPa,  $G = 60.11$  GPa,  $K = 104.49$  GPa,  $E = 151.31$  GPa,  $\nu = 0.2586$ , and  $H = 10.85$  GPa [159, 160].

The unit cell-internal parameters (Wyckoff positions) are summarized in [Table 6](#) for the  $\text{Al}_3\text{Zr}_5$  and  $\text{Al}_4\text{Zr}_5$  intermetallic phases.

**Table 6.** Unit cell-internal parameters for the  $\text{Al}_3\text{Zr}_5$  and  $\text{Al}_4\text{Zr}_5$  intermetallics [106].

Intermetallic Phase	Lattice parameters ( $\text{\AA}$ )	Atom site	Wyck	Atom position		
				X	Y	Z
$\text{Al}_3\text{Zr}_5$	$a = b = 8.184$ $c = 5.702$	Zr	6g	0.23	0.00	0.25
		Zr	4d	0.33	0.66	0.00
		Al	6g	0.59	0.00	0.25
$\text{Al}_4\text{Zr}_5$	$a = b = 8.437$ $c = 5.800$	Zr	6g	0.29	0.00	0.25
		Al	6g	0.62	0.00	0.25
		Zr	4d	0.33	0.66	0.00
		Al	2b	0.00	0.00	0.00

Even though the  $\text{Al}_3\text{Zr}_5$  and  $\text{Al}_4\text{Zr}_5$  phases possess the same space group and symmetry, their atomic configurations differ from each other, especially in the Al atomic positions in the corners of the hexagon, as depicted in [Figure 18](#). Previous studies where  $\text{Al}_4\text{Zr}_5$  and  $\text{Al}_3\text{Zr}_5$  are experimentally observed, state that they are stable phases only at high  $T$ , but have otherwise been described as metastable phases at lower  $T$ . They can be decomposed into more stable phases by the reactions  $\text{Al}_3\text{Zr}_5 \rightarrow \text{AlZr}_2 + \text{Al}_2\text{Zr}_3$  and  $\text{Al}_4\text{Zr}_5 \rightarrow \text{Al}_3\text{Zr}_4 + \text{AlZr}$  [158].



### 3. Scientific objectives

The aim of this study is to investigate the thermodynamic and microstructural stabilities of the  $\text{AlMo}_{0.5}\text{NbTa}_{0.5}\text{TiZr}$  RSA around 1000 °C, and to assess their impact on the mechanical properties of the alloy at both room and high temperatures.

The microstructure, density and compression strength of the novel RSA resembles those of the since long fine-tuned Ni-based alloys, which originally raised the question of its suitability to compete with them. Ni-based alloys are limited to their relatively low melting points, which prevent an increase in the operating temperature of structural components. Thus, understanding the hitherto poorly studied high temperature evolution of the RSA is paramount to unravel its potential. In this work, the following questions will be addressed:

- What is the starting (as-cast) microstructure of the RSA, and how does it relate to the microstructure after its well-established heat treatment? And do current CALPHAD databases reveal consistent solidification and phase transformation pathways both in equilibrium and non-equilibrium states so as to reproduce the experimental results? (Papers I&II)
- How does cooling rate, as a processing parameter, affect the well-established RSA microstructure in terms of phase fraction, size and distribution, as well as the A2/B2 misfit? And how are the associated room temperature nano/microhardness and fracture toughness affected? (Paper III).
- What is the creep behavior of the RSA in the 1000 °C regime as a main high temperature property of the envisioned application for the RSA? And what are the associated micro-mechanisms? (Paper IV)

## **4. Papers**

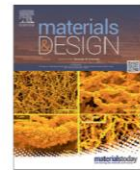
### **4.1 Paper I**

The  $\text{AlMo}_{0.5}\text{NbTa}_{0.5}\text{TiZr}$  refractory high entropy superalloy: Experimental findings and comparison with calculations using the CALPHAD method.



Contents lists available at ScienceDirect

Materials &amp; Design

journal homepage: [www.elsevier.com/locate/matdes](http://www.elsevier.com/locate/matdes)

# The $\text{AlMo}_{0.5}\text{NbTa}_{0.5}\text{TiZr}$ refractory high entropy superalloy: Experimental findings and comparison with calculations using the CALPHAD method

Patricia Suárez Ocaño<sup>a,\*</sup>, Suzana G. Fries<sup>b</sup>, Inmaculada Lopez-Galilea<sup>c</sup>, Reza Darvishi Kamachali<sup>a</sup>, Janina Roik<sup>d</sup>, Leonardo Agudo Jácome<sup>a</sup>

<sup>a</sup> Federal Institute for Materials Research and Testing (BAM), Department for Materials Engineering, Unter den Eichen 87, 12205 Berlin, Germany

<sup>b</sup> Materials Research Department (MRD), Ruhr-University Bochum, Universitätsstr. 150, 44801 Bochum, Germany

<sup>c</sup> Institute for Materials, Ruhr-University Bochum, Universitätsstr. 150, 44801 Bochum, Germany

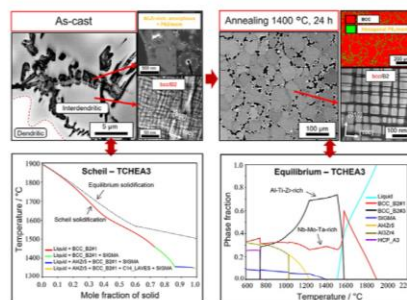
<sup>d</sup> Federal Institute for Materials Research and Testing (BAM), Department of Inorganic Reference Materials, Richard-Willstätter-Strasse 11, 12489 Berlin-Adlershof, Germany



## HIGHLIGHTS

- Microstructural characterization of the  $\text{AlMo}_{0.5}\text{NbTa}_{0.5}\text{TiZr}$  refractory superalloy in the as-cast state is reported for the first time and compared with hitherto known annealed state.
- The detailed CALPHAD analysis with Scheil-Gulliver and equilibrium calculations reveal new insights into understanding the nature of the studied alloy by comparing with the experimental data.
- The equilibrium-based CALPHAD approach used here pinpoints the presence of a miscibility gap between two bcc-based phases, confirming the hypothesis that this alloy is formed by spinodal decomposition.
- Differential thermal analysis was reported for the first time for this alloy, revealing a good agreement between measured phase transformation temperatures and calculated values.

## GRAPHICAL ABSTRACT



## ARTICLE INFO

### Article history:

Received 28 January 2022

Revised 23 March 2022

Accepted 23 March 2022

Available online 26 March 2022

### Keywords:

CALPHAD database analysis

## ABSTRACT

Detailed microstructural characterization of the  $\text{AlMo}_{0.5}\text{NbTa}_{0.5}\text{TiZr}$  refractory high entropy superalloy in the as-cast state is reported for first time and compared with the state annealed at 1400 °C for 24 h. The former shows a dendritic structure, with a mixture of A2/B2 phases < 20 nm in both the dendritic and interdendritic regions. A mostly amorphous phase, rich in Al and Zr, is found within the interdendritic region. The annealed state reproduced the combination of A2/B2/Al-Zr-rich phases reported previously. Calculations from two relevant ThermoCalc databases were compared with the experimental results. Equilibrium calculations were compared with results for the annealed alloy, whereas solidification paths calculated using Scheil-Gulliver model were used for comparison with the as-cast alloy. A previously

\* Corresponding author.

E-mail address: [patricia.suarez-ocano@bam.de](mailto:patricia.suarez-ocano@bam.de) (P. Suárez Ocaño).

<https://doi.org/10.1016/j.matdes.2022.110593>

0264-1275/© 2022 The Authors. Published by Elsevier Ltd.

This is an open access article under the CC BY-NC-ND license (<http://creativecommons.org/licenses/by-nc-nd/4.0/>).

Refractory superalloys  
Chemically complex alloy  
Characterization  
Microstructure.

hypothesized spinodal decomposition during cooling as the mechanism responsible for the patterned A2/B2 microstructure is confirmed via the CALPHAD calculations, pointing to its use as an efficient design tool for such alloys. Finally, the comparison between the experimental and computational findings allowed better understanding the solidification path and equilibrium stability of this alloy, giving a base to make better decisions on the field of new refractory superalloy design.

© 2022 The Authors. Published by Elsevier Ltd. This is an open access article under the CC BY-NC-ND license (<http://creativecommons.org/licenses/by-nc-nd/4.0/>).

## 1. Introduction

To improve the performance of future structural components for high temperature applications, it is necessary to develop new materials that can withstand higher temperatures than at present while retaining high strength and good creep and corrosion resistance. Ni-base superalloys have been in the last decades the material of choice for severe service conditions [1–4]. The realm of chemically complex alloys (CCAs), materials that lack a base element but instead are composed of several of them at high compositions, has been increasingly studied in the last years thanks to their interesting and sometimes unexpected microstructures and properties. The CCAs made of refractory elements such as Mo, Nb and Ta are attractive candidates for use at extremely high temperatures (associated with many technological applications) [5–7]. An example of a refractory CCAs is the  $\text{AlMo}_{0.5}\text{NbTa}_{0.5}\text{TiZr}$ , which has a measured density of  $7.4 \text{ g/cm}^3$ , Vickers microhardness ( $H_v$ ) of  $5.8 \pm 0.1 \text{ GPa} = 591.4 \text{ HV1}$  and a high temperature (compressive) strength of  $772 \text{ MPa}$  at  $1000 \text{ }^\circ\text{C}$  with a fracture strain  $< 50\%$  [8,9]. One drawback of this alloy is its room temperature ductility of  $\delta = 10\%$  [8]. Senkov et al. [8] and Jensen et al. [10] reported that a coherent two-phase nanostructure forms for the  $\text{AlMo}_{0.5}\text{NbTa}_{0.5}\text{TiZr}$  alloy after applying a heat treatment under argon atmosphere. The obtained microstructure resembles the  $\gamma/\gamma$  pattern of the Ni-base superalloys,  $L_{12}$  cuboids ( $\gamma$ ) embedded in a continuous fcc matrix ( $\gamma$ ) [4], therefore naming it *refractory high entropy superalloy* (RSA) [8–11]. This resemblance promotes the possibility of profiting from the long-term knowledge gained on the effectiveness of such microstructures to high temperature performance. However, important differences exist, e.g.: 1) the dimensions of the cuboid/matrix structure are one order of magnitude smaller; 2) the nanostructure is formed by cuboidal A2 phase (discontinuous) particles embedded in a continuous B2 phase matrix, i.e. the matrix is made of an ordered phase, opposite to Ni-base superalloys; and 3) there is a strong partitioning of Mo, Nb and Ta to the A2 phase, and of Al, Ti and Zr to the B2 phase [8,10].

Beyond the high strength at high temperatures, and the presence of refractory elements, the  $\text{AlMo}_{0.5}\text{NbTa}_{0.5}\text{TiZr}$  RSA contains  $\approx 20\%$  of Al (to lower its density) that has been determined to form an intermetallic rich in Al and Zr, but also significantly lowers its melting point. However, there is no clear study in the literature indicating whether this RSA has a higher melting point than Ni-based alloys or not. In the case of having a higher melting point, this alloy could be attractive for use at extremely high temperatures, and therefore, this is also addressed in this contribution. As CCAs contain multiple principal elements, which contrasts with conventional alloys, it has been challenging to understand the phase equilibrium and solidification path of alloys like the RSA. In recent years, CALPHAD-based methodologies have been used largely in the field of CCAs to understand their formation and to their optimization [12–15]. Senkov et al. [16] calculated the equilibrium and non-equilibrium diagrams using the Pandat Ti database and showed the formation of two phases, BCC and  $\text{Al}_2\text{Zr}_3$ , after non-equilibrium solidification and three phases, BCC,  $\text{Ti}_3\text{Al}$  and  $\text{Al}_2\text{Zr}_3$ , in equilibrium. A clear mismatch however was found between these results and their experimental measurements [16]

while the phases formed during casting have not been assessed, e.g., by comparing the as-cast state and the non-equilibrium calculations. Nevertheless, considering the importance of the initial solidification process of refractory alloys with respect to the ability to effectively tune their properties by subsequent heat treatments, a step back to understand the casting behavior of this RSA can shed insights into improving it. Whitfield et al. [17] calculated the phase equilibria using the SSol5 database, which demonstrated better agreement to the phases observed experimentally, although large differences were found in the solvus temperatures, especially for the  $\text{Al}_4\text{Zr}_5$  intermetallic phase. Thus, it seems like the simple use of available databases for CALPHAD calculations of such multi-principal elements is not enough to establish robust phase stability anticipations for this alloy system and presumably its derivatives. Here the use of analytical and of structural characterization methods is still much needed in the field of CCAs [18] to further aid the development and validation of the developing CALPHAD databases.

In the present work, we aim to understand the phase stability and solidification behavior of the RSA  $\text{AlMo}_{0.5}\text{NbTa}_{0.5}\text{TiZr}$  as a base to tackle similar systems. To this end, an approach was implemented where detailed CALPHAD thermodynamic stabilities and solidification paths were calculated and compared with experimental data found for both as-cast, AC, and annealed state, AN (AC +  $1400 \text{ }^\circ\text{C}$  for 24 h). The processing of most HEAs is still based on trial and error. In this context, the study of the as-cast structures needs special attention, to allow better design of heat treatments that may help to overcome the room-temperature embrittlement in this and similar high-temperature alloys or to pinpoint detrimental microstructural features that may not be reverted by heat treatment. In addition, a comparison with CALPHAD Scheil solidification is used to benchmark two published databases and to assist future CALPHAD-integrated RSA design. Furthermore, the results go beyond the state-of-the-art [8,10,17] by directly comparing CALPHAD equilibrium calculations and differential thermal analysis in the annealed state, casting light on the phase transformation pathways and temperatures. The experimental data are accompanied with CALPHAD calculations that were conducted using the commercial thermodynamic software ThermoCalc [19] with two different databases, the established TCNI10 and TCHEA3, in order to evaluate the accuracy for this alloy. The database TCHEA4 was used for all the calculations as well; however, only the results obtained with the TCHEA3 are reported since this shows a better match with the experimental data. The current experimental and computational findings assist the better design of refractory high-entropy alloys.

## 2. Material and methods

### 2.1. Material (as-cast and heat treated)

The  $\text{AlMo}_{0.5}\text{NbTa}_{0.5}\text{TiZr}$  alloy was prepared by vacuum arc melting of the pure elements in an argon atmosphere (purity  $> 99.998\%$ , with small impurities of  $\text{H}_2\text{O}$  ( $< 5 \text{ v-ppm}$ ),  $\text{O}_2$  ( $< 5 \text{ v-ppm}$ ) and  $\text{N}_2$  ( $< 10 \text{ v-ppm}$ ), following the description given by Senkov et al. [16] but with some differences. Aluminum was in the form of granules (2–10 mm) with a purity of 99.99%, molybdenum in the form



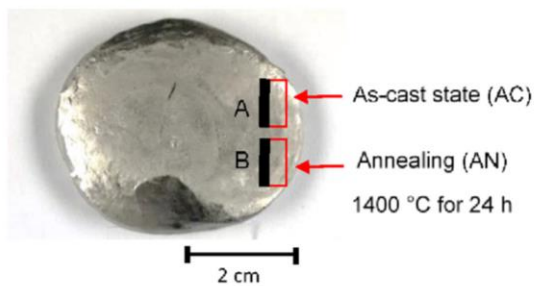


**Fig. 1.** Sample (button) obtained by vacuum arc melting which shows from where the casting and annealed samples were obtained for subsequent characterization. The surfaces marked as “A” and “B”, show the region where the SEM and TEM analysis were performed in the AC and AN, respectively, with the analyzed surfaces being on the black rectangular regions and orthogonal to the plane of the image.

of 0.5 mm thick sheet with a purity of 99.99% and niobium was in form of granules ranging 2–10 mm with 99.9% of purity. Tantalum was in the form of pellets of 6 × 6 mm, titanium in the form of pieces < 5 mm and zirconium in the form of granules (1–3 mm) and their purities were 99.9%, 99.5%, 99.9%, respectively. Arc melting was conducted on a water-cooled copper plate. High-purity molten titanium was used as a getter for residual oxygen, nitrogen, and hydrogen. To achieve a homogeneous distribution of elements in the alloy, the button was re-melted seven times, flipped for each melt, and kept in a liquid state for ≈ 5 min during each melting event. After casting, the sample was cut as is shown in Fig. 1 to get the as-cast sample for characterization. Another piece of sample was cut from the button, as shown in Fig. 1, and was annealed at 1400 °C for 24 h in continuously flowing high-purity argon to homogenize the grain structure, and cooled at a cooling rate after annealing < 4 K/min.

## 2.2. Characterization

The alloy composition was determined by inductively coupled plasma atomic emission spectroscopy (ICP-OES) and is given in Table 1.

Differential Thermal Analysis (DTA, SETARAM TAG24), was used to determine the main temperature transformations. Measurements were conducted by placing a small specimen of ≈ 20 mg in an open corundum crucible at a heating rate of 5 K/min up to a maximum temperature of 1620 °C (limit of the DTA facility). Cooling to room temperature was carried out at –5 K/min. For signal correction, a measurement of an empty crucible was conducted with the same experimental conditions.

Bulk phase analysis was conducted by X-ray diffractometry (Seifert PTS 3000), Co K $\alpha$  radiation ( $\lambda_{K\alpha 1} = 1.7902 \text{ \AA}$ ) and a  $2\Theta$  scattering range of 10–100° for the as-cast state (AC), and 10–120° for the annealed (AN) alloy. The identification was carried out by comparing the experimental patterns with patterns simulated using PowderCell [20].

The microstructures of the AC and AN alloy were analyzed by scanning electron microscopy (SEM, FEI Quanta 3D) equipped with backscatter electron (BSE) and energy-dispersive X-ray spectroscopy (EDX, EDAX Octane Elect SDDs) detectors. The average grain size for the AN alloy was determined in accordance with

ASTM E112 [21]. Also, electron backscattered diffraction (EBSD, SEM LEO Gemini 1530 V P Zeiss, EBSD detector Bruker e-flash HD with Bruker Esprit 1.9 EBSD-Software package) was conducted on the AN alloy at a medium magnification to determine the polycrystallinity of the A2/B2 grains and to characterize the phases forming at grain boundaries. For transmission electron microscopy (TEM), samples were cut in slices ≈ 500  $\mu\text{m}$  in thickness, after which thin foils with 3 mm in diameter were prepared by mechanical polishing (Struers Tenupol-3) in an electrolyte consisting of 950 mL ethanol (86.4%), 100 mL butanol (9.1%) and 50 mL perchloric acid (4.5%) at –30 °C and 30 V. The TEM was equipped with a field emission gun (FEG) source (TEM, JEOL JEM-2200FS) working at an acceleration voltage of 200 kV. Conventional (C) TEM was conducted for acquisition of energy filtered (EF) selected area diffraction patterns (SADPs) as well as bright field (BF)/dark field (DF) micrographs. Bright field and high angle annular (HAA) DF micrographs were also acquired in the scanning (S) TEM mode, the former for diffraction contrast and the latter for atomic number contrast. The SADPs were indexed with the aid of the Java version of the electron microscopy suite (JEMS) [22]. The volume fraction of the A2/B2 phases in both states was estimated using the image analysis package ImageJ [23].

## 2.3. Thermodynamic calculations

CALCulation of PHase Diagram (CALPHAD) is an important thermodynamic methodology based on the minimization of the total Gibbs energy of the system with different phases for a given alloy system that enables to calculate not only the phase diagram but also different thermodynamic properties of the system [24]. The CALPHAD calculations were developed using the TCNI10 and TCHEA3 databases via ThermoCalc software. Although TCNI10 is primarily optimized for Ni-based superalloys, it does cover all the edge binaries and several ternary phase diagrams of the Al-Mo-Nb-Ta-Ti-Zr system. Scheil and equilibrium solidification were calculated for the RSA using the composition determined experimentally (cf. Table 1). The Scheil-Gulliver equation describes the solute redistribution during solidification of an alloy, if perfect mixing in the liquid and no diffusion in the solid phase is assumed [25]. All calculations were performed using the experimental chemical composition in Table 1 to compare the results with the experimental data. Note that the phases will reflect their names as they are expressed in each commercial database. Thus, body centered cubic (bcc)-based phases called “BCC\_B2#1” and “BCC\_B2#3” do not necessarily mean that the phase is “B2”.

## 3. Results

### 3.1. Microstructural characterization

#### 3.1.1. As-cast state (AC)

The AC alloy has a typical dendritic structure with an average grain size of  $75 \pm 19 \mu\text{m}$ , as is shown in Fig. 2a–b. The presence of a strong segregation can also be seen inside the grains between dendritic and interdendritic regions. Due to elemental partitioning that results in different mean atomic numbers, the dendritic regions exhibit a brighter contrast and interdendritic regions exhibit darker contrast in the BSE-SEM images. A higher magnification

**Table 1**  
Experimental chemical composition of the AlMo<sub>0.5</sub>NbTa<sub>0.5</sub>TiZr sample represented in mole %.

Al	Mo	Nb	Ta	Ti	Zr
21.03	10.19	20.23	6.76	20.79	21.00

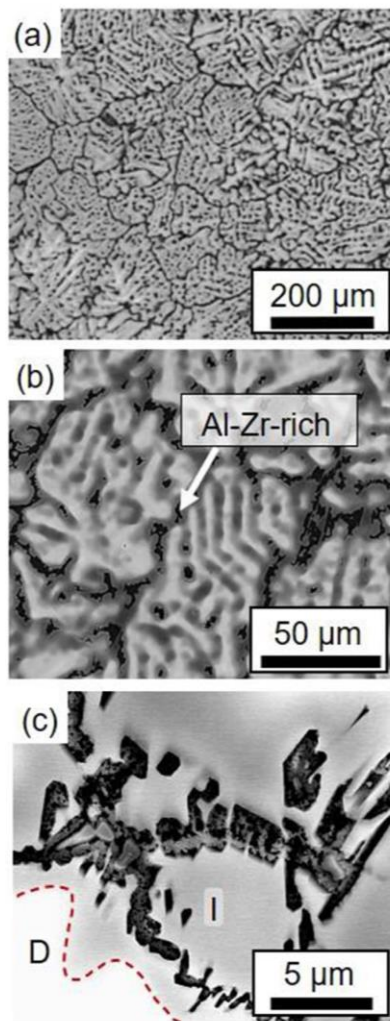


**Fig. 2.** SEM-BSE micrographs of the RSA in AC (a) sample center (see cut “A” in Fig. 1) (b) higher magnification showing the presence of a darker phase within the interdendritic region with the presence of an Al-Zr-rich phase (c) detail of the dark Al-Zr-rich phase acquired at a grain boundary; letters “D” and “I” respectively mark dendritic and interdendritic regions, with their diffuse boundary highlighted by a dotted red line. (For interpretation of the references to color in this figure legend, the reader is referred to the web version of this article.)

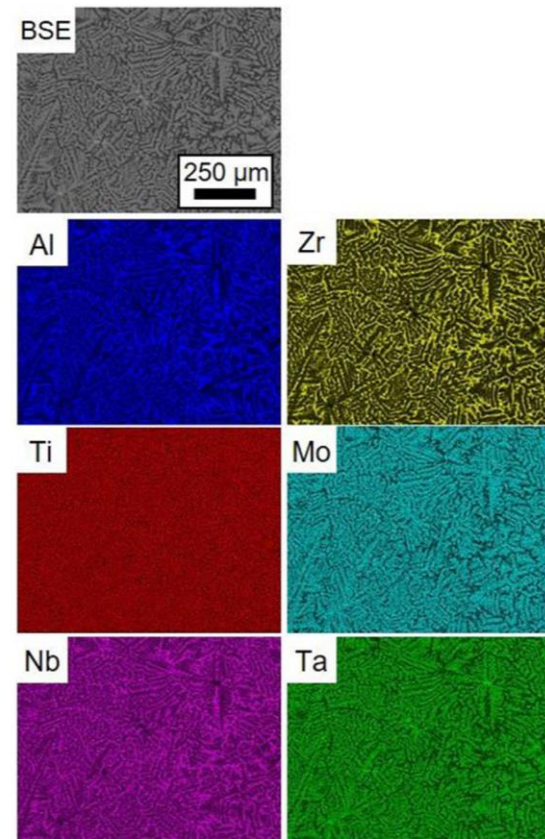


**Fig. 3.** EDX element mapping of components in the RSA/AC-alloy.

reveals the presence of an Al-Zr-rich network, as determined by EDX (summarized in Table 2), with the darkest contrast in the interdendritic regions (Fig. 2b-c).

Compositional maps of the alloying elements Al, Zr, Nb, Mo, Ta and Ti are shown in Fig. 3. As it can be qualitatively seen, Mo and Ta, with the highest melting points, are located preferably inside the dendritic regions, and of Al, Zr and Nb partition stronger to interdendritic regions. Ti is distributed almost evenly between dendritic and interdendritic regions, although a weak partitioning towards the latter is still visible.

In Fig. 4a-b, EBSD data is respectively presented as a pattern quality (PQ) map and inverse pole figure (IPF) from a TEM sample

**Table 2**

Chemical composition of the phases in the different regions in mole fraction (%) for the AC and AN alloy. The error bar is given by the standard deviation. Bold numbers show the elements of which the phase is rich.

State	Phase	Method	Region	Composition (mole fraction /%)					
				Al	Mo	Nb	Ta	Ti	Zr
<b>As-cast (AC)</b>	Al-Zr-rich	TEM-EDX	Neighboring region marked as SAD in green in Fig. 6a	<b>34 ± 4</b>	6 ± 5	9 ± 2	2 ± 1	8 ± 2	<b>41 ± 5</b>
	A2/B2	SEM-EDX	Interdendritic, e.g., “I” in Fig. 1c	<b>27 ± 1</b>	8 ± 1	17 ± 1	4 ± 1	<b>21 ± 1</b>	<b>23 ± 1</b>
	A2/B2	SEM-EDX	Dendritic, e.g., “D” in Fig. 1c	20 ± 1	<b>14 ± 1</b>	<b>23 ± 1</b>	<b>9 ± 1</b>	21 ± 1	13 ± 1
<b>Annealed (AN)</b>	Al-Zr-rich	TEM-EDX	Grain boundary in a similar region marked with blue row in Fig. 7b	<b>32 ± 2</b>	3 ± 1	10 ± 1	2 ± 1	7 ± 1	<b>47 ± 1</b>
	A2	TEM-EDX	Grain core (bright precipitates in Fig. A3a of supplementary data)	7 ± 1	<b>20 ± 1</b>	<b>35 ± 2</b>	<b>13 ± 1</b>	16 ± 1	9 ± 3
	B2	TEM-EDX	Grain core (dark channels in Fig. A3a of supplementary data)	<b>20 ± 1</b>	9 ± 1	19 ± 1	3 ± 1	<b>19 ± 1</b>	<b>30 ± 1</b>
	A2	SEM-EDX	Bright rim surrounding the Al-Zr-rich grain boundary in Fig. 7b	9 ± 1	<b>17 ± 1</b>	<b>25 ± 1</b>	<b>13 ± 1</b>	26 ± 1	10 ± 1



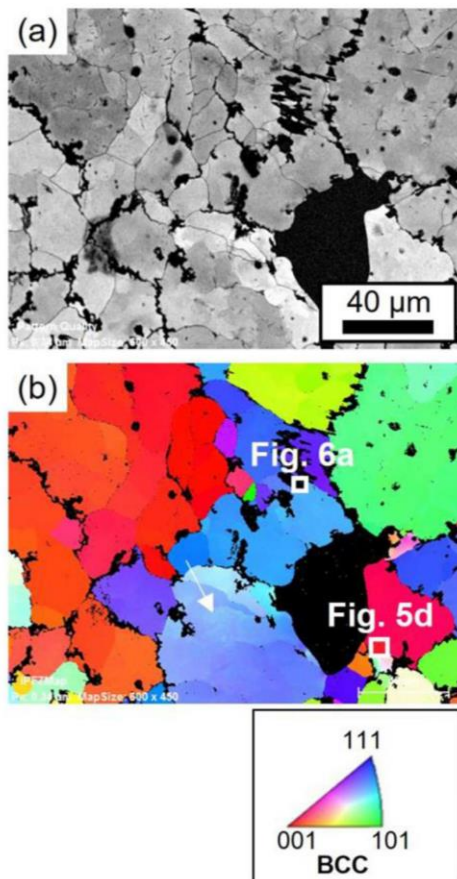


Fig. 4. EBSD maps of RSA in AC. (a) pattern quality, (b) inverse pole figure (IPFZ).

of the RSA in the AC condition (with an electron-transparent region close to large hole on lower right). The EDX-coupled EBSD system indexes the large equiaxed grains in Fig. 4 as “BCC” (Body-Centered Cubic), irrespective of location, i.e. the dendritic structure is not resolved. In turn, the IPFZ map shows subgrains separated by non-indexed regions, which have comparable sizes to secondary dendritic arms (cf. Fig. 2b). Within these subgrains, a further subdivision into smaller regions with varying orientations is seen, e.g., purplish-bluish grain bordering left side of large whole (shown by the white arrow in Fig. 4b). The grain and subgrain boundary regions rich in Al and Zr, as seen in Fig. 2, are not indexed in this map.

The nanostructure of the AC alloy was revealed by TEM. Fig. 5 shows two CTEM-DF images (a and b) and their corresponding zone axis ( $Z = [001]$ ) SAD pattern (P) (c). In green, Fig. 5c shows the reflections selected to retrieve the diffraction contrasts in Fig. 5a-b. Since the image in Fig. 5a was formed using a superlattice 100 reflection and the image in Fig. 5b was formed using a 200 reflection, the interdendritic region can be interpreted as composed of a mixture of two bcc-based phases. The insets in the bottom right of Fig. 5a-b show a magnified region marked by a white square. Three white lines in these insets, placed at the same locations, show that different locations are illuminated in both images. Furthermore, the bright regions seem strongly interconnected in Fig. 5a. Thus,

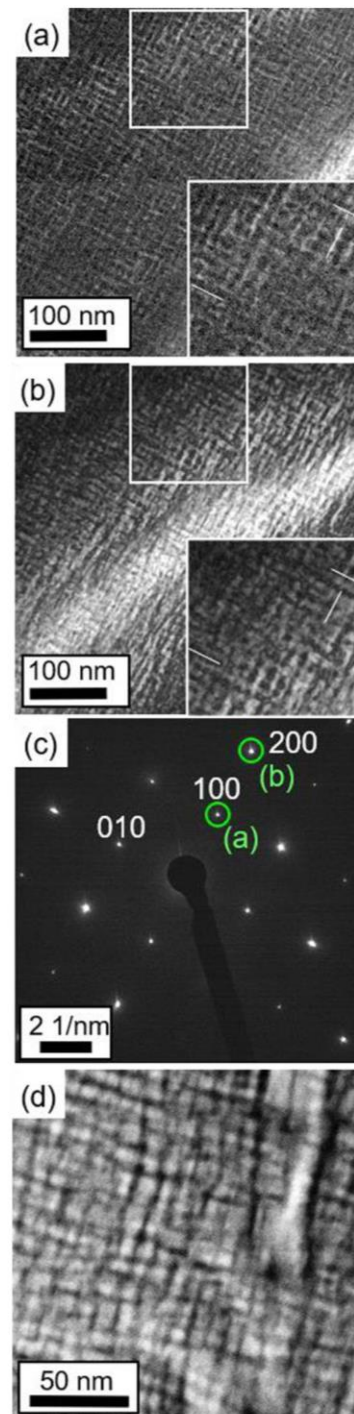
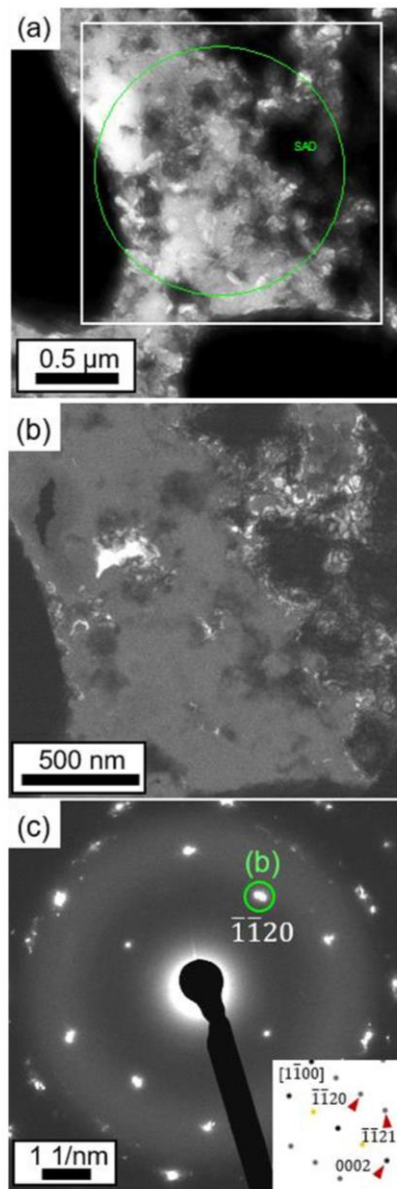


Fig. 5. (C)TEM-DF micrographs of the interdendritic zone in AC oriented along  $[001]$  zone axis: (a) using superlattice reflection (100) in (c); and (b) using reflection (200). (c) SADP with contrast apertures marked in green for images in (a) and (b). (d) STEM-HAADF micrograph of the region marked as “Fig. 5d” in the IPFZ in Fig. 4b. (For interpretation of the references to color in this figure legend, the reader is referred to the web version of this article.)



the phase with the bright contrast in Fig. 5a (matrix channels) is ordered (B2) while the remaining phase is disordered (A2). The STEM-HAADF image in Fig. 5d, acquired at a similar interdendritic location, more clearly reveals a continuous region with a low mean atomic number (dark), while discrete bright regions in between are associated to a large mean atomic number.

The Al-Zr-rich region (cf. Fig. 2b-c) was also characterized by TEM, as presented in Fig. 6. Fig. 6a shows a CTEM-BF of the Al-Zr-rich region (mostly bright areas) surrounded by thicker regions



**Fig. 6.** (a) (C) TEM-BF micrograph of an Al-Zr-rich region in the interdendritic zone (region marked as “Fig. 6a” in the IPFZ in Fig. 4b). (b) (C) TEM-DF micrograph marked with white rectangle in (a). (c) SADP from the region marked in green in (a). Inset on bottom right shows the indexed simulated diffraction pattern. For details see text. (For interpretation of the references to color in this figure legend, the reader is referred to the web version of this article.)

such as those in Fig. 5. Most of the SADP (Fig. 6c) can be indexed (cf. inset simulated diffraction pattern on bottom right) as either  $\text{Al}_3\text{Zr}_5$  or  $\text{Al}_4\text{Zr}_5$ , both along the zone axis  $[1\bar{1}00]$ . Both Al-Zr-rich phases are hexagonal, having the  $\text{P6}_3/\text{mcm}$  space group ( $\text{Al}_3\text{Zr}_5$ : ICDD- 04-003-0819,  $\text{Al}_4\text{Zr}_5$ : ICDD -00-048-1382). More details about the hexagonal phase will be discussed in Section 4. The CTEM-DF image (Fig. 6b) shows two types of contrast. One is very bright which comes from the reflection  $(\bar{1}\bar{1}20)$  in the diffraction pattern, around which the contrast aperture was placed, to which discrete nano-sized regions can be associated. The second contrast is weaker and covers the region that also appears bright in Fig. 6a. This contrast may be associated to the diffused ring of which center of mass coincides with  $(\bar{1}\bar{1}21)$  in Fig. 6c, typical for amorphous material. This reflection is also the strongest for powder diffraction patterns of either Al-Zr-rich candidates. For the estimation of the volume fraction in the AC alloy, SEM-BSE images were used for the Al-Zr-rich phase in the grain boundaries and STEM-DF images for the A2 and B2 phases. The volume fraction was estimated to be  $(8 \pm 4)\%$  for the hexagonal Al-Zr-rich phase,  $(36 \pm 4)\%$  for the B2 phase, and the rest for the A2 phase.

### 3.1.2. Annealed state (AN)

After annealing, the dendritic structure cannot be discerned anymore and the equiaxed grains become clearer (Fig. 7a), forming grain and subgrain boundaries. The average grain size is  $78 \pm 10 \mu\text{m}$ . Large second phase precipitates (black core surrounded by bright rim) are found at the grain boundaries (blue arrows in Fig. 7a-b). Also, the subgrain boundaries are found to be replaced with a black-bright dual phase that is also a common feature within the large grains (red arrows in Fig. 7b-c). These interfacial layers can be as thick as  $1 \mu\text{m}$ . Fig. 7d show the structure inside the equiaxed grains at a high magnification, which also reveals a now continuous black phase that surrounds bright precipitates. The large second phase precipitates at the grain boundaries are rich in Al and Zr (see Fig. A1- Appendix A of supplementary data), whereas the bright interfacial layer surrounding the Al-Zr particles is rich in Nb, Mo and Ta. This elemental partitioning also applies to the dual phase structure found at subgrain boundaries at a higher magnification (Fig. 7c), as revealed by qualitative EDX points of these regions, i.e., a dark phase rich in Al and Zr, and a bright phase rich in Nb, Mo and Ta (cf. Table 2).

To identify the phases mentioned above, X-ray diffraction (XRD) patterns were indexed as shown in Fig. 8. Three phases, (B2, A2 and hexagonal intermetallic phase) are identified by comparing their patterns based on PowderCell simulations for both states. The A2 and B2 match well with the pattern acquired for the AC alloy (Fig. 8a), with corresponding lattice parameters  $a_1 = 3.28 \text{ \AA}$  and  $a_2 = 3.32 \text{ \AA}$ . The lattice parameters of the A2 and B2 phases in the AN alloy are determined as  $a_3 = 3.27 \text{ \AA}$  and  $a_4 = 3.31 \text{ \AA}$ , respectively (Fig. 8b). Based on previous results of an alloy of similar composition [10,17], the peaks that do not match with neither the A2 nor the B2 phase, are indexed as the hexagonal intermetallic phase (space group:  $\text{P6}_3/\text{mcm}$ ).

The EDX-coupled EBSD system indexes the large equiaxed grains in the AN as “BCC” (rich in Nb, Ti and Zr), even though it has a dual A2/B2 nanostructure (see separate peaks in Fig. 8b), and the precipitates located at the grain boundaries are indexed as a hexagonal crystal structure (space group:  $\text{P6}_3/\text{mcm}$ ) with a composition rich in Al and Zr. (cf. Fig. A2- Appendix A of supplementary data), corroborating the results obtained by XRD and by Jensen et al. [26]. TEM results demonstrate a heterogeneous nanostructure that consists of precipitates with B2 phase (plate-like with thickness  $\approx 10 - 100 \text{ nm}$ ) embedded in a continuous phase (chan-

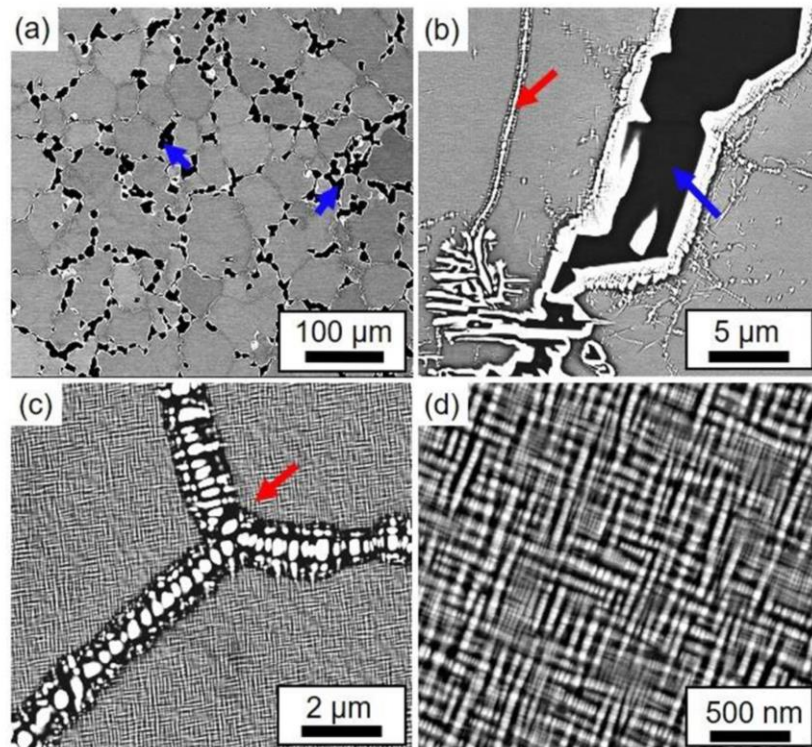


**Fig. 7.** SEM-BSE micrographs of the AN alloy, revealing features at different length scales. (a) Low magnification image showing an equiaxed microstructure with large secondary precipitates at grain boundaries. (b) Detail of coarsened precipitate at grain boundaries. (c) Detail of two-phase replacing the subgrain grain boundaries (d) High magnification image showing a nanometric two-phase basket-weave lamellar structure within grains. Blue and red arrows respectively mark coarse grain boundary precipitates and finer subgrain boundary precipitates. (For interpretation of the references to color in this figure legend, the reader is referred to the web version of this article.)

nels with thickness  $\approx 3 - 30$  nm). For a detailed description of the TEM analysis see Fig. A3 of [supplementary data](#).

These results show that the microstructure in the annealed state with the condition in the present work (1400 °C for 24 h and cooled at  $\leq 4$  K/min) reproduces the microstructure reported with the conditions in the literature (1400 °C for 24 h + hot isostatic pressing at 1400 °C for 4 h and 205 MPa, cooled at 10 K/min) [8,10].

**Table 2** summarizes the chemical composition of the phases in the different regions for the AC and AN alloy. For the estimation of the volume fraction in the AN alloy, SEM-BSE images were used for the Al-Zr-rich phase in the grain boundaries and STEM-DF images for the A2 and B2 phases. The volume fraction was estimated to be  $(13 \pm 6)\%$  for the hexagonal Al-Zr-rich phase,  $(34 \pm 8)\%$  for the B2 phase, and the rest for the A2 phase.

### 3.2. Differential thermal analysis (DTA)

**Fig. 9** shows that two peaks are distinguished at the following temperature ranges: the first peak is detected between  $\approx 820$  °C and 1543 °C, which has an exothermic character; the second and smallest peak, with an endothermic character, is detected between 1555 °C and 1613 °C. The final 7 °C of the curve show a steep path towards the maximum temperature of the analysis shown by the dashed line at the end of the last peak (which coincides with the maximum temperature of the equipment), and it therefore could extend to higher temperatures.

### 3.3. Thermodynamic calculations

#### 3.3.1. Scheil simulation for non-equilibrium

In **Fig. 10**, the fraction of the dependences of the solid phases on the temperature during solidification is shown for the studied RSA based on the experimentally measured composition in **Table 1**. The temperatures of start,  $T_{L,Scheil}$  (solid  $< 0.01\%$ ), and completion,  $T_{S,Scheil}$ , of Scheil modeling and the temperatures of start,  $T_{L,Eq}$ , and completion,  $T_{S,Eq}$ , of equilibrium are given in **Table 3**, as calculated using the TCNI10 and TCHEA3 database.

**Fig. 10** represents the Scheil solidification diagram using the TCHEA3 database, which shows the formation of a single disordered A2 phase (BCC\_B2#1) that is rich in Al, Ti and Zr. Solidification starts at  $T_{L,Scheil} = 1895$  °C and ends at  $T_{S,Scheil} = 1345$  °C with a solidification range of  $\Delta T_{S,Scheil} = 550$  °C. When BCC\_B2#1 reaches a fraction of solid  $\approx 0.72$ , the SIGMA phase starts solidifying between 1475 °C and 1360 °C. At this temperature, the intermetallic phase Al4Zr5 appears with approx.  $X = 0.85$  until almost the end of the solidification, where the C14\_LAVES phase then appears. The Scheil-Gulliver model diagram was also calculated for the TCNI10 database (see Fig. B1-Appendix B of [supplementary data](#)), and it shows the same results as the TCHEA3 database.

#### 3.3.2. Equilibrium

The property diagrams of the RSA alloy with the chemical composition given in **Table 1** were calculated using CALPHAD analysis. The property diagram describes the relative amount of the phases in equilibrium as a function of their evolution with temperature,



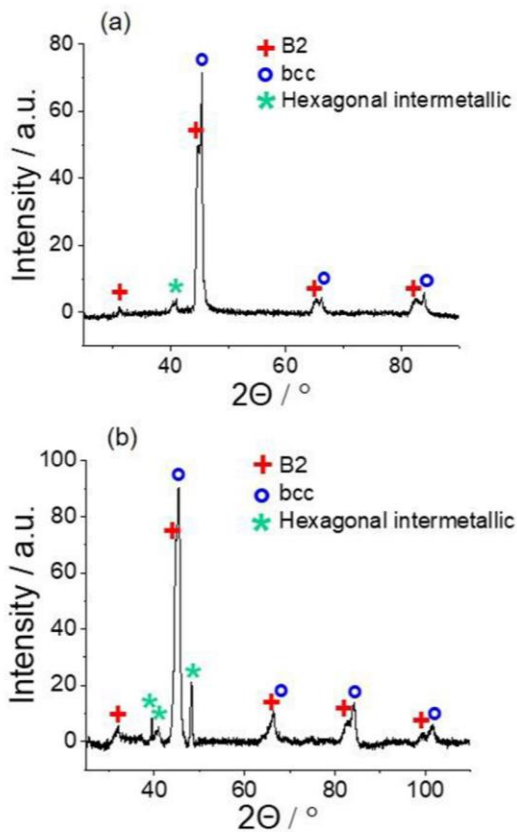


Fig. 8. XRD pattern (a) AC state (b) AN state.

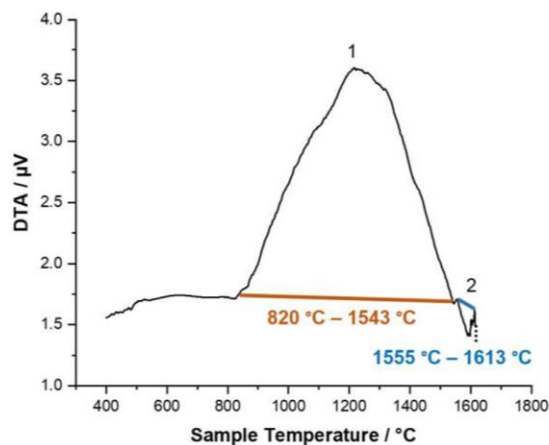


Fig. 9. DTA signal of the AN specimen as a function of the temperature recorded during the heating ramp up to 1620 °C. The signal is corrected by a blank measurement.

assuming the transformation rate is extremely slow or that species diffuse at a very fast rate [27]. The calculated equilibrium phases and their volume fractions in the temperature range from 600 °C to 2000 °C are shown in Fig. 11 for the TCHEA3 database. A detailed

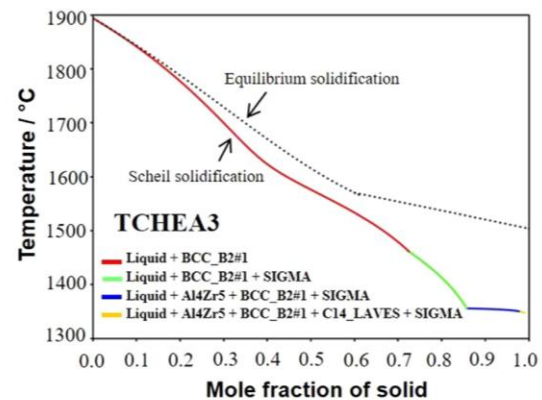


Fig. 10. Scheil solidification diagram for the RSA using the ThermoCalc software with database TCHEA3 database (cf. Fig. B1-Appendix B of supplementary data for database TCNI10).

Table 3

Liquidus and solidus temperature for Scheil and equilibrium solidification in both databases.

Database	$T_L$ (Scheil-Eq.) / °C	$T_S$ (Scheil) / °C	$T_S$ (Eq.) / °C
TCHEA3	1895	1345	1503
TCNI10	1895	1345	1503

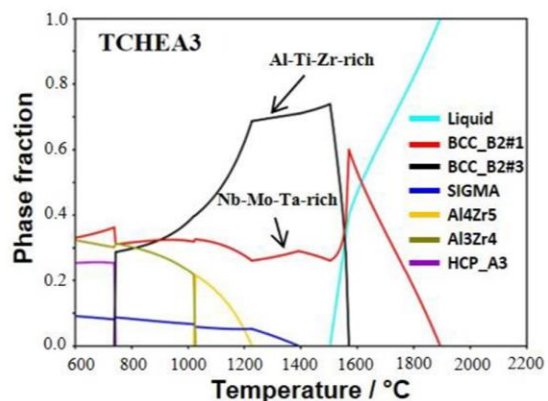


Fig. 11. Property diagram for the RSA using ThermoCalc software (TCHEA3 database). (cf. Fig. B2 and Table B2-Appendix B of supplementary data for database TCNI10).

description of the equilibrium phase transformation temperatures (in °C) in the studied alloy is given in Table B1 and Table B2 (Appendix B of supplementary data) for TCHEA3 and TCNI10, respectively. In Fig. 11 the beginning of solidification is marked by the formation of a single bcc phase at 1895 °C (Table B1-Appendix B of supplementary data), which is rich in Nb, Mo and Ta (BCC\_B2#1), until another bcc phase named BCC\_B2#3 and rich in Al, Ti and Zr starts appearing at 1570 °C. The formation of SIGMA at  $T = 1388$  °C is also indicated with a low final fraction of the phase (<10%). At 1225 °C, a phase rich in Al and Zr appears, i.e., Al4Zr5, and at 1025 °C this phase seems to transform into Al3Zr4, which continues forming below 600 °C. Lastly, at 743 °C the formation of HCP\_A3 is anticipated, which is mostly rich in Ti. The results obtained for the TCNI10 database are the same for the TCHEA3 database (see Fig. B2 and Table B2-Appendix B).

Fig. 12 represents a comparison of the mole fraction of the elements in the equilibrium bcc phases calculated at 1000 °C with the TCHEA3 database (cf. Table B4-Appendix B of supplementary data for the TCNI10 database). At 1000 °C, the two databases show the presence of two bcc phases in equilibrium and in both cases, these are one Al-Ti-Zr-rich and one Mo-Nb-Ta-rich phase. The phase composition indicates that the first phase to solidify is rich in Nb, Mo and Ta while the second one is rich in Al, Ti and Zr (cf. Fig. 11). In addition, the temperature where the first and second phase appear is similar for both databases (cf. Table B1 and Table B2-Appendix B of supplementary data). The HCP\_A3 phase, rich in Al, Ti and Zr (cf. Table B7 and Table B8-Appendix B of supplementary data), is anticipated to form at lower temperatures. TCNI10 and TCHEA3 indicate the formation of the phase SIGMA at the same temperature with a very small amount (<10%). Both databases indicate the formation of Al-Zr-rich phases (Al4Zr5 and Al3Zr4).

Fig. 13a represents a simulation assuming that the bcc phases are the only solid phases that are formed, in order to identify the miscibility gap and the difference in composition and volume fraction of the bcc phases. Here, the mole fraction of Al is plotted against temperature, indicating how the formation of the bcc phases varies with varying Al and Zr content, while the composition of the rest of the elements remains fixed (at  $X_{Mo} = 0.1019$ ,  $X_{Nb} = 0.2023$ ,  $X_{Ta} = 0.0676$ ,  $X_{Ti} = 0.2079$ ). The color-coded legend inset in Fig. 13a denotes the boundaries at which a phase transformation exists. The incomplete light blue line (BCC\_B2#3) is due to a lack of information on that special projection. The marked region of dashed gray lines in the graph (Fig. 13a) is made as an attempt to show where the miscibility gap region closes. However, the exact composition at which the miscibility gap closes is not known since the diagram is a projection. Considering the experimentally determined mole fraction of Al in the alloy ( $X_{Al} = 0.2103$ ), the equilibrium conditions were calculated at 2000, 1700, 1520 and 1200 °C (red vertical line in Fig. 13a), as shown in Fig. 13b (calculated phase fractions and composition of the phases are summarized in Table B9-Appendix B of supplementary data). At 2000 °C, only the liquid is present whereas at 1700 °C the first bcc phase (BCC\_B2#1) already appears. At this temperature, the volume fraction of BCC\_B2#1 (rich in Nb, Mo, and Ta) is 0.32 and the rest is liquid. At 1520 °C, the BCC\_B2#1 (Nb-Mo-Ta-rich), BCC\_B2#3 (Al-Ti-Zr-rich) and liquid are in equilibrium with mole fractions of 0.26, 0.64 and 0.10, respectively. Finally, at 1200 °C, only BCC\_B2#1

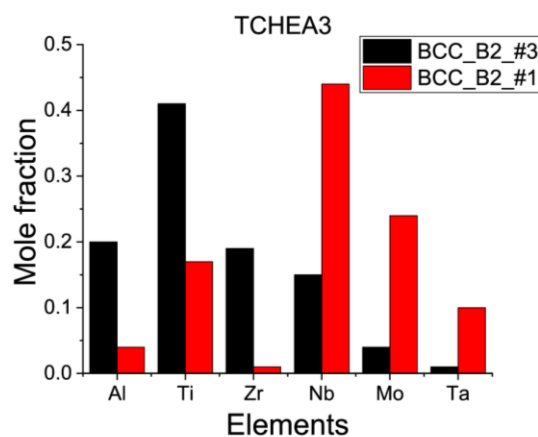


Fig. 12. Mole fraction of the elements in equilibrium phases for the studied alloy at  $T = 1000$  °C (1273 K) as calculated with the TCHEA3 database (cf. Table B4-Appendix B of supplementary data for the TCNI10 database).

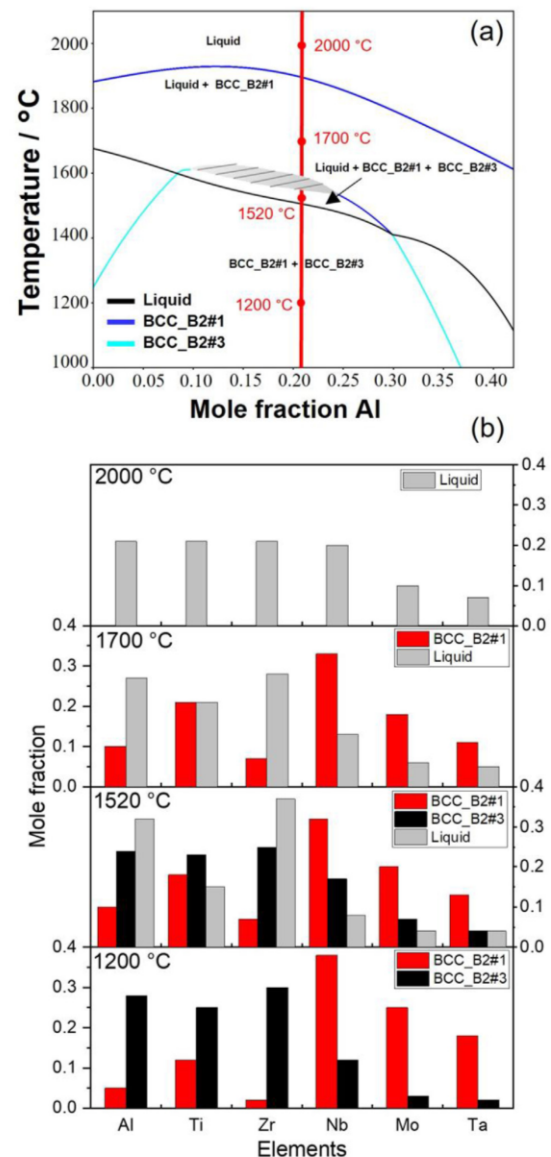


Fig. 13. (a) Mole fraction of Al vs temperature in equilibrium considering only the formation of bcc phases and liquid, using the TCHEA3 database. A miscibility gap region that closes in the region marked with dashed gray lines is shown. (b) Mole fractions of the elements of equilibrium phases in the studied alloy, considering only the formation of bcc phases at 2000, 1700, 1520 and 1200 °C respectively, calculated with the TCHEA3 database.

and BCC\_B2#3 will be in equilibrium with mole fractions of 0.30 and 0.70, respectively.

#### 4. Discussion

The microstructural analysis demonstrates that the  $AlMo_{0.5}NbTa_{0.5}TiZr$  RSA in AC condition presents dendritic and interdendritic zones with differences in composition and a mixture of A2/B2 phases  $\approx 2 - 20$  nm, and the presence of a residual eutectic rich in Al and Zr inside the interdendritic region (Fig. 2c). The diffuse

ring and the presence of bright areas in Fig. 6b reveal that the Al-Zr-rich phase region in the AC is formed by crystalline as well as amorphous portions, the latter being larger, with a  $95 \pm 4\%$  of area fraction. Thus, at this cooling rate and probably due to the strong solute segregation to the interdendritic region, the conditions for forming an amorphous phase are fulfilled. In fact, Zr-Al alloys are well-known for their glass-forming ability [28,29], which is even further pronounced in the presence of the other elements. On the other hand, the AN state shows the presence of larger ( $\approx 10 - 100$  nm) A2/B2 phases than in the AC state, and an increment of  $\approx 5\%$  in the volume fraction of the Al-Zr-rich phase (hexagonal  $P6_3/mcm$ ), which can be due to its full crystallization. A good agreement with what was reported by Senkov et al. [8] and Jensen et al. [10,26] for the fully heat-treated state is thus found, with the results shown here for only annealing at  $1400^\circ\text{C}$  (without hot isostatic pressing treatment at the same temperature for further 4 h).

The AC results obtained experimentally may be primarily simulated by the Scheil model, which assumes total diffusion in the liquid and no diffusion in the solid. In the Scheil solidification model, both databases evaluated here show that even at  $1400^\circ\text{C}$ , complete solidification is not reached. The Scheil model indicates the formation of a single Al-Ti-Zr-rich bcc (A2) phase until the fraction of solid reaches  $\approx 72\%$  (Fig. 10). However, a separation of the two bcc phases should be visible when comparing with the experimental AC state. Therefore, additional calculations using the uncommon miscibility gap option were performed, still showing the formation of a single A2 phase.

On the other hand, the formation of the intermetallic  $\text{Al}_4\text{Zr}_5$  phase is indicated in the Scheil solidification. Unlike the calculations, the hexagonal phase in the experimental results does not show an  $\text{Al}_4\text{Zr}_5$  stoichiometry. In fact, the average pattern quality shown in Fig. 4b for these regions is poor yet still indexable: considering the experimental conditions in the present work, the manual indexing of individual high quality Kikuchi patterns (not shown here) suggests evidence of an unknown stoichiometry ( $\text{Al}_x\text{Zr}_y$ ) for a phase with hexagonal symmetry but that is not identified as hexagonal solid solution (HCP), the latter being reported elsewhere [9]. Evaluating the differences between the lattice cells of the two possible experimental ordered hexagonal phases ( $\text{Al}_3\text{Zr}_5$  and  $\text{Al}_4\text{Zr}_5$ ) shows that the surplus of Al atoms found in the  $\text{Al}_4\text{Zr}_5$  phase is distributed along the c axis on the corners of the hexagon, only causing a slight repositioning of the remaining atoms in the cell when compared to  $\text{Al}_3\text{Zr}_5$  (see Fig. C1-Appendix C of supplementary data). Although the distribution of the atoms is different, both phases belong to the same space group ( $P6_3/mcm$ ). However, a detailed identification of this phase is beyond the scope of this publication and will follow in a separate contribution. Since the diffraction patterns between  $\text{Al}_3\text{Zr}_5$  and  $\text{Al}_4\text{Zr}_5$  resemble each other and considering that probably the  $\text{Al}_x\text{Zr}_y$  phase of the present alloy probably is an intermediate phase between those two ( $\text{Al}_{4-x}\text{Zr}_5$ ,  $0 \leq x \leq 1$ ), the diffraction pattern shown in the Fig. 6c was indexed as the  $\text{Al}_4\text{Zr}_5$  phase.

To understand the solidification path of the alloy, the Scheil model was implemented using the TCHEA3 database to calculate the mole fraction of solid vs the mole fraction of each element in the liquid (Fig. 14). This simulation evidences that there is a high segregation in the last liquid (85% of solid formation), rich in Al and Zr, regarding the original alloy composition. The calculated ratio  $X_{\text{Zr}} / X_{\text{Al}}$  at 85% of solid formation (Table 4) matches the experimental ratio  $X_{\text{Zr}} / X_{\text{Al}}$  of the Al-Zr-rich phase (Table 2), which is also close to the stoichiometry of the  $\text{Al}_4\text{Zr}_5$  phase. This phase is stable almost at the end of solidification according to the calculations, and the Al-Zr-rich intermetallic phase is found in the interdendritic zone, which is also the last region that solidifies, showing a good agreement between the calculations and the experimental findings.

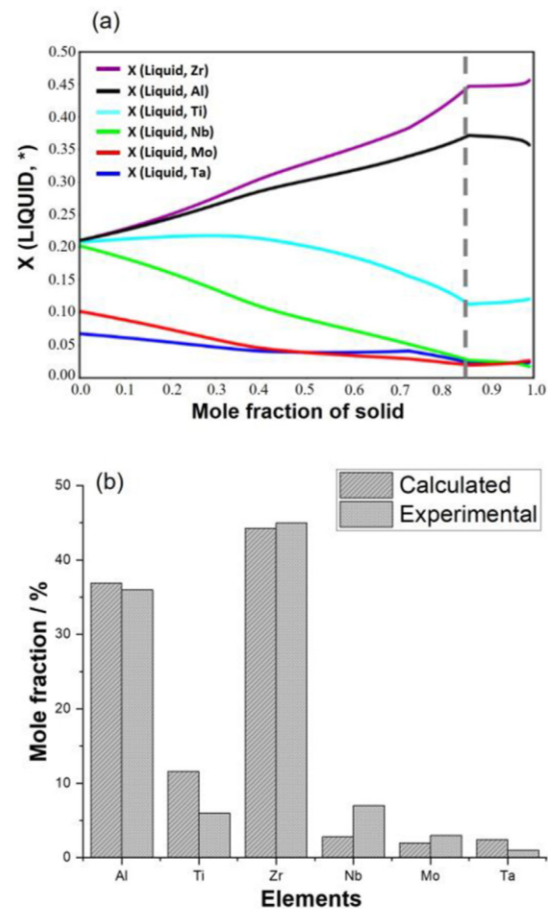


Fig. 14. (a) Mole fraction of solid vs mole fraction of each element in the liquid using Scheil model with the TCHEA3 database.  $X(\text{Liquid}, *)$  = mole fraction of element "\*" in the liquid. (b) Comparison between calculated liquid composition at 0.85 mol fraction (85%) of the solid (dashed line in (a) and Table 4) and experimental composition of the Al-Zr-rich phase in the interdendritic region in AC (Table 2).

On the other hand, the microstructure of the AN alloy emerged after high temperature annealing at  $1400^\circ\text{C}$  followed by furnace cooling and, as such, even only after 24 h, it is believed to be indicative of the stable high temperature phases. Therefore, the experimental results of the AN alloy are compared with the equilibrium calculations. In equilibrium, both databases (TCNI10 and TCHEA3) show the formation of two disordered bcc phases, one that is rich in Al, Zr and Ti, and another, rich in Nb, Mo and Ta. Furthermore, in the binary diagrams as well as in the ternaries calculated within the databases under study (not shown here), there is no modeling for a B2 (ordered) phases, so it is to be expected that the A2 (disordered) phase is the default phase. Thus, considering that the databases used in this paper do not distinguish between order and disorder, and based on the experimental phase composition of the bcc phases, it could be assumed that the calculated Al-Zr-Ti-rich phase is the B2, and the Nb-Mo-Ta-rich phase is the A2 obtained experimentally. In fact, the databases only indicate the presence of these two bcc phases (named BCC\_B2#1 and BCC\_B2#3) at that temperature ( $1400^\circ\text{C}$ ) and, in both databases, solidification starts with the formation of the BCC\_B2#1 (rich in higher melting Mo, Nb and Ta).



**Table 4**

Calculated composition of the last 15% of the liquid phase according to the Scheil solidification as shown in Fig. 14.

Database	Phase	Sol. mole fraction $X_{sol}$	Al	Mo	Nb	Ta	Ti	Zr	$X_{Zr}/X_{Al}$
TCHEA3	liquid	0.85	36.90	1.99	2.82	2.43	11.60	44.26	1.2

Experimental results show the presence of a dual phase structure composed of A2 and B2 phase in the AN alloy with channels and precipitates as in the AC alloy, but with smaller sizes for the latter. Jensen et al. [26], proposed that the precipitation of these phases may occur by spinodal decomposition during cooling, due to the compositional fluctuations in high temperature phases. Kadirval et al. [30] analyzed the details of a possible phase transformation pathway for this alloy, including a congruent spinodal decomposition upon heat treatment. The Fig. 13 confirms that a miscibility gap already exists at 1400 °C at the exact composition of the original alloy, where the two bcc phases coexist and the constituents are not completely miscible, pinpointing the possibility of a spinodal decomposition as suggested in the previous works [26,30] and the experimental results found in the present work. Moreover, the dual phase structure being present at compositions found in the interdendritic region of the AC alloy and the dendritic regions of the AN alloy is also in line with the wide miscibility gap found Fig. 13a, where both phases are indicated to coexist.

Although experimental evidence of SIGMA is neither shown in the AC state nor in the AN state, under equilibrium conditions, the stability of this phase has been studied on several occasions for both conventional and multicomponent alloys [35–38] where both temperature and annealing time play an important role, and there is evidence that longer annealing times (>500 h) are required to stabilize this phase. Therefore, SIGMA may be thermodynamically stable but still not developed after 24 h of annealing. The other phases proposed to be formed in equilibrium conditions (Al<sub>3</sub>Zr<sub>4</sub> and HCP\_A3), are stable at temperatures below the annealing temperature, so they are not expected to appear in the experimental results.

The Scheil diagram, Fig. 10, indicates that, due to the strong solute segregation, the last drop of liquid may solidify at a temperature as low as 1345 °C, about 50 °C below the annealing temperature (1400 °C) and 150 °C lower than the equilibrium solidus temperature (1503 °C). This means that the local melting temperature at the grain boundaries and subgrain boundaries can be relatively low. Together with the assistance from additional interfacial energies released, these can result in the formation of liquid-like interfacial phases during the annealing at 1400 °C, as observed in several ceramics [31–34]. The formation of such liquid-like phases dramatically enhances the diffusion of solute atoms at the interfacial regions. This can then explain the coarsened microstructure at the grain and subgrain boundaries, especially the formation of large secondary Al-Zr-rich precipitates with the continuous surrounding layer around them (c.f. Fig. 7 for the details) in the AN sample. The formation of interfacial phases at both grain and subgrain boundaries has important consequences for the mechanical performance of the RSA, the detailed study of which will be presented elsewhere.

Senkov et al. [16] studied the AlMo<sub>0.5</sub>NbTa<sub>0.5</sub>TiZr alloy using the Pandat Ti database to model Scheil solidification. They found that solidification starts with the formation of a bcc phase (enriched with Mo, Nb and Ta), and that a very small amount ( $\approx$  0.3%) of the intermetallic phase Al<sub>2</sub>Zr<sub>3</sub> forms at the end of solidification. Furthermore, they showed the formation of three phases at equilibrium: “bcc1”, Ti<sub>3</sub>Al and Al<sub>2</sub>Zr<sub>3</sub>. Furthermore, Whitfield et al. [17] anticipated the formation of two bcc phases at high temperature using the SSol5 database, whereas Al<sub>4</sub>Zr<sub>5</sub> formed close to 1000 °C, and a B2 and HCP phase formed below 1000 °C (in equi-

librium conditions) in their calculations. The latter resembles the results obtained in the calculations from the present work. Unfortunately, the composition of each phase was not reported by Whitfield et al., which makes a comparison with the results presented here impossible. However, later analyses by XRD and TEM have demonstrated that the “B2” phase described by the SSol5 database is in fact a disordered A2 phase [39]. Thus, it must be considered that the databases usually do not make a distinction between order and disorder, which leads to a decline of accuracy in the calculations.

Finally, from the differential thermal analysis shown in Fig. 9, the observed peaks can be related to the phase transformations according to the experimental observation, and these phase transformations can be compared with the thermodynamic calculations presented in Fig. 11 (equilibrium conditions). The first peak can be associated with solid–solid phase transformations and the second peak with a melting process (Fig. 9). Although exact equilibrium conditions cannot be achieved during DTA, the results are obtained in conditions close to equilibrium because a slow heating rate of 5 K/min was used and therefore, these results may be used to verify the thermodynamic calculations. The widest peak, observed between 820 °C and 1543 °C, is likely to be composed of several overlaying peaks. These could be related to the increase of amount and final dissolution of the major phase BCC\_B2, enriched in Al, Zr and Ti (BCC\_B2#3 according to both databases) as well as early stages of a premelting at grain boundaries. The last peak at a temperature above 1555 °C can be related to a first event of bulk melting, which can be clearly seen in the equilibrium calculations (Fig. 11). Note that even from the equilibrium calculations, the liquid and the two bcc phases (BCC\_B2#1 and BCC\_B2#3) coexist already at 1503 °C. Considering the broadness of the second peak, it is possible that an overlap of different peaks takes place, suggesting that liquification may start happening in parallel to dissolution of the BCC\_B2 phase. These results indicate that, from the point of view of hot cracking, the alloy starts the formation of liquid at a temperature  $\approx$  200 °C higher than the temperature where liquid appears in single crystal (SX) Ni-based superalloys (1345 °C for the SX CMX4 alloy). However, grain boundary instabilities and lack of room temperature ductility were observed (not shown here), and therefore, mechanical properties at high temperature, as well as corrosion behavior should be assessed to establish whether this alloy has potential for high temperature applications such as Ni-based superalloy.

## 5. Summary and conclusions

In the present work, an approach to study the phase stability and solidification behavior of the RSA AlMo<sub>0.5</sub>NbTa<sub>0.5</sub>TiZr was implemented using CALPHAD calculations with two different databases (TCNI10 and TCHEA3), and compared with experimental data from as-cast, AC, and annealed state, AN (AC + 1400 °C for 24 h). The as-cast state was compared with Scheil, whereas the annealed state was compared with equilibrium calculations. The following conclusions can be drawn from the results:

- The as-cast state shows a dendritic structure with a A2/B2 phase structure in both the dendritic and interdendritic regions, which are an order of magnitude smaller than the A2/B2 phase structure reported previously and reproduced in the present

work. Annealing at 1400 °C for 24 h crystallizes completely a mostly amorphous phase that is rich in Al and Zr within the interdendritic region in the as-cast state.

- Thermodynamic calculations using the Scheil-Gulliver model indicated the formation of a single bcc phase in both databases, although the presence of both A2 and B2 was experimentally demonstrated for the as-cast state. Phases such as SIGMA and LAVES also appear in the Scheil calculations even though no evidence is found in the experimental data for the conditions evaluated here. However, both databases anticipated the formation of the  $Al_4Zr_5$  intermetallic phase, which has the space group of the Al-Zr-rich intermetallic found experimentally ( $Al_{4-x}Zr_5$ ,  $0 \leq x \leq 1$ ), thus showing a partial agreement with the experimental data.
- Equilibrium thermodynamic calculations show the formation of two bcc phases, i.e., one rich in Al, Zr and Ti and a second one, rich in Mo, Nb and Ta, which is supported by the present and previous experimental results, although the calculations do not reflect the differences between ordered and disordered phases. The possibility of a spinodal decomposition resulting in the patterned microstructure observed experimentally was confirmed through the miscibility gap calculations.
- DTA results proved that in this alloy the liquid phase appears at a temperature higher than for Ni-base alloys, which could make it attractive for high temperature applications. However, other properties of this material, such as tensile behavior and corrosion resistance, need to be evaluated when pondering this RSA for structural applications. In particular, the role and mechanisms of interfacial phase changes during annealing need to be explored. Further efforts are currently in progress with a focus on these aspects.
- Finally, both databases evaluated here reproduce the same results, showing that the TCNI10 database is as useful for this alloy as the TCHEA3 database. However, there are still many discrepancies between calculations and experimental results. Therefore, more research should be developed to improve the modeling, including B2 ordering, and more effort could be made by experimentalists to investigate important ternaries that could provide information for the model improvements.

#### CRediT authorship contribution statement

**Patricia Suárez Ocaño:** Experimental Methodology, CALPHAD Calculations TCNI10 and TCHEA3, Formal analysis, Data curation, Writing – original draft. **Suzana G. Fries:** CALPHAD Calculations TCNI10 database, Formal analysis, Writing – review & editing. **Inmaculada Lopez-Galilea:** DTA Analysis, Writing – review & editing. **Reza Darvishi Kamachali:** Funding acquisition, Writing – review & editing. **Janina Roik:** ICP-OES measurements. **Leonardo Agudo Jácome:** Conceptualization, Methodology, Formal analysis, Writing – original draft, Supervision, Funding acquisition.

#### Declaration of Competing Interest

The authors declare that they have no known competing financial interests or personal relationships that could have appeared to influence the work reported in this paper.

#### Acknowledgement

PSO and LAJ acknowledge funding by the Deutsche Forschungsgemeinschaft (DFG) within the Project n°. 398838389. ILG acknowledge funding by the Deutsche Forschungsgemeinschaft (DFG) in the framework of the collaborative research center SFB/

TR 103 through project T4. All authors acknowledge Dipl.-Ing. Hans Chen, Dr. Alexander Kaufmann, Prof. Martin Heilmaier from Karlsruhe Institut for Technology for the fabrication of the alloy. PSO and LAJ acknowledge Prof. Gert Nolze, Romeo Saliwan Neumann for the EBSD analysis, Hennig Goldbeck for XRD, René Hesse for the EDX maps, Carlos Abad for the ICP-OES measurements and Stefan Reinsch for the DTA measurements. PSO and SGF thank the use of the facilities of ZGH (Center for Interface-Dominated High-Performance Materials). All authors acknowledge Dr. Axel Kranzmann for the fruitful discussion, and Dr. Julian Rosalie for the support in the data process.

#### Supplementary data

Supplementary data to this article can be found online at <https://doi.org/10.1016/j.matdes.2022.110593>.

#### References

- [1] A.P. Mouritz, Superalloys for gas turbine engines, *Introduction to Aerospace Mater.* (2012) 251–267, <https://doi.org/10.1533/9780857095152.251>.
- [2] L. Liu, J. Zhang, C. Ai, Nickel-Based Superalloys, *Encyclopedia Mater.: Metals Alloys 1* (2022) 294–304, <https://doi.org/10.1016/B978-0-12-803581-8.12093-4>.
- [3] F. Zhang, C. Wang, Y. Wu, L. Zhou, Q. Tian, Microstructural stability and mechanical properties of GH742 Ni-based wrought superalloy for turbine disk applications, *Mater. Sci. Eng., A* 832 (2022) 142488, <https://doi.org/10.1016/j.msea.2021.142488>.
- [4] R.C. Reed, *The Superalloys: Fundamentals and Applications* Cambridge University Press, 2006: p. 372pp. <https://doi.org/10.1017/S0001924000087509>.
- [5] M. Wang et al., Designing VxNbMoTa refractory high-entropy alloys with improved properties for high-temperature applications, *Scr. Mater.* 191 (2021) 131–136, <https://doi.org/10.1016/j.scriptamat.2020.09.027>.
- [6] W. Wei, T. Wang, C. Wang, M. Wu, Y. Nie, J. Peng, Ductile W0.4MoNbTaTi refractory high-entropy alloys with excellent elevated temperature strength, *Mater. Lett.* 295 (2021) 129753, <https://doi.org/10.1016/j.matlet.2021.129753>.
- [7] Y.D. Wu, Y.H. Cai, X.H. Chen, T. Wang, J.J. Si, L. Wang, Y.D. Wang, X.D. Hui, Phase composition and solid solution strengthening effect in TiZrNbMoV high-entropy alloys, *Mater. Des.* 83 (2015) 651–660, <https://doi.org/10.1016/j.matdes.2015.06.072>.
- [8] O. Senkov, D. Isheim, D. Seidman, A. Pilchak, Development of a refractory high entropy superalloy, *Entropy* 18 (3) (2016) 102, <https://doi.org/10.3390/e18030102>.
- [9] O.N. Senkov, J.K. Jensen, A.L. Pilchak, D.B. Miracle, H.L. Fraser, Compositional variation effects on the microstructure and properties of a refractory high-entropy superalloy AlMo0.5NbTa0.5TiZr, *Mater. Des.* 139 (2018) 498–511, <https://doi.org/10.1016/j.matdes.2017.11.033>.
- [10] J.K. Jensen, B.A. Welk, R.E.A. Williams, J.M. Sosa, D.E. Huber, O.N. Senkov, G.B. Viswanathan, H.L. Fraser, Characterization of the microstructure of the compositionally complex alloy Al<sub>1</sub>Mo<sub>0.5</sub>Nb<sub>1</sub>Ta<sub>0.5</sub>Ti<sub>1</sub>Zr<sub>1</sub>, *Scr. Mater.* 121 (2016) 1–4, <https://doi.org/10.1016/j.scriptamat.2016.04.017>.
- [11] D.B. Miracle, M.-H. Tsai, O.N. Senkov, V. Soni, R. Banerjee, Refractory high entropy superalloys (RSAs), *Scr. Mater.* 187 (2020) 445–452, <https://doi.org/10.1016/j.scriptamat.2020.06.048>.
- [12] H.L. Chen, H.H. Mao, Q. Chen, Database development and Calphad calculations for high entropy alloys: Challenges, strategies, and tips, *Mater. Chem. Phys.* 210 (2018) 279–290, <https://doi.org/10.1016/j.matchemphys.2017.07.082>.
- [13] O.N. Senkov, C. Zhang, A.L. Pilchak, E.J. Payton, C. Woodward, F. Zhang, CALPHAD-aided development of quaternary multi-principal element refractory alloys based on NbTiZr, *J. Alloy. Compd.* 783 (2019) 729–742, <https://doi.org/10.1016/j.jallcom.2018.12.325>.
- [14] S. Gorsse, O.N. Senkov, About the Reliability of CALPHAD Predictions in Multicomponent Systems, *Entropy* 20 (12) (2018) 899, <https://doi.org/10.3390/e20120899>.
- [15] A.F. Andreoli, R.G. Mendes, V.T. Witusiewicz, O. Shuleshova, M.A. van Huis, K. Nielsch, I. Kaban, Phase constitution and microstructure of the NbTiVZr refractory high-entropy alloy solidified upon different processing, *Acta Mater.* 221 (2021) 117416, <https://doi.org/10.1016/j.actamat.2021.117416>.
- [16] O.N. Senkov, S.V. Senkova, C. Woodward, Effect of aluminum on the microstructure and properties of two refractory high-entropy alloys, *Acta Mater.* 68 (2014) 214–228, <https://doi.org/10.1016/j.actamat.2014.01.029>.
- [17] T.E. Whitfield, H.J. Stone, C.N. Jones, N.G. Jones, Microstructural Degradation of the AlMo<sub>0.5</sub>NbTa<sub>0.5</sub>TiZr Refractory Metal High-Entropy Superalloy at Elevated Temperatures, *Entropy* 23 (1) (2021) 80, <https://doi.org/10.3390/e23010080>.
- [18] D.B. Miracle, O.N. Senkov, A critical review of high entropy alloys and related concepts, *Acta Mater.* 122 (2017) 448–511, <https://doi.org/10.1016/j.actamat.2016.08.081>.



- [19] J.O. Andersson et al., Thermo-Calc & DICTRA, computational tools for materials science, *Calphad* 26 (2) (2002) 273–312, [https://doi.org/10.1016/S0364-5916\(02\)00037-8](https://doi.org/10.1016/S0364-5916(02)00037-8).
- [20] W. Kraus, G. Nolze, POWDER CELL - a program for the representation and manipulation of crystal structures and calculation of the resulting X-ray powder patterns, *J. Appl. Cryst.* 29 (3) (1996) 301–303, <https://doi.org/10.1107/S0021889895014920>.
- [21] *Standard Test Methods for Determining Average Grain Size*. ASTM Designation: E112 – 13, 2013.
- [22] P.A. Stadelmann, EMS - a software package for electron diffraction analysis and HREM image simulation in materials science, *Ultramicroscopy* 21 (2) (1987) 131–145, [https://doi.org/10.1016/0304-3991\(87\)90080-5](https://doi.org/10.1016/0304-3991(87)90080-5).
- [23] C.A. Schneider, W.S. Rasband, K.W. Eliceiri, NIH Image to ImageJ: 25 years of image analysis, *Nat. Methods* 9 (7) (2012) 671–675, <https://doi.org/10.1038/nmeth.2089>.
- [24] H.L. Lukas, S.G. Fries, B. Sundman, COMPUTATIONAL THERMODYNAMICS The Calphad Method. (2010), <https://doi.org/10.1017/CBO9780511804137>.
- [25] D. Pelton, A. Equilibrium and Scheil-Gulliver Solidification, *Phase Diagrams and Thermodynamic Modeling of Solutions* 8 (2019) 133–148, <https://doi.org/10.1016/B978-0-12-801494-3.00008-7>.
- [26] J.K. Jensen, Characterization of a High Strength, Refractory High Entropy Alloy, AlMo<sub>0.5</sub>NbTa<sub>0.5</sub>TiZr, PhD Dissertation. The Ohio State University, 2017: p. 1–227. [http://rave.ohiolink.edu/etdc/view?acc\\_num=osu1492175560975813](http://rave.ohiolink.edu/etdc/view?acc_num=osu1492175560975813).
- [27] N. Saunders, A.P. Miodownik, CALPHAD Calculation of Phase Diagrams, *Pergamon Materials Series* 1 (1998) 299–408, [https://doi.org/10.1016/S1470-1804\(98\)80030-8](https://doi.org/10.1016/S1470-1804(98)80030-8).
- [28] T. Wang, Z. Jin, J.-C. Zhao, Thermodynamic assessment of the Al-Zr binary system, *J. Phase Equilibria and Diffusion* 22 (5) (2001) 544–551, <https://doi.org/10.1007/s11669-001-0072-4>.
- [29] A. Takeuchi, A. Inoue, Classification of bulk metallic glasses by atomic size difference, heat of mixing and period of constituent elements and its application to characterization of the main alloying element, *Mater. Trans.* 46 (12) (2005) 2817–2829, <https://doi.org/10.2320/matertrans.46.2817>.
- [30] K. Kadirvel, Z. Kloenne, J.K. Jensen, H. Fraser, Y. Wang, Phase-field modelling of transformation pathways and microstructural evolution in multi-principal element alloys, *Appl. Phys. Lett.* 119 (17) (2021) 171905, <https://doi.org/10.1063/5.0065522>.
- [31] J. Luo, S.J. Dillon, M.P. Harmer, Interface Stabilized Nanoscale Quasi-Liquid Films, *Microscopy Today* 17 (4) (2009) 22–27, <https://doi.org/10.1017/S15519295090001212>.
- [32] J. Luo, Stabilization of Nanoscale Quasi-Liquid Interfacial Films in Inorganic Materials: A Review and Critical Assessment, *Crit. Rev. Solid State Mater. Sci.* 32 (1–2) (2007) 67–109, <https://doi.org/10.1080/10408430701364388>.
- [33] J. Luo, V.K. Gupta, D.H. Yoon, H.M. Meyer, Segregation-induced grain boundary premelting in nickel-doped tungsten, *Appl. Phys. Lett.* 87 (23) (2005) 231902, <https://doi.org/10.1063/1.2138796>.
- [34] S.J. Dillon, M.P. Harmer, Multiple grain boundary transitions in ceramics: A case study of alumina, *Acta Mater.* 55 (15) (2007) 5247–5254, <https://doi.org/10.1016/j.actamat.2007.04.051>.
- [35] G. Laplanche et al., Phase stability and kinetics of  $\sigma$ -phase precipitation in CrMnFeCoNi high-entropy alloys, *Acta Mater.* 161 (2018) 338–351, <https://doi.org/10.1016/j.actamat.2018.09.040>.
- [36] J. Wan, H. Ruan, J. Wang, S. Shi, The Kinetic diagram of  $\sigma$  phase and its precipitation hardening effect on 15Cr-2Ni duplex stainless steel, *Mater. Sci. Eng., A* 711 (2018) 571–578, <https://doi.org/10.1016/j.msea.2017.11.079>.
- [37] L.u. Zhang, L.i. Zhang, H. Wang, J. Li, J. Man, Z. Xu, J. Yu, G. Wan, W. Wang, B. Wu, Evolution of the microstructure and mechanical properties of a sigma-hardened high-entropy alloy at different annealing temperatures, *Mater. Sci. Eng., A* 831 (2022) 142140, <https://doi.org/10.1016/j.msea.2021.142140>.
- [38] S. Antonov, J. Huo, Q. Feng, D. Isheim, D.N. Seidman, R.C. Helmink, E. Sun, S. Tin,  $\sigma$  and  $\eta$  Phase formation in advanced polycrystalline Ni-base superalloys, *Mater. Sci. Eng., A* 687 (2017) 232–240, <https://doi.org/10.1016/j.msea.2017.01.064>.
- [39] M.J. Krieger et al., High-temperature phase equilibria with the bcc-type  $\beta$  (AlMo) phase in the binary Al-Mo system, *Intermetallics* 83 (2017) 29–37, <https://doi.org/10.1016/j.intermet.2016.12.004>.

**Supplementary Material related to the article entitled:  
“The AlMo<sub>0.5</sub>NbTa<sub>0.5</sub>TiZr refractory high entropy superalloy:  
Experimental findings and comparison with calculations using the  
CALPHAD method.”**

Patricia Suárez Ocaño<sup>a,\*</sup>, Suzana G. Fries<sup>b</sup>, Inmaculada Lopez-Galilea<sup>c</sup>, Reza Darvishi Kamachali<sup>a</sup>,  
Janina Roik<sup>d</sup>, Leonardo Agudo Jácome<sup>a</sup>

a Federal Institute for Materials Research and Testing (BAM), Department for Materials Engineering, Unter den Eichen 87, 12205 Berlin, Germany.

b Materials Research Department (MRD), Ruhr-University Bochum, Universitätsstr. 150, 44801 Bochum, Germany.

c Institute for Materials, Ruhr-University Bochum, Universitätsstr. 150, 44801 Bochum, Germany.

d Federal Institute for Materials Research and Testing–BAM, Department of Inorganic Reference Materials, Richard-Willstätter-Strasse 11, 12489 Berlin-Adlershof, Germany.

\*Corresponding author: [patricia.suarez-ocano@bam.de](mailto:patricia.suarez-ocano@bam.de)

These supplementary materials provide additional information regarding the above-mentioned article. It is divided into three appendixes:

1. Appendix A – Supporting experimental data.
2. Appendix B – Supporting CALPHAD calculations.
3. Appendix C – Model crystal lattices.

## **1. Appendix A – Supporting experimental data.**

The EDX elemental map shown in [Fig. A1](#) confirms that the large second phase precipitates at the grain boundaries are rich in Al and Zr.

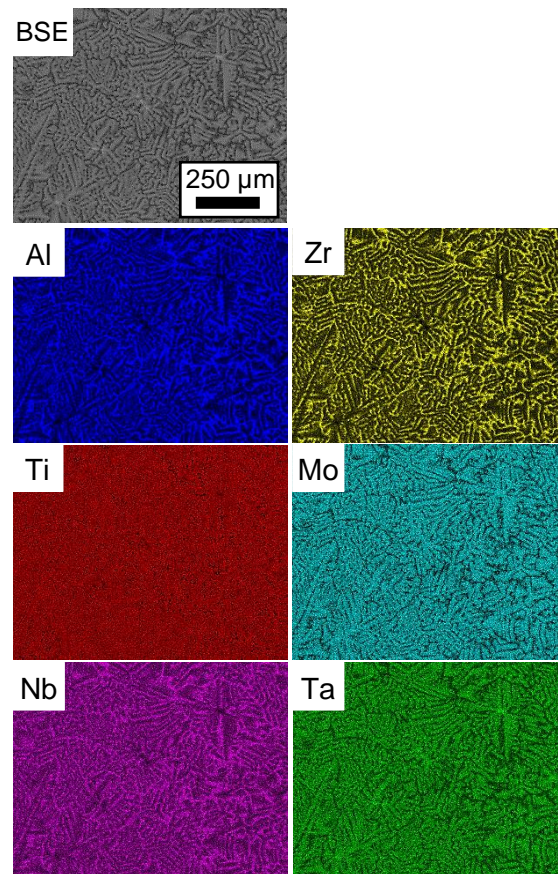


**Fig. A1.** EDX element Mapping of the AN alloy.

The EBSD pattern quality (PQ), inverse pole figure in Z (IPFZ) and phase map of the RSA in the AN are respectively shown in Fig. A2a-c. The EDX-coupled EBSD system indexes the large equiaxed grains in Fig. A2c as “BCC” with a composition rich in Nb, Ti and Zr. The IPFZ Map shows no sign of crystallographic texture of the large A2/B2 grains. The precipitates located at the grain boundaries are indexed as a hexagonal crystal structure with a composition rich in Al and Zr. The hexagonal intermetallic phase shows a trend of preferred orientation (mostly blue in Fig. A2b) along various grain boundaries and across grains.

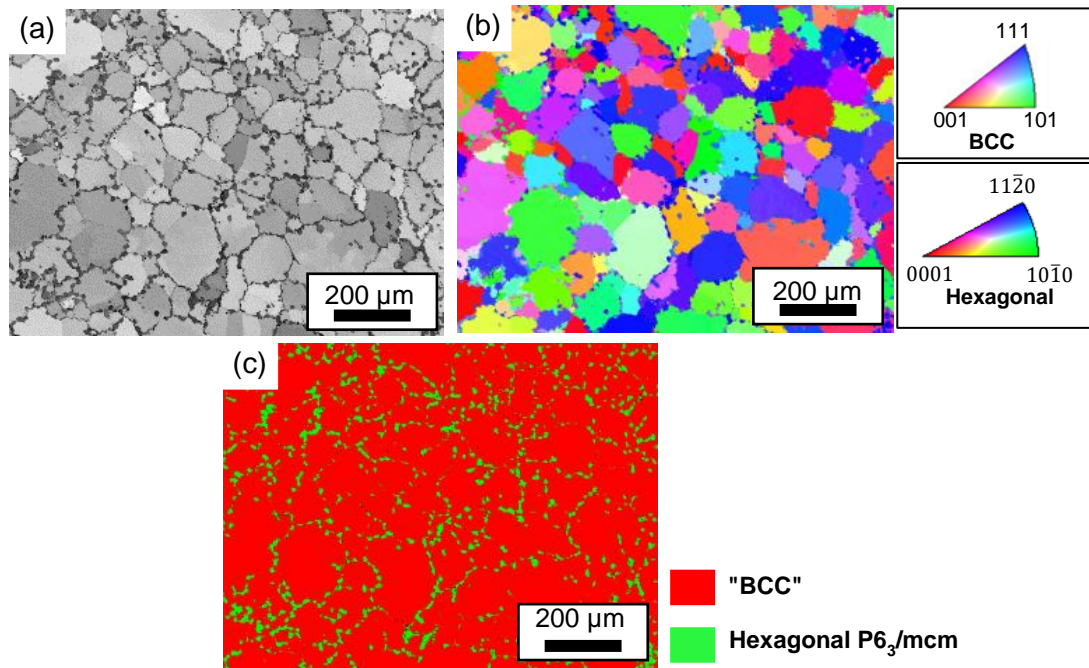


**Fig. A2.** EBSD maps of RSA in AN state. (a) pattern quality map, (b) inverse pole figure (IPFZ) map and (c) phase map identifying a BCC phase and the hexagonal  $P6_3/mcm$ .

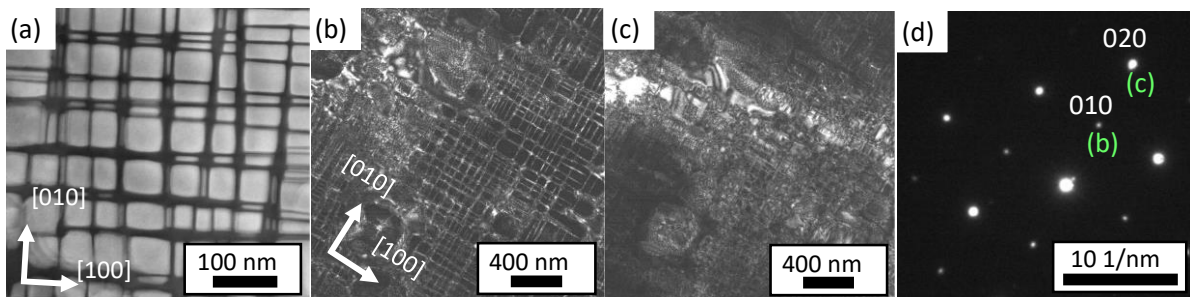


**Fig. A3.** (a) STEMDF micrograph of the RSA after annealing at 1400 °C for 24 hours oriented along [001] zone axis. (b) DF3, using superlattice reflection 010 in (d). (c) DF4, using reflection 020. (d) SADP with contrast apertures marked in green for DF3 (b), DF4 (c).

A closer look into the center of a grain indexed as “BCC” via EBSD is presented by using TEM in Fig. A3 on a grain cut close to (001) and correspondingly imaged along the [001] zone axis. The enhanced atomic number contrast in the STEM-HAADF image of Fig. A3a, similar to the SEM-BSE micrograph in Fig. 7d (main manuscript), reveals the nanostructure known to be characteristic for this alloy. The STEM-DF micrograph shows a heterogeneous nanostructure that consists of bright (larger mean atomic number,  $\bar{Z}$ ) cuboidal (edge length  $< 100$  nm) and plate-like (thickness  $\approx 10 - 100$  nm) precipitates embedded in a continuous darker (lower  $\bar{Z}$ ) phase (thickness  $\approx 3 - 30$  nm). Fig. A3b-c show CTEM-DF images, respectively associated to the 010 and 020 reflections marked in green on their corresponding SADP (Fig. A3d). In green, Fig. A3d shows the location of

the apertures, which leads to the diffraction contrasts in Fig. A3b-c. The microstructure reports a mixture of channels / precipitates with B2 (lower  $\bar{Z}$ ) / A2 (higher  $\bar{Z}$ ) phase, respectively.

## 2. Appendix B – Supporting CALPHAD calculations

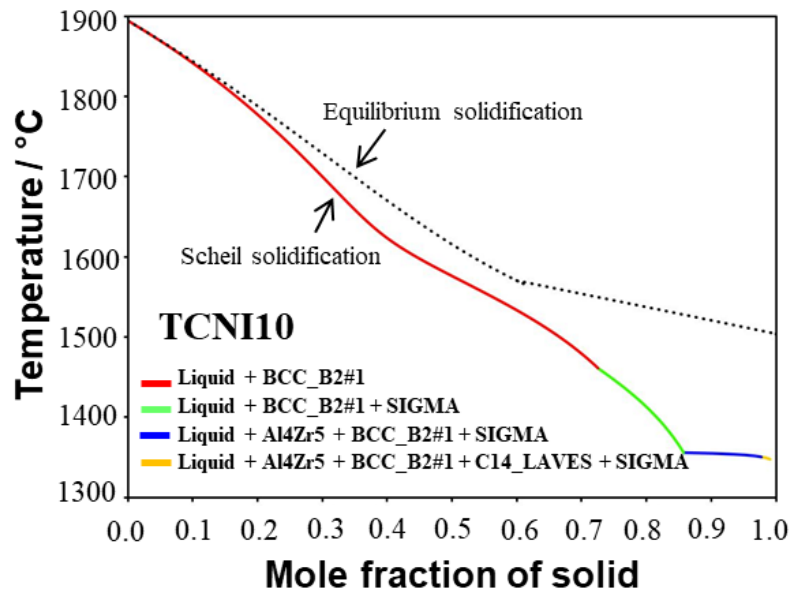


**Fig. B1.** Scheil solidification diagram for the RSA using the Thermo-Calc software with database TCNI10 database.

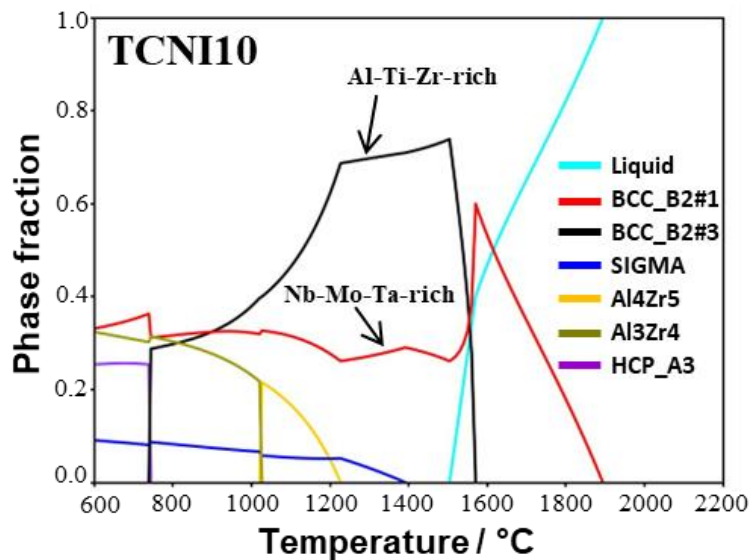


**Fig. B2.** Property diagram for the RSA using Thermo-Calc software (TCNI10 database).



**Table B1.** Equilibrium phase transformation temperatures (in °C) in the studied alloys. Simulated results using TCHEA3 database.

Phase Transformation	T (°C)
L → BCC_B2#1 + L	1895
L → BCC_B2#1 + BCC_B2#3 + L	1570
L → BCC_B2#1 + BCC_B2#3	1505
BCC_B2#1 + BCC_B2#3 → BCC_B2#1 + BCC_B2#3 + SIGMA	1388
BCC_B2#1 + BCC_B2#3 + SIGMA → BCC_B2#1 + BCC_B2#3 + SIGMA + Al4Zr5	1225
BCC_B2#1 + BCC_B2#3 + SIGMA + Al4Zr5 → BCC_B2#1 + BCC_B2#3 + SIGMA + Al3Zr4	1025
BCC_B2#1 + BCC_B2#3 + SIGMA + Al3Zr4 → BCC_B2#1 + SIGMA + Al3Zr4 + HCP_A3	743

**Table B2.** Equilibrium phase transformation temperatures (in °C) in the studied alloys. Simulated results using TCNI10 database.

Phase Transformation	T (°C)
L → BCC_B2#1 + L	1895
L → BCC_B2#1 + BCC_B2#3 + L	1570
L → BCC_B2#1 + BCC_B2#3	1505
BCC_B2#1 + BCC_B2#3 → BCC_B2#1 + BCC_B2#3 + SIGMA	1388
BCC_B2#1 + BCC_B2#3 + SIGMA → BCC_B2#1 + BCC_B2#3 + SIGMA + Al4Zr5	1225
BCC_B2#1 + BCC_B2#3 + SIGMA + Al4Zr5 → BCC_B2#1 + BCC_B2#3 + SIGMA + Al3Zr4	1025
BCC_B2#1 + BCC_B2#3 + SIGMA + Al3Zr4 → BCC_B2#1 + SIGMA + Al3Zr4 + HCP_A3	743

**Table B3.** Calculated elements mole fractions of equilibrium phases in the studied alloy at T = 1000 °C (1273 K). Database TCHEA3.

Phases	Sublattice	Al	Ti	Zr	Nb	Mo	Ta	Phase rich in
BCC_B2_#1	1	0.04	0.16	0.02	0.44	0.24	0.10	Mo-Nb-Ta
	2	0.04	0.16	0.02	0.44	0.24	0.10	
BCC_B2_#3	1	0.20	0.41	0.20	0.14	0.04	0.01	Al-Ti-Zr
	2	0.20	0.41	0.20	0.14	0.04	0.01	
Al3Zr4	1	1.00	0.00	0.00	0.00	0.00	0.00	Al-Zr
	2	0.00	0.00	1.00	0.00	0.00	0.00	
SIGMA	1	0.98	0.00	0.00	0.01	0.00	0.01	-
	2	0.00	0.00	0.00	0.01	0.98	0.01	
	3	0.00	0.00	0.00	0.17	0.00	0.83	

**Table B4.** Calculated elements mole fractions of equilibrium phases in the studied alloy at T = 1000 °C (1273 K). Database TCNI10.

Phases	Sublattice	Al	Ti	Zr	Nb	Mo	Ta	Phase rich in
BCC_B2_#1	1	0.04	0.16	0.02	0.44	0.24	0.10	Mo-Nb-Ta
	2	0.04	0.16	0.02	0.44	0.24	0.10	
BCC_B2_#3	1	0.20	0.41	0.20	0.14	0.04	0.01	Al-Ti-Zr
	2	0.20	0.41	0.20	0.14	0.04	0.01	
Al3Zr4	1	1.00	0.00	0.00	0.00	0.00	0.00	Al-Zr
	2	0.00	0.00	1.00	0.00	0.00	0.00	
SIGMA	1	0.98	0.00	0.00	0.01	0.00	0.01	-
	2	0.00	0.00	0.00	0.01	0.98	0.01	
	3	0.00	0.00	0.00	0.17	0.00	0.83	

**Table B5.** Calculated elements mole fractions of equilibrium phases in the studied alloy at T = 1500 °C (1773 K).

Database TCNI10

Phases	Sublattice	Al	Ti	Zr	Nb	Mo	Ta	Phase rich in
BCC_B2_#3	1	0.25	0.22	0.27	0.16	0.06	0.04	Al-Ti-Zr
	2	0.25	0.22	0.27	0.16	0.06	0.04	
BCC_B2_#1	1	0.09	0.17	0.06	0.32	0.21	0.15	Mo-Nb-Ta
	2	0.09	0.17	0.06	0.32	0.21	0.15	

**Table B6.** Calculated elements mole fractions of equilibrium phases in the studied alloy at T = 1500 °C (1773 K).

Database TCHEA3

Phases	Sublattice	Al	Ti	Zr	Nb	Mo	Ta	Phase rich in
BCC_B2_#3	1	0.25	0.22	0.27	0.16	0.06	0.04	Al-Ti-Zr
	2	0.25	0.22	0.27	0.16	0.06	0.04	
BCC_B2_#1	1	0.09	0.17	0.06	0.32	0.21	0.15	Mo-Nb-Ta
	2	0.09	0.17	0.06	0.32	0.21	0.15	

**Table B7.** Calculated elements mole fractions of equilibrium phases in the studied alloy at T = 700 °C (973 K).

Database TCNI10

Phases	Sublattice	Al	Ti	Zr	Nb	Mo	Ta	Phase rich in
BCC_B2#1	1	0.01	0.10	0.00	0.55	0.26	0.08	Nb-Mo-Ta
	2	0.01	0.10	0.00	0.55	0.26	0.08	
Al3Zr4	1	1.00	0.00	0.00	0.00	0.00	0.00	Al-Zr
	2	0.00	0.00	1.00	0.00	0.00	0.00	
HCP_A3	1	0.18	0.66	0.13	0.03	0.00	0.00	Al-Ti-Zr
	2	VA	VA	VA	VA	VA	VA	
SIGMA	1	1.00	0.00	0.00	0.00	0.00	0.00	-
	2	0.00	0.00	0.00	0.01	0.99	0.00	
	3	0.00	0.00	0.00	0.08	0.00	0.92	

**Table B8.** Calculated elements mole fractions of equilibrium phases in the studied alloy at T = 700 °C (973 K).

Database TCHEA3

Phases	Sublattice	Al	Ti	Zr	Nb	Mo	Ta	Phase rich in
BCC_B2#1	1	0.01	0.10	0.00	0.55	0.26	0.08	Nb-Mo-Ta
	2	0.01	0.10	0.00	0.55	0.26	0.08	
Al3Zr4	1	1.00	0.00	0.00	0.00	0.00	0.00	Al-Zr
	2	0.00	0.00	1.00	0.00	0.00	0.00	
HCP_A3	1	0.18	0.66	0.13	0.03	0.00	0.00	Al-Ti-Zr
	2	VA	VA	VA	VA	VA	VA	
SIGMA	1	1.00	0.00	0.00	0.00	0.00	0.00	-
	2	0.00	0.00	0.00	0.01	0.99	0.00	
	3	0.00	0.00	0.00	0.08	0.00	0.92	



**Table B9.** Calculated elements mole fractions of equilibrium phases in the studied alloy at 2000, 1700, 1520 and 1200 °C. Data base TCHEA3.

Temperature (°C)	Phases	Volume fraction of phase	Sublattice	Al	Ti	Zr	Nb	Mo	Ta
2000	Liquid	1.00		0.21	0.21	0.21	0.20	0.10	0.07
1700	BCC_B2#1	0.32	1	0.10	0.21	0.07	<b>0.33</b>	<b>0.18</b>	<b>0.11</b>
			2	0.10	0.21	0.07	<b>0.33</b>	<b>0.18</b>	<b>0.11</b>
	Liquid	0.68		0.27	0.21	0.28	0.13	0.06	0.05
1520	BCC_B2#1	0.26	1	0.10	0.18	0.07	<b>0.32</b>	<b>0.20</b>	<b>0.13</b>
			2	0.10	0.18	0.07	<b>0.32</b>	<b>0.20</b>	<b>0.13</b>
	BCC_B2#3	0.64	1	<b>0.24</b>	<b>0.23</b>	<b>0.25</b>	0.17	0.07	0.04
			2	<b>0.24</b>	<b>0.23</b>	<b>0.25</b>	0.17	0.07	0.04
	Liquid	0.10		0.32	0.15	0.37	0.08	0.04	0.04
1200	BCC_B2#1	0.30	1	0.05	0.12	0.02	<b>0.38</b>	<b>0.25</b>	<b>0.18</b>
			2	0.05	0.12	0.02	<b>0.38</b>	<b>0.25</b>	<b>0.18</b>
	BCC_B2#3	0.70	1	<b>0.28</b>	<b>0.25</b>	<b>0.30</b>	0.12	0.03	0.02
			2	<b>0.28</b>	<b>0.25</b>	<b>0.30</b>	0.12	0.03	0.02

### 3. Appendix C – Model crystal lattices

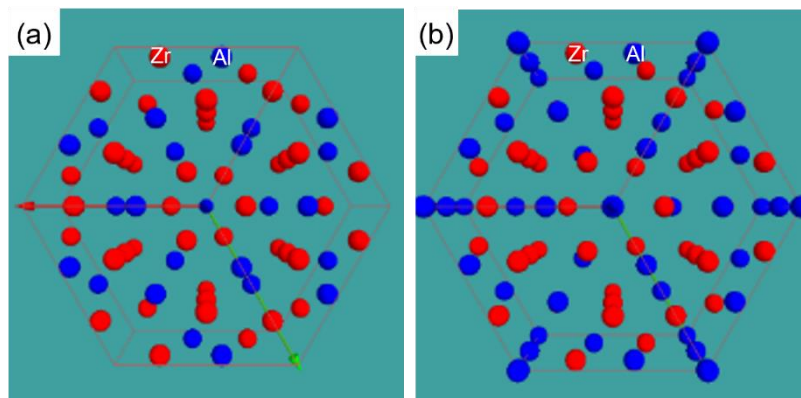


**Fig. C1.** Schematic representation of the crystalline structure of hexagonal Al-Zr phase (unit-cell) with (a) Al<sub>3</sub>Zr<sub>5</sub> and (b) Al<sub>4</sub>Zr<sub>5</sub> stoichiometry. Al atoms are in blue and Zr atoms are in red.

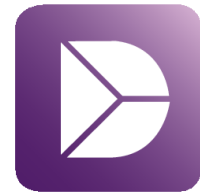
## 4.2 Paper II

Data regarding the experimental findings compared with CALPHAD calculations of the  $\text{AlMo}_{0.5}\text{NbTa}_{0.5}\text{TiZr}$  refractory high entropy superalloy.



Contents lists available at ScienceDirect

## Data in Brief

journal homepage: [www.elsevier.com/locate/dib](http://www.elsevier.com/locate/dib)

## Data Article

# Data regarding the experimental findings compared with CALPHAD calculations of the $\text{AlMo}_{0.5}\text{NbTa}_{0.5}\text{TiZr}$ refractory high entropy superalloy



Patricia Suárez Ocaño<sup>a,\*</sup>, Leonardo Agudo Jácome<sup>a</sup>,  
Inmaculada Lopez-Galilea<sup>b</sup>, Reza Darvishi Kamachali<sup>a</sup>,  
Suzana G. Fries<sup>c</sup>

<sup>a</sup>Department for Materials Engineering, Bundesanstalt für Materialforschung und -prüfung (BAM), Unter den Eichen 87, Berlin 12205, Germany

<sup>b</sup>Institute for Materials, Ruhr-University Bochum, Universitätsstr. 150, Bochum 44801, Germany

<sup>c</sup>Materials Research Department (MRD), Ruhr-University Bochum, Universitätsstr. 150, Bochum 44801, Germany

## ARTICLE INFO

## Article history:

Received 1 September 2022

Revised 19 December 2022

Accepted 20 December 2022

Available online 24 December 2022

Dataset link: [Data regarding the  \$\text{AlMo}\_{0.5}\text{NbTa}\_{0.5}\text{TiZr}\$  refractory high entropy superalloy \(Original data\)](#)

## Keywords:

Transmission electron microscopy

Scanning electron microscopy

Microstructural characterization

Refractory high entropy alloys

## ABSTRACT

This contribution contains the raw data used to compare experimental results with thermodynamic calculations using the CALPHAD method, which is related to the research article “The  $\text{AlMo}_{0.5}\text{NbTa}_{0.5}\text{TiZr}$  refractory high entropy superalloy: experimental findings and comparison with calculations using the CALPHAD method” [1], and therefore this article can be used as a basis for interpreting the data contained therein. The  $\text{AlMo}_{0.5}\text{NbTa}_{0.5}\text{TiZr}$  refractory superalloy was characterized in the cast and annealed condition (1400 °C for 24 h) in order to measure grain size and to identify and measure the size and area fraction of the phases present. The raw data of this article include X-ray diffraction (XRD) measurements, microstructural characterization by scanning and transmission electron microscopy (SEM and TEM), and elemental analysis by energy dispersive X-ray spectroscopy (EDX). XRD includes the determination of phases and the lattice parameters (A2, B2, and hexagonal structure). Microstructural analysis by scanning and transmission electron

DOI of original article: [10.1016/j.matdes.2022.110593](https://doi.org/10.1016/j.matdes.2022.110593)

\* Corresponding author.

<https://doi.org/10.1016/j.dib.2022.108858>

2352-3409/© 2022 The Authors. Published by Elsevier Inc. This is an open access article under the CC BY license (<http://creativecommons.org/licenses/by/4.0/>)

microscopy includes (1) identification of composition, size, and volume fraction of the present phases and (2) determination of grain size. Based on these experimental data, it is possible to identify similarities and discrepancies with the data calculated using the CALPHAD method for the alloy under study in Ref. [1], which provides the basis for better and more efficient development of reliable databases.

© 2022 The Authors. Published by Elsevier Inc.

This is an open access article under the CC BY license (<http://creativecommons.org/licenses/by/4.0/>)

## Specifications Table

Subject	Material Science
Specific subject area	Microstructural characterization of a refractory high entropy superalloy
Type of data	Tables Images (SEM-BSE, TEM) Excel Files (XRD)
How the data were acquired	XRD: Seifert XRD 3000 PTS diffractometer SEM: FEI Quanta 3D ESEM SEM-EDX: EDAX Octane Elect SDDs TEM: JEOL JEM-2200FS TEM-EDX: Jeol JED-23000BU Si (Li) semiconductor with ultrathin organic/Al window.
Data format	ImageJ and Fiji: Image Analysis Software. Measured raw (XRD patterns, EDX analysis of the phases). Analyzed (lattice parameters, indexation of diffraction patterns in TEM, average grain sizes, thickness of bcc (A2) plates, B2 channels, and area fraction of B2 and Al-Zr-rich phase. Area fraction of the amorphous phase in the Al-Zr-rich phase.
Description of data collection	The XRD patterns were acquired using Seifert XRD 3000 PTS diffractometer operating with a Co-K $\alpha$ radiation source ( $\lambda = 1.7902 \text{ \AA}$ ). The SEM images were acquired using an FEI Quanta 3D ESEM integrated with an EDX EDAX Octane Elect SDDs detector: using an acceleration voltage between 20 kV and 30 kV and working distances between 5 and 10 mm. Metallographic samples were prepared by grinding and polishing and used for collecting the SEM-EDX and XRD data. The TEM images and TEM-EDX data were acquired using a JEOL JEM-2200FS TEM and a JED-23000BU EDX detector for the elemental analysis, respectively. The images were taken in conventional dark field (CTEM-DF) and scanning high angle annular dark field (STEM-HAADF) mode. TEM foils were prepared by electropolishing to collect the TEM and TEM-EDX data.
Data source location	Institution: Bundesanstalt für Materialforschung und -prüfung (BAM) City/Town/Region: Berlin Country: Germany Institution: Institute for Materials and Center for Interface-Dominated High-Performance Materials (ZGH), Ruhr-Universität Bochum. City/Town/Region: Bochum/ North Rhine-Westphalia (NRW) Country: Germany
Data accessibility	Repository name: Mendeley Data Direct URL to data: <a href="https://data.mendeley.com/datasets/d742ccty5f/4">https://data.mendeley.com/datasets/d742ccty5f/4</a>
Related research article	P. Suárez Ocaño, S.G. Fries, I. Lopez-Galilea, R. Darvishi Kamachali, J. Roik, L. Agudo Jácome, The AlMo <sub>0.5</sub> NbTa <sub>0.5</sub> TiZr refractory high entropy superalloy: Experimental findings and comparison with calculations using the CALPHAD method. Mater. Des. 217 (2022) 110,593. <a href="https://doi.org/10.1016/j.matdes.2022.110593">https://doi.org/10.1016/j.matdes.2022.110593</a>

## Value of the Data

- The data presented in this article includes all the raw data and processing for the AlMo<sub>0.5</sub>NbTa<sub>0.5</sub>TiZr refractory high entropy superalloy in cast and annealed states reported in the related article (Ref. [1]), which are useful for determining grain size, identification/area fraction of the phase structures and their volume fraction, being important for general alloy characterization.
- The procedures used in the determination of grain size, identification of phases, and their volume fraction could be useful for other researchers interested in determining these parameters in any type of alloy. These data may be useful to scientists and researchers in the high entropy alloy community, a field that is constantly evolving.
- The compilation of these data (BSE microphotographs, XRD patterns, TEM images and EDX spectra, grain size, and area fraction tables) can be used to develop image analysis algorithms to improve computer-aided analysis of microstructures.
- A method for simulating XRD patterns is provided, which can be used in the study of these types of relatively new alloys for which there are few XRD databases. In addition, the composition and structure of each phase in this alloy could be implemented in alloy design software.

## 1. Data Description

The XRD data presented in this article are expressed as  $2\theta$  versus intensity plots obtained for the alloy under study (AlMo<sub>0.5</sub>NbTa<sub>0.5</sub>TiZr refractory superalloy, RSA). The raw XRD data are provided as Excel files (see XRD folder in the dataset), and a summary of the recorded diffraction patterns is shown in Fig. 8 of Ref. [1]. The patterns simulated with PowderCell software [2] are included in the dataset (.cel files) for the different phases in the cast (AC) and annealed (AN, 1400 °C for 24 h) specimens. In both cases, most of the diffraction peaks could be indexed according to body-centered cubic, bcc structures (A2, space group  $Im\bar{3}m$  and B2, space group  $Pm\bar{3}m$ ). Besides the bcc-based peaks, additional peaks, corresponding to the Al-Zr-rich hexagonal intermetallic (space group  $P6_3/mcm$ ), were detected.

Table 1 summarizes the crystal structure of the phases, their space group, and the lattice parameters obtained by simulating the different phases in both states (AC and AN).

The microstructures of the AC and AN were analyzed by scanning electron microscopy (SEM) equipped with a backscatter electron (BSE) detector. BSE micrographs taken at low and medium magnification are presented to document the grain size “*d*” in the two different states (see Figs. 1 and 2 of Section 2). The average grain size for both states is given in Table 2.

Table 3 summarizes the average area fractions of the Al-Zr and B2 phases in AC and AN. In the AC alloy, the nanostructure consisted of plate-like precipitates with  $\approx$  2–20 nm thickness embedded in channels with a thickness of  $\approx$  2–10 nm. The alloy AN exhibited a heterogeneous

**Table 1**

Summary of the different phases found in the samples studied (AC and AN) with their respective space group and lattice parameters.

State	Phase	Space group	Lattice parameters (Å)		
			<i>a</i>	<i>b</i>	<i>c</i>
As-cast (AC)	B2	$Pm\bar{3}m$	3.32	3.32	3.32
	A2	$Im\bar{3}m$	3.28	3.28	3.28
	Hexagonal intermetallic	$P6_3/mcm$	8.31	8.31	5.52
Annealed (AN, 1400 °C for 24 h)	B2	$Pm\bar{3}m$	3.31	3.31	3.31
	A2	$Im\bar{3}m$	3.27	3.27	3.27
	Hexagonal intermetallic	$P6_3/mcm$	8.31	8.31	5.52

4

P. Suárez Ocaño, L. Agudo Jácome and I. Lopez-Galilea et al./Data in Brief 46 (2023) 108858

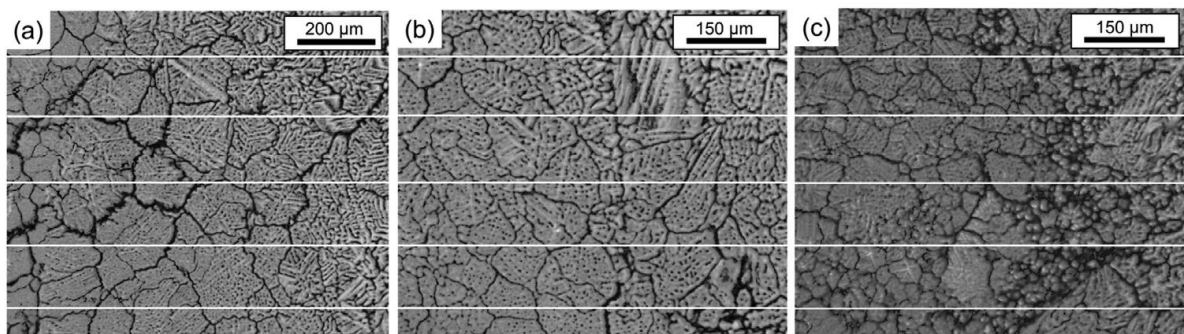


**Fig. 1.** Images for grain size determination in the alloy AC, with the lines drawn to measure the number of intersections with the grain boundaries, (a) 300x and (b, c) 400x.

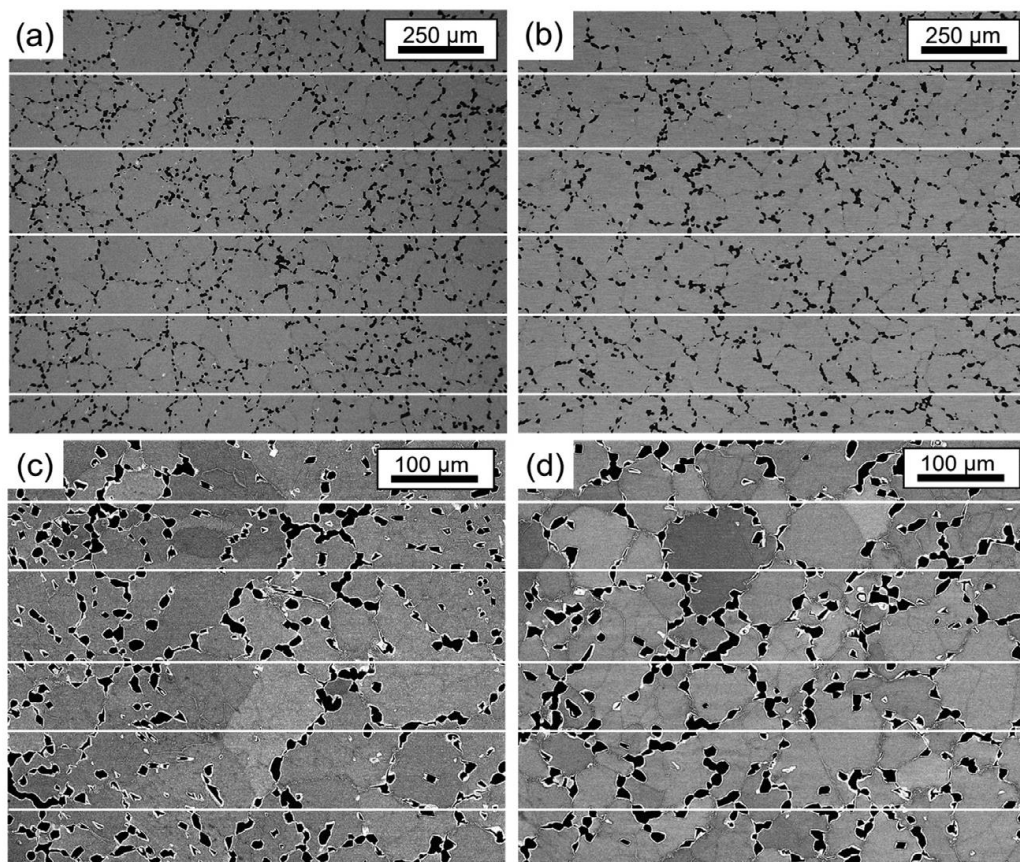


**Fig. 2.** Images for grain size determination in the alloy AN, with the lines drawn to measure the number of intersections with the grain boundaries, (a, b) 200x and (c, d) 500x.

**Table 2**

Average grain size  $d$  of the RSA in the AC and AN state. The uncertainty is given by the standard deviation.

State	Diameter average $d$ ( $\mu\text{m}$ )
As-cast (AC)	$78.3 \pm 19.9$
Annealed (AN, 1400 °C for 24 h)	$77.8 \pm 8.6$

**Table 3**

Average area fraction of the Al-Zr-rich and B2 phases determined with ImageJ software. The uncertainty is given by the standard deviation.

State	Area fraction of the Al-Zr-rich phase (%)	Area fraction of the B2 phase (%)
As-cast (AC)	$8 \pm 4$	$39 \pm 4$
Annealed (AN, 1400 °C for 24 h)	$13 \pm 6$	$37 \pm 9$



**Table 4**

Parameters used for the simulation of the present phases in the studied alloy.

Phase	Space group	Space group number	Lattice parameter (Å)	Elements	Wyck	Atom position		
						X	Y	Z
B2	$Pm\bar{3}m$	221	$a = b = c = 3.32$	Al	1a	0	0	0
				Ti	1a	0	0	0
				Zr	1b	0.5	0.5	0.5
A2	$Im\bar{3}m$	229	$a = b = c = 3.28$	Mo	2a	0	0	0
				Nb	2a	0	0	0
				Ta	2a	0	0	0
Hexagonal intermetallic (Al-Zr-rich)	$P6_3/mcm$	193	$a = b = 8.31$ $c = 5.52$	Al	6g	0.62	0	0.25
				Zr	4d	0.33	0.66	0

nanostructure having plate-like precipitates with a thickness of  $\approx 10$ – $100$  nm embedded in a continuous phase with a thickness of  $\approx 3$ – $30$  nm. The measurements can be found as Excel files in the dataset (channels.csv and precipitates.csv), as well as the images used for the determination.

Since the Al-Zr-rich phase in the AC state is composed of amorphous and crystalline fractions, a method was implemented to determine the crystalline fraction within the analyzed regions (see Section 2). The AC sample analyzed by TEM yielded only  $5 \pm 4\%$  of the Al-Zr-rich regions as crystalline as reported in Ref. [1]. The local chemical compositions of the phases measured at the three different phases in SEM- and TEM-EDX for the studied alloy are given in Table 2 of Ref. [1] and the raw data can be found in the dataset (EDX folder). A table with the name, format, and a brief description of each dataset file contained in Mendeley, is provided at the end of this work.

## 2. Experimental Design, Materials and Methods

XRD analysis were conducted for the investigated alloy using a Seifert PTS 3000 diffractometer operating with a Co  $K\alpha$  radiation source ( $\lambda_{K\alpha 1} = 1.7902$  Å). The patterns were acquired using a scattering range of  $10$ – $100^\circ$  for the as-cast state (AC) and  $10$ – $120^\circ$  for the annealed (AN) state with a step size of  $0.05^\circ$  and Bragg-Brentano geometry. To obtain the lattice parameters listed in

Table 1, patterns of the identified phases were simulated using the PowderCell software [2], and the crystal files were manually edited considering the present elements of each phase, the space-group number, the position of the atomic species, and the occupancy of the specific coordinates of the lattice. The lattice parameters were then modified until the exact positions of the peaks in the experimental pattern were reached. Table 4 lists all the parameters chosen to determine the simulated patterns for the lattice parameter identification. Finally, the identification was performed by comparing the experimental and simulated patterns.

Samples for scanning electron microscopy were prepared by conventional metallography with emery paper (SiC) grades p320, p600, p1200, p2500, and p4000 and polished with a silica solution of 50 nm particle size. Backscattered electron (BSE) images were acquired using a Quanta 3D scanning electron microscope (SEM, FEI Company) with an accelerating voltage of 20–30 kV and a working distance of  $\approx 5$ – $10$  mm. Grain size ( $d$ ) was determined using the Heyn linear intercept method described in ASTM E112 standard [4], using four images for each condition. Five lines were drawn in each image, as shown in Figs. 1 and 2 for AC and AN, respectively, to measure the number of intersections of each line with the grain boundaries. The average grain diameter (size) is then given by  $d = \text{line length}/\text{number of intersections}$ . 221 intersections were counted for the AC and 270 for the AN. Tables 5 and 6 summarize the parameters and average

**Table 5**

Parameters and average grain size “*d*” in the AC state for each drawn line in the four images of Figs. 1 and 2a of Ref. [1]. The uncertainty is given by the standard deviation of the average grain size of each BSE image.

Figure	Line N°	N° intersections	Line length (μm)	<i>d</i> (μm)
Fig. 1a	1	13	993.8	76.4
	2	13	993.8	76.4
	3	13	993.8	76.4
	4	12	993.8	82.8
	5	15	993.8	66.3
				Average
Fig. 1b	1	13	750.0	57.7
	2	12	750.0	62.5
	3	12	750.0	62.5
	4	12	750.0	62.5
	5	12	750.0	62.5
				Average
Fig. 1c	1	16	750.0	46.9
	2	14	750.0	53.6
	3	8	750.0	93.8
	4	9	750.0	83.3
	5	11	750.0	68.2
				Average
Fig. 2a of Ref. [1]	1	6	750.0	125.0
	2	6	750.0	125.0
	3	8	750.0	93.8
	4	7	750.0	107.1
	5	9	750.0	83.3
				Average

grain diameter *d* (used to determine the average grain size in Table 2) in the AC and AN states, respectively, for each line drawn in the four images in Figs. 1 and 2.

The specimens for TEM were cut into slices of  $\approx 500 \mu\text{m}$  thickness and ground to a thickness of  $\approx 100 \mu\text{m}$  on both sides with SiC emery paper of grades p320, p600, and p1200. Then, they were punched out into 3 mm diameter disks for electropolishing in a twin-jet Struers Tenupol-3, using an electrolyte consisting of 950 ml ethanol (86.4%), 100 ml butanol (9.1%), and 50 ml perchloric acid (4.5%) at  $-30 \text{ }^\circ\text{C}$ , 30 V and 3.1 flow rate.

Transmission electron microscopy images were acquired using a TEM JEOL JEM-2200FS with a field emission gun (FEG), operating at an accelerating voltage of 200 kV. BF and DF CTEM images with their respective selected area diffraction patterns (SADPs) were acquired to identify the phases, in addition to STEM-HAADF and BF images to determine the volume fraction. For the alloy AC, CTEM-DF micrographs and their respective SADPs were taken in the interdendritic zone.

Fig. 3 shows a CTEM-BF micrograph of the interdendritic region in AC (a), with the respective SADP along the [001] zone axis (b) used to identify the phases in the interdendritic region. The SADPs used to characterize the bcc-based structures (A2 and B2) were indexed by measuring the lengths of two diffraction vectors and the angle formed by them, and the ratio A/B was compared with the diffraction patterns described in Appendix 4 – Ref. [5] for bcc alloys. The lines labeled “A” and “B” in Fig. 3b were measured, and the ratio  $A/B = 1.414$ , with a relative angle of  $45^\circ$  corresponds to bcc oriented along the [001] zone axis, as shown in Fig. 3b.

**Table 6**

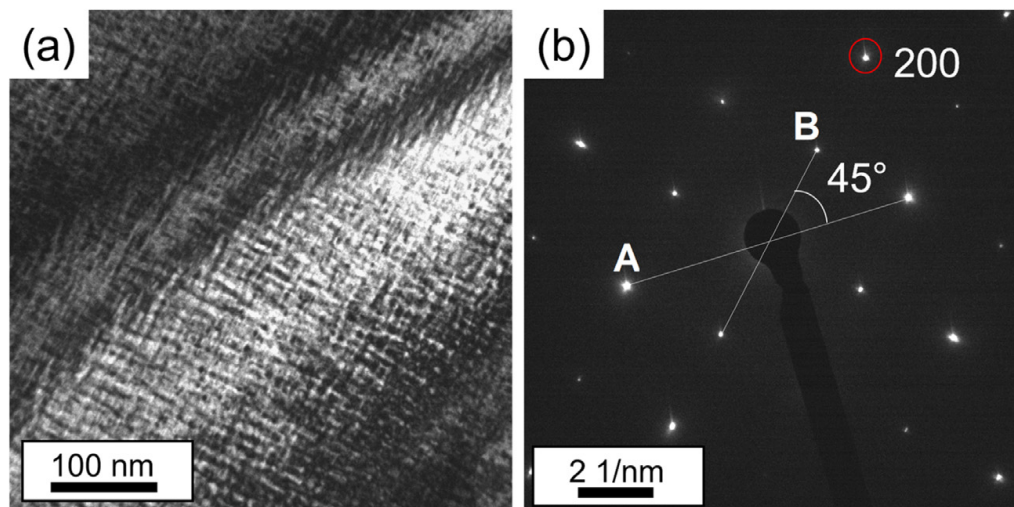
Parameters and average grain size “d” in the AN state for each drawn line in the four images shown in Fig. 2. The uncertainty is given by the standard deviation of the average grain size of each BSE image.

Figure	Line N°	N° intersections	Line length (μm)	d (μm)
Fig. 2a	1	18	1506.9	83.7
	2	18	1506.9	83.7
	3	17	1506.9	88.6
	4	20	1506.9	75.3
	5	19	1506.9	79.3
				Average
Fig. 2b	1	17	1494.6	87.9
	2	16	1494.6	93.4
	3	17	1494.6	87.9
	4	17	1494.6	87.9
	5	17	1494.6	87.9
				Average
Fig. 2c	1	8	589.2	73.6
	2	8	589.2	73.6
	3	9.5	589.2	62.0
	4	6.5	589.2	90.6
	5	8	589.2	73.6
				Average
Fig. 2d	1	10.5	746.2	71.1
	2	10.5	746.2	71.1
	3	10	746.2	74.6
	4	11	746.2	67.8
	5	12	746.2	62.2
				Average

For the Al-Zr-rich phase region, the SADPs were indexed using the Java version of the electron microscopy suite (JEMS) [6], (Al<sub>3</sub>Zr<sub>5</sub>: ICDD- 04-003-0819, Al<sub>4</sub>Zr<sub>5</sub>: ICDD-00-048-1382, see zip file). The inset in Fig. 6c of Ref. [1] shows a simulated diffraction pattern using the ICDD crystal file 00-048-1382.

The area fractions of the Al-Zr-rich phase were determined for both states using BSE images and the B2/A2 phases using STEM-HAADF images with the image analysis software (ImageJ) [3] (Table 3). Four BSE images were used to determine the area fraction of the Al-Zr-rich phase in both states. The images were converted to binary images and separated into two different phases using the “threshold” tool of ImageJ. After this step, the binary image was divided into 16 images, which were analyzed separately. Fig. 4 (AC) and Fig. 5 (AN) show the images used to determine the area fraction (left), with the respective binary image separating the Al-Zr-rich phase from the rest of the area (right, black phase on white background). Table 7 (AC) and Table 8 (AN) show the percentage area of the Al-Zr-rich phase for each analyzed image in Fig. 4 and Fig. 5, respectively. For the determination of the area fraction of the B2 phase, two images were used for the AC alloy (Fig. 6 and Fig. 5d in Ref. [1]) and three images were used for the AN alloy (Fig. 7 and Fig. A3a in the supplementary material of Ref. [1]).

Fig. 6 (AC) and Fig. 7 (AN) also show the corresponding binary images in which the B2 phase channels (black) are separated from the rest of the region (white background). Table 9 (AC) and Table 10 (AN) show the area fraction in% of the B2 phase for each analyzed image in Fig. 6 and Fig. 7, respectively. The thickness of the B2 channels and A2 plates were measured manually ≈ 200 times using the ImageJ program.



**Fig. 3.** (a) CTEM-BF micrograph of the interdendritic region in AC (CTEM bright field image of the Fig. 5b from Ref. [1]). (b) SADP from (a) obtained along the [001] zone axis, showing the angle between “A” and “B” (modified version of Fig. 5c from Ref. [1]).

**Table 7**

Area fraction of the Al-Zr-rich phase in the AC state, determined from the micrographs in Fig. 4, using ImageJ. The uncertainty is given by the standard deviation.

Sub-images in the binarized images (shown in Fig. 4e-h)	Fig. 4e	Fig. 4f	Fig. 4g	Fig. 4h
	% Area Al-Zr phase (AC alloy)			
1	11.1	6.5	7.6	9.5
2	6.2	10.4	6.7	8.1
3	8.6	7.5	6.6	8.9
4	6.9	8.2	6.8	8.6
5	8.1	5.8	6.9	4.9
6	17.0	5.7	7.5	10.2
7	4.1	7.0	9.1	6.0
8	1.4	7.7	10.2	5.8
9	15.1	7.2	8.2	11.7
10	17.1	9.0	5.8	8.1
11	14.1	6.2	5.7	8.2
12	5.2	7.5	6.2	7.0
13	15.2	7.7	8.1	9.5
14	18.7	7.1	5.8	5.3
15	2.7	8.4	5.3	3.7
16	19.4	9.3	11.3	7.0

Fig. 8 shows the procedure undertaken to determine the area fraction of the amorphous Al-Zr-rich phase for the original CTEM-DF micrograph in Fig. 6b of Ref. [1]. The tool “Trainable Weka Segmentation”, embedded in the Fiji of ImageJ [3], allows the separation of three different regions of interest for their area fraction measurement, as shown in Fig. 6b in Ref. [1] (crystalline (bright regions), amorphous (light gray regions) Al-Zr-rich phase, A2/B2 regions (dark)). In Fig. 8a, the red color is the amorphous Al-Zr-rich phase (cf. light gray in Fig. 6b of Ref. [1]), the blue region is the crystalline region (cf. bright regions in Fig. 6b of Ref. [1]), and the lilac region is the surrounding thick A2/B2 in the micrograph (cf. dark regions in Fig. 6b of Ref. [1]).



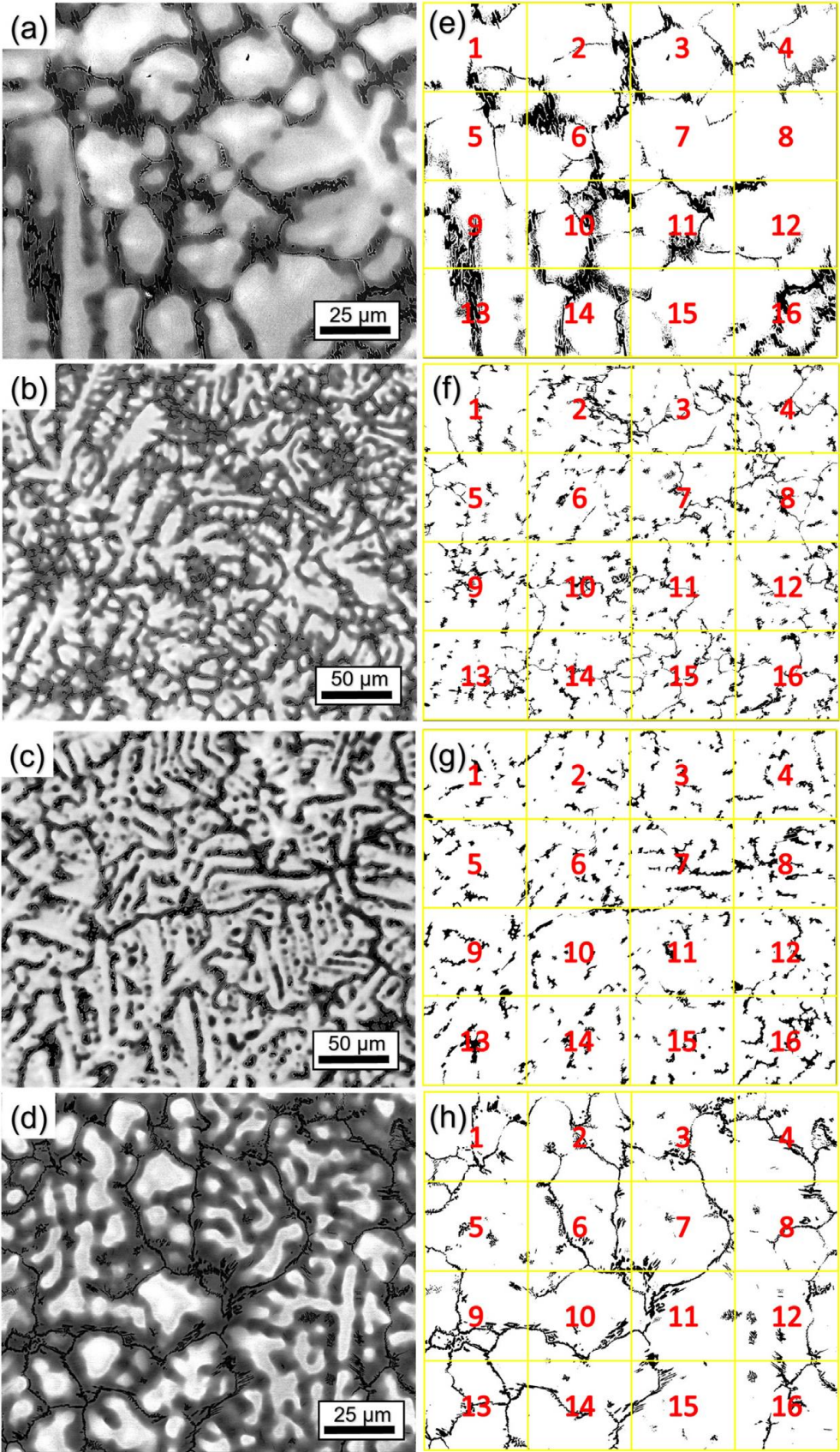


**Fig. 4.** BSE micrographs of AC alloy taken at (a) 2000x, (b) 1000x and (c) 1000x (d) 2000x magnification. (e–h) Binarized images of (a–d), respectively. The black phase shown in (e–h) represents the Al-Zr-rich phase. The binarized images were divided into 16 images, as shown by the yellow squares and red numbers.



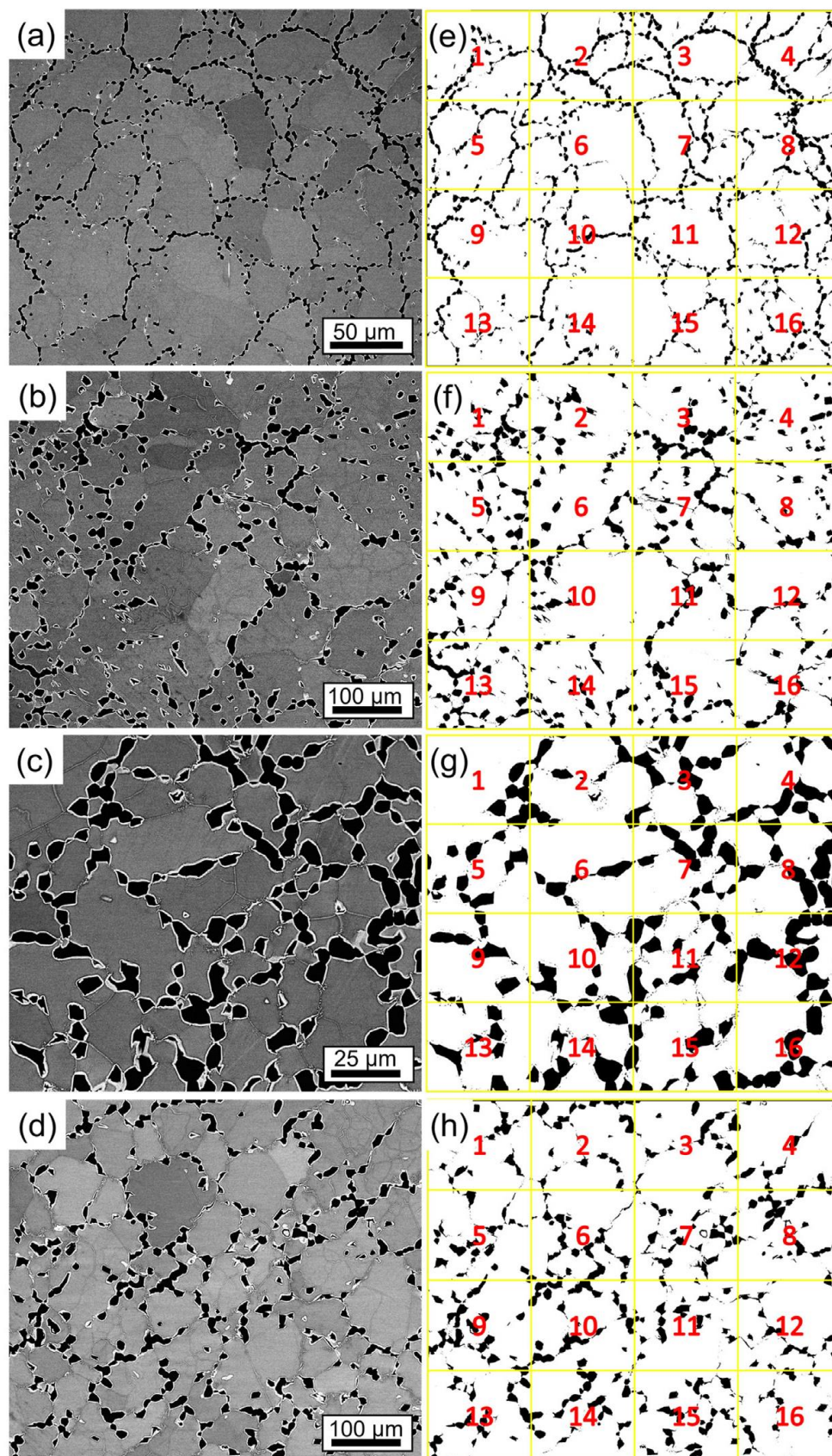
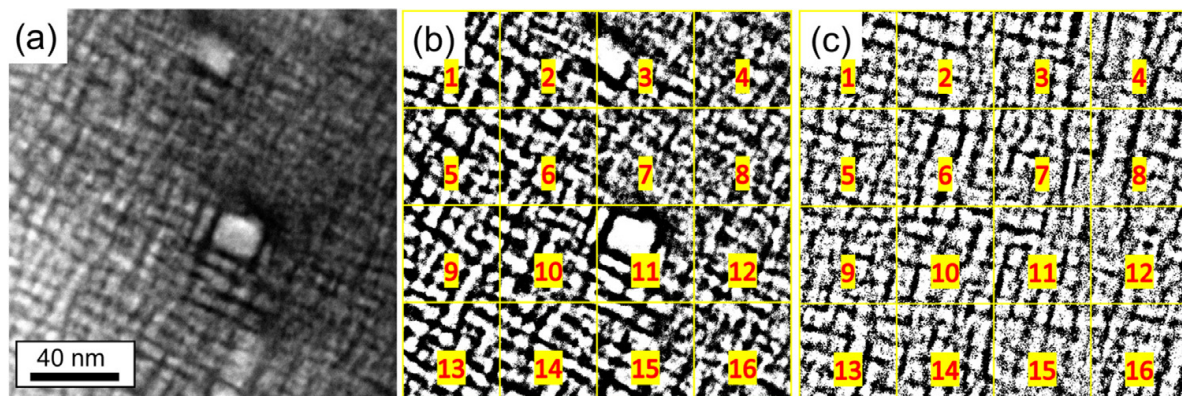


**Fig. 5.** BSE micrographs of the AN alloy taken at (a) 260x and (b) 500x (c) 1000x (d) 500x magnification. (e–h) Binarized images of (a–d), respectively. The black phase shown in (e–h) represents the Al-Zr-rich phase. The binarized images were divided into 16 images, as shown by the yellow squares and red numbers.

**Table 8**

Area fraction of the Al-Zr-rich phase in the AN state, determined from the micrographs in Fig. 5, using ImageJ. The uncertainty is given by the standard deviation. .

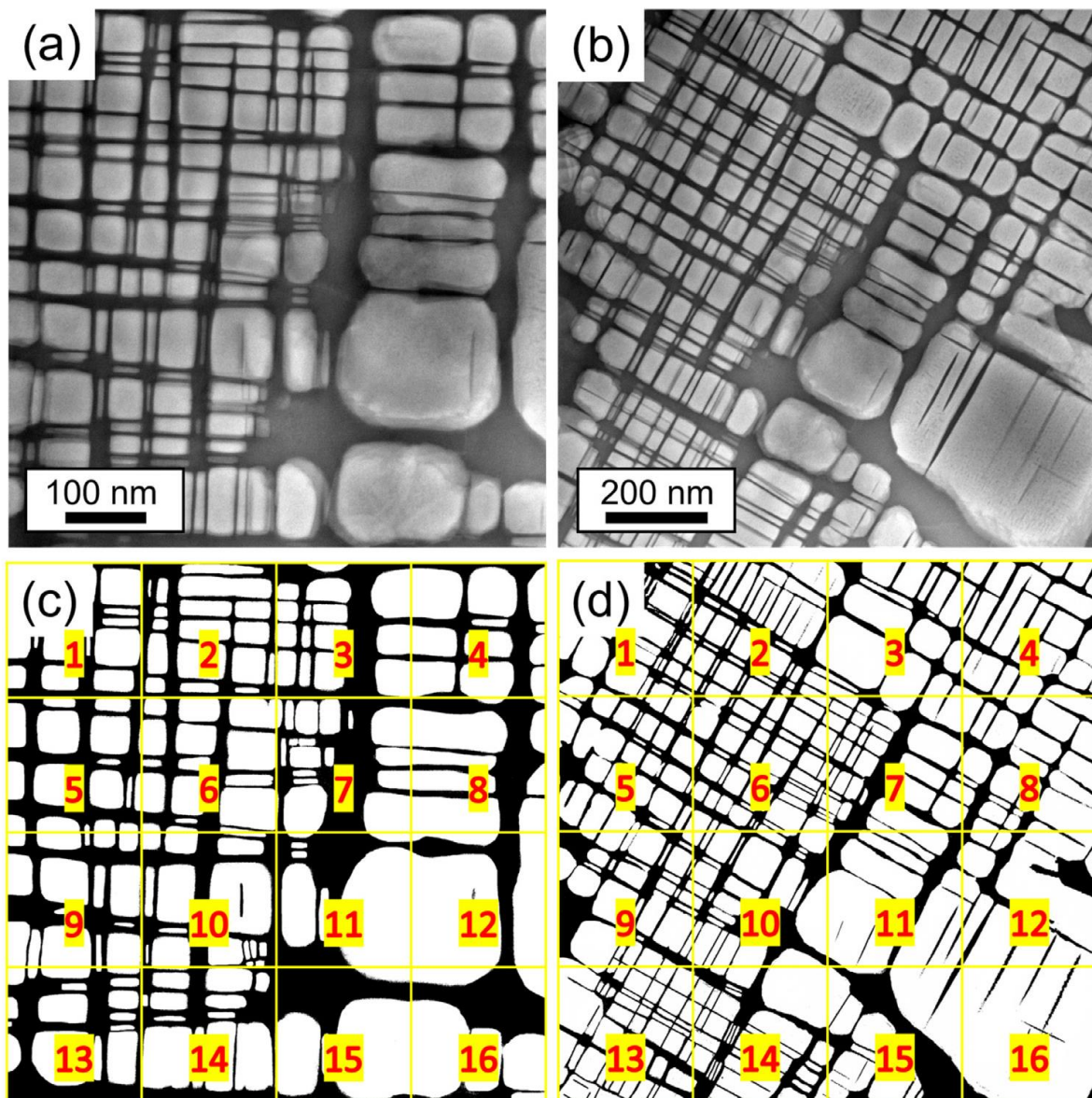
Sub-images in the binarized images (shown in Fig. 5e-h)	Fig. 5e	Fig. 5f	Fig. 5g	Fig. 5h
	% Area Al-Zr phase (AN alloy)			
1	8.6	17.5	13.5	10.4
2	11.6	8.9	13.2	11.3
3	12.2	12.5	24.7	9.8
4	12.0	9.7	21.7	5.7
5	9.0	12.2	17.3	9.9
6	6.9	10.3	11.0	12.6
7	9.4	12.8	22.4	12.3
8	12.4	8.1	30.9	12.5
9	9.0	10.3	15.5	14.6
10	7.4	7.2	19.8	16.3
11	8.5	9.7	23.4	8.5
12	9.4	6.6	31.7	8.6
13	5.3	17.6	14.0	11.4
14	5.9	10.6	28.9	11.9
15	5.1	11.2	18.2	14.8
16	10.8	11.0	22.3	6.9



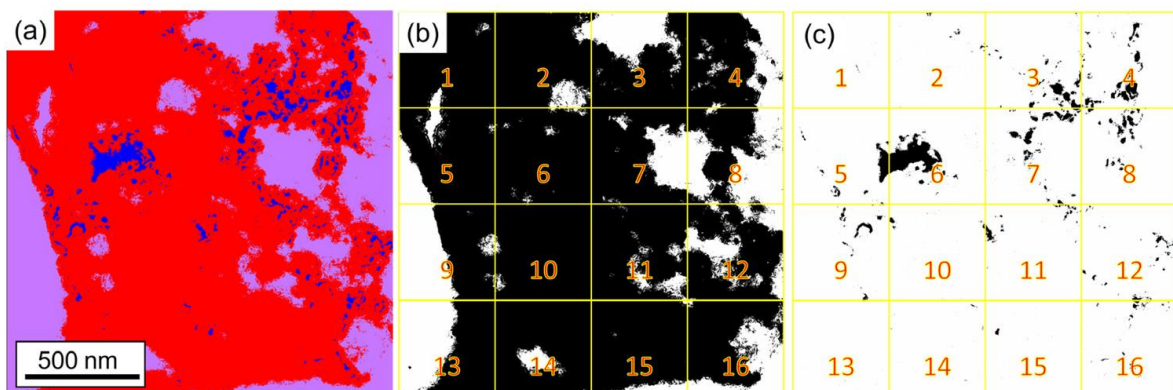
**Fig. 6.** (a) STEM-HAADF micrograph of the AC alloy used to determine the area fraction of A2/B2 phases (800kx). (b) Binarized image of (a). (c) Binarized image of Fig. 5d in Ref. [11]. The black phase shown in (b) and (c) represents the B2 phase (channels). The binarized images were divided into 16 images, as shown by the yellow squares and red numbers.

Fig. 8a is then binarized (Fig. 8b), where the entire black region is the Al-Zr-rich phase (including the amorphous and crystalline structure, i.e., red plus blue in Fig. 8a), and the “white region” is the rest of the sample (i.e., thick A2/B2 region in lilac, Fig. 8a). Fig. 8b is divided into 16 sub-images to analyze their area fraction separately. Finally, Fig. 8a is binarized again (Fig. 8c), but now considering only the crystalline region (blue phase in Fig. 8a) and divided into 16 images. Table 11 presents the area fraction of the total Al-Zr-rich phase (second column, from the black phase in Fig. 8b) and the crystalline phase (third column, from the black phase in Fig. 8c). Weighing the area fraction of the crystalline phase relative to the total Al-Zr-rich phase, the fourth column in Table 11 gives the amount of crystalline phase embedded in the Al-Zr-rich phase.





**Fig. 7.** (a,b) STEM-HAADF micrographs of the AN alloy used for the area fraction determination at (a) 200kx and (b) 120kx. (b,c) Binarized images of (a) and (b), respectively. The black phase shown in (c,d) represents the B2 phase (channels). The binarized images were divided into 16 images, as shown by the yellow squares and red numbers.



**Fig. 8.** Determination of the percentage (%) of the amorphous phase in the Al-Zr-rich phase (a) separation of the three different phases using the software's "Trainable Weka Segmentation" tool (b) binary image considering the fully Al-Zr-rich phase region (c) binary image only considering the crystal phase in the Al-Zr-rich region.

**Table 9**

Area fraction (%) of the B2 phase in the AC state, determined from Fig. 6b and c, using ImageJ software. The uncertainty is given by the standard deviation.

Sub-images in the binarized images (shown in Fig. 6b and c)	Fig. 6b	Fig. 6c
	Area fraction of B2 phase in AC alloy (%)	
1	38.0	42.6
2	35.6	53.3
3	32.9	41.8
4	30.4	40.8
5	38.6	43.2
6	37.0	40.7
7	30.7	38.9
8	32.6	40.7
9	38.0	40.7
10	39.7	42.0
11	34.5	40.4
12	33.4	39.6
13	39.9	42.4
14	39.2	41.2
15	34.9	37.9
16	34.7	41.6

**Table 10**

Area fraction (%) of the B2 phase in the AN state, determined from Fig. 7c and d, using the program ImageJ. The uncertainty is given by the standard deviation.

Sub-images in the binarized images (shown in Fig. 7c and d)	Fig. 7c	Fig. 7d
	Area fraction of B2 phase in AN alloy (%)	
1	45.1	40.8
2	32.9	42.7
3	25.1	43.9
4	23.8	42.7
5	36.5	37.5
6	29.8	40.1
7	35.5	63.6
8	22.1	48.4
9	40.5	42.4
10	28.9	42.4
11	24.8	36.4
12	21.9	25.6
13	12.3	57.6
14	10.9	40.1
15	18.1	33.7
16	4.2	33.7

The average chemical compositions of the phases listed in Table 2 of Ref. [1] were determined using energy dispersive spectroscopy (EDX) in a Quanta 3D SEM with an EDAX Octane Elect SDDs detector at 30 kV (WD 10 mm) and in a JEOL JEM-2200FS TEM with an EDX Jeol JED-23000BU Si (Li) detector with ultrathin organic/Al window at 200 kV.

The Al-Zr-rich phase composition was determined from the average of the analyzes of two regions with TEM-EDX measurements for each state (AC and AN). The dendritic and interdendritic compositions were determined from the average of five spot analyzes (SEM-EDX) for the AC in the electron-transparent regions (thickness < 1  $\mu\text{m}$ ) of a TEM specimen.

The chemical compositions of the A2 and B2 phases were determined from the average of three spot analyzes (TEM-EDX) for the AN specimen, and finally, the chemical composition of the bright phase surrounding the Al-Zr-rich phase was determined using the average of three spot analyzes (SEM-EDX) in the AN alloy.

**Table 11**

Area fraction of the Al-Zr-rich phase and crystalline phase in the Al-Zr-rich phase determined from the images in Fig. 8a–c.

Sub-images from Fig. 8b,c	Area fraction only Al-Zr-phase (Fig. 8b)	Area fraction only crystalline phase (Fig. 8c)	Area fraction of crystalline phase
1	98.0	0.6	0.6
2	90.8	0.9	1.0
3	65.2	5.3	8.1
4	68.8	7.6	11.1
5	79.6	2.6	3.3
6	97.2	14.4	14.8
7	76.4	7.5	9.8
8	44.4	5.3	11.9
9	46.4	3.0	6.5
10	97.3	1.7	1.8
11	90.3	2.0	2.2
12	72.7	2.9	4.0
13	44.7	0.3	0.7
14	93.8	0.5	0.5
15	90.6	0.7	0.8
16	64.1	1.9	3.0
Average	76.3 ± 19.2	3.6 ± 3.7	5.0 ± 4.7

Name, description and format of each dataset files hosted in Mendeley Repository.

Folder	File name	Description	Format
XRD	Al4Zr5_00-048-1382.cif	Diffraction data of the Al <sub>4</sub> Zr <sub>5</sub> phase used to simulate the diffraction pattern (.cif file)	Raw
	AlTiZr_Struktur_annealing.cel	Simulated diffraction pattern of the B2 phase after annealing obtained with Powdercell software	Analyzed
	AlTiZr_Struktur_as-cast.cel	Simulated diffraction pattern of the B2 phase after casting obtained with Powdercell software	Analyzed
	AlZr_Hexagonal.cel	Simulated diffraction pattern of the Al-Zr-rich phase after casting obtained with Powdercell software	Analyzed
	MoNbTa_Struktur_annealing.cel	Simulated diffraction pattern of the A2 phase after annealing obtained with Powdercell software	Analyzed
	MoNbTa_Struktur_as-cast.cel	Simulated diffraction pattern of the B2 phase after casting obtained with Powdercell software	Analyzed
	XRDPattern_annealed_10-120.xlsx	Experimental XRD pattern of the sample in annealed state	Raw
	XRDPattern_as-cast_10-100.xlsx	Experimental XRD pattern of the sample in cast state	Raw
SEM	Micrograph_grainsize_AC_BSE_01.tif	SEM-BSE micrograph N° 1 used to get the grain size in cast state	Raw
	Micrograph_grainsize_AC_BSE_02.tif	SEM-BSE micrograph N° 2 used to get the grain size in cast state	Raw
	Micrograph_grainsize_AC_BSE_03.tif	SEM-BSE micrograph N° 3 used to get the grain size in cast state	Raw
	Micrograph_grainsize_AC_BSE_04.tif	SEM-BSE micrograph N° 4 used to get the grain size in cast state	Raw
	Micrograph_grainsize_AN_BSE_01.tif	SEM-BSE micrograph N° 1 used to get the grain size in annealed state	Raw
	Micrograph_grainsize_AN_BSE_02.tif	SEM-BSE micrograph N° 2 used to get the grain size in annealed state	Raw

(continued on next page)



Folder	File name	Description	Format
	Micrograph_grainsize_AN_BSE_03.tif	SEM-BSE micrograph N° 3 used to get the grain size in annelaed state	Raw
	Micrograph_grainsize_AN_BSE_04.tif	SEM-BSE micrograph N° 4 used to get the grain size in annelaed state	Raw
	BSE_AC_01_processed.tif	SEM-BSE micrograph N° 1 used to get the volume fraction of the Al-Zr-rich phase in cast state	Raw
	BSE_AC_01_processed_Threshold.tif	Threshold processed SEM-BSE micrograph N° 1 used to get the volume fraction of the Al-Zr-rich phase in cast state	Analyzed
	BSE_AC_01_processed_Threshold_16images.csv	Excel file that contains the% of area fraction of the Al-Zr-rich phase in the cast state, after division of the Threshold image into 16 fields of the SEM-BSE micrograph N° 1	Analyzed
	BSE_AC_02_processed_processed.tif	SEM-BSE micrograph N° 2 used to get the volume fraction of the Al-Zr-rich phase in cast state	Raw
	BSE_AC_02_processed_Threshold.tif	Threshold processed SEM-BSE micrograph N° 2 used to get the volume fraction of the Al-Zr-rich phase in cast state	Analyzed
	BSE_AC_02_processed_Threshold_16images.csv	Excel file that contains the% of area fraction of the Al-Zr-rich phase in the cast state, after division of the Threshold image into 16 fields of the SEM-BSE micrograph N° 2	Analyzed
	BSE_AC_03_processed.tif	SEM-BSE micrograph N° 3 used to get the volume fraction of the Al-Zr-rich phase in cast state	Raw
	BSE_AC_03_processed_Threshold.tif	Threshold processed SEM-BSE micrograph N° 3 used to get the volume fraction of the Al-Zr-rich phase in cast state	Analyzed
	BSE_AC_03_processed_Threshold_16images.csv	Excel file that contains the% of area fraction of the Al-Zr-rich phase in the cast state, after division of the Threshold image into 16 fields of the SEM-BSE micrograph N° 3	Analyzed
	BSE_AC_04_processed.tif	SEM-BSE micrograph N° 4 used to get the volume fraction of the Al-Zr-rich phase in cast state	Raw
	BSE_AC_04_processed_Threshold.tif	Threshold processed SEM-BSE micrograph N° 4 used to get the volume fraction of the Al-Zr-rich phase in cast state	Analyzed
	BSE_AC_04_processed_Threshold_16images.csv	Excel file that contains the% of area fraction of the Al-Zr-rich phase in the as-cast state, after division of the Threshold image into 16 fields of the SEM-BSE micrograph N° 4	Analyzed
	BSE_AN_01_processed_Threshold.tif	Threshold processed SEM-BSE micrograph N° 1 used to get the volume fraction of the Al-Zr-rich phase in annealed state	Analyzed
	BSE_AN_01_processed_Threshold_16images.csv	Excel file that contains the% of area fraction of the Al-Zr-rich phase in annealed state, after division of the Threshold image into 16 fields of the SEM-BSE micrograph N° 1	Analyzed
	BSE_AN_02_processed_Threshold.tif	Threshold processed SEM-BSE micrograph N° 2 used to get the volume fraction of the Al-Zr-rich phase in annealed state	Analyzed
	BSE_AN_02_processed_Threshold_16images.csv	Excel file that contains the% of area fraction of the Al-Zr-rich phase in annealed state, after division of the Threshold image into 16 fields of the SEM-BSE micrograph N° 2	Analyzed

(continued on next page)

Folder	File name	Description	Format
	BSE_AN_03_processed_Threshold.tif	Threshold processed SEM-BSE micrograph N° 3 used to get the volume fraction of the Al-Zr-rich phase in annealed state	Analyzed
	BSE_AN_03_processed_Threshold_16images.csv	Excel file that contains the% of area fraction of the Al-Zr-rich phase in annealed state, after division of the Threshold image into 16 fields of the SEM-BSE micrograph N° 3	Analyzed
	BSE_AN_04_processed_Threshold.tif	Threshold processed SEM-BSE micrograph N° 4 used to get the volume fraction of the Al-Zr-rich phase in annealed state	Analyzed
	BSE_AN_04_processed_Threshold_16images.csv	Excel file that contains the% of area fraction of the Al-Zr-rich phase in annealed state, after division of the Threshold image into 16 fields of the SEM-BSE micrograph N° 4.	Analyzed
TEM	CTEM-DF_AC_Al-Zr-phase.dm3	CTEM-DF micrograph in the Al-Zr-rich region (Including amorphous and crystalline regions) of the sample in the cast state. Fig. 6b of Ref. [1]	Raw
	CTEM-BF_AC_interdendritic_001zoneaxis_a.dm3	CTEM-BF micrograph in the interdendritic region oriented along the 001 zone axis of the sample in the cast state Fig. 3a)	Raw
	SADP_AC_interdendritic_001zoneaxis_b.dm3	Selected area diffraction pattern (SADP) in the interdendritic region oriented along the 001 zone axis of the sample in the cast state (Fig. 3b)	Raw
	CTEM-DF_AC_Al-Zr-Classified image.tif	CTEM-DF micrograph of the sample in the cast state in the Al-Zr-rich region with separation of the three different phases (surrounding, Al-Zr-rich amorphous phase, and Al-Zr-rich crystalline phase) using the software "Trainable Weka Segmentation" tool of FIJI (Fig. 8a of present work)	Analyzed
	CTEM-DF_AC_Al-Zr_amorphous_only_bin.tif	Binary image of the CTEM-DF micrograph of the sample in the cast state in the Al-Zr-rich region considering the fully Al-Zr-rich phase region and the surrounding (Fig. 8b)	Analyzed
	CTEM-DF_AC_Al-Zr_amorphous_only_bin.csv	Excel file that contains the% of area fraction of the complete area of Al-Zr-rich phase in the cast state (Fig. 8b)	Analyzed
	CTEM-DF_AC_Al-Zr_Crystals.tif	Binary image of the CTEM-DF micrograph of the sample in the Al-Zr-rich region only considering the crystal phase in the cast state (Fig. 8c)	Analyzed
	CTEM-DF_AC_Al-Zr_crystals.csv	Excel file that contains the% of area fraction of the crystalline area (Al-Zr-rich phase) in the cast state (Fig. 8c)	Analyzed
	STEM-HAADF_AC_bcc-B2areafraction.dm3	STEM-HAADF micrograph N° 1 of the AC alloy used to determine the area fraction of A2/B2 phases (Fig. 6a)	Raw
	STEM-HAADF_AC_bcc-B2fraction_Bandpassfilter.tif	STEM-HAADF micrograph N° 1 of the AC alloy used to determine the area fraction of A2/B2 phases with Bandpass filter applied with FIJI software	Analyzed
	STEM-HAADF_AC_bcc-B2fraction_T_16images.tif	Threshold separation of the STEM-HAADF micrograph of the AC alloy used to determine the area fraction of A2/B2 phases with Bandpass filter applied with FIJI software (Fig. 6b)	Analyzed
	STEM-HAADF_AC_bcc-B2fraction_T_16images.cvs	Excel file that contains the% of area fraction of the A2/B2 phases in the cast state of the micrograph N° 1	Analyzed

(continued on next page)

Folder	File name	Description	Format
	STEM-HAADF_AC_bcc-B2fraction_2.dm3	STEM-HAADF micrograph N° 2 of the AC alloy used to determine the area fraction of A2/B2 phases (Fig. 5d of Ref. [1])	Raw
	STEM-HAADF_AC_bcc-B2_2_Bandpassfilter.tif	STEM-HAADF micrograph N° 2 of the AC alloy used to determine the area fraction of A2/B2 phases with Bandpass filter applied with Fiji software	Analyzed
	STEM-HAADF_AC_bcc-B2_2_Bandpassfil_16images.tif	Threshold separation of the STEM-HAADF micrograph of the AC alloy used to determine the area fraction of A2/B2 phases with Bandpass filter applied with Fiji software (Fig. 6c)	Analyzed
	STEM-HAADF_AC_bcc-B2_2_Bandpassfilter_16ima.cvs	Excel file that contains the% of area fraction of the A2/B2 phases in the cast state of the micrograph N° 2	Analyzed
	STEM-HAADF_AN_bcc-B2fraction_01.dm3	STEM-HAADF micrograph N° 1 of the AN alloy used to determine the area fraction of A2/B2 phases (Fig. 6a)	Raw
	STEM-HAADF_AN_bcc-B2fraction_01_threshold_16images.jpg	Threshold separation of the STEM-HAADF micrograph N° 1 of the AC alloy used to determine the area fraction of A2/B2 phases with Bandpass filter applied with Fiji software (Fig. 6b)	Analyzed
	STEM-HAADF_AN_bcc-B2fraction_01_threshold.cvs	Excel file that contains the% of area fraction of the A2/B2 phases in the annealed state of the micrograph N° 1	Analyzed
	STEM-HAADF_AN_bcc-B2fraction_02.dm3	STEM-HAADF micrograph N° 2 of the AN alloy used to determine the area fraction of A2/B2 phases (Fig. 6a)	Raw
	STEM-HAADF_AN_bcc-B2fraction_02_threshold_16images.tif	Threshold separation of the STEM-HAADF micrograph N° 2 of the AN alloy used to determine the area fraction of A2/B2 phases with Bandpass filter applied with Fiji software (Fig. 6b)	Analyzed
	STEM-HAADF_AN_bcc-B2fraction_02_threshold_.cvs	Excel file that contains the% of area fraction of the A2/B2 phases in the annealed state of the micrograph N° 2	Analyzed
	precipitates_as-cast.cvs	Excel file that contains the length of the A2 phase (precipitates) in the annealed state	Analyzed
	precipitates_annealed.cvs	Excel file that contains the length of the A2 phase (precipitates) in the cast state	Analyzed
	channels_annealed.cvs	Excel file that contains the length of the B2 phase (channels) in the annealed state	Analyzed
	channels_as-cast.cvs	Excel file that contains the length of the B2 phase (channels) in the cast state	Analyzed
EDX	Mapping_Annealing	This folder contains the raw data of the EDX elemental map for the AN sample shown in Fig. A1 in supplementary data of Ref. [1].	Raw
	Mapping_As-cast	This folder contains the raw data of the EDX elemental map for the AC sample shown in Fig. 3 of Ref. [1].	Raw
	EDX-SEM_AC_Al-Zr-phase_01.docx	EDX Point analysis used to determine the average chemical composition of the Al-Zr-rich phase in the AC sample using SEM	Raw
	EDX-SEM_AC_dendritic-interdendritic_01.docx	EDX Point analysis used to determine the average chemical composition of the dendritic and interdendritic regions of the AC sample	Raw
	EDX-TEM_AC_Al-Zr-phase_02.ppt	EDX area analysis used to determine the average chemical composition of the Al-Zr-rich phase in the AC sample using TEM	Raw

(continued on next page)

Folder	File name	Description	Format
	EDX-TEM_AN_Al-Zr-phase.dm3	STEM micrgraph of the region used to determine the chemical composition of the Al-Zr-rich phase in the AN sample using EDX-TEM	Raw
	EDX-TEM_AN_Al-Zr-phase.ppt	EDX area analysis used to determine the average chemical composition of the Al-Zr-rich phase in the AN sample using TEM	Raw
	EDX-TEM_AN_bcc-B2-phase.dm3	STEM micrgraph of the region used to determine the chemical composition of the A2 and B2 phases in the AN sample using EDX-TEM	Raw
	EDX-TEM_AN_bcc-B2-phase.ppt	EDX point analysis used to determine the average chemical composition of the A2 and B2 phases in the AN sample using TEM	Raw

### Ethics Statements

This work does not require any ethical statement.

### Declaration of Competing Interest

The authors declare that they have no known competing financial interests or personal relationships that could have appeared to influence the work reported in this paper.

### Data Availability

[Data regarding the AlMo<sub>0.5</sub>NbTa<sub>0.5</sub>TiZr refractory high entropy superalloy \(Original data\)](#) (Mendeley Data).

### CRedit Author Statement

**Patricia Suárez Ocaño:** Methodology, Software, Data curation, Writing – original draft; **Leonardo Agudo Jácome:** Conceptualization, Methodology, Writing – review & editing, Supervision, Funding acquisition; **Inmaculada Lopez-Galilea:** Writing – review & editing; **Reza Darvishi Kamachali:** Writing – review & editing; **Suzana G. Fries:** Writing – review & editing.

### Acknowledgments

This work was supported by the [Deutsche Forschungsgemeinschaft](#) (DFG) [398838389]; ILG acknowledges funding by the Deutsche Forschungsgemeinschaft (DFG) in the framework of the collaborative research center SFB/TR 103 through project T4.

All authors acknowledge Dr. Hans Chen, Dr. Alexander Kaufmann, and Prof. Martin Heilmaier from Kalsruher Institut of Technology for the alloy fabrication. PSO and LAJ acknowledge Hennig Goldbeck for XRD. PSO and SGF thank the use of the facilities of ZGH (Center for Interface-Dominated High-Performance Materials).

### References

- [1] P. Suárez Ocaño, S.G. Fries, I. Lopez-Galilea, R.D. Kamachali, J. Roik, L. Agudo Jácome, The AlMo<sub>0.5</sub>NbTa<sub>0.5</sub>TiZr refractory high entropy superalloy: experimental findings and comparison with calculations using the CALPHAD method, *Mater. Des.* 217 (2022) 110593, doi:[10.1016/j.matdes.2022.110593](https://doi.org/10.1016/j.matdes.2022.110593).

- [2] W. Kraus, G. Nolze, POWDER CELL - a program for the representation and manipulation of crystal structures and calculation of the resulting X-ray powder patterns, *J. Appl. Cryst.* 29 (1996) 301–303, doi:[10.1107/S0021889895014920](https://doi.org/10.1107/S0021889895014920).
- [3] C.A. Schneider, W.S. Rasband, K.W. Eliceiri, NIH Image to ImageJ: 25 years of image analysis, *Nat. Methods* 9 (2012) 671–675, doi:[10.1038/nmeth.2089](https://doi.org/10.1038/nmeth.2089).
- [4] American Society for Testing and Materials (ASTM) ASTM E112-13: Standard Test Methods for Determining Average Grain Size, ASTM International, West Conshohocken, PA, USA, 2013.
- [5] J.W. Edington, in: *Practical Electron Microscopy in Materials Science*, 1st ed, Van Nostrand Reinhold Company, New York, 1976, pp. 303–313. *Practical electron microscopy in materials science (1976 edition) | Open Library*.
- [6] P.A. Stadelmann, EMS - a software package for electron diffraction analysis and HREM image simulation in materials science, *Ultramicroscopy* 21 (1987) 131–145, doi:[10.1016/0304-3991\(87\)90080-5](https://doi.org/10.1016/0304-3991(87)90080-5).



### 4.3 Paper III

Influence of cooling rate and lattice misfit on the microstructure and mechanical properties in the refractory  $\text{AlMo}_{0.5}\text{NbTa}_{0.5}\text{TiZr}$  high entropy superalloy.



Contents lists available at ScienceDirect

## Journal of Alloys and Compounds

journal homepage: [www.elsevier.com/locate/jalcom](http://www.elsevier.com/locate/jalcom)

## Influence of cooling rate on the microstructure and room temperature mechanical properties in the refractory $\text{AlMo}_{0.5}\text{NbTa}_{0.5}\text{TiZr}$ superalloy

Patricia Suárez Ocaño<sup>a,\*</sup>, Anna Manzoni<sup>a</sup>, Inmaculada Lopez-Galilea<sup>b</sup>, Benjamin Rutttert<sup>b</sup>, Guillaume Laplanche<sup>b</sup>, Leonardo Agudo Jácome<sup>a</sup>

<sup>a</sup> Bundesanstalt für Materialforschung und -prüfung (BAM), Department for Materials Engineering, Unter den Eichen 87, 12205 Berlin, Germany

<sup>b</sup> Institute for Materials, Ruhr-University Bochum, Universitätsstr. 150, 44801 Bochum, Germany

## ARTICLE INFO

## Article history:

Received 19 January 2023

Received in revised form 25 March 2023

Accepted 28 March 2023

Available online 29 March 2023

## Keywords:

High entropy alloys  
Mechanical properties  
Fracture toughness  
Microstructure  
Nanoindentation

## ABSTRACT

Refractory chemically complex alloys with bcc-based microstructures show great potential for high-temperature applications but most of them exhibit limited room-temperature ductility, which remains a challenge. One such example is the  $\text{AlMo}_{0.5}\text{NbTa}_{0.5}\text{TiZr}$  alloy, mainly consisting of a nano-scaled structure with an ordered B2 matrix and a high-volume fraction of aligned cuboidal and coherently embedded A2 precipitates. This work aims to investigate how the cooling rate after hot isostatic pressing of the  $\text{AlMo}_{0.5}\text{NbTa}_{0.5}\text{TiZr}$  alloy affects its microstructure and its resulting hardness and fracture toughness at room temperature. A slow cooling rate of 5 °C/min leads to a coarse microstructure consisting of aligned slabs (mean A2 precipitate = 25 nm) with a nanohardness of about 8 GPa. In contrast, after the fastest cooling rate (30 °C/min), the A2 precipitates become more cubic with an edge length of = 16 nm, resulting in an increase in nanohardness by 10 %. The fracture toughness is roughly independent of the cooling rate and its mean value ( $\approx 4.2 \text{ MPa}\cdot\text{m}^{1/2}$ ) resembles that of some B2 intermetallics and other A2/B2 alloys. As the lattice misfit between the A2 and B2 phases is known to play a key role in microstructure formation and evolution, its temperature dependence between 20 and 900 °C was investigated. These findings offer insights into the evolution of the microstructure and room-temperature mechanical properties of the  $\text{AlMo}_{0.5}\text{NbTa}_{0.5}\text{TiZr}$  alloy, which could help the development of advanced chemically complex alloys.

© 2023 The Authors. Published by Elsevier B.V. This is an open access article under the CC BY license (<http://creativecommons.org/licenses/by/4.0/>).

### 1. Introduction

Chemically complex alloys (CCAs) are a class of materials with unique microstructures and properties. They have been studied for the past 20 years because they open a wide range of possible combinations of alloying elements with high concentrations that can satisfy the ever-growing requirements of, e.g., high-temperature materials, as conventional one-element-based materials reach their limits [1,2]. Refractory (r)CCAs, which were first reported by Naka [3], contain high concentrations of elements such as Mo, Nb, and Ta and have been widely studied in recent years as a possible solution to the limitations of conventional alloys [4–6], e.g., as potential candidates for improving the efficiency of components used in high-temperature structural applications such as gas turbines [7–9]. One promising example of rCCAs is the  $\text{AlMo}_{0.5}\text{NbTa}_{0.5}\text{TiZr}$  alloy (here, the Mo and Ta mol fractions are half those of Al, Nb, Ti, and Zr, corresponding to  $\text{Al}_{20}\text{Mo}_{10}\text{Nb}_{20}\text{Ta}_{10}\text{Ti}_{20}\text{Zr}_{20}$  in at%), which was

produced for the first time by Senkov et al. [10] and has been replicated and later studied by other authors [11–14]. After cooling from 24 h at 1400 °C, this rCCA decomposes spinodally into a dual-phase A2/B2 (*Strukturbericht* designation [15]) microstructure, also known as  $\alpha/\alpha'$  microstructure in Fe-based alloys [16], which resembles the  $\gamma/\gamma'$  microstructure of well-known Ni-based superalloys [17]. For this reason, together with its good compression properties at room and high temperatures (i.e., yield strength of 2000 MPa and 745 MPa, at 23 and 1000 °C, respectively), this rCCA has also been called refractory superalloy (RSA) by Senkov et al. [10]. It also contains a minor Al-Zr-rich hexagonal intermetallic phase decorating the grain boundaries. The A2/B2 microstructure has also been reported for other CCAs that also form by spinodal decomposition [18].

While its compressive strength is high, the ductility of this RSA and other bcc-based rCCAs [19] is still a great concern. Some efforts have already been undertaken to reduce the room-temperature (RT) brittle behavior of CCAs [20–23], and of the RSA [24]. For example, Soni et al. [25] demonstrated that the RT ductility of the  $\text{Al}_{0.5}\text{NbTa}_{0.8}\text{Ti}_{1.5}\text{V}_{0.2}\text{Zr}$  A2/B2-structured alloy can be improved through phase inversion by controlling the annealing process. Recently, Dong et al. [22] reported that replacing Ta with Ti increases

\* Corresponding author.

E-mail address: [patricia.suarez-ocano@bam.de](mailto:patricia.suarez-ocano@bam.de) (P. Suárez Ocaño).

the ductility of the  $\text{Al}_5(\text{NbTaTiZr})_{95}$  alloy, although it may compromise the compressive yield strength. In the case of the  $\text{AlMo}_{0.5}\text{NbTa}_{0.5}\text{TiZr}$  RSA, reducing the Mo content also reduces the brittle behavior under compression at RT, although it decreases the strength of the alloy and leads to the formation of a finer Al-Zr-rich phase at grain boundaries [24]. Due to this limitation, the quest to optimize the composition of these alloys and/or to establish new processing routes to improve their properties continues.

Recent studies in the field of CCAs demonstrate that their microstructures and their resulting mechanical properties could be tuned by adjustments of the processing route [26–28]. For instance, Wang et al. [29] determined that an increase in the amplitude of ultrasound solidification refined the L1<sub>2</sub>/B2 eutectic microstructure and therefore improved the strength and ductility of the  $\text{FeCoNi}_2\text{Al}_{0.9}$  alloy. Cooling rates can have a significant effect on the microstructure and mechanical properties of Ni- and Co-based superalloys [30,31] and of CCAs [32,33], e.g., Munitz et al. [34] demonstrated that changes in the heat treatments and cooling rates lead to microstructural changes of the  $\text{AlCrFeNiTi}_{0.5}$  CCA, i.e., heat treatment at 650 °C increased the amount of A2/B2 phases and decreased the amount of the ductile fcc phase, thus increasing the hardness but reducing the ductility. In the  $\text{Al}_{0.5}\text{CoCrFeNi}$  CCA, consisting of fcc, bcc and B2 phases, Xiong et al. [35] found that faster cooling rates resulted in larger volume fractions of the B2 phase, which in turn promoted the hardness at the expense of ductility. While these studies suggest that higher cooling rates generally result in higher strength and lower ductility, the specific results may depend on the nature of the alloy.

Given these recent studies that show the potential for modifying the microstructure and mechanical properties of CCAs by controlling their processing routes, the effects of the cooling rate on the microstructure and room temperature mechanical properties of the  $\text{AlMo}_{0.5}\text{NbTa}_{0.5}\text{TiZr}$  RSA are investigated here. Specifically, this study focuses on following the microhardness, nanohardness and fracture toughness of the alloy as a function of cooling rate (5, 10 and 30 °C/min).

## 2. Materials and methods

### 2.1. Material

Pure elements were vacuum arc melted under Ar atmosphere and allowed to solidify to produce an ingot of approximately  $20 \times 20 \times 50 \text{ mm}^3$ . For details related to arc melting, the reader may refer to Ref. [13]. The ingot was subsequently homogenized at 1400 °C for 24 h (under Ar, purity > 99.998 %) and cooled at < 4 °C/min. Then, three slices with dimensions  $20 \times 20 \times 6 \text{ mm}^3$  were individually HIPed (Quintus QIH-9 URQ from Quintus Technologies AB equipped with a Molybdenum furnace) at 1370 °C for 4 h under 170 MPa to close porosity introduced via casting, after which each slice was cooled at a different rate of 5, 10, and 30 °C/min. The cooling rate was controlled by natural cooling (free convection) in combination with regulated gas flow of cold gas and heating intervals while the temperature was monitored with 4 thermocouples. Thus, it was possible to control the cooling rates. After processing, metallographic specimens were ground using SiC abrasive papers (p320, p600, p1200, p2500, and p4000) followed by polishing for 10 min using colloidal silica with a 50-nm grain size.

### 2.2. Mechanical properties

Nano and microindentation tests at RT were conducted on the metallographically prepared specimens that underwent different cooling rates (5, 10, and 30 °C/min). While the microhardness tests were averaged over several phases and grains of the matrix, 10–16 local nanoindentation tests were performed to evaluate the

nanohardness of intermetallics forming at grain boundaries and two-phase (A2/B2) regions within grains. The nanoindentation measurements were performed using a Hysitron TriboIndenter (Hysitron TI 980 Bruker) equipped with a Berkovich diamond indenter tip, a maximum load of 8 μN, a holding duration of 10 s, and a speed of 0.8 μN/s. The displacement ( $h$ ) was monitored as a function of the load ( $P$ ) throughout each load-unload cycle. The indentation modulus  $E_r$  was determined from the slope of the unloading curve at maximum load using the classical relationship [36]:

$$E_r = \frac{1}{2} \frac{\sqrt{\pi}}{\sqrt{A}} \frac{dP}{dh} \quad (1)$$

The elastic (Young's) modulus ( $E$ ) of the alloy can then be calculated from [37]:

$$\frac{1}{E_r} = \frac{1 - \nu^2}{E} + \frac{1 - \nu_i^2}{E_i} \quad (2)$$

where  $\nu$  (assumed to be equal to 0.3) and  $\nu_i$  (= 0.07) are the Poisson's ratios of the specimen and diamond indenter tip, respectively, and  $E_i$  represents the Young's modulus of the indenter tip ( $E_i$  = 1141 GPa [38]).

Microhardness measurements were performed following the DIN EN ISO 6507-2 standard with a testing machine (KB 30 SR FA Basic) equipped with a Vickers indenter tip. Measurements were performed with three different weights of 1, 20, and 30 kg (loads of 9.8 N, 196 N, and 294 N, respectively) and about 20 indentations for each load. Subsequently, both diagonals of each remnant indent were measured by optical microscopy to estimate the hardness. To avoid interactions between indents, the latter were performed 2 mm apart. The fracture toughness ( $K_{IC}$ ) of the RSA was estimated using the model described in Ref. [39]. To this end, the lengths of the cracks formed at the corners of the indenter tip were measured using a scanning electron microscope (SEM) equipped with a field emission gun (FEG) and a backscatter electron detector (BSE) at an acceleration voltage of 25 kV (SEM, FEI Quanta 3D). First, only remnant indents whose four primary cracks emanated straight and radially from each corner (as described in the ISO 21618 standard [40]) were considered. Then, indents with spalled edges, asymmetrical, split, or forked cracks were also considered to compare the final values between the subset and the full set of microindents. SEM images were acquired in the specimens after microhardness testing with 20 and 30 kg. Additionally, the fraction of cracks,  $F_c$ , at the corners of the indents was determined using  $F_c$  = total number of cracks / (number of indents × 4). To make a comparison of the fracture toughness of the RSA with different relevant engineering materials, including bcc-structured alloys, an Ashby plot was generated using the GRANTA Edupack software (ANSYS, Inc.), which shows the fracture toughness as a function of Vickers microhardness.

### 2.3. Characterization

The microstructures of the specimens cooled under different conditions were analyzed before mechanical testing using the previously mentioned SEM. The latter is equipped with an energy-dispersive X-ray spectroscopy (EDS, EDAX Octane Elect SDDs) detector that allowed for determining the compositions of different phases and two-phase regions. The average grain size was determined according to ASTM E112 [41]. SEM-EDS analyses of large regions ( $\approx 2 \text{ mm}^2$ ) were performed on the three specimens cooled at 5, 10, and 30 °C/min (see Table S1 of Supplementary Material). Table 1 shows the average chemical composition of the  $\text{AlMo}_{0.5}\text{NbTa}_{0.5}\text{TiZr}$  RSA.

For transmission electron microscopy (TEM), samples were prepared as described elsewhere [13]. Conventional (C)TEM was used to acquire selected area diffraction patterns (SADPs), bright-field (BF), and dark-field (DF) micrographs. Scanning (S)TEM was conducted



**Table 1**

Chemical composition of the RSA obtained using semi-quantitative SEM-EDS averaged over large regions. All concentrations are in at%.

	Al	Mo	Nb	Ta	Ti	Zr
Concentrations in at%	22	12	20	8	20	18

using the high-angle annular (HAA)DF mode for atomic number contrast imaging (Z-contrast). The TEM (JEOL JEM-2200FS), equipped with a FEG, was operated at an acceleration voltage of 200 kV.

The size of the bcc (A2) precipitates, and B2 channels, as well as the area fractions of the present phases in the HIPed samples after different cooling rates, were estimated using the image analysis package Fiji [42].

X-ray diffraction (XRD) patterns were recorded at RT, 200, 600, 800, and 900 °C with a D8 Advance Bruker diffractometer using the Bragg-Brentano geometry, a Cu K $\alpha$ 1 radiation ( $\lambda_{K\alpha1} = 0.15406$  nm), and a  $2\theta$  scattering range between 10° and 140°. For the high-temperature measurements, an Anton Paar furnace under vacuum ( $\approx 5 \cdot 10^{-2}$  mbar) was employed. The identification of the phases was carried out by comparing the experimental patterns with simulated patterns using the PowderCell software package [43]. The lattice parameters of the different phases were determined from the peak positions ( $2\theta$ ) in combination with Bragg's law.

The temperature dependence of the lattice parameters and the misfit between the A2 and B2 phases were additionally calculated using the ThermoCalc software (version 2020b) [44] in combination with the TCHEA3 database. For this purpose, the molar volumes ( $V_m$ ) of the A2 and B2 phases were calculated as a function of temperature and the corresponding lattice parameters ( $a$ ) were deduced from:

$$a = \left[ \frac{2V_m}{N_A} \right]^{\frac{1}{3}} \quad (3)$$

where  $V_m$  is the molar volume and  $N_A$  is the Avogadro's constant. The lattice misfit  $\delta$  in % was subsequently determined from  $a_{A2}$  and  $a_{B2}$  using Eq. (4):

$$\delta = \frac{2(a_{A2} - a_{B2})}{a_{A2} + a_{B2}} 100 \quad (4)$$

### 3. Results and discussion

#### 3.1. Effect of the cooling rate on the A2/B2 microstructure after HIP

Fig. 1 shows the microstructure of the RSA at different magnifications for the specimens cooled at 5 °C/min (1st column), 10 °C/min (2nd column), 30 °C/min (3rd column). The microstructure in the three cases consists of equiaxed grains (first row of Fig. 1) containing subgrain boundaries. Grain and subgrain boundaries are marked with blue and red arrows, respectively, in the second row of Fig. 1. The average grain size is found to be nearly independent of cooling rate, i.e.,  $151 \pm 32 \mu\text{m}$  for 5 °C/min,  $147 \pm 26 \mu\text{m}$  for 10 °C/min, and  $154 \pm 25 \mu\text{m}$  for 30 °C/min. This shows that the three specimens experienced similar thermal histories and the region of the ingot from where they were extracted had a homogeneous grain size. At low magnification, contrast variations are visible within grains, indicating that the dendritic microstructure was not fully homogenized during our heat treatment (1400 °C for 24 h).

In the 5-°C/min sample (Fig. 1a), the grain boundaries are almost completely covered by dark precipitates surrounded by a bright rim (Fig. 1b). They occupy  $7 \pm 1$  % of the surface (see Fig. S1 of supplementary material and Table 2) and were identified in previous studies as a hexagonal Al-Zr-rich phase ( $\text{Al}_{4-x}\text{Zr}_5$ , with  $0 \leq x \leq 1$ ) with a  $\text{P6}_3/\text{mcm}$  space group while the bright regions surrounding the

precipitates correspond to a Nb-Mo-Ta-rich A2 phase ( $< 1$  %) [10,11,13]. These phases were also identified in the sample cooled at 10 and 30 °C/min, but the area fractions of the Al-Zr-rich phase were  $3 \pm 1$  % and  $< 1$  %, i.e., 2.3 and 7 times lower than in the 5-°C/min specimen, respectively (Fig. S1 and Table 2). Based on this observation, it can be concluded that a lower cooling rate promotes the precipitation of the Al-Zr-rich phase. When the cooling rate is sufficiently slow, Al and Zr diffuse towards grain boundaries and allow the Al-Zr-rich phase to grow while Ti, Ta, and Nb diffuse in the opposite direction and accumulate at the rim of these intermetallic particles. Note that the amount of the Al-Zr-rich phase is disputed in the literature. For the same heat treatment (1400 °C for 24 h) and cooling rate (10 °C/min), three different area fractions were reported for the Al-Zr-rich phase, e.g., Jensen found 16 % [45], Senkov et al., 6 % [10] and Whitfield et al. less than 1 % [12]. This discrepancy cannot be solved at this point.

At higher magnification (3rd row of Fig. 1), the well-known nanostructure described previously [10,24] with aligned cuboidal A2 precipitates embedded in a continuous B2 matrix appears for the three different cooling rates. However, the cooling rate is found to strongly affect the length scale of the nanostructure: the greater the cooling rate, the finer the nanostructure.

Due to their small size, the A2 precipitates were further characterized by TEM. Fig. 2a-c show CTEM-DF micrographs and corresponding SADPs of the 5, 10, and 30-°C/min specimens, respectively, viewed along the [001] zone axis. By selecting the superlattice reflection (100) marked with green circles in the SADPs (shown as insets), the ordered B2 channels appear bright while the disordered A2 precipitates are dark. A more detailed analysis of the CTEM-DF micrographs is provided in Figs. S2-S4 of the supplementary material. The contrast in the STEM-HAADF micrographs in Fig. 2d-f is equivalent to the BSE contrast in Fig. 1a-c but with a better resolution, i.e., the A2 precipitates appear brighter than the B2 matrix owing to their higher Z-contrast. SEM-EDS and TEM-EDS analyses in Table S2 of supplementary material confirmed that the A2 phase is Mo-Nb-Ta-rich while the B2 phase is Al-Zr-rich and the hexagonal  $\text{P6}_3/\text{mcm}$  phase is Al-Zr-rich, consistent with previous reports on the  $\text{AlMo}_{0.5}\text{NbTa}_{0.5}\text{TiZr}$  RSA [10,24]. The diffraction contrast in the STEM-BF images did not reveal the presence of dislocations at the A2/B2 interfaces after cooling from 1370 °C (see Fig. S5 and Fig. S6 of supplementary material), so that all the aligned cuboidal precipitates were fully coherent unless found at defective regions, e.g., subgrain boundaries (see red arrows in Fig. 1b, e and h), which were not quantified here.

The relative area fractions of the A2 and B2 phases were determined from STEM-HAADF micrographs (see Fig. S7 of supplementary material). The mean grain size, the area fractions of the different phases, the range of precipitate and channel sizes as well as their average sizes for the RSA cooled at different rates are summarized in Tables 2 and S3. It is also visible in Fig. 2d-f that the B2 phase presents narrow and wide channels, whose widths are provided in Table 2.

The variations in area fractions of the A2 and B2 phases after different cooling rates (cf. Table 2) are small compared to the error bars, indicating that they are approximately independent of cooling rates. In contrast, the average edge length ( $d$ ) of the A2 precipitates and the width of the wide B2 channels significantly decrease by 36 % and 61 % with increasing cooling rates from 5° to 30 °C/min, respectively (cf. Table 2). At this point,  $d$  disregards the elongated character of the A2 precipitates. This aspect is now investigated in more detail in Fig. 3, which shows the aspect ratio (AR) histograms of the A2 precipitates in the RSA cooled at different rates. The AR of each precipitate is calculated as:  $AR = \text{narrow edge length} / \text{wide edge length}$ , with  $0 \leq AR \leq 1$ , so that the projection of the particle is an almost perfect square when AR is close to 1. These projected square-shaped particles are mostly located at the intersections of

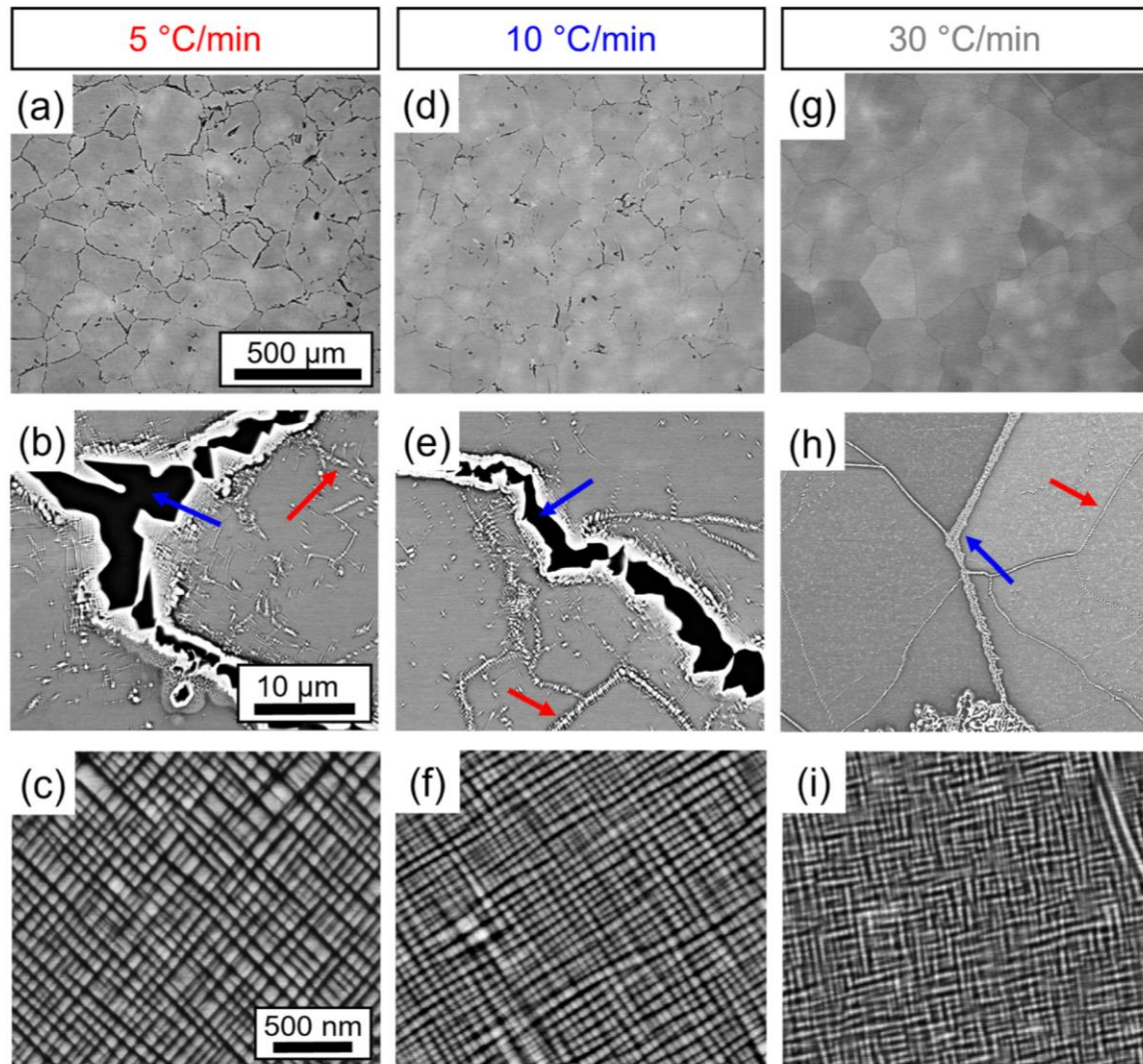


**Fig. 1.** BSE micrographs of the RSA after annealing (1400 °C for 24 h) followed by HIP (1370 °C for 4 h at 170 MPa) and cooling at (a-c) 5 °C/min, (d-f) 10 °C/min, and (g-i) 30 °C/min. Note that the magnification within a given row is the same. The blue and red arrows indicate grain and subgrain boundaries, respectively.

**Table 2**

Grain size, area fractions of the different phases, edge length of the A2 precipitates, and width of the B2 channels in the RSAs cooled at different rates. The error bars correspond to the standard deviations.

Cooling rate (°C/min)	Grain size (μm)	Phase area fraction (%)			Phase average size (nm)		
		B2 channels	A2 precipitates	$Al_{4-x}Zr_5$ , $0 \leq x \leq 1$	B2 channel width		A2 precipitate edge length (d)
					narrow	wide	
5	151 ± 32	54 ± 7	39 ± 7	7 ± 2	4 ± 1	46 ± 20	25 ± 15
10	147 ± 26	62 ± 2	35 ± 2	3 ± 1	3 ± 1	31 ± 12	18 ± 9
30	154 ± 25	54 ± 4	45 ± 4	< 1	3 ± 1	18 ± 8	16 ± 7

two perpendicular rows of aligned precipitates, i.e. each row is delimited by wide channels, Fig. 2d-f. A comparison of Fig. 3a-c reveals that the percentage of A2 particles with a nearly perfect square shape (see black arrows) declines with a decreasing cooling rate, indicating that the elastic strain energy of rows of aligned slabs becomes lower than that of cubes as the particles coarsen. Apart

from the sharper maximum at  $AR \approx 1$  for higher cooling rates, the AR distribution shows a broad asymmetric maximum. The position of this broad maximum as well as its width are found to increase with an increasing cooling rate. It is thus clear that there is a tendency to form more symmetric precipitates (with higher AR values) in the RSA as the cooling rate increases. Note that the composition of the



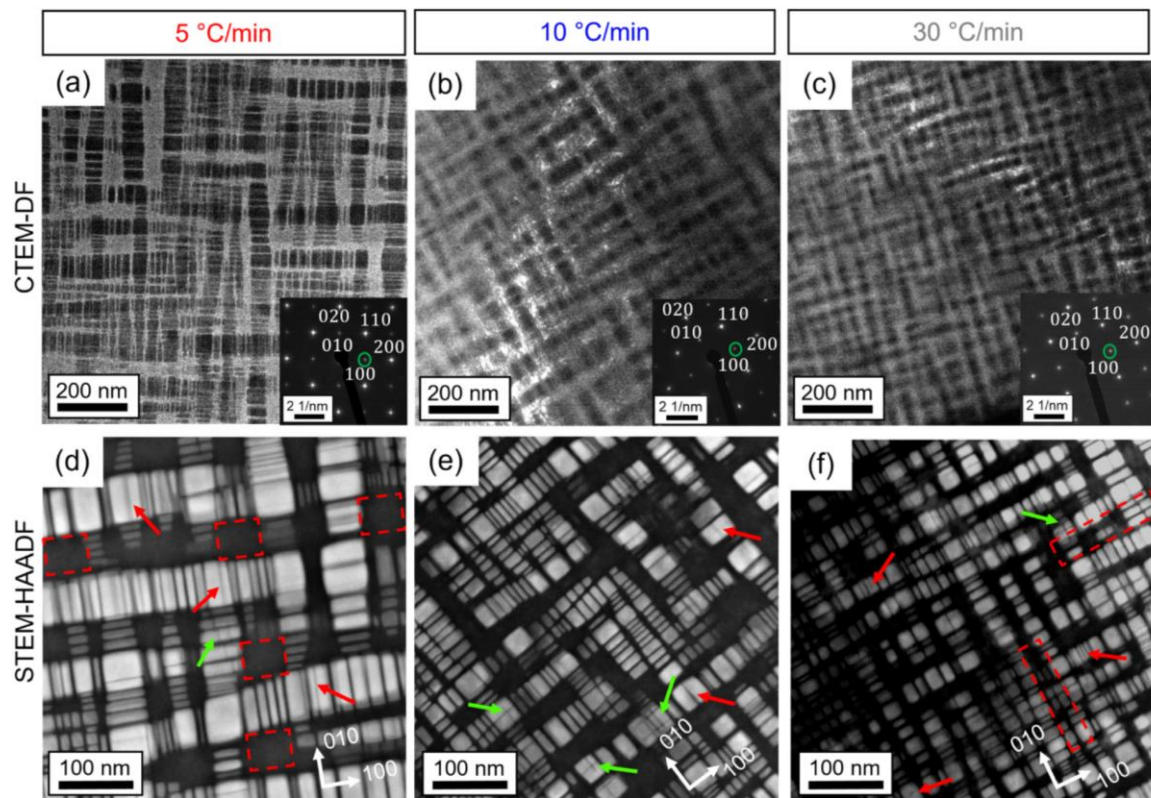


**Fig. 2.** (a–c) CTEM-DF micrographs of the nanostructure within equiaxed grains oriented along the [001] zone axis with their respective SADPs (insets) for RSAs cooled after HIP at (a) 5 °C/min, (b) 10 °C/min, and (c) 30 °C/min. Superlattice reflections (100) used for imaging are marked with green circles. In this diffraction condition, the B2 phase appears brighter while the A2 phase is darker. (d–f) Equivalent STEM-HAADF micrographs for (d) 5 °C/min, (e) 10 °C/min, and (f) 30 °C/min. The fact that the contrast of the A2 slabs and cubes is brighter in (d–f) indicates that these precipitates have a higher density than the B2 matrix. The red and green arrows in Fig. 2d–f, and red dashed rectangles in Fig. 2d and f, represent a comparison with the mechanisms proposed by Wang et al. [46]. For details see Section 3.4 and Fig. 7.

A2 and B2 phases remains approximately the same in all three states, as determined with TEM EDS (Table 3).

Based on these results, it can be concluded that the cooling rate affects the microstructure of the RSA in terms of morphology, size, and distribution of both B2 channels and A2 precipitates, as well as the precipitation of the Al–Zr-rich phase. The area fractions of B2 and A2 phases fluctuate around rather constant values and the width of the thin B2 channels remains roughly constant.

As shown previously, a slow cooling rate promotes the heterogeneous precipitation of an Al–Zr-rich phase at grain boundaries. Since this phase grows at the expense of the B2 phase [22], one may expect the B2-phase volume fraction in the vicinity of grain boundaries to be locally lower. However, since the area fractions and compositions of the A2 and B2 phases (cf. Table 3) were determined in the center of the grains, their values are unlikely to be affected by the presence of the Al–Zr-rich phase. This may be the reason why the area fractions and compositions of the A2 and B2 phases listed in Table 3 do not significantly depend on the cooling rate.

### 3.2. Effect of cooling rate on the lattice misfit

The XRD patterns at RT of the RSA cooled at 5, 10, and 30 °C/min are displayed in Fig. 4 as black, light and dark purple lines, respectively. The A2 and B2 phases as well as a hexagonal  $Al_{4-x}Zr_5$  intermetallic were identified. The lattice parameters of these phases (see Tables 3 and 4) agree well with those previously determined for the

$AlMo_{0.5}NbTa_{0.5}TiZr$  RSA [10,12,13,45]. The lattice misfit,  $\delta$ , between the A2 and B2 phases was calculated using Eq. (4) [48], resulting in negative lattice misfits (Table 4).

As the lattice parameters of the hexagonal intermetallic phase were found to be nearly independent of the cooling rate, we provide their average values in Table 4. In contrast, when the cooling rate increases, the lattice parameters of the A2 and B2 phases in Table 4 increase and decrease respectively, resulting in a decreasing magnitude of the apparent lattice misfit. In principle, there are three potential contributions to this evolution, namely (1) the formation of a dislocation network at the A2/B2 interface that may relax the misfit (resulting in stronger differences between  $a_{A2}$  and  $a_{B2}$ ), (2) a change in the composition between the A2 and B2 phases, and (3) a size effect related to the density of A2/B2 interfaces. (1) As no dislocations were observed by TEM at the A2/B2 interfaces regardless of the cooling rate (cf. Fig. S5 and Fig. S6 of the supplementary material), we conclude that the investigated cooling rates are fast enough to avoid the formation of dislocations upon cooling. Therefore, this contribution can be neglected. (2) TEM-EDS observations (cf. Table 3) show that the composition of the A2 and B2 phases does not change significantly with the cooling rate. A contribution of the composition on the lattice misfit can thus be ruled out. (3) When the cooling rate is slow, there is a low number density of large precipitates. As the lattice misfit across a coherent interface induces an elastic strain [49], the lattice parameters of the A2 and B2 phases in the vicinity of the interface are constrained, resulting in a small local “constrained”

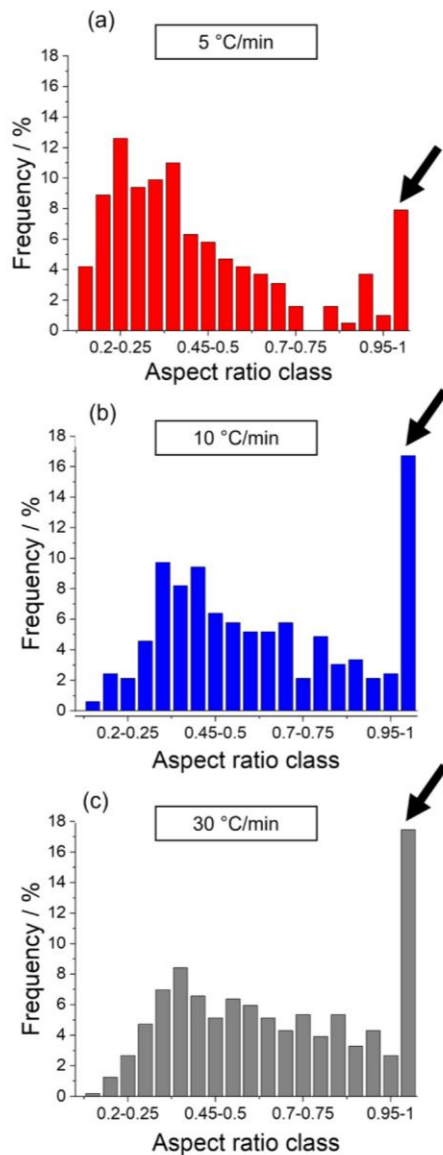


**Fig. 3.** Histograms showing the relative frequency distributions of A2-particles aspect ratios in the RSAs cooled at (a) 5 °C/min, (b) 10 °C/min, and (c) 30 °C/min.

misfit. However, these constraints are progressively relaxed as one moves away from an interface. As a result, the cores of the large A2 precipitates and wide B2 channels are less affected by the coherency misfit and the local apparent misfit is larger there. When there is a high number density of small precipitates (e.g., for a high cooling rate), the density of A2/B2 interfaces is larger, resulting in a greater effective volume affected by elastic strains and therefore the magnitude of the apparent macroscopic lattice misfit is smaller. This latter contribution is in line with our experimental results in Table 4.

Now we compare our results with those reported in the literature. All recorded A2/B2 lattice misfits of the  $\text{AlMo}_{0.5}\text{NbTa}_{0.5}\text{TiZr}$  RSA at RT are between  $-1$  and  $-2\%$ . (cf. Table 3). Compared to  $\delta$  in fcc-structured superalloys, which are usually in the order of  $-0.1\%$  (in many commercial Ni-based superalloys) or  $+0.3\%$  (Co-base) [50],

the misfit value in the  $\text{AlMo}_{0.5}\text{NbTa}_{0.5}\text{TiZr}$  RSA is very large. A detailed comparison of our lattice misfit data with the works from Senkov et al. ( $\delta = -1.1\%$  [10]), Kloenne et al. ( $\delta = -2.1\%$  [14]) and Whitfield et al. ( $\delta = -1.51\%$  [12]) proves challenging on different levels, e.g., the uncertainty of some of those measurements was either not given [12], or led to variations of up to  $\Delta\delta = 0.6\%$  [10], albeit, in the latter case, the authors did not focus on the subject of lattice misfit. In two of the works summarized in Table 3 [10,12], the final microstructure arose after cooling from 1400 °C at 10 °C/min, while in the work by Kloenne et al. [14], the lattice misfit was studied after aging at 1000 °C for 6 h and subsequent water quenching (cf. Table 3).

The work of Senkov et al. [10] reported  $|\delta| \approx 1.07\%$ . If we use the measurement uncertainty given by Senkov et al. to find the lower and higher limits for their  $a_{A2}$  and  $a_{B2}$  and apply Eq. 4, we find the range  $-1.37\% < \delta < -0.76\%$  (cf. 4th row in Table 3). The  $a_{A2}$  and  $a_{B2}$  values reported by Whitfield et al. [12] (cf. 5th row in Table 3) yield  $\delta \approx -1.51\%$ . They did not report an uncertainty for the measurements. However, their  $\delta$  is more negative than that of Senkov et al. [10], and thus closer to what we found. Considering the three possible contributions to the lattice misfit mentioned previously, we can state the following: (1) the A2/B2 images reported by Senkov et al. [10] (cf. their Figs. 5 and 6) do not show the presence of misfit dislocations, as in our case. The SEM images reported by Whitfield et al. [12] reveal an A2/B2 microstructure with flat interfaces and sharp corners resembling our dislocation-free interfaces. (2) The chemical composition of Senkov's A2 and B2 phases is similar to ours (Table 3) but no information on A2 and B2 compositions was reported by Whitfield et al. [12]. (3) By inspection of the (S)TEM images from Senkov et al. [10] and from their stated values, both the average edge length of their A2 precipitates and the width of their wide B2 channels are smaller than our measured values. They report a higher fraction of the A2 phase than we do. These values would represent an increased density of A2/B2 interfaces in their material state, which in turn would lead to a stronger constrain of the respective inner phase regions by the latter, and thus to a smaller value of  $|\delta|$ . As for a comparison with the work by Whitfield et al. [12], no conclusion can be drawn because their SEM-BSE image does not show the widths of the channels precisely enough.

In the third work, Kloenne et al. [14] used a different material condition: their alloy was aged at 1000 °C for 6 h and water quenched. After aging, the authors found that an array of misfit dislocations formed at the A2/B2 interfaces to relax the coherency strains. Based on the spacing between dislocations, Kloenne et al. [14] estimated a "relaxed" lattice misfit of  $-2.1\%$ , which is more negative than our "constrained" values for fully coherent A2/B2 interfaces.

### 3.3. Temperature dependence of the lattice misfit $\delta$

To determine the temperature-dependent lattice parameters of the A2 and B2 phases, as well as the lattice misfit between them, *in-situ* XRD was performed between RT and 900 °C in an RSA that was cooled at 10 °C/min. The *in-situ* XRD patterns are shown in Fig. 5 where the inset allows us to distinguish the 110 peaks of the A2 and B2 phases. At RT, the A2 and B2 peaks are clearly separated. With increasing temperature, the intensity of the 110 peaks of the A2 phase decreases due to its progressive dissolution. Moreover, the distance between the 110 peaks of the A2 and B2 phases decreases between RT and 900 °C, indicating that the difference between the lattice parameters decreases. From the XRD patterns in Fig. 5, the obtained lattice parameters ( $a_{A2}$  and  $a_{B2}$ ) and the lattice misfit are summarized in Table 5 and their temperature dependences are shown on the left and right axes of Fig. 6a, respectively. With increasing temperature from RT to 200 °C, as the atomic mobilities are extremely low, the microstructure must remain constant and the changes in  $a_{A2}$  and  $a_{B2}$  reflect thermal expansion. In Fig. 6a,  $a_{A2}$  is



**Table 3**

Phases, compositions, microstructural features, and processing parameters of the  $\text{AlMo}_{0.5}\text{NbTa}_{0.5}\text{TiZr}$  RSA from this work and other studies. The phase and alloy compositions were determined by TEM-EDS and SEM-EDS, respectively. In this table, we also list the area fractions (AF) of the different phases, the lattice parameters of the cubic phases, the lattice misfit ( $\delta$ ) between the A2 and B2 phases, the A2/B2 coherency, the corresponding heat treatments, and sources.

Phase / alloy	Concentration (at%)						AF (%)	<i>a</i> (Å)	$\delta$ (%)	A2/B2 coherency	(Final heat treatment step) cooling <sup>a</sup>	Source
	Al	Ti	Zr	Mo	Nb	Ta						
A2	5 ± 1	17 ± 1	8 ± 1	17 ± 1	30 ± 1	23 ± 1	39	3.2632	-1.65 > $\delta$ > -1.77	Fully coherent	(1370 °C, 4 h)	This work
B2	27 ± 1	23 ± 1	25 ± 1	8 ± 1	13 ± 1	4 ± 1	54	3.3196				
$\text{Al}_{4-x}\text{Zr}_5$ alloy	40 ± 1	9 ± 2	34 ± 1	3 ± 1	11 ± 1	2 ± 1	7					
A2	4 ± 1	15 ± 1	11 ± 1	17 ± 1	29 ± 1	24 ± 1	35	3.2616	-1.54 > $\delta$ > -1.73	Fully coherent	(1370 °C, 4 h)	This work
B2	26 ± 1	21 ± 1	25 ± 1	9 ± 1	14 ± 1	5 ± 1	62	3.3155				
$\text{Al}_{4-x}\text{Zr}_5$ alloy	39 ± 1	9 ± 1	34 ± 1	4 ± 1	11 ± 1	20	3					
A2	5 ± 1	16 ± 1	10 ± 1	16 ± 1	27 ± 1	26 ± 1	45	3.2616	-1.20 > $\delta$ > -1.52	Fully coherent	(1370 °C, 4 h)	This work
B2	27 ± 1	22 ± 1	24 ± 1	8 ± 1	14 ± 1	5 ± 1	54	3.3155				
$\text{Al}_{4-x}\text{Zr}_5$ alloy	40 ± 1	9 ± 1	35 ± 1	3 ± 1	10 ± 1	3 ± 1	< 1					
A2	4	17	10	16	32	22	45	3.2690	-0.76 > $\delta$ > -1.37	Fully coherent	(1400 °C, 24 h)	[10,45]
B2	26	25	26	6	14	4	39	3.3040				
$\text{Al}_{4-x}\text{Zr}_5$ alloy	37	10	38	3	9	3	16	(± 0.005)				
A2	18	21	22	9	19	11	50	3.2700	-1.51*	Fully coherent	(1400 °C, 24 h)	[12]
B2							50	3.3200				
$\text{Al}_{4-x}\text{Zr}_5$ alloy							< 1					
A2	12	20	9	15	28	16		3.3100	-2.00 > $\delta$ > -2.19	Relaxed by misfit dislocations	(1400 °C, 24 h)	[14,47]
B2	30	25	24	6	12	3		3.3800				
$\text{Al}_{4-x}\text{Zr}_5$ alloy												

\* Calculated using Eq. 4, from values of lattice parameter described in [12]

◇ All works treated the alloy to 1400 °C for 24 h before final cooling step

• For simplification, we assume that the Al-Zr-rich phase, reported by other authors, corresponds to our  $\text{Al}_{4-x}\text{Zr}_5$  phase.

◆ Assumption based on provision of material by O. Senkov, as stated in their acknowledgement [14].

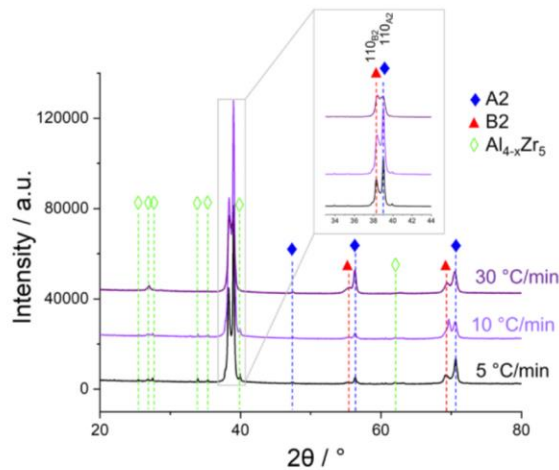


**Fig. 4.** XRD patterns of the RSA cooled at 5 °C/min (black), 10 °C/min (light purple), and 30 °C/min (dark purple). The (110) reflections of the A2 and B2 phases are magnified in the inset. The dashed lines represent the position of the peaks in the sample cooled at 5 °C/min for the A2 (blue), B2 (red), and  $\text{Al}_{4-x}\text{Zr}_5$  (green) phases.

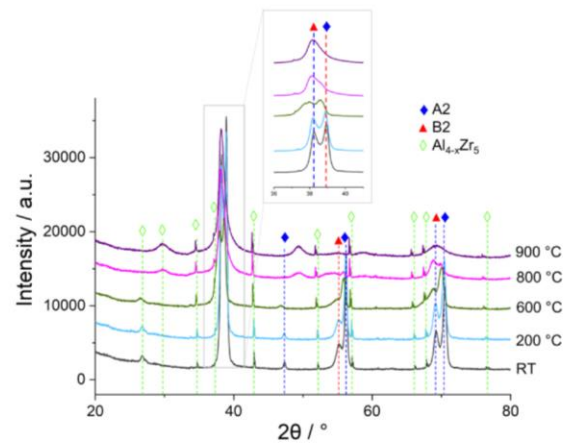


**Fig. 5.** In-situ XRD patterns of the 10-°C/min sample at different temperatures (RT, 200, 600, 800, and 900 °C). The dashed lines represent the position of the peaks in the sample at RT for the A2 (blue), B2 (red), and  $\text{Al}_{4-x}\text{Zr}_5$  (green) phases. As the temperature increases, the thermal expansion induces a peak shift towards lower angles.

**Table 4**

Lattice parameters of the A2 and B2 phases ( $a_{A2}$  and  $a_{B2}$ ) determined by XRD in the samples cooled at different rates and corresponding apparent lattice misfits. Also shown are the lattice parameters (*a*, *c*) of the Al-Zr-rich hexagonal phase. The uncertainties in "a", associated with the fit of the 2 $\theta$  peaks in the A2/B2 phases, are given by the standard deviation of several peaks for the  $\text{Al}_{4-x}\text{Zr}_5$  phase and are calculated by the laws of error propagation for the lattice misfit.

Cooling rate	Lattice parameters (Å)			Lattice misfit $\delta$ (%)
	$a_{A2}$	$a_{B2}$	$\text{Al}_{4-x}\text{Zr}_5$ , $0 \leq x \leq 1$	
5 °C/min	3.2632 ± 0.0006	3.3196 ± 0.0010	<i>a</i> = 8.0565 ± 0.0063	-1.71 ± 0.06
10 °C/min	3.2616 ± 0.0009	3.3155 ± 0.0016	<i>c</i> = 5.4504 ± 0.0119	-1.64 ± 0.09
30 °C/min	3.2689 ± 0.0033	3.3138 ± 0.0019		-1.36 ± 0.16

found to increase at a slightly higher rate than  $a_{B2}$  with increasing temperature from RT to 200 °C, thus resulting in an increase of the misfit, which becomes less negative. These variations can be explained as follows: as the atoms in an ordered intermetallic are more strongly bonded compared to a disordered solid solution with the same structure, the binding energy-vs.-distance curve of the B2 phase is expected to be narrower than that of the A2 phase. Therefore, the former should have a lower coefficient of thermal expansion than the latter [51], consistent with our experimental results and those reported in the field of Ni-based superalloys [52].

Between 200 and 600 °C,  $\delta$  strongly increases from  $-1.54 \pm 0.05$  to  $-1.23 \pm 0.27$  (see Table 5). As atomic mobilities become sufficiently large at 600 °C, diffusion becomes significant and allows microstructural changes. At 600 °C, the driving force for A2 precipitation must be large and we believe that nanoscale A2 precipitates may form within the B2 channels, similar to the precipitation of tertiary  $\gamma'$  typically observed in Ni-based superalloys in this temperature range [17,53]. However, further work is still required to confirm or discard this hypothesis.

When the temperature is further increased between 600 and 900 °C,  $\delta$  continues to increase probably due to thermal expansion and an eventual change of the A2 and B2 compositions.

Using Thermo-Calc in combination with the TCHEA3 database, we also computed the evolutions of  $a_{A2}$ ,  $a_{B2}$ , and  $\delta$  by changing the temperature, the effects of which are shown with gray, black, and red lines in Fig. 6b, respectively. Here, the colored backgrounds indicate the temperature domains in which different phases are stable, e.g., A2 + B2 +  $\sigma$  + Al<sub>3</sub>Zr<sub>4</sub> in beige. While the  $\sigma$  phase is one of the most commonly reported intermetallics in steels [54,55], Ni-based superalloys [56], HEAs [57] and compositionally complex alloys [20], this phase was not observed in the present work after cooling from high temperatures. Recently, Whitfield et al. [12] performed long-term 1000-h anneals to investigate the phase stability of the Al-Mo<sub>0.5</sub>NbTa<sub>0.5</sub>TiZr alloy between 800 and 1200 °C. The authors reported that the  $\sigma$  phase is not stable in this temperature range, indicating that the TCHEA3 database should be improved to ensure better predictions.

Since ThermoCalc predicts that the A2 and B2 phases are in equilibrium above  $\approx 750$  °C [13], the dotted beige region between 750 and 900 °C in Fig. 6a,b highlights this temperature range in which the experimental and calculated data can be compared.

The temperature-dependence of the calculated and experimental lattice misfit show opposite trends between 800 and 900 °C (compare red curves in Fig. 6a,b). This may be related to the presence of the  $\sigma$  phase in the thermodynamic calculations, which was not detected experimentally. Furthermore, in the TCHEA3 database, all

**Table 5**

Lattice parameters of the A2 and B2 phases at different temperatures, measured via *in-situ* XRD using the sample cooled at 10 °C/min.

Temperature (°C)	Lattice parameter (Å)		Lattice misfit B2/A2 (%)
	$a_{A2}$	$a_{B2}$	$\delta$
RT	$3.2616 \pm 0.0009$	$3.3155 \pm 0.0016$	$-1.64 \pm 0.09$
200	$3.2749 \pm 0.0006$	$3.3258 \pm 0.0008$	$-1.54 \pm 0.05$
600	$3.2912 \pm 0.0005$	$3.3319 \pm 0.0073$	$-1.23 \pm 0.27$
800	$3.2979 \pm 0.0027$	$3.3362 \pm 0.0016$	$-1.15 \pm 0.11$
900	$3.2970 \pm 0.0036$	$3.3342 \pm 0.0012$	$-1.12 \pm 0.13$

phases are considered as disordered even though the B2 and Al-Zr-rich phases are ordered intermetallics. That is, ThermoCalc in combination with TCHEA3 computes phase equilibria based only on phase compositions. Another reason for the discrepancies between the ThermoCalc results and our data is that ThermoCalc considers stable states at different equilibrium temperatures after long-term anneals while our samples were continuously cooled at different rates from high temperatures. The *in-situ* experiment, which led to a reduction of the apparent lattice misfit with increasing temperature, took a few minutes at each temperature and the obtained temperature-dependent lattice misfit may thus correspond to metastable states. Therefore, it cannot be directly compared with equilibrium data, nor with the long-term exposure experiment performed by Kloenne et al. [14]. Further investigations on long-term exposure are planned for a subsequent investigation. The short hold times in the *in-situ* experiment reflect rather the evolution of the lattice misfit while cooling from 900 °C to RT, which as expected shows a continuous increase in lattice misfit as the temperature is lowered.

Finally, these results demonstrate that a faster cooling rate during solidification can promote the formation of a finer and more homogeneous A2/B2 microstructure in the RSA with a more constrained lattice misfit between the A2/B2 phases.

#### 3.4. A2/B2 microstructure: origin of narrow and wide B2 channels as well as plate and cubic-shaped A2 precipitates

The A2/B2 microstructure of the AlMo<sub>0.5</sub>NbTa<sub>0.5</sub>TiZr RSA was reported to form by spinodal decomposition [10]. Based on experimental observations and phase-field simulations, the specific pathway was later proposed to occur in three steps upon cooling [45,47]: (1) congruent ordering (A2 to B2 phase); (2) spinodal decomposition of B2 into Al-Zr-rich and Mo-Nb-Ta-rich regions; and (3) disordering of Mo-Nb-Ta-rich B2 regions to A2, which form

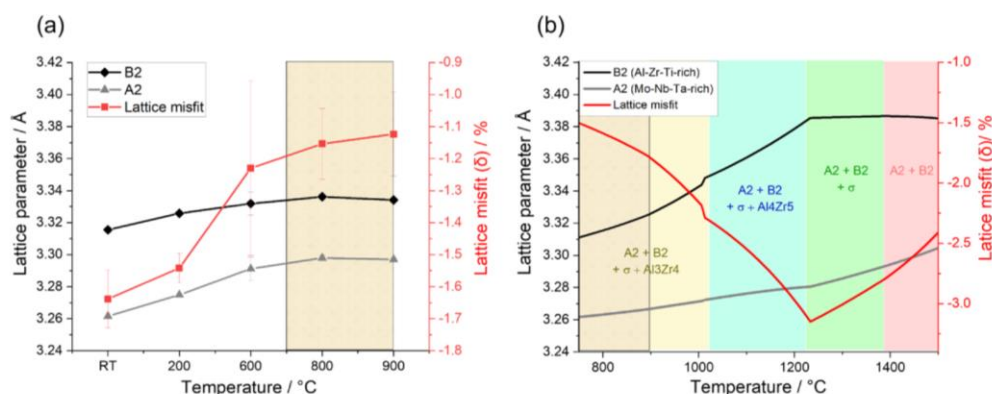


**Fig. 6.** Lattice parameters (left axis), and lattice misfit (right axis) of the A2 and B2 phases as a function of temperature. (a) Experimentally measured using *in-situ* XRD and (b) calculated using ThermoCalc (TCHEA3 database, version 2020b).



coherently embedded cuboids with edge lengths aligned along the elastically soft  $\langle 100 \rangle$  directions to minimize the elastic strain energy [11,45]. In our case, for a slow cooling rate, the structure dwells longer at higher temperatures, where the wavelength of the fastest growing concentration waves from the spinodal decomposition is longer [58] and thus the size scale of the final A2 and B2 microstructure is coarser. Hence, a slow cooling rate leads to the formation of a low number density of large A2 precipitates, as also observed in spinodally decomposed Fe-Cr alloys with a high Cr content (e.g., 40 wt% Cr) [59].

Our TEM investigations in Fig. 2 show the presence of wide and narrow B2 channels as well as cubic and plate-shaped A2 precipitates in the  $\text{AlMo}_{0.5}\text{NbTa}_{0.5}\text{TiZr}$  RSA. These features were already described by Senkov et al. [10], who reported that the large matrix channels are much more depleted in refractory elements than the narrow channels and the authors suggested that the former are too depleted in refractory elements to form the A2 precipitates. They argued that the spinodal decomposition takes place in two stages at different temperatures upon cooling: the high-temperature stage is responsible for the formation of refractory depleted wide B2 channels; during the second, low-temperature stage, thin B2 channels with higher amounts of refractory elements form. Thus, their reasoning is thermodynamic in nature [10]. Another explanation was proposed by Jensen [45] according to whom the formation of thin plate-shaped and cubic A2 precipitates in the RSA can be attributed to overlapping compositional waves on two orthogonal  $\langle 100 \rangle$  directions. His assumption is that the superposition of two orthogonal wave maxima leads to the precipitation of A2 cuboids and that of two orthogonal wave minima leads to large, squared regions of the B2 phase (e.g., see red dashed framed regions in Fig. 2d). When a wave maximum overlaps with a minimum of an orthogonal wave, it leads to the formation of thin A2 plates separated by thin B2 channels. This process thus yields a mixture of cuboidal and platelet precipitates, as well as wide regions in between, especially for slow cooling rates. However, the latter mechanism proposed by Jensen seems incomplete. Overlaps between orthogonal waves, as such, do not have fast-changing compositional variations allowing phase separation. Instead, an additional step such as that proposed by Senkov et al. [10] at these locations would be required to rapidly reach the thermal equilibrium compositions that then allow the precipitation of thin A2 platelets separated by thin B2 channels. This step may happen simultaneously with the precipitation of the main overlapping maxima and not necessarily at low temperatures. Additional

mechanisms may also play a role in shaping the microstructure of the RSA, as discussed in the following.

The three schematic drawings in Fig. 7, which were adapted from the work of Wang et al. [46], illustrate the microstructural evolution upon coarsening of a spinodally decomposed alloy with a lattice misfit between the two phases, which was described by Wang et al. [46], in the following manner: At the beginning of coarsening (Fig. 7a), the microstructure consists of a periodic array of aligned cubic precipitates with some defects. In our case this array could be found in the two incomplete rows of precipitates, highlighted by red dashed frames in Fig. 7a (described by Wang et al.) and Fig. 2f (our experimental findings). This array is reminiscent of the extra half planes of atoms associated with an edge dislocation. Thus, at the end of these rows, there is a “macrodislocation” (according to Wang et al.) in reference to its resemblance to pure edge dislocations observed edge-on at atomic resolution. As a result of coarsening, the simulations by Wang et al. showed that the extra rows of precipitates are less stable and dissolve following a process similar to dislocation climb, leading to the coarsening of the A2 precipitates as well as the B2 channel width, which were also observed in our experiment (see dashed red rectangles in Figs. 7b,c and 2 d).

Additionally, the red and green arrows in Fig. 2d-f mark doublets of parallel A2 plates and presumably octets of A2 cuboids (which we cannot capture in our 2D images), respectively, that presumably formed by the splitting of initially large cuboidal precipitates (note that the splitting is often asymmetric). These results can be rationalized based on the 2D simulations of spinodal decomposition in cubic alloys reported by Wang et al. [46], who showed that when the elastic energy contribution dominates significantly over the interfacial energy contribution, the fastest way to relax the starting non-equilibrium shape to an equilibrium one of a precipitate could be via splitting.

Therefore, we think that the heterogeneous microstructure with wide and narrow B2 channels as well as cubic and plate-shaped A2 precipitates could result from the dynamic processes, described by Wang et al. [46], associated with the complex coarsening behavior of the A2/B2 microstructure that is strongly affected by the lattice misfit between the A2/B2 phases as a function of time and temperature. The A2 platelets may either form through the mechanism proposed by Wang et al. [46], the mechanism proposed by Jensen [45], or a combination of the two. It may not, however, be ruled out that the mechanism of formation of the bimodal channel width simultaneously occurs by multiple times of

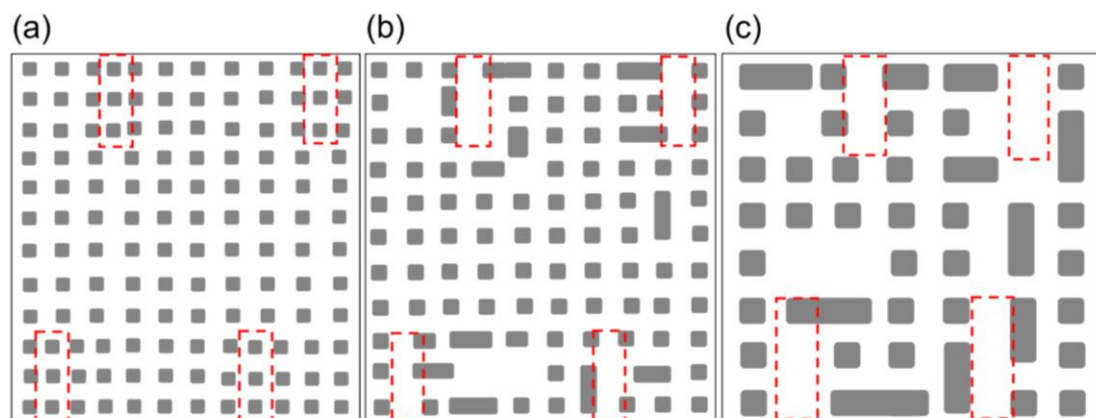


**Fig. 7.** Morphological evolutions upon coarsening in alloys undergoing an asymmetrical spinodal decomposition under a high strain energy (coherent lattice misfit) as described by Wang et al., [46], (a) beginning of the process (b) middle and (c) end of coarsening. The sketch was adapted from Figures 3b3-d3 in Ref [46].

**Table 6**

Vickers microhardness of the  $\text{AlMo}_{0.5}\text{NbTa}_{0.5}\text{TiZr}$  RSA after different cooling rates for different applied loads ranging from 1 to 30 kg. At least 19 indentation tests were performed for each condition. The proportion ( $F_c$ ) of cracks that developed at the corners of the indenter at a given load is indicated, e.g.,  $F_{cHV30} = 76/80$  means that among the 80 corners of the 20 remnant indents, 76 exhibited cracks. The uncertainties are given by the standard deviations.

State	Cooling rate ( $^{\circ}\text{C}/\text{min}$ )	Hardness (HV1)	Hardness (HV20)	Hardness (HV30)	$F_{cHV20}$	$F_{cHV30}$
Annealing + HIP	5	$629 \pm 18$	$606 \pm 12$	$592 \pm 8$	51/76	76/80
	10	$644 \pm 6$	$623 \pm 10$	$609 \pm 11$	48/76	66/80
	30	$667 \pm 11$	$652 \pm 10$	$634 \pm 11$	22/76	56/80

spinodal decomposition at different temperatures during cooling as proposed by Senkov et al. [7]. More experimental evidence is required to confirm this mechanism.

### 3.5. Influences of cooling rate and microstructure on room temperature strength

Indentation methods were employed to assess different aspects of the mechanical behavior of the RSA at different length scales. Microhardness tests with weights up to 30 kg were performed to estimate the strength of the alloy and fracture toughness averaged over several grains. Nanoindentation tests were carried out to evaluate the strength of the  $\text{Al}_{4-5}\text{Zr}_5$  hexagonal intermetallic at the grain boundaries, the strength of the A2/B2 microstructure within grains, and their contributions to the microhardness of the alloy. Table 6 summarizes the microhardness values of the RSA for different applied loads and different cooling rates. As expected, the microhardness of a given sample slightly decreases by  $\approx 6\%$  with increasing applied load from 9.8 to 294 N. This size effect arises from the fact that, as the indented volume increases with increasing applied load, the probability of finding crystalline defects or pre-existing cracks in the indented volume increases, resulting in a lower hardness. The cooling rate is found to have a similar effect on strength, i.e., the microhardness increases by 6–8%, regardless of the applied load when the cooling rate increases from  $5^{\circ}$  to  $30^{\circ}\text{C}/\text{min}$ .

Nanoindentation tests were performed with a maximum applied load of 8  $\mu\text{N}$  to evaluate the nanohardness of the hexagonal Al-Zr-rich intermetallic phase, and the A2/B2 regions for different cooling rates, cf. Table 7 and Fig. 8a. The nanohardness of the Al-Zr-rich intermetallic compound is  $\approx 60\%$  larger than that of the A2/B2 nanostructure (Fig. 8a), i.e.,  $\approx 13\text{ GPa}$  and  $\approx 8\text{ GPa}$  for the Al-Zr-rich phase and A2/B2 regions, respectively, for a cooling rate of  $30^{\circ}\text{C}/\text{min}$ . The nanohardness of the Al-Zr-rich intermetallic is approximately independent of the cooling rate because the morphology and composition of this hexagonal phase do not change with increasing cooling rate (see Fig. 1 and Table S2). In contrast, the nanohardness of the A2/B2 regions increases by  $\approx 10\%$  when the cooling rate increases from  $5^{\circ}$  to  $30^{\circ}\text{C}/\text{min}$ , which is consistent with the microhardness results. However, it is worth noting that, owing to the low applied load, the nanohardness of the A2/B2 regions is not affected by grain boundaries, the Al-Zr-rich intermetallic phase, nor pre-existing cracks, contrary to the microhardness data. This is probably the reason for the smaller effect of cooling rate on microhardness ( $\approx 6\%$ ) compared to that on nanohardness ( $\approx 10\%$ ). As the cooling rate decreases, the strength of the A2/B2 regions decreases but this effect

is mitigated by the increase in volume fraction of the hard Al-Zr-rich precipitates present at the grain boundaries.

To correlate the variation of strength with microstructural changes, we show in Fig. 8b how nanohardness depends on the mean edge length ( $d$ ) of the A2 precipitates. Here, the nanohardness decreases from 8.8 GPa to 8.0 GPa while  $d$  increases from 16 to 25 nm, respectively. This size-dependence of the nanohardness ( $H$ ) can be well described by the following empirical relationship:  $\log H = \log H_0 + s \log d$ , where  $H_0$  is a constant ( $\approx 15.8\text{ GPa}$ ) and  $s$  ( $\approx -0.2$ ) is the slope of the  $\log H$ -versus- $\log d$ -curve obtained by regression fitting of the data. It is expected that the parameters contributing to the nanohardness of the A2/B2 regions are related to the precipitate and channel sizes, the compositions of the A2 and B2 phases and the associated coherency stresses.

In the field of Ni- and Co-based superalloys, if the volume fraction of  $\gamma'$  phase remains constant, studies show that the size of the  $\gamma'$  precipitates becomes smaller by increasing the cooling rate. This results in an increase in hardness, which varies inversely with the size of the  $\gamma'$  precipitates [30,31]. This evolution can be attributed to an increase in dislocation density within the  $\gamma$  channels due to the disruption of dislocation motion by obstacles (precipitates) [31]. Since the RSA has a similar two-phase nanostructure with a cube-on-cube orientation relationship, the behavior of the bcc-structured RSA may be analogous to that of fcc-structured superalloys. However, the main difference is that, in the RSA, the matrix consists of a strong and ordered intermetallic reinforced by isolated cuboidal precipitates of a softer and disordered phase while in fcc-structured superalloys, the soft disordered matrix is reinforced by stronger ordered precipitates. Consequently, in the  $\text{AlMo}_{0.5}\text{NbTa}_{0.5}\text{TiZr}$  RSA, dislocations must nucleate in the A2 precipitates while the B2 phase is still deformed elastically, resulting in a load transfer to the stronger B2 phase. The dislocations probably glide within A2 precipitates until they are stopped at the A2/B2 interfaces where they relax the lattice misfit. Based on this scenario, there are three main contributions to the strength of the alloy: the intrinsic properties of the individual phases, the coherency stresses and an Orowan contribution ( $\tau_{\text{Orowan}} = \mu b/d$ , where  $\mu$  is the shear modulus,  $b$  the magnitude of the Burgers vector, and  $d$  is assumed as the narrowest average width within the A2 precipitates contained in the dislocation glide plane [60]). Of these three contributions, only the Orowan stress is microstructure-dependent and may be invoked to rationalize the evolution of nanohardness with the A2 size in Fig. 8b.

From the load-displacement curves obtained by nanoindentation (Fig. S9), we also determined the indentation moduli of the Al-Zr-rich intermetallic and the A2/B2 regions, see Table 7. Since the A2 precipitates and B2 channels are nanoscale (16–25 nm and 3–45 nm,

**Table 7**

Nanohardness, indentation modulus ( $E_r$ ), and elastic modulus ( $E$ ) calculated assuming a Poisson's ratio of 0.3 for each phase of the RSA after different cooling rates.

Cooling rate ( $^{\circ}\text{C}/\text{min}$ )	Nanohardness (GPa)		$E_r$ (GPa)		$E$ (GPa)	
	Al-Zr-rich phase	A2/B2	Al-Zr-rich Phase	A2/B2	Al-Zr-rich phase	A2/B2
5	$13.1 \pm 0.5$	$8.0 \pm 0.4$	$137 \pm 8$	$112 \pm 5$	$142 \pm 8$	$113 \pm 5$
10	$13.2 \pm 0.5$	$8.5 \pm 0.8$	$155 \pm 10$	$121 \pm 6$	$163 \pm 10$	$123 \pm 6$
30	$13.3 \pm 0.7$	$8.8 \pm 0.6$	$151 \pm 9$	$115 \pm 5$	$159 \pm 9$	$116 \pm 5$



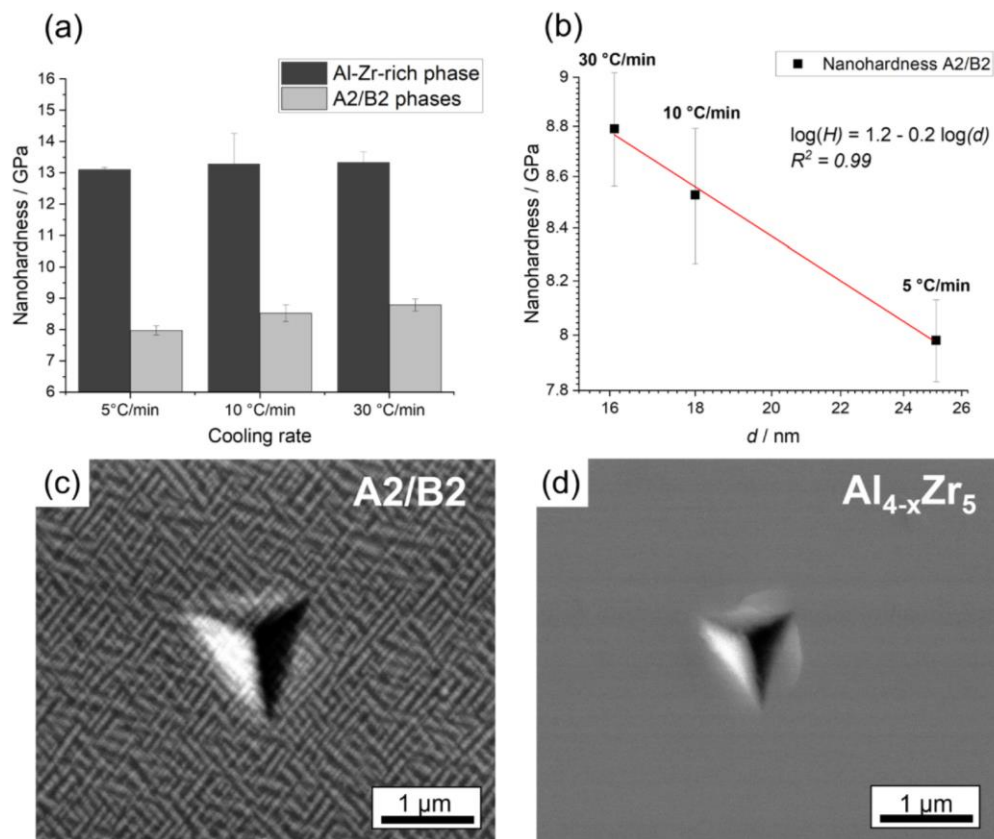


**Fig. 8.** (a) Nanohardness vs. cooling rate of different regions: within the A2/B2 substructure and the Al-Zr-rich phase, for the samples cooled at 5, 10, and 30 °C/min. (b) Nanohardness of the A2/B2 phase substructure vs. A2 precipitate mean size  $d$ . The red line in (b) represents the regression line obtained from the data. The error bars are given by the standard deviation. Representative BSE micrographs of remnant indents in the A2/B2 microstructure and the Al-Zr-rich phase are shown in (c) and (d), respectively.

respectively, see Table 2), their elastic moduli and hardness could not be measured separately by nanoindentation. Given experimental uncertainties, the indentation and Young's moduli are nearly independent of the cooling rate. The Al-Zr-rich intermetallics are  $\approx 25\%$  stiffer than the A2/B2 regions. Assuming a Poisson's ratio of 0.3, the Young's modulus of the A2/B2 regions, which constitute at least 93 vol% of the alloy depending on the cooling rate, is  $120 \pm 5$  GPa, consistent with the value reported by Senkov et al. [24] (122 GPa), which was obtained from compression tests.

### 3.6. Effect of cooling rate on fracture toughness

The fracture toughness ( $K_{IC}$ ) was estimated from the length and morphology of the cracks that formed at the corners of the micro-indenter tip. While no cracks were found after microindentation with an applied weight of 1 kg, cracks were clearly visible with higher weights of 20 and 30 kg. To estimate the fracture toughness, it is first necessary to determine the nature of the cracks. For this purpose, the ratios  $c/h$  and  $l/h$  were determined, where  $h$  is the length between the center and the corner of a remnant imprint,  $c$  is the crack length from the center of the indent to the crack tip, and  $l$  is the length between the corner of the indent and the tip of the crack, as exemplarily shown in Fig. 9. According to Niihara et al. and

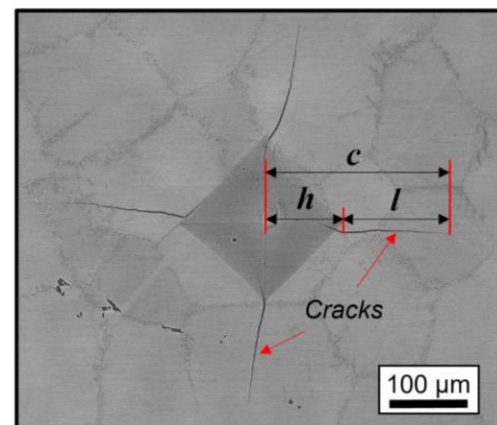


**Fig. 9.** BSE micrograph of a representative remaining Vickers indent with cracks emanating from all four corners, where  $h$  is the length of the half-diagonal of the indent and  $l$  is the crack length from the corner of the indent to the tip of the crack. The microhardness test was performed with a weight of 20 kg using an RSA cooled at 10 °C/min.

**Table 8**

Microhardness, crack length ( $l$ ), indent diagonal ( $h$ ),  $l/h$  ratio, and fracture toughness ( $K_{IC}$ ) of the RSA for the three studied cooling rates at different loads. Also shown in this table are elastic moduli determined by nanoindentation.

Cooling rate	$F$ (N)	Hardness (GPa)	$E$ (GPa)	$h$ ( $\mu\text{m}$ )	$c$ ( $\mu\text{m}$ )	$l$ ( $\mu\text{m}$ )	$l/h$	$K_{IC}$ ( $\text{MPa}\cdot\text{m}^{1/2}$ ) [a]	$K_{IC}$ ( $\text{MPa}\cdot\text{m}^{1/2}$ ) [b]
5 °C/min	294.0	5.8 ± 0.1	115.3 ± 3.3	148.2 ± 0.6	309.6 ± 35.4	171.8 ± 36.5	1.2 ± 0.2	4.6 ± 0.5	4.6 ± 0.5
	196.0	5.9 ± 0.1		119.7 ± 1.1	264.7 ± 41.4	157.9 ± 40.2	1.3 ± 0.3	4.0 ± 0.5	3.9 ± 0.5
10 °C/min	294.0	6.0 ± 0.1	123.9 ± 3.4	144.0 ± 2.0	342.2 ± 54.4	212.4 ± 48.8	1.5 ± 0.3	4.5 ± 0.5	4.4 ± 0.5
	196.0	6.1 ± 0.1		116.0 ± 1.0	273.8 ± 29.7	168.7 ± 26.8	1.5 ± 0.3	3.8 ± 0.5	3.9 ± 0.4
30 °C/min	294.0	6.2 ± 0.1	116.2 ± 2.6	141.9 ± 1.3	348.1 ± 46.4	221.9 ± 40.8	1.6 ± 0.3	-	4.2 ± 0.4
	196.0	6.4 ± 0.1		115.9 ± 0.6	278.2 ± 20.1	175.6 ± 22.4	1.5 ± 0.2	-	3.8 ± 0.3

[a] considering only the indentations for which four primary cracks emanated straight and radially from each corner. When no value is provided, it means that there were no indentations with four primary cracks.

[b] considering all indentations that contained at least one crack emanating from a corner.

Schiffmann [39,61], the cracks either have a half-penny shape that joins the tips of two cracks located on opposite sides of the indent when  $c/h \geq 2.5$  (the total length of a half-penny crack projected on the sample surface corresponds to  $2c$ ) or they are of Palmqvist type when  $0.25 \leq l/h \leq 2.5$ , i.e., they are much shorter and form circular arcs right below the visible cracks (projected length of each crack:  $l$ ).

In this study, since  $0.25 \leq l/h \leq 2.5$  in the  $\text{AlMo}_{0.5}\text{NbTa}_{0.5}\text{TiZr}$  RSA, the cracks are of Palmqvist type and the fracture toughness  $K_{IC}$ , also known as indentation fracture resistance [62] can be calculated using:

$$K_{IC} = A \left( \frac{E}{H} \right)^{2/5} \frac{P}{h^{1/2}} \quad (5)$$

where factor  $A$  is a constant equal to 0.009.  $E$  is the elastic modulus obtained from the nanoindentation tests,  $H$  is the measured microhardness, and  $P$  is the indentation load. The parameters in Eq. 5 required to compute  $K_{IC}$  are listed in Table 8 for the samples cooled at different rates. The fracture toughness ( $K_{IC}$ ) of the RSA was calculated using two different criteria. In the first case [a], we only considered at least five remnant indents with cracks emanating from each corner following the standard test method ISO 21618 [40], see  $K_{IC}$  [a] in Table 8. In the second case [b], all the indents (10–15 independent measurements) that showed at least one crack were considered to

estimate  $K_{IC}$  [b]. Given the experimental errors, the average  $K_{IC}$  value of  $4.2 \pm 0.4$  is not significantly affected by criteria [a] and [b], the applied load, and cooling rate, see Table 8.

Additionally, we estimated in Table 6 another parameter that is related to the fracture toughness, i.e., the fraction of cracks ( $F_c$ ) observed at the corners of the remnant microindents as described in Section 2.2. The fraction of cracks is found to increase with increasing applied load for a given cooling rate. We believe that this is related to a sampling effect, i.e., the larger the applied load, the greater the indented volume, and the higher the likelihood to nucleate a crack at a defect.  $F_c$  decreases with increasing cooling rate. There may be two microstructural features that contribute to this phenomenon. First, as the cooling rate increases, the precipitation of the brittle Al-Zr-rich intermetallic at grain boundaries is progressively suppressed. Second, as the size of the A2 precipitates decreases at an increased cooling rate, the density of A2/B2 interfaces, which may impede crack nucleation and propagation, increases.

With all this new data, the alloy can now be compared to other material classes. The Ashby plot displayed in Fig. 10 shows the fracture toughness as a function of Vickers microhardness for different groups of engineering materials. These groups, marked with gray areas, include foams, elastomers, polymers, composites, technical and non-technical ceramics, glasses, and engineering alloys as well as other bcc-structured alloys that are highlighted in color. For

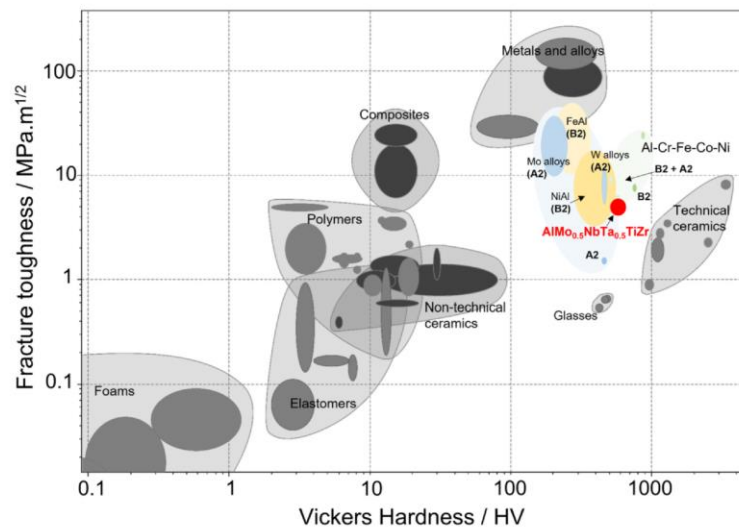


**Fig. 10.** Ashby plot, obtained with the Granta Edupack software, of different engineering materials showing their fracture toughness vs. Vickers microhardness. The red area highlights the  $\text{AlMo}_{0.5}\text{NbTa}_{0.5}\text{TiZr}$  RSA investigated in the present study. The other colored regions correspond to other bcc-structured alloys.



**Table 9**

Mechanical properties at RT (Vickers hardness and fracture toughness) of different alloys and intermetallics with bcc structures reported in the literature.

Alloys	Structure	Hardness (HV)	Fracture toughness (MPa·m <sup>1/2</sup> )	Method	Reference
NiAl	B2	330 [63]	5.08 – 6.42	Vickers indentation (ring on ring disk bend test)	[65]
NiAl	B2	460–560 (4.5–5.5 GPa) [64]	10.6 – 14.8	Fatigue tests of pre-cracked specimens following the ASTM E399 standard	[66]
NiAl	B2		13.0 – 17.0	Double cantilever beam	[67]
Ni-50Al	B2		3.79 – 9.31	Fatigue tests of pre-cracked specimens following the ASTM E399 standard	[68]
Ni-46Al			3.00 – 3.09		
Fe40Al	B2 + A2 Fe (Al)	867	23.8	Vickers indentation	[69]
Co-40Al	B2		2.20	Fatigue tests of pre-cracked specimens following the ASTM E399 standard	[68]
Co-49Al			3.08		
Fe-40Al	B2	197–380 [70]	33.3 – 55.8		[68]
Fe-48Al			11.7		
W and some W-alloy	A2	367–389 [71]	5.4 – 13.5		[72]
Molybdenum-base alloys					
TZM-Mo	A2	230–262 [73]	10.0 – 27.5		[74]
ODS-Mo			27.8 – 147.32		
LCAC			14.6 – 38.5		
Al <sub>23</sub> Co <sub>15</sub> Cr <sub>23</sub> Cu <sub>8</sub> Fe <sub>15</sub> Ni <sub>15</sub>	A2 + B2 + fcc	545 (5.3 GPa)	5.8	Pre-cracked ASTM E399	[67]
			5.4	Chevron notched rectangular bar (CVNRB)	
Al <sub>18</sub> Cr <sub>21</sub> Fe <sub>20</sub> Co <sub>20</sub> Ni <sub>21</sub>	A2 + B2 + fcc	508	9.0	Pre-cracked ASTM E399	[75]
FeCoNiCrAl <sub>3</sub>	B2	740	7.6	Vickers indentation	[76]
Nb <sub>25</sub> Mo <sub>25</sub> Ta <sub>25</sub> W <sub>25</sub>	A2	455 (4.46 GPa) [77]	1.6	Bending of notched micro-cantilever	[78]
HfNbTaTiZr	A2	509 [79]	210	Single specimen compliance method for J-integral measurement (ASTM E1820–17 standard)	[80]
AlCuTaVW	two fcc + B2	1326 (13 GPa)	8.36	Vickers indentation	[81]

instance, the toughness/hardness combination of the Al-Mo<sub>0.5</sub>NbTa<sub>0.5</sub>TiZr RSA (red dot in Fig. 10, present work) is compared to those of B2 intermetallics (NiAl and FeAl, orange areas), single-phase A2 metals and alloys (blue regions), and two-phase A2/B2 compositionally complex alloys from the Al-Cr-Fe-Co-Ni system (green) and the corresponding data is summarized in Table 9. As shown in Fig. 10, the fracture toughness and Vickers hardness of the RSA are intermediate between those of technical ceramics and engineering alloys. However, its toughness/hardness combination is similar to those of B2 intermetallics and two-phase A2/B2 alloys.

#### 4. Conclusion and summary

In the present work, the effects of the cooling rate on microstructure, hardness, and fracture toughness of AlMo<sub>0.5</sub>NbTa<sub>0.5</sub>TiZr RSA were investigated. From our results, it can be concluded that increasing the cooling rate produces a finer and more homogeneous A2/B2 substructure and suppresses grain boundary precipitation of the hexagonal Al<sub>4-x</sub>Zr<sub>5</sub> intermetallic phase, which improves the hardness of the alloy but does not reduce its brittleness. Some of the key findings can be summarized as follows:

1. The volume fraction of the hexagonal Al<sub>4-x</sub>Zr<sub>5</sub> intermetallic compound can be reduced to < 1 % with a cooling rate of at least 30 °C/min. In contrast, the relative volume fractions of the A2 and B2 phases remain approximately unaffected by the cooling rate. The nanohardnesses of the Al<sub>4-x</sub>Zr<sub>5</sub> intermetallic and A2/B2 regions are ≈ 13 and 8–9 GPa, respectively.
2. The cooling rate affects the size, aspect ratio, and size distribution of the A2 cuboidal precipitates. When the cooling rate increases from 5° to 30°C/min, the size of the A2 precipitates decreases from 25 to 16 nm, resulting in an increase in microhardness of ≈ 6 % (averaged over different phases and grains). In addition, a high cooling rate promotes the formation of more cubic precipitates while they are elongated and form slabs at lower cooling rates.

The cooling rate does not affect the composition of the A2 and B2 phases.

3. While the lattice parameter of the hexagonal Al-Zr-rich phase is unaffected by the cooling rate, those of the A2 and B2 phases become more similar with an increasing cooling rate, thus resulting in a decrease of the constrained lattice misfit.
4. With increasing temperature, the lattice parameter of the A2 phase expands at a higher rate than that of the B2 phase, owing to a higher coefficient of thermal expansion of the former, thus resulting in a decrease of the lattice misfit, which becomes less negative.
5. The fracture toughness  $K_{IC} = 4.2 \pm 0.4$  MPa·m<sup>1/2</sup> of the RSA is independent of the cooling rate and its value is comparable to that of most B2 intermetallics and two-phase A2/B2 alloys reported in the literature. From a general viewpoint, the fracture toughness of the RSA lies between that of engineering alloys and ceramics.

While this paper focuses on the room temperature properties of the RSA, it is important to note that the tensile properties at high temperatures are also critical for its potential use in structural applications. Therefore, results of tensile creep tests will be presented in a subsequent contribution, which will provide a more complete picture of the suitability of the alloy for high-temperature applications.

#### CRedit authorship contribution statement

**Patricia Suárez Ocano:** Experimental methodology, Formal analysis, Data curation, Writing – original draft. **Anna Manzoni:** XRD and *in-situ* XRD analysis, Methodology, Writing – review & editing. **Inmaculada Lopez-Galilea** and **Benjamin Ruttart:** Methodology (HIP treatment), Writing – review & editing. **Guillaume Laplanche:** Conceptualization, Methodology, Writing – review & editing, Supervision. **Leonardo Agudo Jácome:** Conceptualization,

P. Suárez Ocaño, A. Manzoni, I. Lopez-Galilea et al.

Journal of Alloys and Compounds 949 (2023) 169871

Methodology, TEM measurements, Formal analysis, Writing – review & editing, Supervision and Funding acquisition.

#### Data availability

Data will be made available on request.

#### Declaration of Competing Interest

The authors declare that they have no known competing financial interests or personal relationships that could have appeared to influence the work reported in this paper.

#### Acknowledgements

PSO, LAJ and GL acknowledge funding through projects n°. 398838389 and LA/3607-2, respectively, from the Deutsche Forschungsgemeinschaft (DFG). ILG acknowledge the DFG for the funding through project No. 503229465 and the Collaborative Research Center SFB/TR 103 (Project T4). The authors thank Stephan Laube, Dr. Alexander Kaufmann, Prof. Martin Heilmaier, at KIT for the fabrication of the alloy as well as Prof. Theisen at RUB for HIP treatment. The authors acknowledge Steffen Thärig, Christine Krimmling, and Dr. Birgit Rehmer, and Oliver Schwarze at BAM for assistance with the microhardness and nanoindentation tests, respectively. The authors acknowledge R. Schwidessen and M. Tovar for helping in performing the *in-situ* X-ray diffraction experiments and the HZB X-ray Core Lab. Parts of this work were performed at the electron microscopy center at BAM. PSO acknowledge Suzana G. Fries at RUB and Huahai Mao at Thermocalc for valuable opinions about the CALPHAD analysis. The authors acknowledge Prof. Yunzhi Wang for the fruitful discussion on the microstructural mechanisms.

#### Appendix A. Supporting information

Supplementary data associated with this article can be found in the online version at doi:10.1016/j.jallcom.2023.169871.

#### References

- B.Q. Chen, L.C. Zhuo, Latest progress on refractory high entropy alloys: composition, fabrication, post processing, performance, simulation and prospect, *Int. J. Refract Met Hard Mater.* 110 (2023), <https://doi.org/10.1016/j.jrmhm.2022.105993>
- S.K. Dewangan, A. Mangish, S. Kumar, A. Sharma, B. Ahn, V. Kumar, A review on high-temperature applicability: a milestone for high entropy alloys, *Eng. Sci. Technol.* 35 (2022), <https://doi.org/10.1016/j.jestch.2022.101211>
- S. Naka, Development of intermetallic materials for structural applications: toward designing multi-constituent and/or multi-phase alloys, *J. Phys. IV C (2)* (1996) 147–152, <https://doi.org/10.1051/jp4:1996220>
- M. Wang, Z.L. Ma, Z.Q. Xu, X.W. Cheng, Designing VxNbMoTa refractory high-entropy alloys with improved properties for high-temperature applications, *Scr. Mater.* 191 (2021) 131–136, <https://doi.org/10.1016/j.scriptamat.2020.09.027>
- W.J. Huang, X.J. Wang, J.W. Qiao, Y.C. Wu, Microstructures and mechanical properties of TiZrHfNbTaWx refractory high entropy alloys, *J. Alloy Compd.* 914 (2022), <https://doi.org/10.1016/j.jallcom.2022.165187>
- H.J. Zhang, Y.H. Du, L.M. Lai, N. Guo, N. Li, S.F. Guo, The as-cast Al<sub>3</sub>CrTaTi refractory medium entropy alloys with good room-temperature mechanical properties and high-temperature oxidation resistance, *J. Alloy Compd.* 932 (2023), <https://doi.org/10.1016/j.jallcom.2022.167675>
- D.B. Miracle, M.H. Tsai, O.N. Senkov, V. Soni, R. Banerjee, Refractory high entropy superalloys (RSAs), *Scr. Mater.* 187 (2020) 445–452, <https://doi.org/10.1016/j.scriptamat.2020.06.048>
- O.N. Senkov, S. Gorsse, D.B. Miracle, High temperature strength of refractory complex concentrated alloys, *Acta Mater.* 175 (2019) 394–405, <https://doi.org/10.1016/j.actamat.2019.06.032>
- J. Startt, A. Kustas, J. Pegues, P. Yang, R. Dingreville, Compositional effects on the mechanical and thermal properties of MoNbTaTi refractory complex concentrated alloys, *Mater. Des.* 213 (2022), <https://doi.org/10.1016/j.matdes.2021.110311>
- O. Senkov, D. Isheim, D. Seidman, A. Pilchak, Development of a refractory high entropy superalloy, *Entropy* 18 (3) (2016) 102, <https://doi.org/10.3390/e18030102>
- J.K. Jensen, B.A. Welk, R.E.A. Williams, J.M. Sosa, D.E. Huber, O.N. Senkov, G.B. Viswanathan, H.L. Fraser, Characterization of the microstructure of the compositionally complex alloy Al<sub>1</sub>Mo<sub>0.5</sub>Nb<sub>1</sub>Ta<sub>0.5</sub>Ti<sub>1</sub>Zr<sub>1</sub>, *Scr. Mater.* 121 (2016) 1–4, <https://doi.org/10.1016/j.scriptamat.2016.04.017>
- T.E. Whitfield, H.J. Stone, C.N. Jones, N.G. Jones, Microstructural degradation of the AlMo<sub>0.5</sub>NbTa<sub>0.5</sub>TiZr refractory metal high-entropy superalloy at elevated temperatures, *Entropy* 23 (1) (2021) 80, <https://doi.org/10.3390/e23010080>
- P. Suárez Ocaño, S.G. Fries, I. Lopez-Galilea, R.D. Kamachali, J. Roik, L. Agudo Jácome, The AlMo<sub>0.5</sub>NbTa<sub>0.5</sub>TiZr refractory high entropy superalloy: experimental findings and comparison with calculations using the CALPHAD method, *Mater. Des.* 217 (2022) 110593, <https://doi.org/10.1016/j.matdes.2022.110593>
- Z.T. Kloenne, J.-P. Couzinié, M. Heczko, R. Gröger, G.B. Viswanathan, W.A.T. Clark, H.L. Fraser, On the bcc/B2 interface structure in a refractory high entropy alloy, *Scr. Mater.* 223 (2023) 115071, <https://doi.org/10.1016/j.scriptamat.2022.115071>
- M.J. Mehl, D. Hicks, C. Toher, O. Levy, R.M. Hanson, G. Hart, S. Curtarolo, The AFLOW library of crystallographic prototypes: part 1, *Comp. Mater. Sci.* 136 (2017) S1–S828, <https://doi.org/10.1016/j.commatsci.2017.01.017>
- L.A. Morales, N. Luo, K. Li, C.H. Zenk, C. Korner, On stabilizing an  $\alpha/\alpha'$  microstructure in ferritic superalloys, *J. Alloy. Compd.* 911 (2022) 164996, <https://doi.org/10.1016/j.jallcom.2022.164996>
- R.C. Reed, K.A. Green, P. Caron, T.P. Gabb, M.G. Fahrman, E.S. Huron, S.A. Woodard, *Superalloys 2008*, TMS, Warrendale PA, 2008. doi: 10.1017/S0001924000087509.
- J.L. Li, Z. Li, Q. Wang, C. Dong, P.K. Liaw, Phase-field simulation of coherent BCC/B2 microstructures in high entropy alloys, *Acta Mater.* 197 (2020) 10–19, <https://doi.org/10.1016/j.actamat.2020.07.030>
- N. Yurchenko, E. Panina, A. Tojibaev, V. Novikov, G. Salishchev, S. Zherbetsov, N. Stepanov, Effect of B2 ordering on the tensile mechanical properties of refractory Al<sub>3</sub>Nb<sub>40</sub>Ti<sub>40</sub>V<sub>20-x</sub> medium-entropy alloys, *J. Alloy Compd.* 937 (2023), <https://doi.org/10.1016/j.jallcom.2022.168465>
- A. Asabre, P. Gemagami, A.B. Parsa, C. Wagner, A. Kostka, G. Laplanche, Influence of Mo/Cr ratio on the lamellar microstructure and mechanical properties of as-cast Al<sub>0.75</sub>CoCrFeNi compositionally complex alloys, *J. Alloy. Compd.* 899 (2022) 163183, <https://doi.org/10.1016/j.jallcom.2021.163183>
- J.Y. Pang, H.W. Zhang, L. Zhang, Z.W. Zhu, H.M. Fu, H. Li, A.M. Wang, Z.K. Li, H.F. Zhang, Simultaneous enhancement of strength and ductility of body-centered cubic TiZrNb multi-principal element alloys via boron-doping, *J. Mater. Sci. Technol.* 78 (2021) 74–80, <https://doi.org/10.1016/j.jmst.2020.10.043>
- Y.G. Dong, S. Chen, N.N. Jia, Q.H. Zhang, L. Wang, Y.F. Xue, K. Jin, Microstructures and mechanical properties of Ta-Nb-Zr-Ti-Al refractory high entropy alloys with varying Ta/Ti ratios, *Tungsten* 3 (4) (2021) 406–414, <https://doi.org/10.1007/s42864-021-00111-8>
- T.E. Whitfield, G.J. Wise, H.J. Stone, N.G. Jones, The influence of the Nb:Ta ratio on the microstructural evolution in refractory metal superalloy systems, *Appl. Phys. Lett.* 119 (21) (2021), <https://doi.org/10.1063/5.0068045>
- O.N. Senkov, J.K. Jensen, A.L. Pilchak, D.B. Miracle, H.L. Fraser, Compositional variation effects on the microstructure and properties of a refractory high-entropy superalloy AlMo<sub>0.5</sub>NbTa<sub>0.5</sub>TiZr, *Mater. Des.* 139 (2018) 498–511, <https://doi.org/10.1016/j.matdes.2017.11.033>
- V. Soni, O.N. Senkov, B. Gwalani, D.B. Miracle, R. Banerjee, Microstructural design for improving ductility of an initially brittle refractory high entropy alloy, *Sci. Rep.* 8 (2018), <https://doi.org/10.1038/s41598-018-27144-3>
- X. Liu, K. Vecchio, Processing, microstructure evolution and mechanical property improvements of an Al-V-Cr-Mn-Fe-Ni CCA with an as-cast BCC/B2 coherent nanostructure, *Mater. Sci. Eng. a Struct.* 852 (2022), <https://doi.org/10.1016/j.msea.2022.143698>
- Z.J. Xu, Z.T. Li, Y. Tong, W.D. Zhang, Z.G. Wu, Microstructural and mechanical behavior of a CoCrFeNiCu<sub>4</sub> non-equiatomic high entropy alloy, *J. Mater. Sci. Technol.* 60 (2021) 35–43, <https://doi.org/10.1016/j.jmst.2020.03.078>
- M. Wischi, K.N. Campo, L.F. Starck, E.B. da Fonseca, S.N. Lopes, R. Caram, Microstructure and mechanical behavior of the directionally solidified AlCoCrFeNi<sub>21</sub> eutectic high-entropy alloy, *J. Mater. Res Technol.* 20 (2022) 811–820, <https://doi.org/10.1016/j.jmrt.2022.07.065>
- X. Wang, W. Zhai, J.Y. Wang, B. Wei, Strength and ductility enhancement of high-entropy FeCoNi<sub>2</sub>Al<sub>0.9</sub> alloy by ultrasonically refining eutectic structures, *Scr. Mater.* 225 (2023), <https://doi.org/10.1016/j.scriptamat.2022.115154>
- M.A. Ali, I. López-Galilea, S. Gao, B. Ruttart, W. Amin, O. Shchyglo, A. Hartmaier, W. Theisen, I. Steinbach, Effect of  $\gamma'$  precipitate size on hardness and creep properties of Ni-base single crystal superalloys: experiment and simulation, *Materialia* 12 (2020) 100692, <https://doi.org/10.1016/j.mtla.2020.100692>
- H.R. Abedi, O.A. Ojo, X. Cao, Effect of cooling rate on precipitation behavior of gamma prime in a newly developed co-based superalloy, *JOM* 72 (2020) 4054–4059, <https://doi.org/10.1007/s11837-020-04241-1>
- H.L. Huang, Y. Sun, P.P. Cao, Y. Wu, X.J. Liu, S.H. Jiang, H. Wang, Z.P. Lu, On cooling rates dependence of microstructure and mechanical properties of refractory high-entropy alloys HfTaTiZr and HfNbTiZr, *Scr. Mater.* 211 (2022), <https://doi.org/10.1016/j.scriptamat.2022.114506>
- W. Lonski, M. Spilka, M. Kadziolka-Gawel, P. Gebara, A. Radon, T. Warski, K. Mlynarek-Zak, R. Babilas, The effect of cooling rate on the structure and selected properties of AlCoCrFeNiSi<sub>x</sub> (x=0; 0.25; 0.5; 0.75) high entropy alloys, *J. Alloy Compd.* 905 (2022), <https://doi.org/10.1016/j.jallcom.2022.164074>
- A. Munitz, S. Salhov, G. Guttman, N. Derimow, M. Nahmany, Heat treatment influence on the microstructure and mechanical properties of AlCrFeNiTi<sub>0.5</sub> high entropy alloys, *Mater. Sci. Eng. a Struct.* 742 (2019) 1–14, <https://doi.org/10.1016/j.msea.2018.10.114>



- [35] K. Xiong, L. Huang, X.F. Wang, L. Yu, W. Feng, Cooling-rate effect on microstructure and mechanical properties of  $\text{Al}_{0.5}\text{CoCrFeNi}$  high-entropy alloy, *Metals* 12 (8) (2022), <https://doi.org/10.3390/met12081254>
- [36] A.C. Fischer-Cripps, *Nanoindentation*, Springer, New South Wales, Australia, 2011, <https://doi.org/10.1007/978-1-4757-5943-3>
- [37] W.C. Oliver, G.M. Pharr, An improved technique for determining hardness and elastic-modulus using load and displacement sensing indentation experiments, *J. Mater. Res.* 7 (1992) 1564–1583, <https://doi.org/10.1557/JMR.1992.1564>
- [38] Y.L. Shen, Handbook of mechanics of materials, in: S. Schmauder, C.S. Chen, K. Chawla, N. Chawla, W. Chen, Y. Kagawa (Eds.), *Nanoindentation for Testing Material Properties*, Springer, Singapore, 2019, pp. 1981–2012, [https://doi.org/10.1007/978-981-10-6884-3\\_46](https://doi.org/10.1007/978-981-10-6884-3_46)
- [39] K. Niihara, R. Morena, D.P.H. Hasselman, Evaluation of  $K_{Ic}$  of brittle solids by the indentation method with low crack-to-indent ratios, *J. Mater. Sci. Lett.* 1 (1) (1982) 13–16, <https://doi.org/10.1007/Bf00724706>
- [40] Fine ceramics (advanced ceramics, advanced technical ceramics), Test Method for Fracture Resistance of Monolithic Ceramics at Room Temperature by Indentation Fracture (IF) Method, International Standard ISO 21618, 2019, 4–9.
- [41] Standard Test Methods for Determining Average Grain Size, ASTM Designation: E112, 2013. doi:
- [42] J. Schindelin, I. Arganda-Carreras, E. Frise, V. Kaynig, M. Longair, T. Pietzsch, S. Preibisch, C. Rueden, S. Saalfeld, B. Schmid, J.Y. Tinevez, D.J. White, V. Hartenstein, K. Eliceiri, P. Tomancak, A. Cardona, Fiji: an open-source platform for biological-image analysis, *Nat. Methods* 9 (7) (2012) 676–682, <https://doi.org/10.1038/nmeth.2019>
- [43] W. Kraus, G. Nolze, POWDER CELL - a program for the representation and manipulation of crystal structures and calculation of the resulting X-ray powder patterns, *J. Appl. Crystallogr.* 29 (1996) 301–303, <https://doi.org/10.1107/S0021889895014920>
- [44] H.L. Chen, H.H. Mao, Q. Chen, Database development and Calphad calculations for high entropy alloys: challenges, strategies, and tips, *Mater. Chem. Phys.* 210 (2018) 279–290, <https://doi.org/10.1016/j.matchemphys.2017.07.082>
- [45] J.K. Jensen, Characterization of a high strength, refractory high entropy alloy,  $\text{AlMo}_{0.5}\text{NbTa}_{0.5}\text{TiZr}$ , *Mater. Sci. Eng. Ohio State Univ.* (2017) 227.
- [46] Y. Wang, L.Q. Chen, A.G. Khachatryan, Kinetics of strain-induced morphological transformation in cubic alloys with a miscibility gap, *Acta Metall.* 41 (1) (1993) 279–296, [https://doi.org/10.1016/0956-7151\(93\)90359-Z](https://doi.org/10.1016/0956-7151(93)90359-Z)
- [47] K. Kadirvel, Z. Kloenne, J.K. Jensen, H. Fraser, Y.Z. Wang, Phase-field modelling of transformation pathways and microstructural evolution in multi-principal element alloys, *Appl. Phys. Lett.* 119 (17) (2021) 171905, <https://doi.org/10.1063/5.0065522>
- [48] Y. Ma, B. Jiang, C. Li, Q. Wang, C.D. 1, P.K. Liaw, F. Xu, Lixian, The BCC/B2 morphologies in  $\text{Al}_x\text{NiCoFeCr}$  high-entropy alloys, *Metals* 7 (2017) 57, <https://doi.org/10.3390/met7020057>
- [49] M. Akhlaghi, T. Steiner, S.R. Meka, E.J. Mittemeijera, Misfit-induced changes of lattice parameters in two phase systems: coherent/incoherent precipitates in a matrix, *J. Appl. Crystallogr.* 49 (2016) 69–77, <https://doi.org/10.1107/S1600576715022608>
- [50] H. Mughrabi, The importance of sign and magnitude of  $\gamma/\gamma'$  lattice misfit in superalloys-with special reference to the new  $\gamma'$ -hardened cobalt-base superalloys, *Acta Mater.* 81 (2014) 21–29, <https://doi.org/10.1016/j.actamat.2014.08.005>
- [51] D.A. Porter, K.E. Easterling, M.Y. Sherif, *Phase Transformations in Metals and Alloys*, CRC Press, 2009.
- [52] A.J. Goodfellow, L.R. Owen, K.A. Christofidou, J. Kelleher, M.C. Hardy, H.J. Stone, The effect of temperature and Mo content on the lattice misfit of model Ni-based superalloys, *Metals* 9 (6) (2019) 700, <https://doi.org/10.3390/met9060700>
- [53] M.P. Jackson, R.C. Reed, Heat treatment of UDIMET 720Li: the effect of microstructure on properties, *Mater. Sci. Eng. A* 259 (1) (1999) 85–97, [https://doi.org/10.1016/S0921-5093\(98\)00867-3](https://doi.org/10.1016/S0921-5093(98)00867-3)
- [54] M. Schwind, J. Kallqvist, J.O. Nilsson, J. Agren, H.O. Andren,  $\sigma$ -phase precipitation in stabilized austenitic stainless steels, *Acta Mater.* 48 (10) (2000) 2473–2481, [https://doi.org/10.1016/S1359-6454\(00\)00699-0](https://doi.org/10.1016/S1359-6454(00)00699-0)
- [55] Y.S. Sato, H. Kokawa, Preferential precipitation site of sigma phase in duplex stainless steel weld metal, *Scr. Mater.* 40 (6) (1999) 659–663, [https://doi.org/10.1016/S1359-6462\(98\)00483-7](https://doi.org/10.1016/S1359-6462(98)00483-7)
- [56] C.M.F. Rae, R.C. Reed, The precipitation of topologically close-packed phases in rhenium-containing superalloys, *Acta Mater.* 49 (19) (2001) 4113–4125, [https://doi.org/10.1016/S1359-6454\(01\)00265-8](https://doi.org/10.1016/S1359-6454(01)00265-8)
- [57] F. Otto, A. Dlouhý, K.G. Pradeep, M. Kubšnová, D. Raabe, G. Eggeler, E.P. George, Decomposition of the single-phase high-entropy alloy CrMnFeCoNi after prolonged anneals at intermediate temperatures, *Acta Mater.* 112 (2016) 40–52, <https://doi.org/10.1016/j.actamat.2016.04.005>
- [58] J.W. Cahn, J.E. Hilliard, Free energy of a nonuniform system. I. Interfacial Free Energy, *J. Chem. Phys.* 28 (2) (1958) 258–267, <https://doi.org/10.1063/1.1744102>
- [59] X. Xu, J. Odqvist, M.H. Colliander, S. King, M. Thuvander, A. Steuwer, P. Hedström, Effect of cooling rate after solution treatment on subsequent phase separation during aging of Fe-Cr alloys: a small-angle neutron scattering study, *Acta Mater.* 134 (2017) 221–229, <https://doi.org/10.1016/j.actamat.2017.06.001>
- [60] G. Kosterz, H.A. Calderon, J.L. Martin, Fundamental Aspects of Dislocation Interactions: Low-Energy Dislocation Structures III, *Mater. Sci. Eng. A Structural Materials Properties Microstructure and Processing* Ascona, Switzerland, 1993. doi: 10.1016/C2013-0-12062-4.
- [61] K.I. Schiffmann, Determination of fracture toughness of bulk materials and thin films by nanoindentation: comparison of different models, *Philos. Mag.* 91 (7–9) (2011) 1163–1178, <https://doi.org/10.1080/14786435.2010.487984>
- [62] G.D. Quinn, Fracture toughness of ceramics by the vickers indentation crack length method: a critical review, *Ceram. Eng. Sci. Proc.* 27 (2) (2007) 45–62, <https://doi.org/10.1002/9780470291313.ch5>
- [63] T. Haubold, R. Bohn, R. Birringer, H. Gleiter, Nanocrystalline intermetallic compounds—structure and mechanical properties, in: Proceedings of the Second International ASM Conference on High Temperature Aluminides and Intermetallics, High Temperature Aluminides and Intermetallics San Diego, CA, USA, 1992, 679–683.
- [64] T. Chen, J.M. Hampikian, N.N. Thadhani, Synthesis and characterization of mechanically alloyed and shock-consolidated nanocrystalline NiAl intermetallic, *Acta Mater.* 47 (8) (1999) 2567–2579, [https://doi.org/10.1016/S1359-6454\(99\)00059-2](https://doi.org/10.1016/S1359-6454(99)00059-2)
- [65] T. Kim, K.T. Hong, K.S. Lee, The relationship between the fracture toughness and grain boundary character distribution in polycrystalline NiAl, *Intermetallics* 11 (2003) 33–39, [https://doi.org/10.1016/S0966-9795\(02\)00167-X](https://doi.org/10.1016/S0966-9795(02)00167-X)
- [66] J.W. Hoehn, S.K. Venkataraman, H. Huang, W.W. Gerberich, Micromechanical toughness test applied to NiAl, *Mater. Sci. Eng. A* 192 (1995) 301–308, [https://doi.org/10.1016/0921-5093\(94\)03259-9](https://doi.org/10.1016/0921-5093(94)03259-9)
- [67] U. Roy, H. Roy, H. Daoud, U. Glatzel, K.K. Ray, Fracture toughness and fracture micromechanism in a cast  $\text{AlCoCrCuFeNi}$  high entropy alloy system, *Mater. Lett.* 132 (2014) 186–189, <https://doi.org/10.1016/j.matlet.2014.06.067>
- [68] K.M. Chang, R. Darolia, H.A. Lipsitt, Cleavage fracture in B2 aluminides, *Acta Metall.* 10 (1992) 2727–2737, [https://doi.org/10.1016/0956-7151\(92\)90343-D](https://doi.org/10.1016/0956-7151(92)90343-D)
- [69] X.T. Luo, C.J. Li, Dual-scale oxide dispersoids reinforcement of Fe-40at%Al intermetallic coating for both high hardness and high fracture toughness, *Mater. Sci. Eng. A* 555 (2012) 85–92, <https://doi.org/10.1016/j.msea.2012.06.037>
- [70] D. Siemiaszko, I. Garwacka, Unexpected high ductility of Fe40Al alloys at room temperature, *Materials* 14 (17) (2021) 4906, <https://doi.org/10.3390/ma14174906>
- [71] Z.B. Li, H. Zhang, G.H. Zhang, K.C. Chou, Fabrication and characterization of Tungsten heavy alloys with high W content by powder metallurgy, *Metall. Mater. Trans. A* 53 (3) (2022) 1085–1098, <https://doi.org/10.1007/s11661-021-06579-w>
- [72] M. Faleschini, H. Kreuzer, D. Kiener, R. Pippan, Fracture toughness investigations of tungsten alloys and SPD tungsten alloys, *J. Nucl. Mater.* 367–370 (2007) 800–805, <https://doi.org/10.1016/j.jnucmat.2007.03.079>
- [73] M.A.M. Ghazali, M.A. Harimon, M.S. Mustapa, Mechanical behavior and microstructural analysis of molybdenum-TZM alloy subjected to different annealing temperature, *JSE* 1 (2019) 31–35, <https://doi.org/10.30650/jse.v1i1.522>
- [74] B.V. Cockeram, The fracture toughness and toughening mechanisms of wrought low carbon arc cast, oxide dispersion strengthened, and molybdenum-0.5 pct titanium-0.1 pct zirconium molybdenum plate stock, *Metall. Mater. Trans. A* 36 (2005) 1777–1791, <https://doi.org/10.1007/s11661-005-0042-2>
- [75] C. Chen, S.J. Pang, Y.Y. Cheng, T. Zhang, Microstructure and mechanical properties of  $\text{Al}_{20-x}\text{Cr}_{20+0.5x}\text{Fe}_{20}\text{Co}_{20}\text{Ni}_{20+0.5x}$  high entropy alloys, *J. Alloy. Compd.* 659 (2016) 279–287, <https://doi.org/10.1016/j.jallcom.2015.10.258>
- [76] H. Zhang, Y.Z. He, Y. Pan, Enhanced hardness and fracture toughness of the laser-solidified  $\text{FeCoNiCrTiMoAlSiB}_{0.5}$  high-entropy alloy by martensite strengthening, *Scr. Mater.* 69 (4) (2013) 342–345, <https://doi.org/10.1016/j.scriptamat.2013.05.020>
- [77] O.N. Senkov, G.B. Wilks, J.M. Scott, D.B. Miracle, Mechanical properties of  $\text{Nb}_{25}\text{Mo}_{25}\text{Ta}_{25}\text{W}_{25}$  and  $\text{V}_{20}\text{Nb}_{20}\text{Mo}_{20}\text{Ta}_{20}\text{W}_{20}$  refractory high entropy alloys, *Intermetallics* 19 (5) (2011) 698–706, <https://doi.org/10.1016/j.intermet.2011.01.004>
- [78] Y. Zou, P. Okle, H. Yu, T. Sumigawa, T. Kitamura, S. Maiti, W. Steurer, R. Spolenak, Fracture properties of a refractory high-entropy alloy: in situ micro-cantilever and atom probe tomography studies, *Scr. Mater.* 128 (2017) 95–99, <https://doi.org/10.1016/j.scriptamat.2016.09.036>
- [79] H. Döbelstein, E.P. George, E.L. Gurevich, A. Kostka, A. Ostendorf, G. Laplanche, Laser metal deposition of refractory high-entropy alloys for high-throughput synthesis and structure-property characterization, *Int. J. Extrem. Manuf.* 3 (1) (2021) 015201, <https://doi.org/10.1088/2631-7990/abcca8>
- [80] X.J. Fan, R.T. Qu, Z.F. Zhang, Remarkably high fracture toughness of  $\text{HfNbTaTiZr}$  refractory high-entropy alloy, *J. Mater. Sci. Technol.* 123 (2022) 70–77, <https://doi.org/10.1016/j.jmst.2022.01.017>
- [81] R.S. Ganji, K.V. Rajulapati, K.B.S. Rao, Development of a multi-phase  $\text{AlCuTaW}$  high-entropy alloy using powder metallurgy route and its mechanical properties, *Trans. Indian Inst. Met.* 73 (3) (2020) 613–618, <https://doi.org/10.1007/s12666-020-01875-2>

**Supplementary Material related to the article entitled:  
“Influence of cooling rate and lattice misfit on the microstructure  
and mechanical properties in the refractory AlMo<sub>0.5</sub>NbTa<sub>0.5</sub>TiZr  
high entropy superalloy”.**

Patricia Suárez Ocaño <sup>a,\*</sup>, Anna Manzoni <sup>a</sup>, Inmaculada Lopez-Galilea <sup>b</sup>, Benjamin Ruttert <sup>b</sup>,

Guillaume Laplanche <sup>b</sup>, Leonardo Agudo Jácome <sup>a</sup>

<sup>a</sup> Federal Institute for Materials Research and Testing (BAM), Department for Materials Engineering, Unter den Eichen 87, 12205 Berlin, Germany.

<sup>b</sup> Institute for Materials, Ruhr-University Bochum, Universitätsstr. 150, 44801 Bochum, Germany.

\*Corresponding author: [patricia.suarez-ocano@bam.de](mailto:patricia.suarez-ocano@bam.de)

These supplementary materials provide additional information regarding the above-mentioned article. It is divided into four sections:

1. Chemical analysis
2. Microstructural analysis
3. Lattice misfit
4. Mechanical properties

## **1. Chemical Analysis**

**Table S1** shows the chemical composition determined by EDS analysis of the different material states. It can be seen that the chemical composition varies only slightly between the samples and is within the standard deviation, indicating that the material generally has a fairly uniform chemical composition.



**Table S1.** Semi-quantitative energy-dispersive X-ray (EDS) data obtained from  $\text{AlMo}_{0.5}\text{NbTa}_{0.5}\text{TiZr}$  alloy following homogenization heat treatment (AN) at 1400 °C for 24 h and subsequent HIP treatment at 1370 °C for 4 h at 170 MPa with cooling rates of 5, 10 and 30 °C/min. All concentrations in at %, with the uncertainties being the standard deviations in the measurements.

State (cooling rate)	Method	Composition (mole fraction / %)					
		Al	Mo	Nb	Ta	Ti	Zr
AN + HIP (5 °C/min)	SEM-EDS	22 ± 1	11 ± 1	20 ± 1	8 ± 1	21 ± 1	18 ± 1
AN + HIP (10 °C/min)	SEM-EDS	23 ± 1	12 ± 1	20 ± 1	7 ± 1	20 ± 1	18 ± 1
AN + HIP (30 °C/min)	SEM-EDS	22 ± 1	12 ± 1	20 ± 1	8 ± 1	21 ± 1	17 ± 1

To determine the chemical composition of the different phases (A2, B2, and Al-Zr-rich phase), SEM - and TEM-EDS analyses were performed. The composition of the Al-Zr-rich phase was determined from the average of analyses from five regions using SEM-EDS measurements, and the composition of the A2 and B2 phase was determined by TEM-EDS for samples cooled at 5, 10, and 30 °C/min (Figure 1 and 2 of main manuscript). The average chemical compositions are shown in Table S2, with the error given by the standard deviation. It can be clearly observed that the concentration of the individual phases remains constant for the three different samples. From this it can be concluded that the cast bar from which the specimens were taken has a homogeneous chemical composition, so that any artifacts that might be caused by chemical inhomogeneity are excluded.

**Table S2.** Chemical composition of the phases in the different regions in at. % for the RSA cooled at different rates. The error is given by the standard deviation. Bold numbers show the elements in which the phase is rich.

Cooling rate	Phase	Method	Composition (mole fraction / %)					
			Al	Ti	Zr	Mo	Nb	Ta
<b>5 °C/min</b>	Al-Zr-rich	SEM-EDS	<b>40 ± 1</b>	9 ± 2	<b>34 ± 1</b>	3 ± 1	11 ± 1	2 ± 1
	A2	TEM-EDS	5 ± 1	17 ± 1	8 ± 1	<b>17 ± 2</b>	<b>30 ± 1</b>	<b>23 ± 1</b>
	B2 <sup>1</sup>	TEM-EDS	<b>27 ± 1</b>	<b>23 ± 1</b>	<b>25 ± 1</b>	8 ± 1	13 ± 1	4 ± 1
<b>10 °C/min</b>	Al-Zr-rich	SEM-EDS	<b>39 ± 1</b>	9 ± 1	<b>34 ± 1</b>	4 ± 1	11 ± 1	3 ± 1
	A2	TEM-EDS	4 ± 1	15 ± 1	11 ± 1	<b>17 ± 1</b>	<b>29 ± 1</b>	<b>24 ± 1</b>
	B2 <sup>1</sup>	TEM-EDS	<b>26 ± 1</b>	<b>21 ± 1</b>	<b>25 ± 1</b>	9 ± 1	14 ± 1	5 ± 1
<b>30 °C/min</b>	Al-Zr-rich	SEM-EDS	<b>40 ± 1</b>	9 ± 1	<b>35 ± 1</b>	3 ± 1	10 ± 1	3 ± 1
	A2	TEM-EDS	5 ± 2	16 ± 1	10 ± 1	<b>16 ± 1</b>	<b>27 ± 1</b>	<b>26 ± 2</b>
	B2 <sup>1</sup>	TEM-EDS	<b>27 ± 2</b>	<b>22 ± 1</b>	<b>24 ± 1</b>	8 ± 3	14 ± 1	5 ± 1

<sup>1</sup> The measurements were made in the wide channels.

## 2. Microstructural analysis

The microstructural evolution of RSA as a function of cooling rate after annealing and HIP is shown in the BSE micrographs with the same magnification in [Figure S1](#). [Figure S1](#) (a), (c) and (e) show the RSA at low magnification (200X) showing a coarse microstructure with large bcc/B2 grains and a distribution of the Al-Zr-rich intermetallic mainly in the grain boundaries (black phase in the BSE micrographs), for the samples cooled at 5, 10 and 30 °C/min, respectively. To measure the evolution of the Al-Zr-rich intermetallic area fraction with cooling rate, image analysis software “FIJI” [Ref. 23 from main manuscript] was used to obtain the binarized images shown in [Figures S1b, d, and f](#), from the BSE micrographs in [Figures S1a, c and e](#), respectively. A comparison of [Figures S1b, d and f](#) clearly show that the amount of Al-Zr-rich intermetallic increases with slower cooling rates.

The nanostructure of the RSA alloy was revealed by CTEM for the samples annealed at 1400 °C for 24 hours, HIPed at 1370°C for 4 h under 170 MPa, and cooled at 5, 10, and 30 °C/min, as shown in [Figure S2, S3 and S4](#), respectively. [Figure S2](#) shows two (C) TEM-DF images (a and b) and the corresponding zone axes ( $Z = [001]$ ) SAD patterns (P) (c). [Figure S2c](#) shows in green the reflections that were selected to obtain the diffraction contrasts in [Figure S2a and b](#). Since the image in [Figure S2a](#) was formed using a superlattice 100 reflection and the image in [Figure S2b](#) was formed using a 200 reflection, the microstructure can be interpreted as a mixture of two bcc-based phases, i.e., a mixture of channels/cuboidal precipitates with B2/A2 phase, respectively. [Figure S3](#) and [Figure S4](#) show two (C)TEM-DF images (a and b) and the corresponding zone axis ( $Z = [001]$ ) SAD pattern (P) (c), respectively. As in [Figure S2, Figure S3c and Figure S4c](#) show the reflections in green that were selected to determine the diffraction contrasts in [Figure S3a and b](#) and [Figure S4a and b](#), respectively. In these cases, the microstructure can also be interpreted as composed of a mixture of two bcc phases, i.e., a mixture of channels/cuboidal precipitates with B2/A2 phase, respectively.

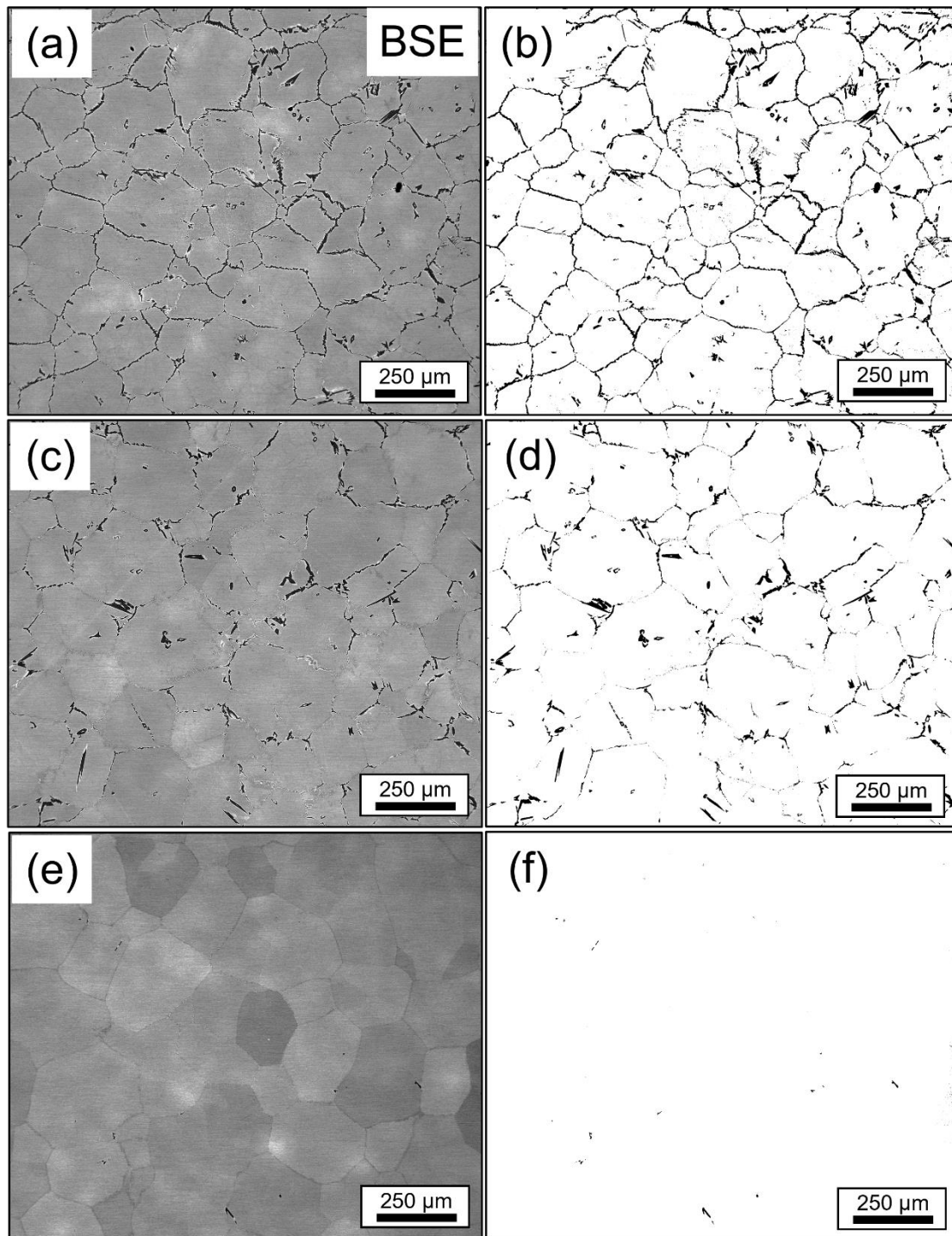


**Figure S1.** SEM-BSE micrographs taken with the same magnification, showing the Al-Zr-rich phase mainly inside the grain boundaries, of the samples cooled at (a) 5 °C/min, (c) 10 °C/min, and (d) 30 °C/min. (b) (d) and (f), represent the binarized images taken from (a) (c) and (d), respectively, using an image analysis software for the area fraction determination where the Al-Zr-rich intermetallics appear as black and the rest of the alloy appears as white.

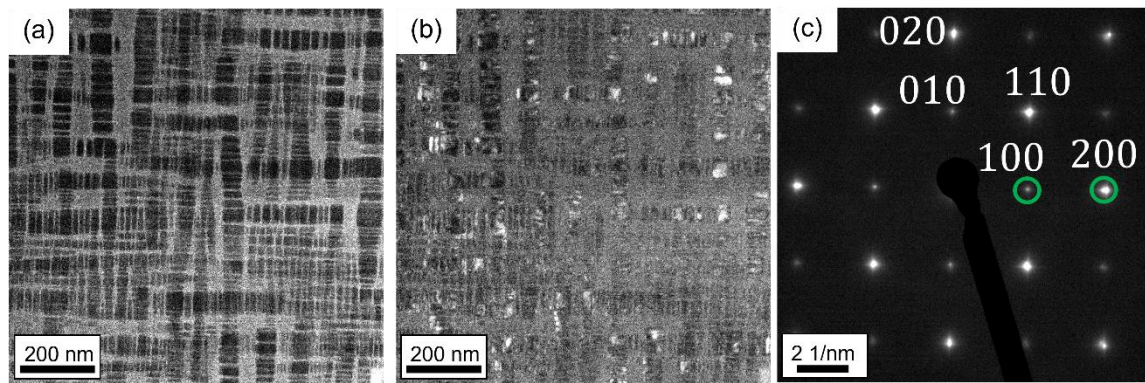


**Figure S2.** (C)TEM-DF micrographs of the nanostructure of the RSA after annealing at 1400 °C for 24 hours and cooled at 5 °C/min, oriented along [001] zone axis (a) using superlattice reflection 100, (b) using reflection 200 in (c). (c) SADP with contrast apertures marked in green for the DF images in (a) and (b).

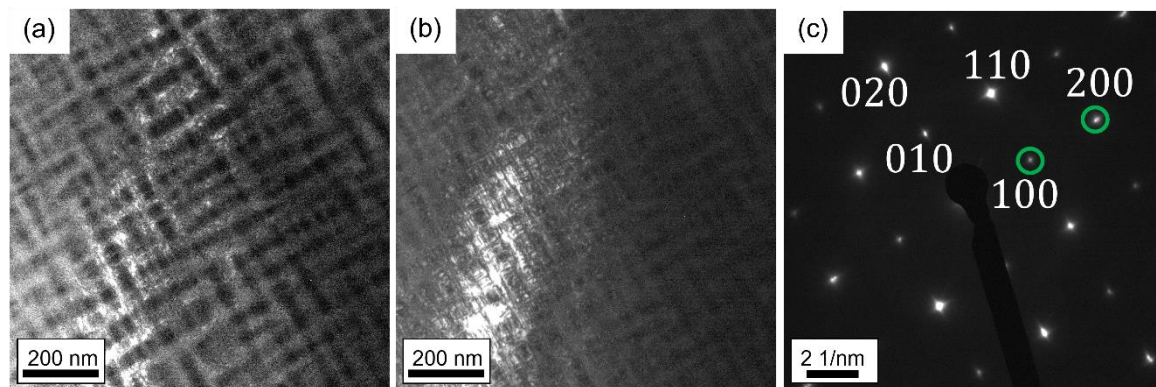


**Figure S3.** (C)TEM-DF micrographs of the nanostructure of the RSA after annealing at 1400 °C for 24 hours and cooled at 10 °C/min, oriented along [001] zone axis (a) using superlattice reflection 100, (b) using reflection 200 in (c). (c) SADP with contrast apertures marked in green for the DF images in (a) and (b).

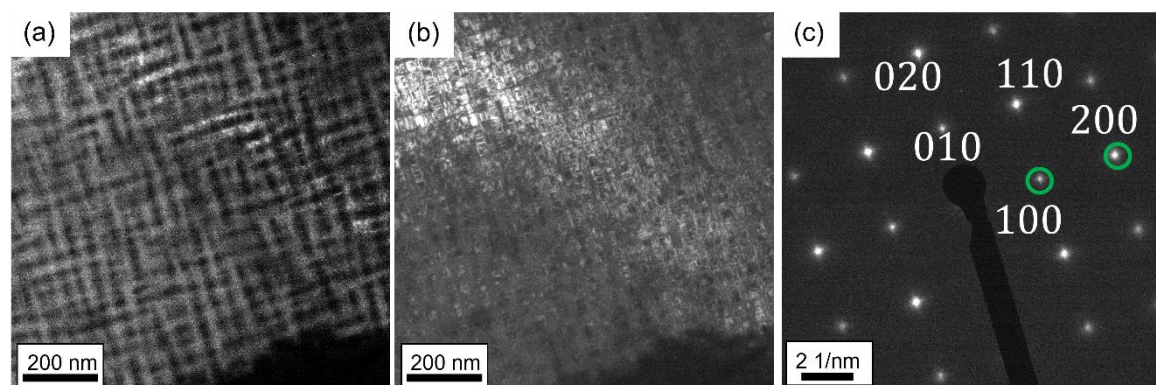


**Figure S4.** (C)TEM-DF micrographs of the nanostructure of the RSA after annealing at 1400 °C for 24 hours and cooled at 30 °C/min, oriented along [001] zone axis (a) using superlattice reflection 100, (b) using reflection 200 in (c). (c) SADP with contrast apertures marked in green for the DF images in (a) and (b).

**Figure S5** shows the STEM-BF micrographs for the samples cooled at 5 °C/min, 10 °C/min, and 30 °C/min along the [001] zone axis. Imaging along low-indexed zone axes in STEM-BF mode is especially suited for dislocation contrast enhancement (*e.g.*, Fig. 6 in [1], or Fig. 1 in [2]). Since



misfit dislocation are not visible at any interface between the A2 and B2 phase, it can be said that the precipitates are coherently embedded in the matrix.

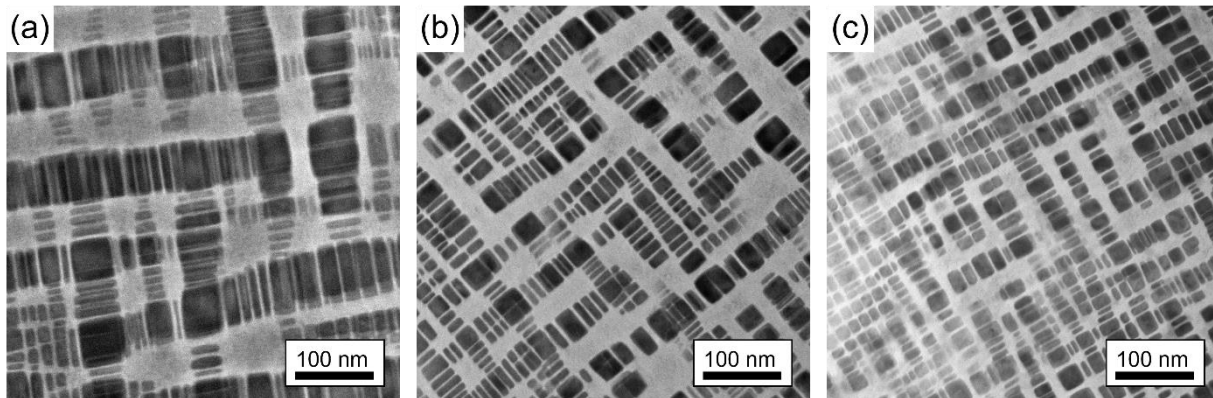


**Figure S5.** STEM-BF micrographs along [001] zone axis for (a) 5 °C/min, (b) 10 °C/min, and (c) 30 °C/min, where fully coherent, *i.e.*, dislocation-free B2/A2 interfaces are visible.

**Figure S6** shows a CTEM-BF micrograph (a) and the corresponding convergent beam diffraction pattern ( $g = 200$ ), of the A2/B2 nanostructure for sample cooled at 5 °C/min, acquired close to a [001] zone axis. The diffraction contrast in the CTEM-BF micrograph shows the presence of continuous coherency stresses (see black line surrounding the A2/B2 interfaces in Figure S6a), typical of fully coherent interfaces. In other words, no disruption of these contrasts by, *e.g.*, dislocation contrast at the A2/B2 interfaces, is observed. Thus, it can be assumed that the samples with the higher cooling rates, with lower misfits and smaller A2 particles, also have coherent A2/B2 interfaces that better accommodate coherency stresses.

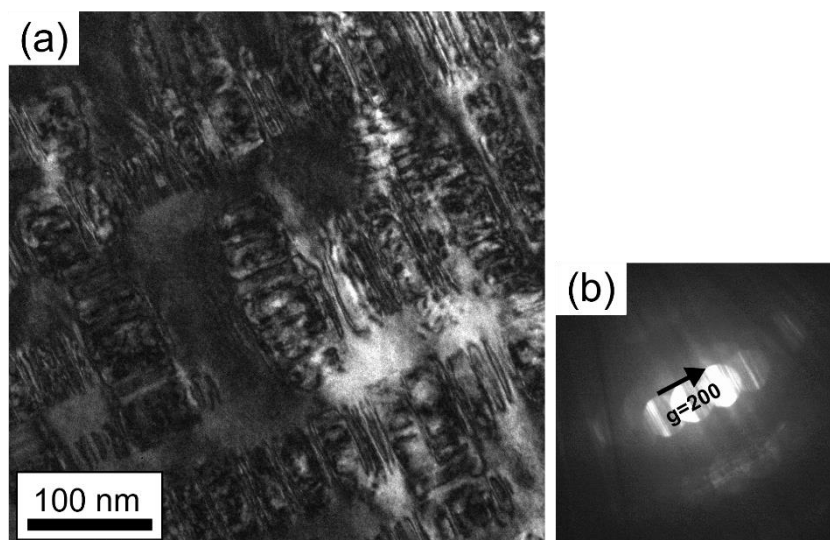


**Figure S6.** (a) CTEM-BF micrograph and (b) corresponding convergent beam diffraction pattern ( $g = 200$ , close to [001] zone axis) for 5 °C/min, where fully coherent, *i.e.*, dislocation-free B2/A2 interfaces show a continuous distortion contrast (black line surrounding each B2 precipitate).

The microstructural evolution of RSA as a function of cooling rate after annealing and HIP is shown in the STEM-HAADF micrographs with the same magnification in [Figure S7](#), respectively. [Figure S7a, c and e](#) show the STEM-HAADF micrographs of the RSA at high resolution (300.000X) with the grain nanostructure consisting only of A2 precipitates embedded in the B2 matrix, for the samples cooled at 5, 10 and 30 °C/min, respectively. To measure area fraction of both A2 and B2 phase and the evolution with the cooling rate, [Figures S7b, d and f](#) were binarized from the STEM-HAADF micrographs in [Figures S7a, c and e](#), respectively. A2 precipitates appear white whereas B2 channels appear black in the binarized images. This trend is quantitatively shown in [Table 3](#) of the main manuscript. A total of four images for each condition were binarized (not shown here) and analyzed to determine the total area fraction with the respective standard deviation. [Table 2](#) shows a summary of the measured size range and average of the A2-precipitates and B2-channels at different cooling rate by FIJI [Ref. 42 from main manuscript], including the precipitates length, precipitates area, small and big channels length.

**Table S3.** Summary of A2 precipitates and B2 channels size in the samples with different cooling rates.

Cooling rate	5 °C/min	10 °C/min	30 °C/min
Precipitates edge length <b>range</b>	4.4 nm – 62.0 nm	4.5 nm – 41.7 nm	3.7 nm – 30.0 nm
Precipitates edge length <b>average</b>	25.1 ± 14.5 nm	18.0 ± 8.6 nm	16.1 ± 6.7 nm
Precipitates area <b>range</b>	18 – 2980 nm <sup>2</sup>	13 – 1025 nm <sup>2</sup>	11 – 688 nm <sup>2</sup>
Precipitates area <b>average</b>	480.5 ± 558.9 nm <sup>2</sup>	254.0 ± 209.0 nm <sup>2</sup>	196.3 ± 139.8 nm <sup>2</sup>
<b>Small</b> channels width <b>range</b>	1.6 nm - 9.1 nm	1.4 nm - 10.2 nm	1.3 nm - 7.6 nm
<b>Small</b> channels width <b>average</b>	3.8 ± 1.1 nm	3.1 ± 1.2 nm	2.7 ± 0.8 nm
<b>Big</b> channels width <b>range</b>	15.4 nm - 91.4 nm	10.8 nm – 70.8 nm	4.4 nm – 49.6 nm
<b>Big</b> channels width <b>average</b>	45.9 ± 19.8 nm	31.2 ± 11.7 nm	17.8 ± 7.9 nm

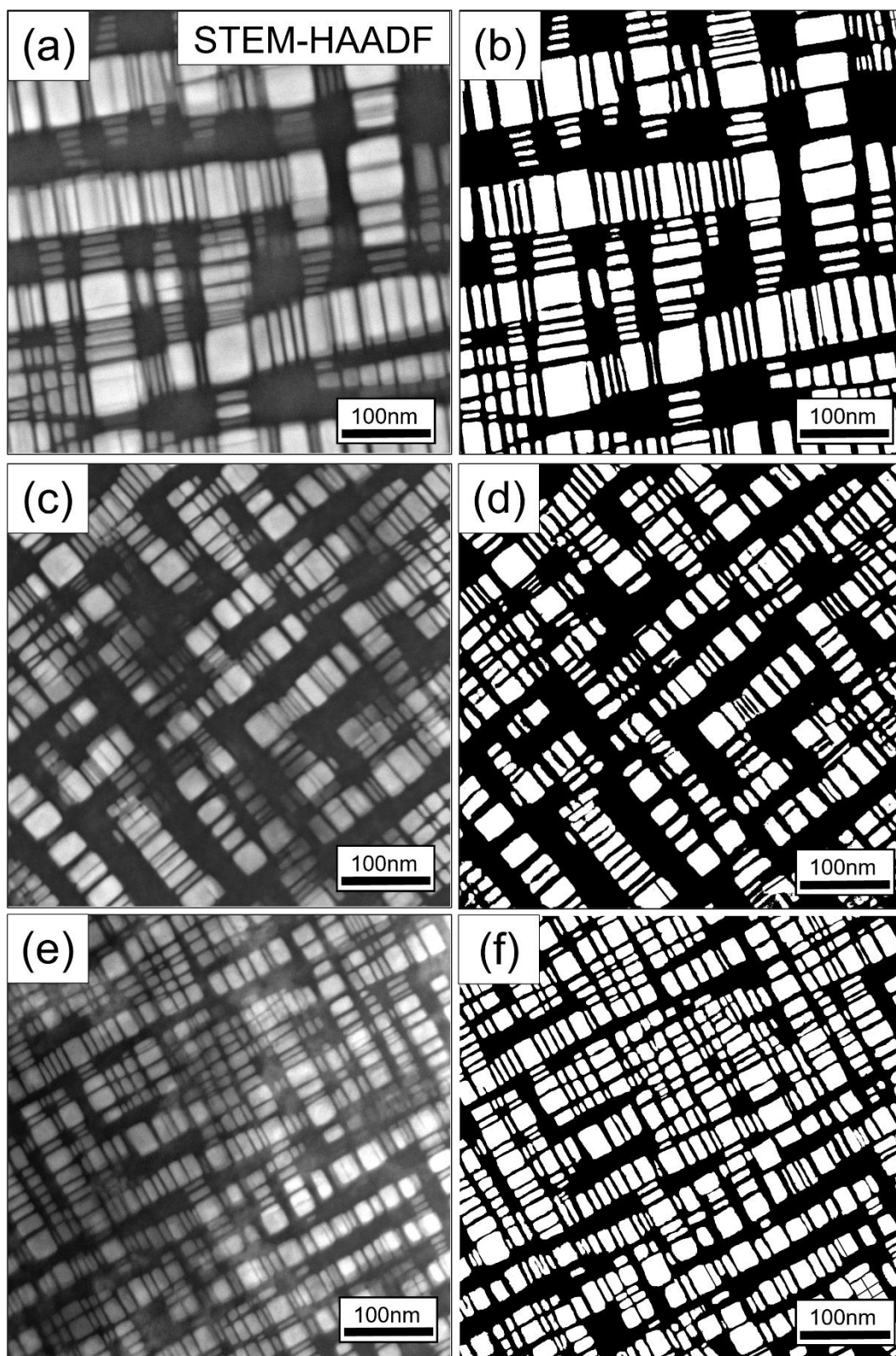


**Figure S7.** STEM-HAADF micrographs taken with the same magnification, showing a region with the A2 and B2 phase, of the samples cooled at (a) 5 °C/min, (c) 10 °C/min, and (d) 30 °C/min. (b) (d) and (f), represent the binarized images taken from (a) (c) and (d), respectively, using an image analysis software for the area fraction determination [Ref. 23 from main manuscript] where A2 precipitates appear as white and the B2 channels as black background.

#### 4. Lattice misfit

The Figure S8 shows the amount of component in each phase as a function of temperature calculated using ThermoCalc software [database TCHEA3 version 2020b, Ref. 44 in the main manuscript] for the BCC#1 phase, which is determined by equilibrium calculations to be rich in Mo, Nb and Ta (A2 phase) and BCC#2 phase, rich in Al, Ti and Zr (B2 phase). Table S4 show the calculated chemical composition of the two bcc phases at different temperatures (800, 900, 1000, 1200 and 1400 °C).

Figure S8 shows that with increasing temperature, the A2 phase, which is Mo-Nb-Ta-rich (Table S4), exhibits a slight decrease in Nb and Mo and a slight increase in Ta in the range of comparison of experimental and simulated data (750–900 °C). Furthermore, it shows a slight increase in Al, Ti, and Zr, although the increase rate of Zr is lower than that of Al and Ti. This behavior suggests that elements such as Ti and Al have a higher solubility in the A2 phase than Zr at higher temperatures. On the other hand, with increasing temperature in the B2 phase, which is Al-Ti-Zr-rich (Table S4), there is a significant decrease in Ti and a slight increase in Al and Zr in the range of comparison of experimental and simulated data (750–900 °C, beige dotted region in Figure S8). Since Al has a smaller atomic radius than the other elements, this could explain the difference between experimental and calculated data in terms of the increase in lattice parameters in phases A2 and B2.

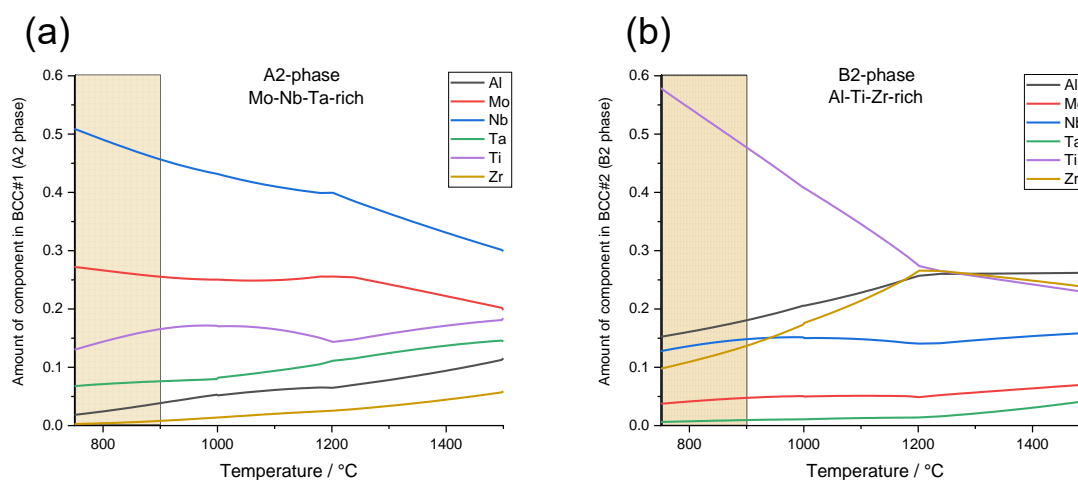


**Figure S8.** Amount of component in the phase as a function of temperature calculated using ThermoCalc (a) BCC#1 phase (A2 phase) and (b) BCC#2 phase (B2 phase). Dotted beige regions refer to high temperature regime investigated in situ (for more details, see main article).



**Table S4.** Calculated element mole fractions of equilibrium phases in the studied alloy at different temperatures using ThermoCalc software. Database TCHEA3. Bold numbers show the elements of which the phase is rich.

Temperature (°C)	Phases	Sublattice	Al	Ti	Zr	Nb	Mo	Ta	Phase rich in
800	BCC_B2_#2	1	<b>0.16</b>	<b>0.54</b>	<b>0.11</b>	0.14	0.04	0.01	Al-Ti-Zr
		2	<b>0.16</b>	<b>0.54</b>	<b>0.11</b>	0.14	0.04	0.01	
	BCC_B2_#1	1	0.02	0.14	0.01	<b>0.49</b>	<b>0.27</b>	<b>0.07</b>	Mo-Nb-Ta
		2	0.02	0.14	0.01	<b>0.49</b>	<b>0.27</b>	<b>0.07</b>	
900	BCC_B2_#2	1	<b>0.18</b>	<b>0.48</b>	<b>0.14</b>	0.15	0.04	0.01	Al-Ti-Zr
		2	<b>0.18</b>	<b>0.48</b>	<b>0.14</b>	0.15	0.04	0.01	
	BCC_B2_#1	1	0.03	0.16	0.01	<b>0.46</b>	<b>0.26</b>	<b>0.08</b>	Mo-Nb-Ta
		2	0.03	0.16	0.01	<b>0.46</b>	<b>0.26</b>	<b>0.08</b>	
1000	BCC_B2_#2	1	<b>0.21</b>	<b>0.41</b>	<b>0.17</b>	0.15	0.05	0.01	Al-Ti-Zr
		2	<b>0.21</b>	<b>0.41</b>	<b>0.17</b>	0.15	0.05	0.01	
	BCC_B2_#1	1	0.05	0.17	0.01	<b>0.43</b>	<b>0.25</b>	<b>0.09</b>	Mo-Nb-Ta
		2	0.05	0.17	0.01	<b>0.43</b>	<b>0.25</b>	<b>0.09</b>	
1200	BCC_B2_#2	1	<b>0.26</b>	<b>0.28</b>	<b>0.26</b>	0.14	0.05	0.01	Al-Ti-Zr
		2	<b>0.26</b>	<b>0.28</b>	<b>0.26</b>	0.14	0.05	0.01	
	BCC_B2_#1	1	0.06	0.14	0.03	<b>0.40</b>	<b>0.26</b>	<b>0.11</b>	Mo-Nb-Ta
		2	0.06	0.14	0.03	<b>0.40</b>	<b>0.26</b>	<b>0.11</b>	
1400	BCC_B2_#2	1	<b>0.26</b>	<b>0.24</b>	<b>0.26</b>	0.15	0.06	0.03	Al-Ti-Zr
		2	<b>0.26</b>	<b>0.24</b>	<b>0.26</b>	0.15	0.06	0.03	
	BCC_B2_#1	1	0.09	0.17	0.05	<b>0.33</b>	<b>0.22</b>	<b>0.14</b>	Mo-Nb-Ta
		2	0.09	0.17	0.05	<b>0.33</b>	<b>0.22</b>	<b>0.14</b>	

## 5. Mechanical properties

The elastic modulus of the material for the three different cooling rates (5, 10 and 30 °C/min) were determine from the load-displacement measurements. [Figure S9](#) show a representation of the load-displacement curves of the RSA for all the considered measured points and the different cooling rates. For the Al-Zr-rich phase in the sample cooled at 5 °C/min, the curves are represented in “red”, and 10/10 measured points were taken to average the value of “stiffness”. For the A2/B2 phases the curves are represented in “blue”, and 15/15 measured points were taken to average the “stiffness”.

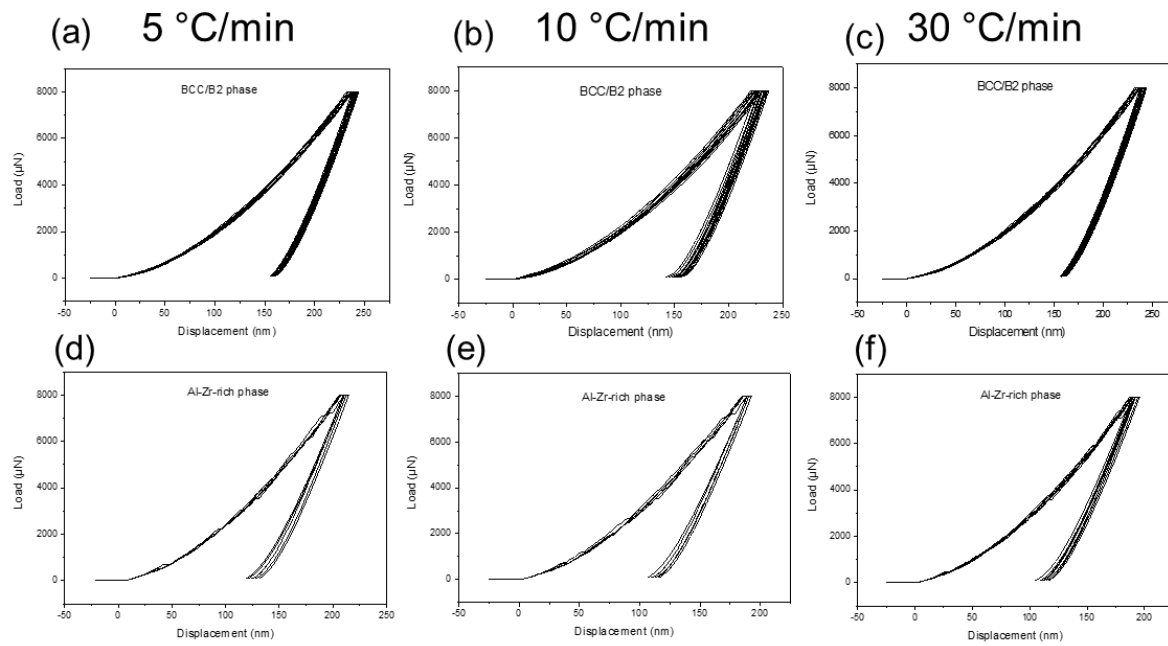


**Figure S9.** The nanoindentation load-displacement curves of the samples (a) BCC/B2 phase cooled at 5 °C/min (b) BCC/B2 phase cooled at 10 °C/min (c) BCC/B2 phase cooled at 30 °C/min (d) Al-Zr-rich phase cooled at 5 °C/min (e) Al-Zr-rich phase cooled at 10 °C/min (f) Al-Zr-rich phase cooled at 30 °C/min.

## References

- [1] L.A. Jácome, G. Gobeni, G. Eggeler, Transmission electron microscopy study of the microstructural evolution during high-temperature and low-stress (011) [11] shear creep deformation of the superalloy single crystal LEK 94, *J. Mater. Res.* 32(24) (2017) 4491-4502. doi: 10.1557/jmr.2017.336.
- [2] L. Heep, C. Schwalbe, C. Heinze, A. Dlouhy, C.M.F. Rae, G. Eggeler, Dislocation networks in  $\gamma/\gamma'$ -microstructures formed during selective laser melting of a Ni-base superalloy, *Scri. Mater.* 190 (2021) 121-125. doi: 10.1016/j.scriptamat.2020.08.019.

## 4.4 Paper IV

Creep degradation of the  $\text{AlMo}_{0.5}\text{NbTa}_{0.5}\text{TiZr}$  refractory high entropy superalloy.

*To be submitted*

# Creep degradation of the AlMo<sub>0.5</sub>NbTa<sub>0.5</sub>TiZr refractory high-entropy superalloy

Patricia Suárez Ocaño <sup>a,\*</sup>, Guillaume Laplanche <sup>b</sup>, Christian Gadelmeier <sup>c</sup>, Uwe Glatzel <sup>c</sup>,  
Leonardo Agudo Jácome <sup>a</sup>

<sup>a</sup> Federal Institute for Materials Research and Testing (BAM), Department for Materials Engineering, Unter den Eichen 87, 12205 Berlin, Germany.

<sup>b</sup> Institute for Materials, Ruhr-University Bochum, Universitätsstr. 150, 44801 Bochum, Germany.

<sup>c</sup> Metals and Alloys, University of Bayreuth, 95447 Bayreuth, Germany.

\*Corresponding author: patricia.suarez-ocano@bam.de

## Abstract

The AlMo<sub>0.5</sub>NbTa<sub>0.5</sub>TiZr alloy exhibits an initial dual-phase microstructure, consisting of a high area fraction ( $\approx 40\%$ ) of cuboidal and plate-like body-centered cubic (A2) particles coherently embedded in a continuous and ordered B2 matrix. Due to the resemblance of this microstructure with those of Ni-based superalloys, this alloy is also referred to as "refractory superalloy" (RSA) in the literature. In this study, tensile creep tests were performed in vacuum at 900–1100 °C and 30–160 MPa. The microstructures in the head and gage of crept samples were investigated *via* scanning and transmission electron microscopy to study the effects of temperature and external load, respectively, and identify the mechanisms that govern the creep behavior. Upon annealing, while the B2 phase is continuous in the initial A2/B2 nanostructure, parts of it transform into an Al<sub>4-x</sub>Zr<sub>5</sub> phase. As A2-formers are released during this transformation, the A2 fraction increases and the disordered A2 solid solution becomes the continuous phase, which is reinforced by Al<sub>4-x</sub>Zr<sub>5</sub> particles. This "topological inversion" probably promotes plasticity and thus degrades creep resistance. As the B2-to-Al<sub>4-x</sub>Zr<sub>5</sub> transformation is not affected by the applied stress ( $\sigma$ ) but is more pronounced at lower temperatures, it is likely responsible for the very low apparent activation energy for creep of the RSA ( $\approx 111$  kJ/mol). Regarding the stress-dependence of creep, the Norton exponent of  $\approx 3$  is nearly independent of temperature at  $\sigma < 90$  MPa, which can be attributed to solute drag creep behavior while its value strongly increases at higher stresses. The RSA is found to have an excellent creep resistance for a bcc-structured alloy, but it cannot compete with cast Ni-based superalloys that are commonly used for structural applications.

**Keywords:** refractory chemically complex alloy (rCCA); electron microscopy; microstructure instability; tensile creep behavior; phase stability.



## 1. Introduction

Complex concentrated alloys (CCAs) [1] are a class of materials that have gained much attention in recent years, both from a fundamental point of view and for their potential in structural applications [2-5]. Refractory (r)CCAs, which are designed to withstand extreme temperatures and harsh environments due to the presence of elements with high melting temperatures (*e.g.*, Mo, Nb, Ta, W, etc.), have emerged as promising materials for high-temperature structural applications [6]. An example of these rCCAs, the  $\text{AlMo}_{0.5}\text{NbTa}_{0.5}\text{TiZr}$ , which was named as "refractory high-entropy superalloy (RSA)" by Senkov *et al.* [7], is the subject of the present investigation. This alloy is polycrystalline with a multiphase microstructure that mainly consists of disordered body-centered cubic (bcc, A2 structure,  $\approx 40\%$ ) cuboidal and plate-shaped precipitates embedded in an ordered bcc matrix (B2 intermetallic compound) [7-10]. Even though the microstructure of the RSA is similar to that of cast superalloys, the disordered and ordered phases play different roles, *i.e.*, in Ni-based superalloys, the matrix is a disordered solid solution reinforced by ordered precipitates with a face-centered cubic (fcc) structure [11].

In terms of mechanical properties, Senkov *et al.* showed that this RSA exhibits an excellent strength (745 MPa) and fracture strain in compression ( $> 50\%$ ) at 1000 °C, superior to state-of-the-art wrought and cast Ni-based superalloys [7]. Based on their short-term compression tests, Senkov *et al.* [7] argued that the retained high-temperature strength (up to 1200 °C) of the RSA is due to the large fraction of interfaces that impedes deformation transfer between phases. Despite the promising properties of the  $\text{AlMo}_{0.5}\text{NbTa}_{0.5}\text{TiZr}$  RSA, there is a lack of tensile creep properties. This makes it difficult to assess its true potential for structural applications where components are subjected to tensile creep loading at slow strain rates. Recently, several studies have investigated the microstructural stability of the RSA at high temperatures [9-11]. It was showed that long-term exposures between 800 and 1200 °C promotes the formation of a hexagonal  $\text{Al}_{4-x}\text{Zr}_5$  intermetallic compound at the expense of the B2 phase, which volume fraction increases with decreasing temperature [10, 12]. It is therefore important to understand how this B2-to- $\text{Al}_{4-x}\text{Zr}_5$  phase transformation may affect the creep behavior of the RSA.

To our knowledge, only a few studies attempted to investigate the creep behavior of rCCAs so far [13-17]. For instance, Liu *et al.* [16] have studied the tensile creep behavior of a single-phase bcc  $\text{HfNbTaTiZr}$  rCCA at 1100–1250 °C and 5–30 MPa. Based on the determined creep parameters (stress exponent  $2.5 < n < 2.8$ , creep activation energy: 273 kJ/mol), the authors suggested that the creep behavior is governed by the slow diffusion of Ta, which contributes the most to drag  $a/2 \langle 111 \rangle$  dislocations. As a result of ordering in the B2 intermetallic compound, the situation should be fundamentally different in the RSA compared to the disordered bcc  $\text{HfNbTaTiZr}$  rCCA. Recently, Kral *et al.* [14] investigated the creep behavior at 800 °C of an  $\text{AlTiVNbZr}_{0.25}$  rCCA

composed of a B2 matrix with  $\approx 13\%$  of coarse  $Zr_5Al_3$ -type precipitates. The authors found that the quasi-stationary creep rate obeys a three-power-law ( $n \approx 3$ ) due to viscous glide creep [18], and that the mean free path of the  $Zr_5Al_3$ -type precipitates did build significant Orowan stresses.

The present work aims to investigate the creep properties of the  $AlMo_{0.5}NbTa_{0.5}TiZr$  RSA at 900-1100 °C and 30-160 MPa, establish the micro-mechanisms of degradation and deformation that govern the creep behavior, and compare the properties with those of bcc-structured materials as well as Ni-based superalloys to assess whether the RSA can compete with these materials.

## 2. Materials and Methods

### 2.1. Material processing

Two batches (I and II) of the  $AlMo_{0.5}NbTa_{0.5}TiZr$  RSA were cast by vacuum arc melting of pure elements (Al, Mo, Nb, Ta, Ti, and Zr) in an Ar atmosphere (purity > 99.998 %) to produce rectangular ingots with dimensions:  $20 \times 20 \times 50 \text{ mm}^3$  (see Figure 1a). More detail regarding this processing route can be found elsewhere [19]. After casting, the alloy was annealed at 1400 °C for 24 h in continuously flowing Ar (purity > 99.998 %) and cooled at  $< 4 \text{ °C/min}$ . It was finally hot isostatically pressed at 1370 °C for 4 h at 170 MPa and cooled at  $10 \text{ °C/min}$ . This material state is hereafter named as-received (AR).

### 2.2. Creep characterization

From the rectangular ingots, creep samples were cut by wire electric discharge machining (EDM), see Figure 1a. The rectangular gage of the creep specimens, located between two markers [20, 21], has a section of  $2.0 \times 2.9 \text{ mm}^2$  and a length of 5 mm (Figure 1b). The thin oxide layer on the surface caused by EDM was removed by grinding with a p2400-grade emery paper.

Constant-load creep tests were performed in a custom-built testing device [22] (Metals and Alloys, University of Bayreuth, Bayreuth, Germany) under vacuum ( $2 \times 10^{-4} \text{ Pa}$ ) to prevent oxidation. The tests were conducted at 900, 1000, and 1100 °C, and the temperature was controlled by a type S thermocouple near the sample gage. The specimens were gripped by  $Al_2O_3$  rods and heated to the test temperature at  $20 \text{ °C/min}$  in an induction furnace. Once the desired test temperature was reached, it was kept constant for 30 min before the load was applied.

Due to the lack of creep data for this alloy, an initial test was performed at 160 MPa and 800 °C. However, the sample failed within a few seconds, so a higher temperature of 1000 °C was applied, which yielded reliable data. Strain was measured using a non-contact video extensometer [23].

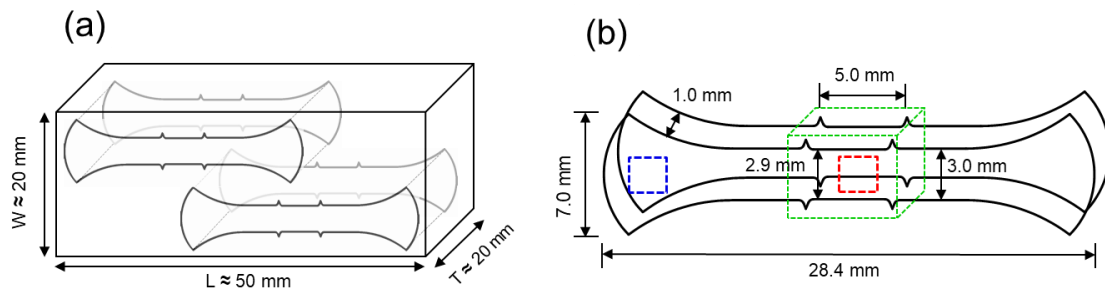


**Figure 1.** (a) Sketch of the vacuum arc melted and heat-treated rectangular ingot showing the locations where creep samples were cut by EDM. (b) Geometry of the creep specimens. The blue and red rectangles in (b) mark regions where the microstructure was analyzed. The region within the gage length marked by the green rectangular prism was cut at different angles for investigations by transmission electron microscopy.

Only tests that failed within the gage length were considered valid. Based on initial tests, further stresses between 30 and 160 MPa were applied. Due to the limited amount of material, a sudden increase in load was applied just after the minimum creep rate was reached in some of the tests [20]. Additional creep tests were performed to failure or were interrupted and cooled under load after reaching the last minimum creep rate of the test, taken as the point with the slowest deformation rate of the experiment. The testing conditions are summarized in the first three columns of [Table 2](#). Samples of the AR material as well as the head and gage of crept specimens (see blue and red frames in [Figure 1b](#), respectively) were metallographically prepared followed by X-ray diffraction (XRD), scanning (S) and transmission (T) electron microscopy (EM) analyses. The specimens were first ground with SiC emery papers up to grade p4000, and either polished with an active oxide polishing suspension (OPS) containing 50-nm particles of colloidal silica for SEM and XRD or electropolished for TEM (see below). A comparison of the microstructures allowed to study the effects of temperature and temperature in combination with stress on phase stability.

### 2.3. Phase and microstructural characterizations

XRD was performed at 20 °C using a Bruker D8 Advance in the Bragg–Brentano geometry with the Cu  $K_{\alpha 1}$  radiation ( $\lambda_{K_{\alpha 1}} = 0.15406$  nm) and a  $2\theta$  scattering range of 10–140°. Phases were identified by comparing experimental XRD patterns with simulated ones using the PowderCell software package [24], and the lattice parameters of the phases were calculated from diffraction peak positions ( $2\theta$ ). SEM analyses were carried out with an SEM (FEI Quanta 3D) equipped with backscatter electron (BSE) and energy-dispersive X-ray spectroscopy (EDS, EDAX Octane Elect SDDs) detectors. Due to the strong morphological anisotropy of the main microstructural features in the RSA, electron channeling contrast (ECC) and visual inspection were used to quantify and compare regions with similar orientations. The chemical composition of the alloy was determined

before creep by SEM-EDS at five distinct regions ( $\approx 2 \text{ mm}^2$ ), the average of which is shown in [Table 1](#). The average grain size prior to creep was determined following the ASTM E112.

**Table 1.** Experimental chemical composition of the RSA determined by semi-quantitative SEM-EDS averaged over five 2-mm<sup>2</sup> regions. All concentrations are in at. %, with a standard deviation of about  $\pm 0.5$  at. %.

Al	Mo	Nb	Ta	Ti	Zr
23	10	19	8	21	19

Electron backscatter diffraction (EBSD) images were acquired at medium and high magnification (SEM LEO Gemini 1530 V P Zeiss, EBSD detector Bruker e-flash HD with Bruker Esprit 1.9 EBSD-Software package). Kikuchi lines were indexed using the built-in crystal files for  $\text{Mo}_{0.67}\text{Ti}_{0.17}\text{Zr}_{0.17}$  (bcc, space group.  $\text{Im}\bar{3}m$ ,  $n^\circ 229$ ) and  $\text{Al}_4\text{Zr}_5$  (hexagonal, space group.  $\text{P6}_3/\text{mcm}$ ,  $n^\circ 193$ ). The EBSD data were then analyzed offline with the software package HKL Channel 5 (Oxford Instruments).

For the TEM observations, 500- $\mu\text{m}$  thick slices were cut from the head and gage of the crept specimens and mechanically ground to 100  $\mu\text{m}$ . From these, 3-mm diameter samples were punched out and thinned by twin-jet electropolishing (Tenupol-3, Struers) in an electrolyte consisting of 950 ml ethanol, 100 ml butanol and 50 ml perchloric acid at  $-30^\circ\text{C}$  and 20 V. After this procedure, regions containing the Al-Zr-rich phase were thinned more strongly than the A2/B2 regions. A TEM with a field emission gun (TEM JEM-2200FS JEOL) was used at an acceleration voltage of 200 kV for imaging in scanning (STEM) bright field (BF)/high angle annular dark field (HAADF) and conventional (CTEM) modes. Both selected area (SA) and convergent beam (CB) diffraction patterns (DPs) were acquired and correlated with CTEM and STEM images. Mean dislocation densities  $\rho_d$  were evaluated from STEM micrographs using the line intercept method [25], where  $\rho_d = 2N/Lt$ , where  $N$  is the number of intersections between test and dislocation lines,  $L$  is the total length of the test lines within a phase, and  $t$  is the thickness of the TEM foil. The value of  $t$  was measured to be 110 nm in the A2/B2 regions by stereoscopy [26] and was determined to be 21 nm in the Al-Zr-rich phase, as the latter was always thinner. The procedures used to determine the thicknesses of the TEM sample in different characteristic regions are shown in the supplementary material ([Figure S1](#)).

The SADPs of the A2 and B2 phases were indexed manually and those of the Al-Zr-rich phase were indexed with the Java version of the electron microscopy suite (JEMS) software [27]. The area fraction of each phase was estimated by image analysis using the software ImageJ [28] [161] using



either SEM-BSE or STEM-HAADF images, depending on their resolution (see [Figures S2-S7](#) of supplementary material).

### 3. Results and discussion

#### 3.1. Creep behavior

The classical creep curves, time ( $t$ ) vs. total strain ( $\epsilon$ ), are displayed in [Figure 2a-c](#) for tests performed at 900, 1000, and 1100 °C, respectively, where a different color is assigned to each applied stress ( $\sigma$ ). Similarly, [Figure 2d-f](#) show the corresponding evolutions of creep rate ( $\dot{\epsilon}$ ) with  $\epsilon$ . In [Figure 2](#), the black circles and crosses at the end of the creep curves indicate interrupted tests and tests to failure, respectively. At 1000 °C (*cf.* [Figure 2b,e](#)) and 1100 °C ([Figure 2c,f](#)), additional tests were performed during which the applied load was suddenly increased from 30 to 60 MPa. This transition is marked by an empty square in [Figure 2b,c,f](#) and the inset of [Figure 2e](#). Creep tests at 1000 and 1100 °C were conducted on samples of two batches, where solid lines correspond to batch I and dotted lines correspond to batch II (*cf.* [Figure 2b,c,e,f](#)).

Even though primary creep presents some differences depending on temperature and stress (see [Figure 2](#)), this study will focus on elucidating creep mechanisms based on the minimum creep rates,  $\dot{\epsilon}_{min}$ , determined at different temperatures and stresses.  $\dot{\epsilon}_{min}$  values were evaluated twice (once for each material batch) for some conditions (*i.e.*, 1000 °C / 30 Ma, 1100 °C / 30, 60, and 90 MPa). [Table 2](#) summarizes the different creep conditions and the obtained data. The minimum creep rates for the same stress and temperature combination were in most cases comparable for the two charges. However, at 1100 °C and 30 MPa, the  $\dot{\epsilon}_{min}$  values differ by factor of  $\approx 6$ . This scatter is expected considering the small sample size and the difficulty of obtaining a completely homogeneous ingot by vacuum arc melting from pure elements with high and low melting temperatures. Below approximately  $\dot{\epsilon} = 10^{-9} \text{ s}^{-1}$ , fluctuations in the measurement curves may occur due to limitations of the optically based strain measurement system, which is the region where  $\dot{\epsilon}_{min}$  is found for  $\sigma = 30 \text{ MPa}$  at both 1000 and 1100 °C (*cf.* [Figure 2d,e](#)).

The creep data were analyzed using the conventional equation [29]:

$$\dot{\epsilon}_{min} = A\sigma^n \exp\left(-\frac{Q_c}{RT}\right) \quad (1)$$

where  $A$  is a material constant,  $n$  the Norton exponent,  $Q_c$  the apparent activation energy for creep,  $R$  the gas constant, and  $T$  the absolute temperature. [Figure 3a](#) shows double-logarithmic plots at different temperatures of  $\dot{\epsilon}_{min}$  vs.  $\sigma$ , which were determined from the creep curves in [Figure 2d-f](#). Straight lines were fitted to each data set in [Figure 3a](#) to determine the  $n$  values, corresponding to the slopes of the lines. From a general point of view, the Norton exponent ( $n \approx 3$ ) is found to be

nearly independent of temperature at low applied stresses and its value strongly increases above a critical stress, indicating a change of creep mechanism, *e.g.*,  $n$  increases from 2.7 at 1000 °C for  $\sigma < 90$  MPa to 5.3 at higher stresses (*cf.* last column in [Table 2](#)). If we fit just one line to all the data obtained at 1000 °C,  $n$  would be 3.3 (*cf.* [Table 2](#)), suggesting that dislocation climb acts as the rate-controlling deformation mechanism [30].

**Table 2.** Creep conditions and data obtained for the RSA. Duration ( $t$ ), total strain ( $\varepsilon$ ), minimum creep rate ( $\dot{\varepsilon}_{min}$ ), and Norton exponent ( $n$ ) of the creep samples tested at temperatures ( $T$ ) of 900, 1000, and 1100 °C under different loads ( $\sigma$ ). Roman numbers I and II denote two different batches of the AR material.

$T / ^\circ\text{C}$	$\sigma / \text{MPa}$	<i>Batch</i>	Type	$t / \text{h}$	$\varepsilon / \%$	$\text{Log}_{10}(\dot{\varepsilon}_{min} / \text{s}^{-1})$	$n$
900	30	II	Interrupted	214	0.53	-9.07	2.7
	60	II	Interrupted	142	0.64	-8.24	
1000	30	I	Load	70	0.13	-8.52	2.7
	60	I	increase-	46	0.34	-8.05	
			interrupted	116	0.47*		
	30	II	Interrupted	1800	1.16	-8.96	3.3
	90	I	Interrupted	46	0.82	-7.43	
	120	I	Failure	99	10.08	-7.12	
1100	160	I	Interrupted	10	2.65	-6.11	5.3
	30	I	Load	154	0.74	-8.40	
	60	I	increase-	46	0.48	-7.77	
			interrupted	200*	1.22*		
	30	II	Interrupted	102	1.03	-8.22	3.4
	60	II	Interrupted	11	0.66	-7.43	
	90	I	Interrupted	6	1.97	-6.46	
	90	II	Interrupted	8	0.92	-6.82	

\*Total value after the experiment

The apparent activation energy for creep in [Equation 1](#) is determined using an Arrhenius-type plot of the natural logarithm of  $\dot{\varepsilon}_{min}$  at a specific  $\sigma$  vs.  $1/T$ , see [Figure 3b](#), where the slope of the curve corresponds to  $-Q_c/R$ . Between 900 and 1100 °C,  $Q_c \approx 119$  kJ/mol for  $\sigma = 30$  MPa, and  $Q_c \approx 103$  kJ/mol for  $\sigma = 60$  MPa, giving an average of  $Q_c = 111 \pm 11$  kJ/mol ([Figure 3b](#)).

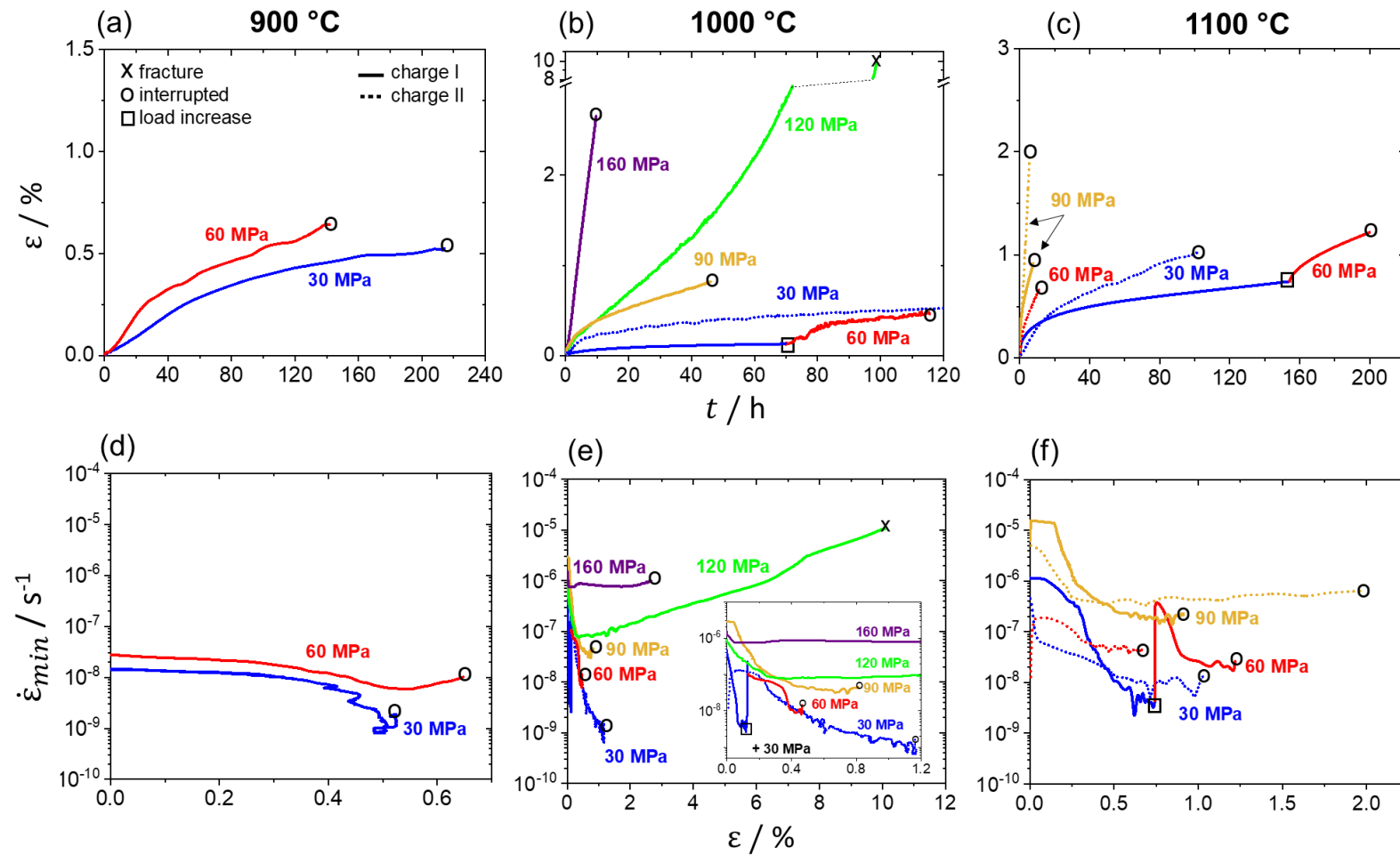


**Figure 2.** Creep behavior of the RSA between 900 and 1100 °C.  $\epsilon$ -vs.- $t$  curves for different  $\sigma$  at (a) 900, (b) 1000, and (c) 1100 °C.  $\dot{\epsilon}$  -vs.- $\epsilon$  for different  $\sigma$  at (d) 900, (e) 1000, and (f) 1100 °C. The tests were either interrupted followed by microstructural investigations (marked by  $\circ$ ), taken to rupture (marked with an "x"), or the  $\sigma$  was suddenly increased (marked by  $\square$ ). Data for specimens from the first and second batch are represented with continuous and dotted lines, respectively.

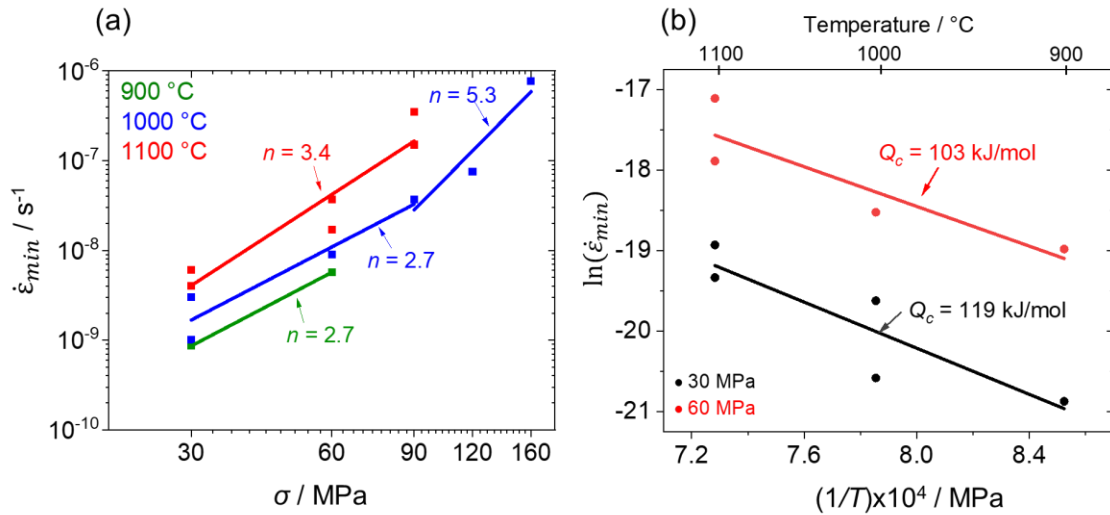


**Figure 3.** (a) Double-logarithmic plot of  $\dot{\epsilon}_{min}$  vs.  $\sigma$  for the RSA at 900, 1000, and 1100 °C. (b) Natural logarithm of  $\dot{\epsilon}_{min}$  as a function of the reciprocal of absolute temperature ( $1/T$ ) for  $\sigma = 30$  and 60 MPa to estimate the apparent activation energy for creep  $Q_c$ .

### 3.2 Microstructure of the $AlMo_{0.5}NbTa_{0.5}TiZr$ RSA in the as-received state

The microstructure of the RSA in the AR state is displayed in Figure 4a-c. The RSA exhibits coarse and equiaxed grains with a mean size of  $744 \pm 185 \mu m$  (*c.f.* triple point in Figure 4a). At a higher magnification in Figure 4b, a lamellar structure, consisting of alternating dark and bright phases, has formed along a grain boundary (GB). The black phase (purple arrow in Figure 4b), rich in Al and Zr as determined by EDS, has been previously identified as a non-stoichiometric  $P6_3/mcm$  hexagonal [31] intermetallic, and named  $Al_{4-x}Zr_5$  with  $0 \leq x \leq 1$  [19]. The bright phase (pink arrow in Figure 4b), which is rich in Nb, Mo, and Ta, has also been previously identified as a disordered bcc (A2) solid solution [7, 19]. Such A2/ $Al_{4-x}Zr_5$  regions are surrounded with orange dashed lines in the remainder of this article (*e.g.*, Figure 4e,f). Within grains of the RSA, a basket-weave substructure is present (see light blue arrows in Figure 4a-c). As shown in previous works [7, 9, 10, 19, 32], this substructure consists of small plate-like and cuboidal A2-precipitates (bright phase) coherently embedded in a continuous B2-matrix (darker phase) with interfaces parallel to  $\{100\}$  [9, 11] planes. In our previous work [33], we showed that the A2 phase has an edge length of  $18 \pm 9$  nm and the B2 phase presents a bimodal distribution of channel widths, with mean values of  $3.8 \pm 1.1$  nm and  $31.2 \pm 11.7$  nm (for details on these measurements, see supplementary material file of Ref. [33]). The area percentages of the phases were estimated as  $\leq 1$  % for the  $Al_{4-x}Zr_5$  phase,  $(62 \pm 2)$  % for the B2 phase, and the rest for the A2 phase [33].

The XRD pattern shown in Figure S8a of the supplementary material confirms the presence of the  $Al_{4-x}Zr_5$  phase, which can be indexed as  $Al_4Zr_5$ . However, in the XRD pattern, the B2 and A2 phases



clearly predominate. The lattice parameters of the phases are  $331.5 \pm 0.2$  and  $326.1 \pm 0.1$  pm for B2 and A2, respectively, and  $a = 805.6 \pm 0.6$  and  $c = 545 \pm 1$  pm for the hexagonal  $\text{Al}_{4-x}\text{Zr}_5$  phase.

### 3.3 Influence of annealing temperature on phase stability and microstructure

To separate the effects of stress-free ( $\sigma \approx 0$ ) high-temperature exposure and creep ( $\sigma \neq 0$ ) on microstructures established at  $\dot{\epsilon}_{min}$ , we analyzed the microstructure in the head of the creep samples (assuming that plastic deformation is negligible in this region,  $\epsilon \approx 0$ ), and within their gage, respectively. In Figure 4, BSE images at different magnifications are compared, which show the microstructure of the RSA before (AR, Figure 4a-c) and after exposure to different temperatures and times, although the latter were chosen to be as close as possible: 900 °C for 142 h (Figure 4d-f), 1000 °C for 116 h (Figure 4g-i), and 1100 ° for 102 h (Figure 4j-l). The corresponding microstructures observed within the gage are displayed in Figure 6 using the same artwork and will be discussed in Section 3.4.

#### Annealing at 900°C

After annealing at 900 °C, grain boundaries show the same combination of A2 and  $\text{Al}_{4-x}\text{Zr}_5$  phases (labeled "GB") as in the AR state but these phases have grown to  $\approx 5$  % of the analyzed area (Figure S3a-c) and occasionally induced faceting of the GB (see lower left corner of Figure 4d). In addition, annealing caused the formation of bright needles or plates near GBs, as well as irregular and bright domains within grains, indicated by arrows in Figure 4d. At a higher magnification in Figure 4e,f, both microstructural features are found to consist of bright and dark phases, corresponding to A2 and  $\text{Al}_{4-x}\text{Zr}_5$ , respectively, as will be shown later.

The needles or plates form variants with different crystallographic orientations that are inclined with respect to the A2/B2 {100} interfaces. They exhibit a lamellar substructure consisting of bright and dark phases (A2 and  $\text{Al}_{4-x}\text{Zr}_5$ , respectively), whose interfaces are parallel to the traces of the needle (or plate), *e.g.*, Figure 4h. Needle or plate-like regions are  $34 \pm 18$   $\mu\text{m}$  in length and account for  $\approx 2$  % of the total analyzed area (see Figure S3).

The irregular domains are magnified in Figure 4e,f and highlighted with orange dashed lines. Compared to the original A2/B2 substructure marked by light blue arrows, the A2/ $\text{Al}_{4-x}\text{Zr}_5$  domains appear brighter. This is because there is more of the bright A2 phase in the A2/ $\text{Al}_{4-x}\text{Zr}_5$  domains ( $42 \pm 2$  %) than in the A2/B2 matrix ( $38 \pm 2$  %), see Figures S4a,d,g and Table S1. The domains exhibit a maze-like substructure where the A2/ $\text{Al}_{4-x}\text{Zr}_5$  interfaces adopt the same traces as those of the A2/B2 substructure, *i.e.*,  $\{001\}_{\text{A2/B2}}$ . However, the former substructure is coarser than the latter (*cf.* Figure 4f), especially toward the center of the domains. For example, the black arrow in Figure 4e points to a coarse A2 particle located in the core of a domain. One could speculate that this is

the nucleation site of the domain, from which it grew radially. Investigations of the as-received material indeed revealed that overgrown A2 precipitates are often heterogeneously distributed within the initial A2/B2 substructures. As these overgrown A2 precipitates have probably a semi-coherent interface with the surrounding B2 phase, they may well act as energetically favorable sites for the B2-to- $\text{Al}_{4-x}\text{Zr}_5$  transformation. Due to the high volume fraction of domains ( $\approx 51\%$ , see [Figures S2a,d,g](#)), they form an almost continuous network with a mean width of  $5 \pm 1\ \mu\text{m}$ . At a lower magnification in [Figure S6](#), domain-free zones are observed near GBs and the mean width of this region is  $18 \pm 7\ \mu\text{m}$ . The presence of this region may be because the B2-to- $\text{Al}_{4-x}\text{Zr}_5$  transformation has already taken place at GBs and induced the formation of a diffusion-affected zone near GBs that is depleted in Al and Zr. As a result, the driving force for the formation of A2/ $\text{Al}_{4-x}\text{Zr}_5$  domains is locally too low in the vicinity of GBs and preclude their formation here. Alternatively, it could be argued that there are fewer overgrown A2 precipitates near GBs in the as-received material, making domain nucleation there more difficult.

In summary, while the AR state had  $\approx 99\%$  of A2/B2 substructure, annealing caused the formation of  $\approx 58\%$  of A2/ $\text{Al}_{4-x}\text{Zr}_5$  substructures with different morphologies, *i.e.*, a lamellar morphology at GBs ( $\approx 5\%$ ), needles or plates ( $\approx 2\%$ ) and most importantly irregularly shaped domains ( $\approx 51\%$ ).

#### *Annealing at 1000°C*

Similar phases and microstructural features were also observed after annealing at 1000 °C for 116 h. However, a few changes are worth mentioning. While the surface percentages of A2/ $\text{Al}_{4-x}\text{Zr}_5$  substructures at GBs ( $\approx 6\%$ ) and needles (or plates,  $\approx 2\%$ ) did not change significantly, the surface percentage of irregularly shaped domains was strongly reduced by a factor of three from  $\approx 51\%$  at 900 °C to  $\approx 16\%$  at 1000°C, see [Figures 4g](#) and [S7b](#). The domains show a similar average size of  $5 \pm 2\ \mu\text{m}$  but the domain-free zone near GBs is reduced from  $18 \pm 7\ \mu\text{m}$  at 900 °C to  $8 \pm 3\ \mu\text{m}$  at 1000 °C. The length of the needles or plates is  $13 \pm 5\ \mu\text{m}$  after annealing at 1000 °C, almost three times shorter than at 900 °C. A comparison of [Figure 4f](#) and [4i](#) reveals that the A2/B2 and A2/ $\text{Al}_{4-x}\text{Zr}_5$  substructures are coarser after annealing at 1000 °C than at 900 °C but both retain the same morphologies and phase fractions, see [Table S1](#).

#### *Annealing at 1100°C*

After annealing for 102 h at 1100 °C, the low-magnification BSE image in [Figure 4j](#) reveals the presence of GB phases and domains within grains as for the 900 and 1000 °C-states, but the absence of needle or plate-like regions. With increasing temperature, the percentage of irregularly shaped domains continues to decrease to  $\approx 9\%$  at 1100 °C. This result is consistent with our previous CALPHAD calculations for the same RSA [19], which suggested that the  $\text{Al}_{4-x}\text{Zr}_5$ -phase fraction

tends to decrease with increasing temperature. The average size ( $4 \pm 1 \mu\text{m}$ ) of the A2/Al<sub>4-x</sub>Zr<sub>5</sub> domains is similar to that obtained at lower annealing temperatures and the width of the domain-free region is  $8 \pm 2 \mu\text{m}$ . While the fractions of A2 and Al<sub>4-x</sub>Zr<sub>5</sub> phases within domains is found to be nearly independent of temperature (see [Figure S4](#)), their morphology differs from those observed at 900 °C and 1000 °C (except for a small region marked with a green arrow in [Figure 4k](#)), *i.e.*, the A2/Al<sub>4-x</sub>Zr<sub>5</sub> substructure loses the {100} directionality of the surrounding A2/B2 region. It is also worth mentioning that the microstructural feature marked in [Figure 4k](#) is reminiscent of rafting in Ni-based superalloys [34] and may be triggered by local variations of coherency stresses between the A2 and B2 phases, which shall promote stress-accelerated coarsening.

The A2/B2 substructure in [Figure 4l](#) after annealing at 1100 °C has strongly coarsened as compared to the 900 and 1000 °C-cases, with an average A2 precipitate edge length in the range of 217–747 nm embedded in wide B2 channels (*cf.* [Figure S5](#)). According to these results, it is evident that the B2-to-Al<sub>4-x</sub>Zr<sub>5</sub> transformation is strongly reduced during annealing at 1100 °C compared to 900 and 1000 °C but this comes at the cost of a much more severe coarsening of the A2/B2 substructure, in which the A2/B2 interfaces become more rounded.

From a specimen annealed at 1100 °C for  $\approx 200$  h, a TEM investigation was performed with a focus on A2/B2 interfaces to identify the microstructural reason for the apparent loss of coherency between these phases. [Figure 5](#) shows STEM-BF micrographs of a coarsened A2/B2 substructure within a grain of the RSA, which was oriented along the  $\langle 111 \rangle_{\text{A2/B2}}$  zone axis (ZA, *cf.* schematic lattice on the right). Finely meshed dislocation networks<sup>1</sup> can be observed at A2/B2 interfaces (see blue-framed region in [Figure 5](#)), while dislocation densities inside the B2 and A2 phases are relatively low (*cf.* [Figure 5](#)). The total dislocation density was determined to be  $\rho_{\text{d}} \approx (3.5 \pm 1.3) \cdot 10^{13} \text{ m}^{-2}$ . In both B2 and A2 phases, dislocation segments are bowed out, indicating the presence of internal stresses. Furthermore, A2 nanoprecipitates (checked by SAD diffraction, see [Figure S9](#) of supplementary material) are found in the B2 phase, which interact with dislocations resulting in jagged lines (*cf.* red-framed region in [Figure 5](#)). Since these precipitates have a nanometric size, we suspect that they have not formed during annealing at 1100 °C for  $\approx 200$  h but upon cooling from 1100°C to 20°C.

---

<sup>1</sup> It can be ruled out that the networks observed at A2/B2 interfaces result from Moiré effects (see [Section e](#) in supplementary material).



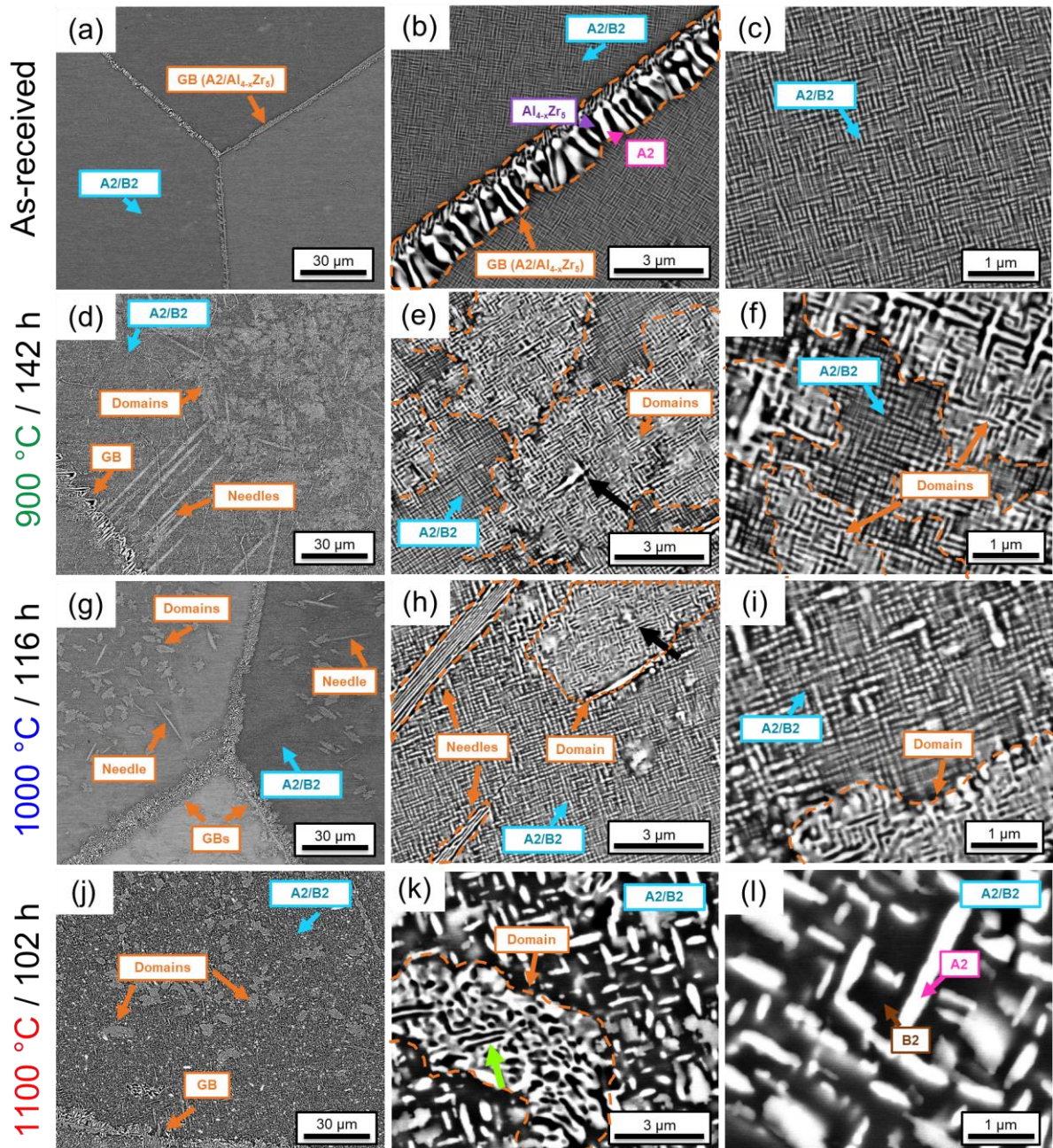


**Figure 4.** Microstructural evolution in the RSA upon annealing between 900 and 1100 °C for 102-142 h. Note that the magnification of the BSE micrographs is the same within a column and increases from left to right. In the rightmost column, the observation direction is close to  $\langle 100 \rangle$ . (a-c) As-received state. (d-l) Microstructures observed at the head of miniaturized creep samples exposed to (d-f) 900 °C for 142 h, (g-i) 1000 °C for 116 h, and (j-l) 1100 °C for 102 h.



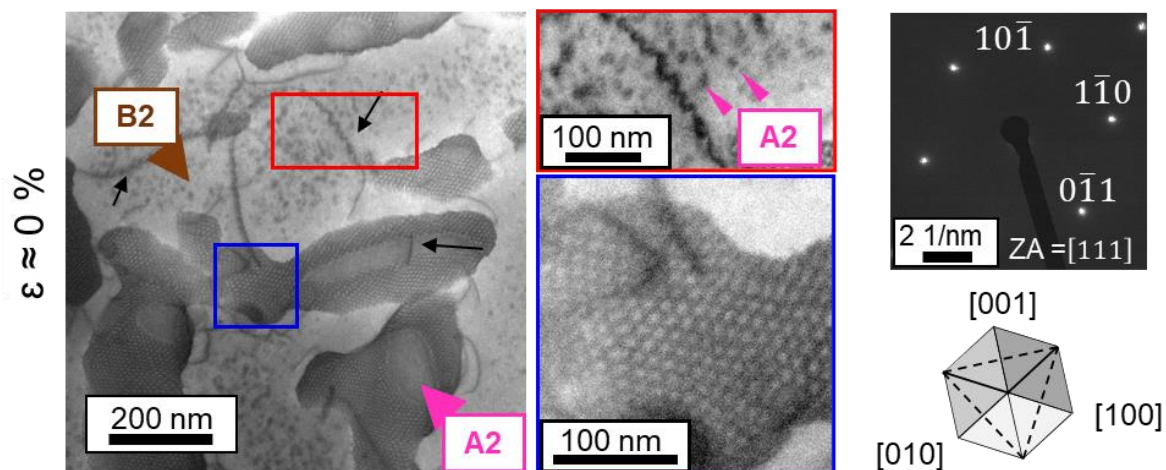


**Figure 5.** STEM-BF micrograph of the A2/B2 substructure in the head of a miniaturized sample ( $\sigma \approx 0$ ) of the RSA after exposure at 1100 °C for  $\approx 200$  h. The zone axis (ZA) is close to  $[111]$  as shown in the diffraction pattern (note that there are no visible superlattice reflections of the B2 phase for this ZA). Two areas of interests are framed in red and blue in the left micrograph and magnified in the middle of the figure. The red framed region shows a wavy dislocation within the B2 matrix reinforced by A2 nanoprecipitates while a dislocation network is visible at the A2/B2 interface in the blue framed region.

### 3.4 Combined effects of applied stress and temperature during creep on microstructure

The effect of the external load on the microstructural evolution of the RSA can be grasped by comparing [Figure 4](#) and [6](#). Besides, [Table S1](#) provides a detailed description of the microstructural parameters obtained on specimens annealed under load (gage of crept specimens) or without any applied stress (head of crept specimens). [Figure 6](#) shows low and high magnification SEM-BSE micrographs of the RSA crept at 900 °C and 60 MPa for 142 h, 1000 °C and 30-60 MPa for 116 h, and 1100 °C and 30 MPa for 102 h. The micrographs display microstructures from the gage ( $\sigma \neq 0$ ) that are comparable to those shown in [Figure 4](#) for the head of the respective samples ( $\sigma \approx 0$ ). For all these samples, the only microstructural feature that seems to be significantly affected by the presence of an external load is the coarsening rate of the A2/B2 substructure, *e.g.*, compare [Figure 6c](#) and [4f](#) after annealing with and without load, respectively.

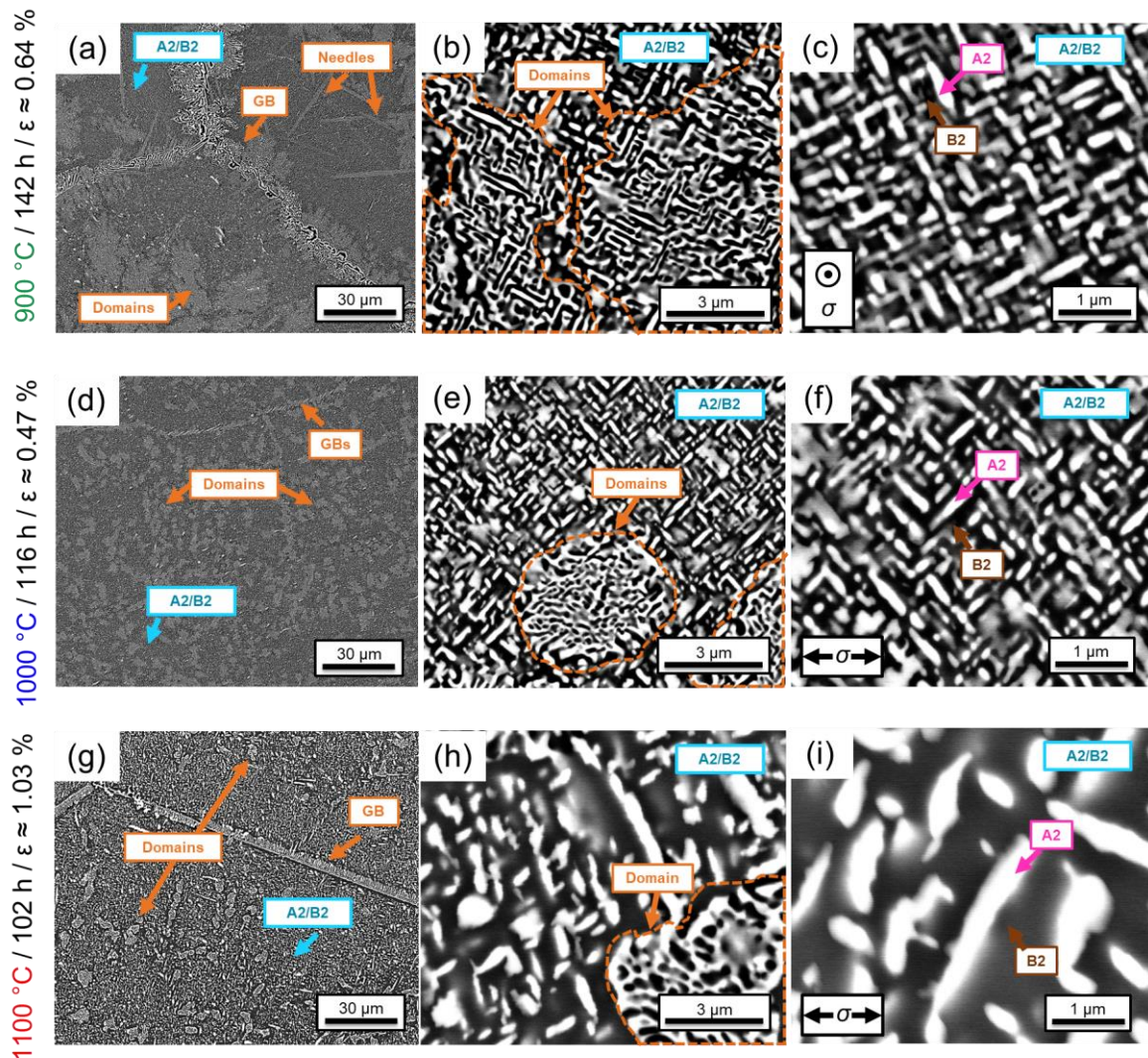


**Figure 6.** Effect of creep temperature on microstructures of the RSA. The magnification of the BSE micrographs is the same within a column and increases from left to right. In the rightmost column, the observation direction is close to  $\langle 100 \rangle$ . Samples crept at (a-c) 900 °C and 60 MPa ( $\epsilon \approx 0.64\%$ ) for 142 h, (d-f) 1000 °C for 116 h ( $\epsilon \approx 0.47\%$ , with a sudden load increase from 30–60 MPa), and (g-i) 1100 °C and 30 MPa ( $\epsilon \approx 1.03\%$ ) for 102 h.

To exemplify how quickly a weak external stress ( $\sigma \approx 60$  MPa) enhances the coarsening rate at 1100 °C, **Figure 7** shows BSE micrographs of the RSA after creep for 11 h, where microstructures at the head ( $\epsilon \approx 0\%$ , **Figure 7a,c**), and the gage region ( $\epsilon \approx 0.66\%$ , **Figure 7b,d**) of the same sample are compared. After this short time, the A2/B2 substructure has already significantly coarsened (**Figure 7c,d**), *i.e.*, the average edge lengths of A2 precipitates are 143–390 nm and 146–475 nm in the head and gage of crept specimens, respectively. For comparison, they are  $18 \pm 9$  nm in the AR state and 217–747 nm after annealing at 1100 °C for 102 h, **Section 3.3**). Thus, the coarsening process seems to be enhanced by a plastic deformation with 18 % larger A2 precipitates in deformed regions than in undeformed regions.



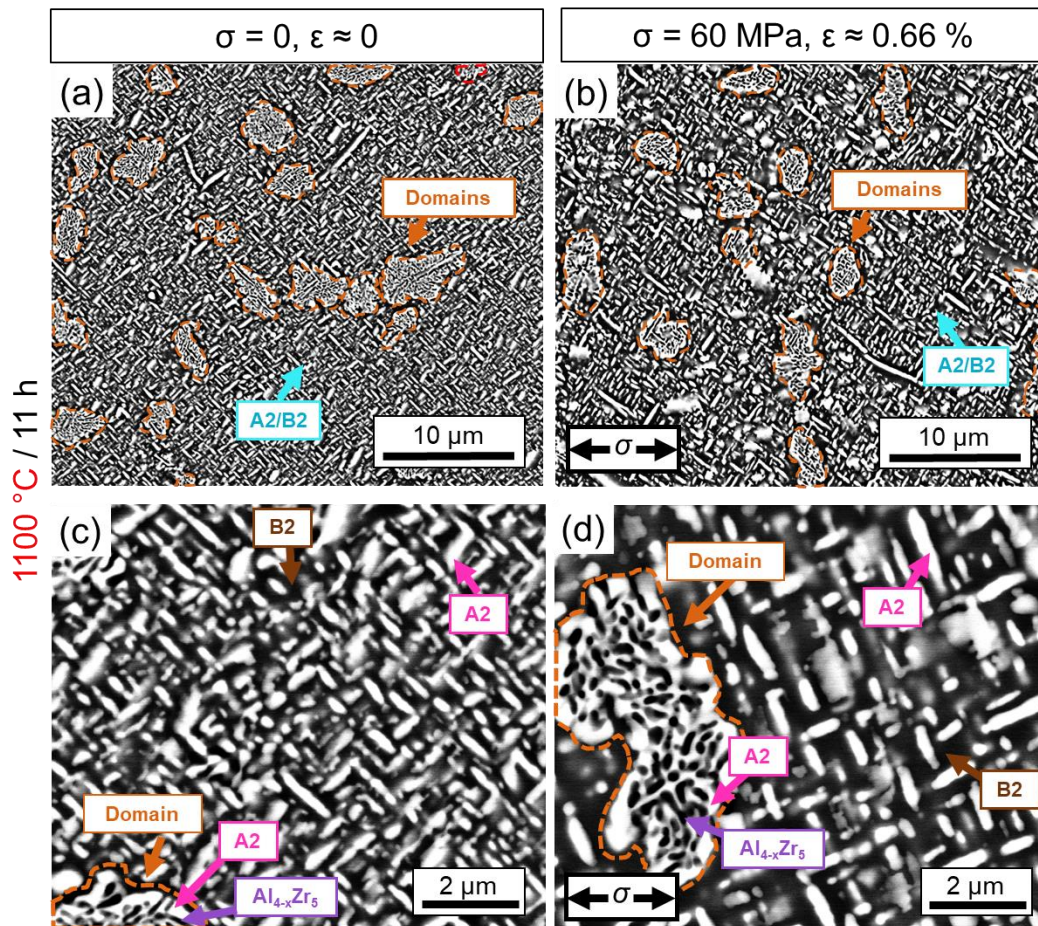


**Figure 7.** Negligible effect of creep load on microstructures in the RSA (a, b) Low and (c, d) high magnification BSE micrographs of the RSA crept at 1100 °C and 60 MPa for 11 h: (a, c) head of the creep sample that is assumed to remain unloaded and to not undergo any plastic deformation, and (b, d) gage section of the sample crept to  $\epsilon \approx 0.66\%$  under 60 MPa. Grains are oriented close to the  $\langle 100 \rangle$  direction.

### 3.5 Orientation relationships (ORs) between A2 and $Al_{4-x}Zr_5$ phases

We have previously showed that parts of the B2 phase transform into  $Al_{4-x}Zr_5$  in regions with different morphologies within grains (irregularly shaped domains, and needles or plates) and at GBs. The aim of this section is to prove this result and to determine the orientation relationships (ORs) between the different phases using EBSD and TEM. The microstructures of the RSA crept at 60 MPa are shown in the BSE micrographs in Figure 8a and b for temperatures of 900 and 1100 °C, respectively. The EBSD maps used to identify the nature of the phases and their orientations were recorded within the white framed regions in Figures 8a,b. Here, the Kikuchi patterns of the dark and bright regions have been indexed according to the crystallographic structures of a hexagonal  $Al_{4-x}Zr_5$  intermetallic, with space group  $P6_3/mcm$ , and A2 phase (space group  $Im\bar{3}m$ ), respectively. The A2 phase exhibits the same orientation in the A2/B2 matrix, A2/ $Al_{4-x}Zr_5$  domains and needles (or plates) and is designated as a1 in Figures 8a,c. Due to their small sizes, cube-on-

cube OR, and small difference in their lattice parameters, the A2 and B2 phases cannot be distinguished by EBSD and are indexed as a single bcc phase. TEM is required to detect the superlattice reflections of the B2 phase, *e.g.*, see our previous work [33] for a detailed characterization of the AR state. The lattice cells in Figure 8a illustrate the crystal orientations of the different constituents of the needle (labeled a1 for A2 and n3 for Al<sub>4-x</sub>Zr<sub>5</sub>) and the domain (a1 and d2 for Al<sub>4-x</sub>Zr<sub>5</sub>) for the RSA crept at 900 °C. Similarly, in Figure 8b, the crystal orientations of the phases in a domain after creep at 1100 °C are named a4 for A2 and d5 for Al<sub>4-x</sub>Zr<sub>5</sub>. Pole figures (PFs) for the A2 (pink) and Al<sub>4-x</sub>Zr<sub>5</sub> (purple) phases in the substructures of the needle and domain in Figures 8a and b are shown in Figures 8c-d, respectively, where the black and gray arrows show the poles of parallel planes and directions that define the OR. The corresponding real space plane normals and directions are represented by black and gray lines on the lattice cells in Figure 8a and b, respectively. For the domains, the OR between the A2 and Al<sub>4-x</sub>Zr<sub>5</sub> phases is the same regardless of temperature:

$$\langle 111 \rangle_{A2} \parallel \langle 0001 \rangle_{Al_{4-x}Zr_5} \text{ and } \{110\}_{A2} \parallel \{10\bar{1}0\}_{Al_{4-x}Zr_5} \quad (2)$$

This OR is consistent with the partial OR reported by Wang *et al.* [35] for the precipitation of a Zr<sub>5</sub>Al<sub>3</sub> phase in an Al<sub>0.4</sub>Nb<sub>0.5</sub>Ta<sub>0.5</sub>TiZr<sub>0.8</sub> RSA with a similar initial A2/B2 microstructure as our alloy, *i.e.*,  $\{110\}_{A2,B2} \parallel \{120\}_{Zr_5Al_3}$ , which coincides with the second term of Equation 2 from the variants we found for the domains.

In contrast, the OR is different within needles (or plates) see Figures 8a,c,d. Their traces, as well as those of the thin elongated A2/Al<sub>4-x</sub>Zr<sub>5</sub> lamellae, are almost parallel to the *c*-axis of Al<sub>4-x</sub>Zr<sub>5</sub>, which in turn seems to run somewhat parallel to one of the {100}<sub>A2</sub> planes (*cf.* Figure 8a). A close inspection of possible crystallographic planes that would yield the least mismatch between the A2 and Al<sub>4-x</sub>Zr<sub>5</sub> phases (see Section e of supplementary material) in the direction orthogonal to the lamellae traces gives:

$$\{100\}_{A2} \parallel \{32\bar{5}1\}_{Al_{4-x}Zr_5} \quad (3),$$

so that a semicoherent substructure could arise with this OR. The PFs at the bottom of Figures 8c,d show that indeed one of the twelve possible  $\{32\bar{5}1\}_{Al_{4-x}Zr_5}$  of n3 is well aligned with one of the {100}<sub>A2</sub> planes of a1.



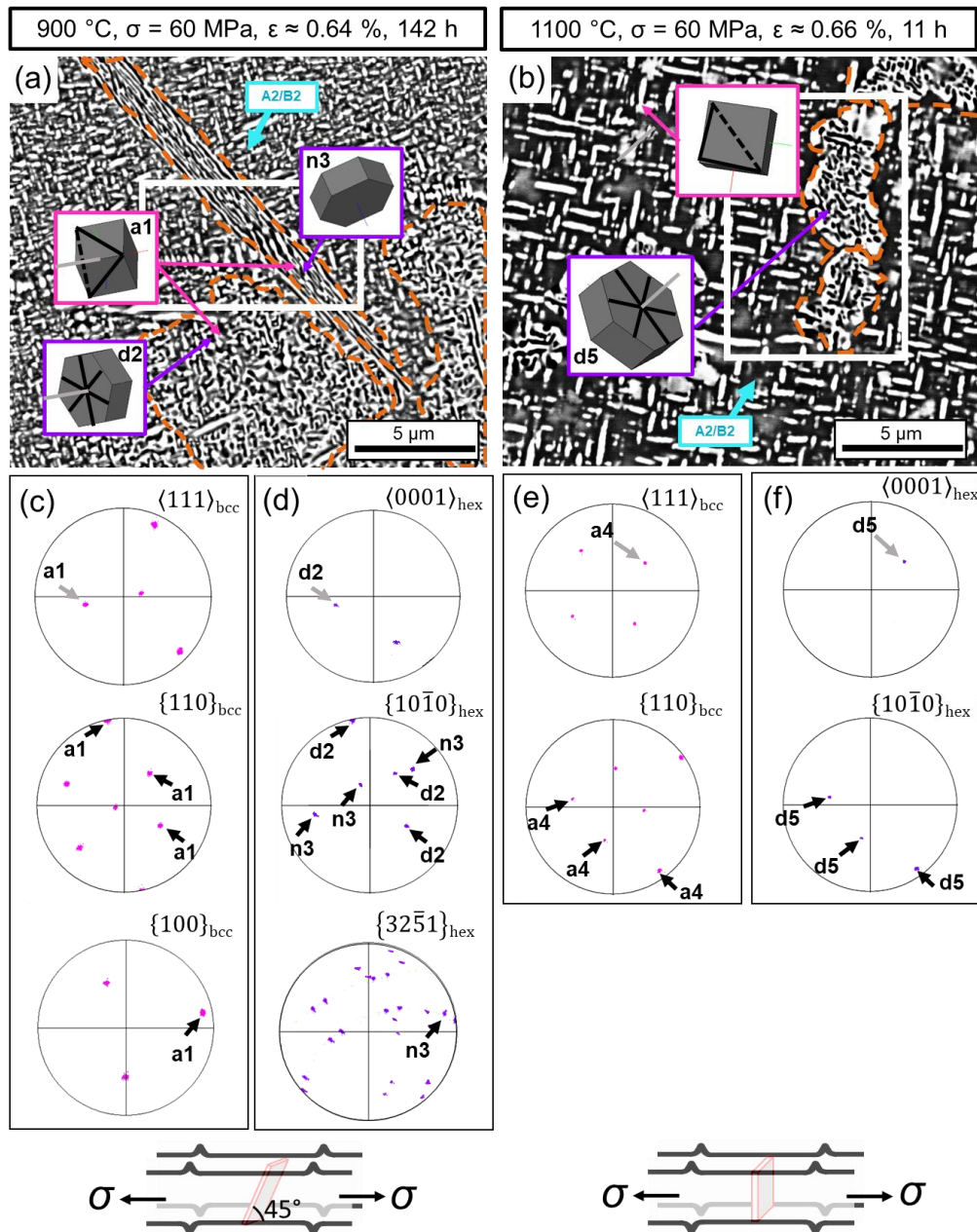


**Figure 8.** Orientation relationship between the A2 and  $Al_{4-x}Zr_5$  phases in grain interiors. BSE micrographs of the RSA recorded within grain cores for samples crept under 60 MPa at (a) 900 °C and  $\epsilon \approx 0.64\%$ , and (b) 1100 °C and  $\epsilon \approx 0.66\%$ . (c, d) and (e, f) Pole figures (PFs) obtained by EBSD and taken from the regions marked with white rectangles in (a) and (b), respectively. (c) A2 phase (a1) in (a); (d)  $Al_{4-x}Zr_5$  phase (d2 and n3) in (a); (e) A2 phase (a4) in (b); and (f)  $Al_{4-x}Zr_5$  in (b). The dashed orange regions enclose A2/ $Al_{4-x}Zr_5$  substructures with either an elongated "needle-like" morphology in (a) or "equiaxed domains" in (a) and (b). Pink and purple colors refer to A2 and  $Al_{4-x}Zr_5$  phases, respectively. Gray lines in (a, b) and gray arrows in (c-f) highlight parallel directions in the A2 and  $Al_{4-x}Zr_5$  phases, while black lines and arrows mark parallel planes. The insets at the bottom of the figure schematically show how the specimens were cut from the gage region prior to SEM and EBSD analyses.

### 3.6 Precipitate morphologies at and near grain boundaries

Representative microstructures at GBs are shown in [Figure 9](#) for samples crept under 60 MPa at 900 °C (left column) and 1100 °C (right). From the white-framed regions in the BSE micrographs ([Figures 9a,b](#)), EBSD analyses were performed, see [Figures 9c-h](#). In both cases, the dark and bright regions at GBs in [Figures 9a,b](#) were identified as a hexagonal  $\text{Al}_{4-x}\text{Zr}_5$  and A2 phases, respectively. Inverse (I)PFs are shown in [Figures 9c](#) and [d](#) where the colors correspond to crystallographic orientations that are normal to the image plane, see colored stereographic triangles at the lower right of [Figure 9](#) for color decoding. The PFs of the A2 and  $\text{Al}_{4-x}\text{Zr}_5$  phases corresponding to [Figures 9c,d](#) are provided in [Figures 9e,f](#), and [Figures 9g,h](#).

For the 900 °C-state, [Figure 9a](#) shows a faceted GB, previously shown in [Figure 4d](#), with bright intrusions adjacent to the boundary on either side. From the edges between facets, thin needles (or plates) have nucleated and grown downwards. Interestingly, the facets of the GB and needles (or plates) are parallel and probably have the same habit plane. In [Figure 9c](#), A2/B2 regions are indexed as bcc (b2/upper red grain and b1/lower green grain) and the purple regions correspond to the hexagonal  $\text{Al}_{4-x}\text{Zr}_5$  phase (n3, dark in [Figure 9a](#)). Except for a few purple islands<sup>2</sup> in the lower grain in [Figure 9c](#), most the  $\text{Al}_{4-x}\text{Zr}_5$  lamellae within needles (or plates) are too thin for EBSD and are indexed as bcc. As the lower grain in [Figure 9a](#) corresponds to the same grain investigated in [Figure 8a](#), the orientations b1 and n3 in the PFs are the same (compare [Figures 8c,d](#) and [9e,f](#)). Since the  $\text{Al}_{4-x}\text{Zr}_5$  phase within needles (or plates) and at the GB has the same crystallographic orientation and that the facets of the GB and the needles are connected and parallel to each other's in [Figure 9a](#), the formation of n3 needles next to the GB may be thus related to the formation of facets at the GB with the same OR ([Equation 3](#)). While neither thin needles nor the same OR is observed in the upper red grain b2 in [Figure 9a](#), red and purple intrusions are found to grow into the green grain. The  $\{110\}_{\text{bcc}}$  pole figure in (e) also shows a subset of three b2 planes aligning with the b1 planes along the trace of n3 structures, *i.e.* along a plane containing the *c*-axis of the hexagonal  $\text{Al}_{4-x}\text{Zr}_5$  phase (*cf.* [Figure 9f](#)).

At the beginning of annealing, the B2 phase is composed of continuous straight channels and cuboidal A2 precipitates. Since the A2 precipitates do not coarsen significantly at 900 and 1000 °C (*cf.* [Figure 5f](#) and [i](#), respectively), fast diffusion pathways are required to enable the B2-to- $\text{Al}_{4-x}\text{Zr}_5$  transformation. The OR between A2 and  $\text{Al}_{4-x}\text{Zr}_5$  within needles (or plates) presented in [Equation 3](#) involves an 0.4 % lattice mismatch at A2/ $\text{Al}_{4-x}\text{Zr}_5$  interfaces, which are probably highly defective.

---

<sup>2</sup> These islands allowed to determine the crystallographic orientation of the  $\text{Al}_{4-x}\text{Zr}_5$  phase within needles (or plates) in [Figure 8a](#).

For this reason, diffusion may be enhanced at these interfaces and thus allows needles (or plates) to grow into the A2/B2 substructure. These interfaces, in turn, being well aligned with the habit planes of the continuous B2 channels, could thus allow almost uninterrupted growth along  $\{100\}_{B2/A2}$  planes (*cf.* Figure 7a).

In contrast to the GB for the 900°C-state, the three GBs connected to the triple point in Figure 9b for the 1100 °C-state rather resembles the original GB morphology of the AR state (*cf.* Figure 4b), with coarse alternating bright/dark regions, with two exceptions: (1) Part of the GB substructure with A2/Al<sub>4-x</sub>Zr<sub>5</sub> lamellae, appears to have grown discontinuously from right to left in the lower right grain (see region with red and blue lamellae at the bottom of Figure 9d); (2) The almost vertical GB at the bottom of Figure 9d exhibits an asymmetric substructure with coarse and fine bright/dark regions on the right and left sides of the GB, respectively. The fine substructure, marked with an orange arrowhead in Figure 9b, is reminiscent of that found in irregularly shaped domains (*e.g.*, Figure 8b) and shows the same OR described by Equation 2 (*cf.* Figures 9g and h). Overall, d7 is the dominant orientation of the Al<sub>4-x</sub>Zr<sub>5</sub> phase at this GB of the triple point in Figures 9d,h. It is also interesting that needles (or plates) were not observed after annealing at 1100 °C. Two reasons can be invoked to rationalize this observation. First, the driving force for B2-to-Al<sub>4-x</sub>Zr<sub>5</sub> transformation is lower at 1100 °C than at 900 and 1000 °C, *i.e.*, the equilibrium Al<sub>4-x</sub>Zr<sub>5</sub>-volume fraction strongly decreases with increasing temperature. Second, the A2/B2 matrix coarsens at a much faster rate at 1100 °C than at lower temperatures (even after only 11 h, *cf.* Figure 7). Since the formation of dislocation networks at A2/B2 interfaces accelerates surface minimization, *i.e.*, spheroidization of the originally straight  $\{100\}$  faceted A2/B2 interfaces, this may impede needle (or plate) formation.

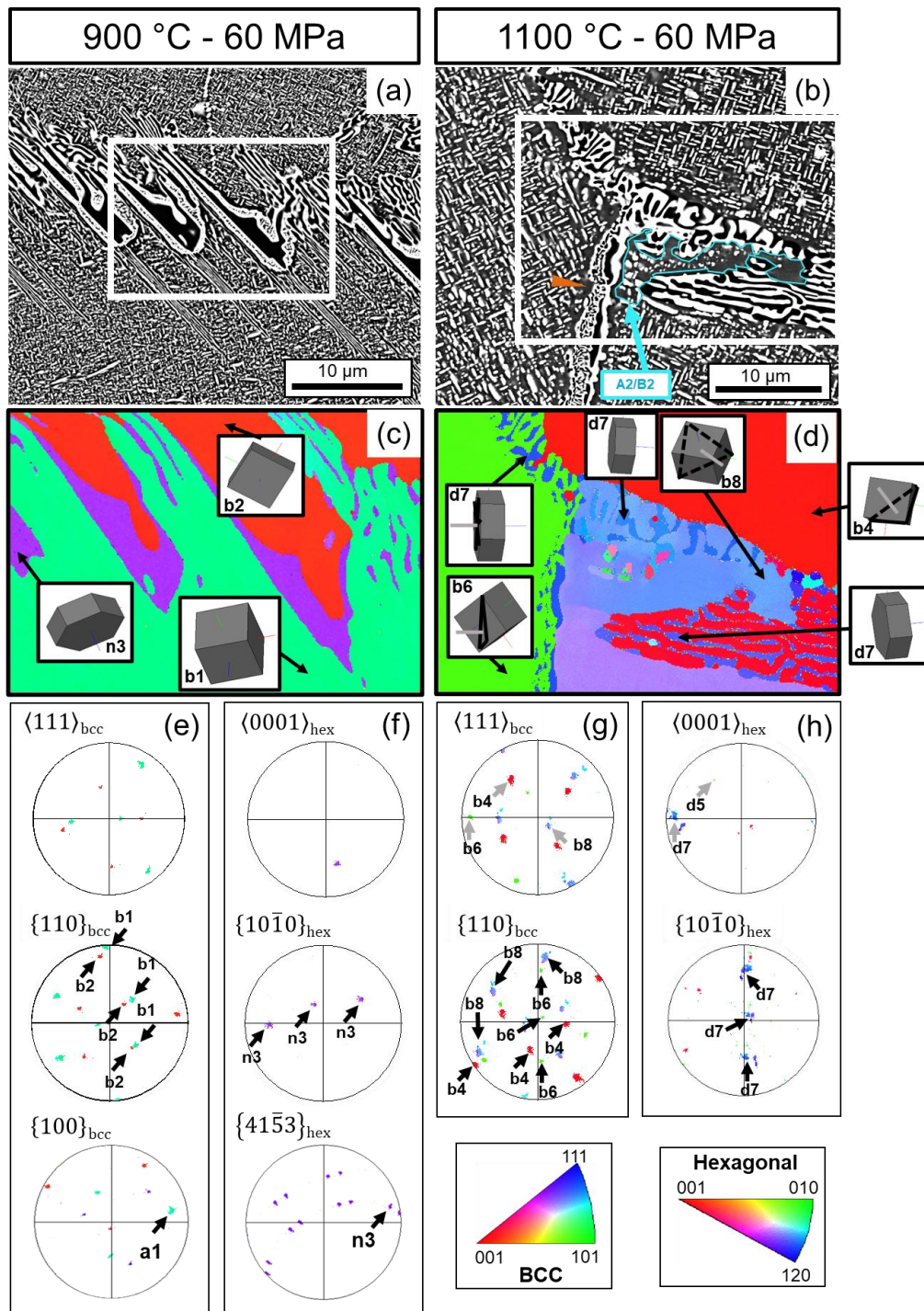


**Figure 9.** Crystallographic aspects of  $\text{Al}_{4-x}\text{Zr}_5$  precipitation at grain boundaries during creep of the RSA. (a, b) BSE micrographs near grain boundaries for samples crept at 60 MPa and (a) 900 °C,  $\varepsilon \approx 0.64\%$ , and (b) 1100 °C,  $\varepsilon \approx 0.66\%$ . (c) and (d) EBSD-IPFZ maps from the white-framed regions in (a) and (b), respectively. PFs of (e) A2 phase (b1 and b2) in (c); (f)  $\text{Al}_{4-x}\text{Zr}_5$  phase (n3) in (c); (g) A2 phase (b4, b6 and b8) in (d); (h)  $\text{Al}_{4-x}\text{Zr}_5$  phase (d7) in (d). Colors in the PFs correspond to the orientation of grains in the IPFZ (for color code, see IPF triangles on the lower right). In (d–h), gray lines/arrows mark parallel directions and black lines/arrows mark normal vectors of parallel planes.



### 3.7 TEM characterization of A2/Al<sub>4-x</sub>Zr<sub>5</sub> and A2/B2 substructures after creep

As the domains are a common microstructural feature of the transformation from A2/B2 to A2/Al<sub>4-x</sub>Zr<sub>5</sub> substructures for all tested conditions, an effort was made to characterize them by TEM. The RSA crept at 1100 °C was exemplarily analyzed in Figure 10. Here, low (Figure 10a) and high-magnification (Figure 10b) STEM-HAADF micrographs of two different A2/Al<sub>4-x</sub>Zr<sub>5</sub> domains in the same grain are displayed. The loading direction is approximately normal to the image plane, as shown in the upper right corner of Figure 10. As the A2/Al<sub>4-x</sub>Zr<sub>5</sub> domains reacted more strongly to the electropolishing agent, they are thinner than the original A2/B2 matrix (for details, see Section 1a of the supplementary material). For this reason, the A2/B2 substructure appears darker in STEM-HAADF micrographs (Figures 10a,b, lower atomic number contrast) and brighter in STEM-BF (thinner, Figures 10c,d). The micrographs in Figures 10a,b show similar bright (A2) and dark (Al<sub>4-x</sub>Zr<sub>5</sub>) contrasts as the BSE images, *e.g.*, Figure 8b, while there is a contrast inversion in the STEM-BF micrographs in Figures 10c,d.

As shown in Figure 10, as well as Figures 4 and 6, the A2 phase in A2/Al<sub>4-x</sub>Zr<sub>5</sub> domains is continuous while the Al<sub>4-x</sub>Zr<sub>5</sub> phase forms isolated islands. In other words, while the continuous phase was originally the B2 intermetallic in the A2/B2 substructure, the disordered A2 solid solution becomes the continuous phase during annealing while the Al<sub>4-x</sub>Zr<sub>5</sub> intermetallic phase is discontinuous. Therefore, the B2-to-Al<sub>4-x</sub>Zr<sub>5</sub> transformation induces a kind of "topological phase inversion". Although most of the A2/Al<sub>4-x</sub>Zr<sub>5</sub> substructure in the domain has a coarse and wavy shape, the central region has a thin, long, and straight shape, parallel to the trace of the (111)<sub>A2</sub> plane (*cf.* blue line in Figure 10a,e) that would be coplanar to (0001)<sub>Al<sub>4-x</sub>Zr<sub>5</sub></sub>, based on the OR in Equation 2. The insets in Figures 10a,b are selected area diffraction patterns (SADP) from the region marked with orange circles within the domains, both of which can be indexed with the hexagonal Al<sub>4-x</sub>Zr<sub>5</sub> and A2 phases observed along the zone axes  $ZA_{Al_4-xZr_5}=[201]$  and  $ZA_{A2}=[111]$ , respectively. These patterns show that the  $\{030\}_{Al_4-xZr_5}$  planes are coplanar with a different set of  $\{110\}_{A2}$  in either pattern, *i.e.*, indicating the existence of two variants within the same grain with the same OR described by Equation 2. Based on this OR, the XRD pattern in Figure S8c reveals that the  $\{300\}_{Al_4-xZr_5}$  diffraction peak is closer to the  $\{110\}_{A2}$  peak than the  $(110)_{B2}$  peak, indicating that there is a larger misfit between the A2 and B2 than between A2 and Al<sub>4-x</sub>Zr<sub>5</sub> phases. Therefore, it can be concluded that the transformation of A2/B2 regions into A2/Al<sub>4-x</sub>Zr<sub>5</sub> domains allows to reduce the overall elastic strain energy stored into the material.

TEM-EDS point analyses of the different phases within and around the domains were performed, and the results are summarized in Table 3. In Figure 10a and Table 3, bcc1 and bcc2 refer to the A2 phase in A2/B2 and A2/Al<sub>4-x</sub>Zr<sub>5</sub> substructures, respectively. In both substructures, the composition of the A2 phase is similar, *i.e.*, the A2 phase is enriched in Mo, Nb, Ta and depleted in Al and Zr

(*cf.* Table 3). Al, Zr and Ti to a much lesser extent are found to partition to the B2 phase. While the B2 phase is slightly enriched in Ti, the  $\text{Al}_{4-x}\text{Zr}_5$  phase is poorer in this element. More importantly, the  $\text{Al}_{4-x}\text{Zr}_5$  phase is more strongly enriched in Al and Zr and depleted in Mo, Nb, Ta than the B2 phase. As A2 formers (*e.g.*, Mo, Nb and Ta) have a lower solubility in  $\text{Al}_{4-x}\text{Zr}_5$  than in B2, these solutes are released during the B2-to- $\text{Al}_{4-x}\text{Zr}_5$  transformation and promote the formation of additional A2 phase. This may be the reason why there is more A2 phase in A2/ $\text{Al}_{4-x}\text{Zr}_5$  domains ( $\approx 43\%$ ) than in the A2/B2 matrix of the as-received material ( $\approx 38\%$ , see Table S1) and this may also contribute to the fact that the A2 phase becomes the continuous phase in A2/ $\text{Al}_{4-x}\text{Zr}_5$  domains.

The framed region in the STEM-BF micrograph in Figure 10c is magnified in Figure 10d, which reveals the presence of dislocations in the A2 (bcc2) phase within domains while  $\text{Al}_{4-x}\text{Zr}_5$  is almost dislocation free. By accounting for the thin character of the TEM foils in the domains, the dislocation density was estimated as  $\rho_{\text{domain}} \approx (2.1 \pm 1.0) \cdot 10^{12} \text{ m}^{-2}$ . Many of the straight dislocation segments found in Figure 10d, *e.g.*, those marked with green and red arrows, have projected line directions parallel to traces of common A2 slip planes, *e.g.*,  $(1\bar{1}0)$  and  $(312)$  [162], which are marked with green and red lines, respectively, in Figures 10d and e.

**Table 3.** Compositions in at.% of the phases in different regions after exposure at 1100 °C for  $\approx 200$  h and  $\varepsilon \approx 1.22\%$ . As a comparison, we also provide in this table the composition of the as-received sample before creep. Elements rich in this phase are highlighted in bold.

Region	Phase fraction / %	Method	Description	Elemental composition / at.%					
				Al	Mo	Nb	Ta	Ti	Zr
Alloy	-	SEM-EDX	Average alloy composition from five different regions at low magnification (200 X)	22	11	20	8	21	18
B2	$33 \pm 3$	TEM-EDX	Dark phase in grain core ( <i>cf.</i> brown arrow in Figure 10)	17	9	20	4	22	28
$\text{Al}_{4-x}\text{Zr}_5$ , $0 \leq x \leq 1$	$14 \pm 1$	TEM-EDX	Dark phase in domains of grain core ( <i>cf.</i> purple arrow in Figure 10)	25	5	13	2	10	45
A2 (bcc1)	$42 \pm 3$	TEM-EDX	Bright phase in grain core ( <i>cf.</i> pink arrow in Figure 10, marked as bcc2)	4	22	33	18	19	3
A2 (bcc2)	$11 \pm 1$	TEM-EDX	Bright phase in domains ( <i>cf.</i> pink arrow Figure 10 marked as bcc1)	5	23	33	17	17	5

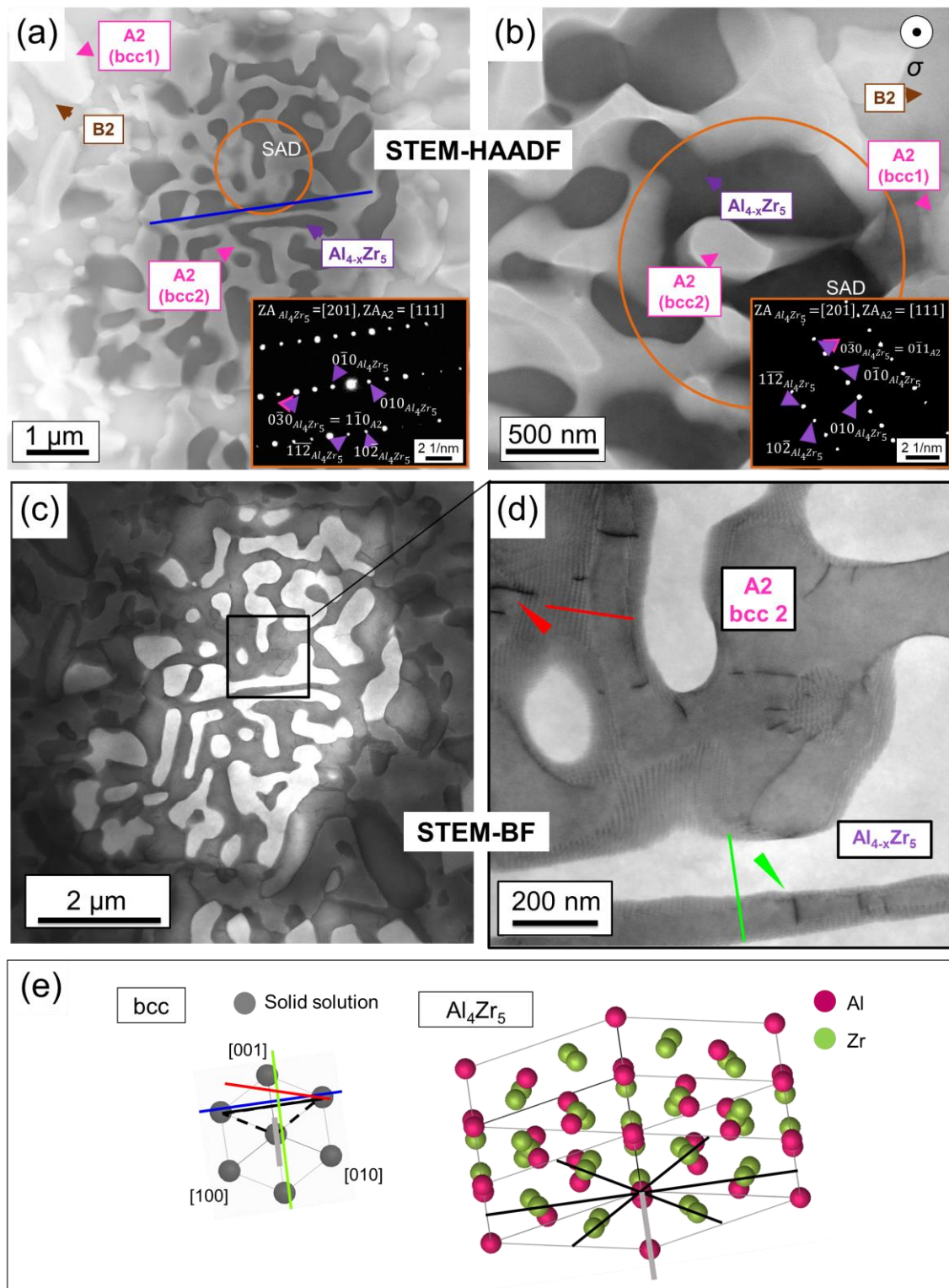


**Figure 10.** STEM micrographs of A2/Al<sub>4-x</sub>Zr<sub>5</sub> domains in the RSA crept at 1100 °C for  $\approx 200$  h to  $\varepsilon \approx 1.22$  %, with a load increase from 30 to 60 MPa after 154 h at  $\varepsilon \approx 0.74$  %. (a) Low and (b) high magnification STEM-HAADF micrographs of two domains. Indexed SAD patterns, displayed as insets. (c) Low and (d) high-magnification STEM-BF micrographs of the domain shown in (a). (e) Simulated bcc (A2) and Al<sub>4</sub>Zr<sub>5</sub> lattices. Blue, red, and green lines in (a,d,e) denote traces of characteristic planes in A2 phase. For more details, see text.

**Figure 11** shows a STEM-BF micrograph of the A2/B2 substructure in the RSA after creep exposure at 1100 °C for  $\approx 200$  h to  $\varepsilon \approx 1.22$  %, with a load increase from 30 to 60 MPa after 154 h at  $\varepsilon \approx 0.74$  %. The region of the foil was oriented along  $ZA = [111]_{A2/B2}$  (*cf.* SADP on the right), about 15° away from the loading direction, which is marked as being orthogonal to the images in **Figure 11**. The image on the left shows A2 precipitates that have grown, coalesced, and lost their straight facets with respect to the original A2/B2 substructure of the AR material. Hexagonal networks of dislocations, with a mean mesh size of  $\approx 6$  nm, are visible at wavy A2/B2 interfaces (see red-framed micrograph in the middle of **Figure 11**). It was recently showed by Kloenne *et al.* [9] that the Burger's vector of these misfit dislocations at A2/B2 interfaces is  $\vec{b} = a_0/2[\bar{1}11]$ .

Although they are scarce, some dislocation segments bow out within A2 precipitates, likely on  $\{110\}$  planes, *e.g.*, the straight segment of the dislocation marked with a green arrow is parallel to the  $(1\bar{1}0)$  trace (green lines in **Figure 11**). These dislocations end at A2/B2 interfaces (*cf.* green arrow in **Figure 11**) so that they interact with the misfit dislocations there by knitting in-knitting out processes. A similar effect is observed in the B2 matrix phase (*cf.* black arrows in **Figure 11**). These interactions result in a dragging contribution that impedes dislocation motion in the A2 phase [37]. Such mechanisms were suggested also for the topologically inverted Ni-based superalloy LEK 94 [38, 39] when its  $\gamma/\gamma'$  structure in fact resembles that of the coarsened A2/B2 in **Figure 11**, but with channel and precipitate widths that double those found here after similar creep exposure.

In the B2 phase, the dislocation lines are either straight or slightly curved (*cf.* black arrows in **Figure 11**), indicating a form of viscous glide that impedes dislocation motion. The B2 phase in A2/B2 substructures is expected to play a role in dislocation transfer between isolated A2 precipitates. Based on the work of Kral *et al.* [14] on a similar B2 phase composition, dislocations in the B2 phase are assumed to have a Burger's vector  $\vec{b} = a_0\langle 111 \rangle$ .

The dislocation density in the interior of the A2 and B2 phases is rather low,  $\rho_{A2/B2} \approx (1.1 \pm 0.5) \cdot 10^{13}$  m<sup>-2</sup>. Interestingly, the dislocation density is higher in the head ( $\sigma \approx 0$ , *cf.* **Figure 5**) than in the gage ( $\sigma \neq 0$ , *cf.* **Figure 11**) of the creep specimen. One possible explanation for this observation can be attributed to the formation of dislocations upon cooling from 1100 °C to 20 °C after creep due to differences in coefficients of thermal expansion of the sample and grips. A comparison of **Figure 5** (annealed without load) and **Figure 11** (crept) further reveals a similar A2/B2 substructure, although the crept microstructure is coarser than the annealed one. Moreover, the fact that A2 nanoprecipitates were observed within the B2 phase of the creep sample head (red-framed micrograph in **Figure 5**) and not in the gage (**Figure 11**) can be explained as follows. After creep testing at 1100 °C, the sample is cooled to 20 °C. As the gage region is cooled at a faster rate than the heads of the creep specimen due to the high thermal inertia associated with the massive clamping



adaptors, the cooling rate within the gage is fast enough to preclude the precipitation of the A2 phase in the supersaturated B2 phase while in the heads, the cooling rate is sufficiently low to allow for precipitation.

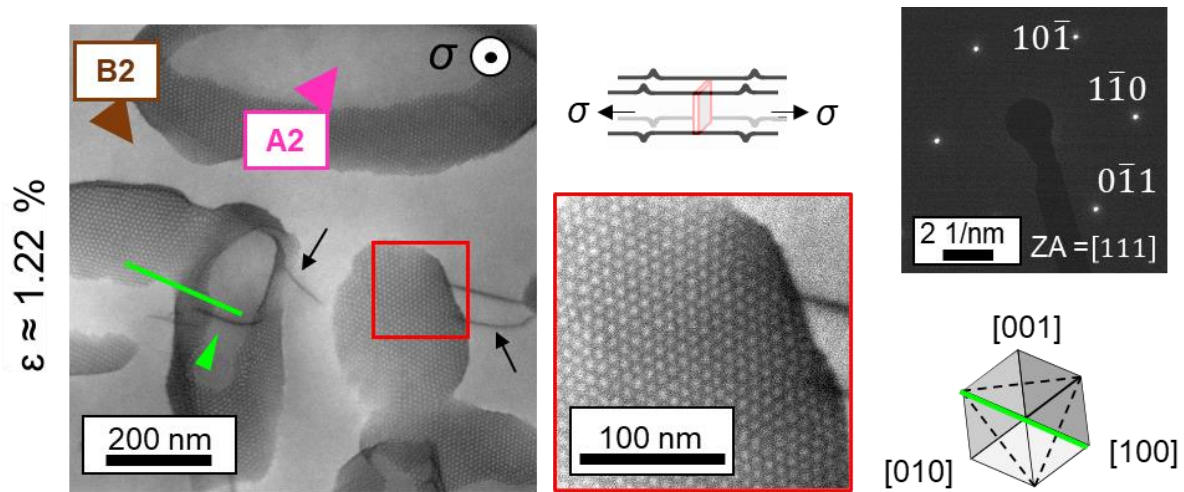


**Figure 11.** Dislocation networks at A2/B2 interfaces in the RSA crept at 1100 °C for  $\approx 200$  h to  $\varepsilon \approx 1.22$  %, with a load increase from 30 to 60 MPa after 154 h at  $\varepsilon \approx 0.74$  %. The left STEM-BF micrograph shows a region observed along a  $\langle 111 \rangle$  direction as shown by the diffraction pattern. In the left image, the red-framed region is magnified in the middle of the figure and reveals a dislocation network at the A2/B2 interface. For details, see text.

### 3.8 Deformation mechanisms and microstructural changes contributing to the creep behavior

The RSA and its creep behavior are complex in many ways: (1) not only the A2 precipitates but also the B2-matrix present a high concentration of various elements (*cf.* Table 3), which is the essence of a complex concentrated alloys; (2) the base microstructure resembles the coherent cube-on-cube substructure of Ni-based superalloys, albeit with an inverted substructure, which is one order of magnitude smaller than the common  $\gamma/\gamma'$  structure, and a different crystallographic structure (fcc in Ni-based superalloys and bcc in the present RSA); (3) a recently studied phase instability occurs [10, 35] during which the A2/B2 structure transforms into what we have named domains that consist of a hard  $\text{Al}_{4-x}\text{Zr}_5$  intermetallic and a soft A2 phase; (4) the GBs of the RSA are fully covered by alternating  $\text{Al}_{4-x}\text{Zr}_5$  and A2 lamellae, which hinders grain boundary sliding and favors the B2-to- $\text{Al}_{4-x}\text{Zr}_5$  transformation during annealing; (5) high temperatures (*e.g.*, 1100 °C) promote

the coarsening rate of the A2/B2 nanostructure and A2/Al<sub>4-x</sub>Zr<sub>5</sub> domains, which reduces the Orowan stress<sup>3</sup>, enables a greater mobility of the dislocations and thus promotes higher creep rates.

In the present work, the temperature and stress dependencies of the minimum creep rate,  $\dot{\epsilon}_{min}$ , in the RSA have been determined and an attempt is made to correlate them with the main deformation mechanisms and microstructural changes observed in the alloy. In Section 3.4, it was shown that, except for a slightly faster coarsening rate of the A2/B2 nanostructure, the presence of an external stress does not significantly affect the microstructural evolution during annealing. For this reason, we believe that the B2-to- Al<sub>4-x</sub>Zr<sub>5</sub> transformation does not significantly affect the Norton exponent. The latter is comprised between 2.7 and 3.4 in the low-stress regime ( $30 < \sigma < 90$  MPa, [Table 2](#) and [Figure 3a](#)). Although coarsening of both the original A2/B2 and the A2/Al<sub>4-x</sub>Zr<sub>5</sub> substructures occurs during creep (*cf.* [Table S1](#)), the Orowan stresses fall in a range well above the applied stress. Thus, the Norton exponent of  $\approx 3$  can be attributed to both dislocation climb and viscous glide acting as the main rate-controlling deformation mechanisms, for which solute drag is usually assumed [40].

The calculated apparent activation energy,  $Q_c$ , has a value of  $\approx 111$  kJ/mol for the RSA between 900 and 1100 °C. This value is very low compared to that of other rCCAs [16] and CCAs [13, 41], which range from 300 to 660 kJ/mol, see [Table 4](#). One possible explanation is that  $Q_c$  was determined in the present work at low homologous temperatures where elastic constants are much stiffer, *i.e.*,  $T/T_m < 0.65$  (where  $T_m \approx 1895$  °C is the melting temperature of the RSA [19]) a factor known to decrease  $Q_c$  in some alloys [18].

The calculation method is also usually suited for five- and not for three-power-law creep and it assumes that the microstructure of the material remains constant, which is not the case here. We observe temperature-dependent microstructural changes that may also contribute to the very low activation energy of the RSA. Therefore, the value of  $Q_c$  determined graphically must be seen skeptically.

The most important microstructural change that was observed during creep is the formation of irregularly shaped A2/Al<sub>4-x</sub>Zr<sub>5</sub> domains from the A2/B2 matrix. This transformation can be seen as a recovery/softening process for several reasons. (1) Since the lattice misfit is lower between the A2 and Al<sub>4-x</sub>Zr<sub>5</sub> phases than at A2/B2 interfaces, the B2-to-Al<sub>4-x</sub>Zr<sub>5</sub> transformation results in a

---

<sup>3</sup> The Orowan stress can be calculated using:  $\tau_{Orowan} = \mu b/d$ , where  $\mu$  is the shear modulus,  $b$  is the magnitude of the Burger's vector, and  $d$  is assumed as the narrowest average width within the phase containing the dislocation glide plane.

decrease of the misfit stresses, which may oppose dislocation glide. (2) The extensive B2-to- $\text{Al}_{4-x}\text{Zr}_5$  transformation within irregular domains leads to a kind of "topological phase inversion" that promotes plasticity, *i.e.*, while the continuous phase is originally the hard B2 intermetallic in the A2/B2 substructure, the soft A2 phase becomes the continuous phase after longer time in A2/ $\text{Al}_{4-x}\text{Zr}_5$  domains, which helps bypassing the strong  $\text{Al}_{4-x}\text{Zr}_5$  precipitates without having to cut through them, as evidenced in [Figure 10d](#).

We now want to explain how the B2-to- $\text{Al}_{4-x}\text{Zr}_5$  transformation, which is associated with recovery processes, may affect the very low apparent activation energy for creep. As shown previously, the lower the temperature is, the larger the volume fraction of A2/ $\text{Al}_{4-x}\text{Zr}_5$  domains, and thus the stronger the recovery. Therefore, we believe that this B2-to- $\text{Al}_{4-x}\text{Zr}_5$  transformation is responsible for the very low apparent activation energy for creep in the RSA.

### *3.9 Comparison of the creep properties of the RSA with those of bcc-structured alloy, other RSAs, and engineering materials*

The creep properties of the RSA are now compared with those of alloy families that present either similar phases (ordered B2, disordered bcc, or a combination of both) or a similar microstructure (matrix reinforced by precipitates such as Ni-based superalloys).

#### *Comparison with bcc-structured alloys*

In alloys with a B2 matrix, such as stoichiometric NiAl single crystals (only a B2-phase) [42], polycrystalline NiAl alloys reinforced by yttria dispersoids [43], and Fe-40Al with small additions of Mo, Zr, Ti, B and C [44, 45], Norton exponents (3-5) are found to be similar to our RSA but the apparent activation energies for creep are much higher (300-400 kJ/mol, attributed to self-diffusion in the B2 phase) due to the B2-to- $\text{Al}_{4-x}\text{Zr}_5$  transformation in the RSA as presented in section 3.8. Overall, under comparable conditions, the minimum creep rates of B2 alloys are much faster by several order of magnitudes than those found in the present work for the RSA, see [Table 4](#).

Recently The  $\text{AlTiVNbZr}_{0.25}$  RSA, composed of a B2 matrix and coarse  $\text{Zr}_5\text{Al}_3$  particles inside the grains and along GBs (with similar lattice parameters as the  $\text{Al}_{4-x}\text{Zr}_5$  phase in our alloy), crept at 800 °C, was reported to have a  $\dot{\epsilon}_{min} \approx 2.9 \times 10^{-7} \text{ s}^{-1}$  at 100 MPa and  $\dot{\epsilon}_{min} \approx 8.0 \times 10^{-7} \text{ s}^{-1}$  at 150 MPa, respectively [14]. Considering the similarity in elemental composition with our alloy, we expect similar creep properties. Based on an extrapolation of our data for the  $\text{AlMo}_{0.5}\text{NbTa}_{0.5}\text{TiZr}$  RSA at 800 °C for applied stresses of 100 and 150 MPa, it is expected that the latter RSA is more creep

resistant, *i.e.*, its  $\dot{\epsilon}_{min}$  value should be 2 orders of magnitude lower for 100 MPa and 1 order of magnitude lower for 150 MPa<sup>4</sup>, than those of AlTiVNbZr<sub>0.25</sub>.

The creep behavior of the HfNbTaTiZr refractory high entropy alloy, which forms a single-phase bcc solid solution has been reported at 1100-1250 °C and 5–30 MPa [16]. Based on the reported data, the only temperature and stress combination that can be compared is 1100 °C / 30 MPa, for which  $\dot{\epsilon}_{min} = 7.9 \times 10^{-6} \text{ s}^{-1}$ . Our RSA deforms under the same conditions with a minimum creep rate of  $4.0 \times 10^{-9} \text{ s}^{-1}$ , which is  $\approx 2000$  times slower. To conclude, the AlMo<sub>0.5</sub>NbTa<sub>0.5</sub>TiZr RSA with a A2/B2 nanostructure is more creep resistance than B2 alloys and bcc solid solutions, thus demonstrating the superior creep behavior of a two-phase material.

#### *Comparison with Ni-based superalloys*

When Senkov *et al.* [7] introduced the AlMo<sub>0.5</sub>NbTa<sub>0.5</sub>TiZr RSA, they showed how its high-temperature compressive strength (also under vacuum) surpassed that of the state-of-the-art polycrystalline precipitation strengthened Ni-based superalloys Inconel 718 (wrought alloy with < 20 Vol.%  $\gamma'$ -precipitates (ordered L1<sub>2</sub>) in a disordered face centered cubic  $\gamma$  matrix ) and Mar-M247 (cast alloy with > 60 Vol.%  $\gamma'$ -phase). In Table 4, a similar comparison can be made for high-temperature creep in terms of  $\dot{\epsilon}_{min}$ ,  $n$ , and  $Q_c$ , which will be discussed in the following.

The creep properties of the AlMo<sub>0.5</sub>NbTa<sub>0.5</sub>TiZr RSA at 900 °C under 30 and 60 MPa resulted in minimum creep rates of  $8.6 \times 10^{-10}$  and  $5.7 \times 10^{-9} \text{ s}^{-1}$ , respectively, which are  $\approx 2$ -4 orders of magnitude lower than those of Inconel 718 [48] and C-264 [50] superalloys (*cf.* Table 4), in other words the RSA is more creep resistant than wrought Ni-based superalloys with < 20 Vol.%  $\gamma'$ . Regarding the creep parameters of the latter wrought alloys at 900 °C and 50-70 MPa, the Norton exponents are comprised between 2.3 and 4.4 and the apparent activation energies for creep ranges from 492 kJ/mol to 550 kJ/mol, which can be attributed to dislocation creep and cutting as the rate controlling mechanisms depending on the stress/temperature combination [48, 50]. Wrought superalloys are not designed to reach temperatures above 900 °C, as dissolution and/or coarsening of the strengthening  $\gamma'$  phase ( $935 \text{ °C} < \gamma'\text{-solvus} < 1015 \text{ °C}$ ) renders it very ductile [50] and transformation of  $\gamma''$  to deleterious  $\delta$  needles or rods in Inconel 718 accelerates damage accumulation with the formation of voids at GBs [48].

---

<sup>4</sup> The extrapolation yield to values of  $\dot{\epsilon}_{min} \approx 9.2 \times 10^{-9} \text{ s}^{-1}$  at 100 MPa and  $\dot{\epsilon}_{min} \approx 7.9 \times 10^{-7} \text{ s}^{-8}$  at 150 MPa, for the RSA. This extrapolation is made assuming that the material's behavior remains constant across the temperature and strength range.



**Table 4.** Comparison of minimum creep rates ( $\dot{\epsilon}_{min}$ ) and creep parameters ( $n$ ,  $Q_c$ ) of the AlMo<sub>0.5</sub>NbTa<sub>0.5</sub>TiZr RSA with those of high-temperature materials and alloys with similar phases.

Starting microstructure	Alloy	$T$ [°C]	$\sigma$ / MPa	$\dot{\epsilon}_{min}$ / s <sup>-1</sup>	$n$	$Q_c$ / kJ/mol	Reference
A2/B2 nanostructure + continuous GB A2/Al <sub>4-x</sub> Zr <sub>5</sub>	RSA	900	30	$8.6 \times 10^{-10}$	$\approx 2.7$	111 ± 11	this work
			60	$5.7 \times 10^{-9}$			
		1000	30	$9.0 \times 10^{-9}$	$\approx 2.7$		
			30 - 60	$1.1 \times 10^{-9}$			
			90	$3.7 \times 10^{-8}$	$\approx 5.5$		
			120	$7.5 \times 10^{-8}$			
		1100	160	$7.7 \times 10^{-7}$	$\approx 3.4$		
			30	$6.0 \times 10^{-9}$			
			60	$3.7 \times 10^{-8}$			
				90	$1.5 \times 10^{-7}$		
Ni-based, $\gamma/\gamma'$ ( $\gamma''$ ) structure + GB precipitates (carbides and/or intermetallics)	Mar-M247	982	150	$1.06 \times 10^{-8}$	-		<i>cf.</i> Table 3, sample 4 in [46]
		950	150	$1.8 \times 10^{-9}$	$\approx 5^*$	660**	<i>cf.</i> Table 1 in [47]
		1000	100	$1.7 \times 10^{-9}$			
		1000	150	$3.6 \times 10^{-8}$			
	In718	900	50	$1.9 \times 10^{-6}$	$\approx 2.3$	492	[48]
	SX DD33	1100	120	$1.8 \times 10^{-7}$	-	-	[49]
			174	$8.3 \times 10^{-6}$			
	C-264	900	60	$1.0 \times 10^{-7}$	$\approx 4.4$	550	[50]
			70	$2.0 \times 10^{-7}$			
			950	$5.0 \times 10^{-6}$			
B2-structured	NiAl single crystals	1000	$\approx 30$	$10^{-5} - 10^{-4}$	5	300	[42]
	NiAl alloyed with fine yttria dispersoids	$\approx 1027$	30	$1.0 \times 10^{-5}$			[43]
		$\approx 1127$		$8.0 \times 10^{-5}$			
	Fe-40Al with small additions of Mo, Zr, Ti, B and C (787)	700	60	$2.5 \times 10^{-7}$	$\approx 3-5$ [44]	300-400 [44]	[45]
90			$3.5 \times 10^{-6}$				
B2-structured + Zr <sub>5</sub> Al <sub>3</sub> -type intermetallic particles	AlTiVNbZr <sub>0.25</sub>	$\approx 800$ °C	100	$2.9 \times 10^{-7}$	-	-	[14]
			150	$8.0 \times 10^{-7}$			

\*Graphically determined from 100 and 150 MPa data points in Figure 9a in [47]

\*\*Determined at 200 MPa (Figure 12 in [47]).

In contrast to wrought superalloys, cast superalloys with higher  $\gamma'$  volume fraction and  $\gamma'$ -solvus (*e.g.*,  $\approx 62$  Vol.%  $\gamma'$  and  $\gamma'$ -solvus  $\approx 1230$  °C in Mar-M247 [46]) can be subjected to temperatures up to 1000 °C with better  $\dot{\epsilon}_{min}$  than the RSA by roughly one order of magnitude. In both wrought and cast superalloys, GBs are pinned by carbides, which prevent GBs from sliding at high temperatures. For cast superalloys, degradation mechanisms include rafting of the  $\gamma'$ -phase and dissolution of carbides. In this sense, similar mechanisms occur in the Mar-M247 cast superalloy and our RSA. For example, both alloys present a high amount of refractory elements that render their nanostructured ordered phases but also their solid solutions more resistant at high temperatures; particle sizes of the same order of magnitude; rafting evolves (*cf.* Figure 6c,f,i) with overlapping internal and external stresses; grain boundary pinning, in the RSA by the A2/Al<sub>4-x</sub>Zr<sub>5</sub> substructure, although its discontinuous growth may ultimately render it too brittle GBs.

To eliminate grain boundary effects, single crystalline superalloys can be produced such as the DD33 and LEK 94 superalloys. These alloys have a microstructure morphology that resembles that of the RSA but is based on the typical  $\gamma/\gamma'$  structure, and which for our coarse-grained RSA is stiff GBs. When comparing the  $\dot{\epsilon}_{min}$  with SX DD33 alloy, it is evident that our RSA presents a faster creep at 1100 °C, *i.e.*, for 90 MPa in the RSA  $\dot{\epsilon}_{min}$  is similar to that of the SX DD33 alloy at 120 MPa (higher stress). Regarding the creep mechanism described for the SX DD33, Yue *et al.* [49] reported that at 1100 °C and stress levels ranging from 120 MPa to 174 MPa,  $\dot{\epsilon}_{min}$  exhibited a significant dependence on stress, with values ranging from approximately  $1.8 \times 10^{-7} \text{ s}^{-1}$  at 120 MPa to around  $8.3 \times 10^{-6} \text{ s}^{-1}$  at 174 MPa. This sudden change was rationalized by a change in controlling mechanisms from dislocation climb to a combination of Orowan looping and  $\gamma'$  particle shearing by perfect superdislocations [49].

For the RSA we also observe a change in creep behavior at 1000 °C from lower to higher applied stress, where the shape of the  $\dot{\epsilon}$  vs  $\epsilon$  curves also imply a change in mechanisms (Figure 2e), also interpretable from the two different linear fits feasible for the 1000 °C temperature, giving rise to Norton exponents  $n \approx 2.7$  for  $\sigma < 90$  MPa and  $\approx 5.3$  for  $\sigma > 90$  MPa. These two  $n$  values are also usually associated with viscous glide / climb-controlled and dislocation creep regimes. Although the A2/B2 substructure of the RSA is inverted, a scenario where dislocations cut the B2 phase at higher resolved shear stresses could be feasible, while our TEM observations in the low-stress regime at 1100 °C (*cf.* Figure 11) support a viscous glide through the B2 with mostly straight dislocation segments.

#### 4. Summary and Conclusions

The creep degradation of the  $\text{AlMo}_{0.5}\text{NbTa}_{0.5}\text{TiZr}$  refractory high entropy superalloy was investigated between 900-1100 °C and 30-160 MPa under vacuum. The main results are summarized as follows:

- (1) The stress exponent of 2.7–3.4 at 30–90 MPa suggests that viscous drag and climb of dislocations may be the deformation mechanisms that govern the creep behavior. At higher stresses ( $> 90$  MPa) and 1000 °C, the stress exponent increases to  $\approx 5$ , indicating that creep may be dominated by dislocation climb.
- (2) Thermal exposure at 1100 °C for  $\approx 200$  h leads to the formation of dislocation networks at A2/B2 interfaces to accommodate the large lattice misfit between these phases, regardless of the applied load.
- (3) During annealing with or without an applied load, the initially B2 matrix reinforced by cuboidal A2 precipitates partially transforms into irregularly-shaped A2/ $\text{Al}_{4-x}\text{Zr}_5$  domains

in which the A2 phase is continuous with discontinuous  $\text{Al}_{4-x}\text{Zr}_5$  precipitates. As a result of this “topological inversion”, the soft A2 phase percolates and dislocations within this phase can easily bypass the  $\text{Al}_{4-x}\text{Zr}_5$  intermetallic phase, which in turn accelerates the creep rate. As the annealing temperature decreases from 1100 °C to 900 °C, this stabilizes the  $\text{Al}_{4-x}\text{Zr}_5$  phase, the volume fraction of A2/ $\text{Al}_{4-x}\text{Zr}_5$  domains strongly increases and this phenomenon thus decreases the apparent activation energy for creep.

- (4) In addition to the previously mentioned formation of A2/ $\text{Al}_{4-x}\text{Zr}_5$  domains, there is another phenomenon that contribute to the temperature dependence of the creep behavior, *i.e.*, high temperatures (*e.g.*, 1100 °C) promote coarsening of the A2/B2 nanostructure and A2/ $\text{Al}_{4-x}\text{Zr}_5$  domains, which reduces the Orowan stress in the B2 and A2 phases and promotes high creep rates. In this case, as coarsening is related to bulk diffusion, the apparent activation energy for creep is usually close to that required for self-diffusion. In the present work, the apparent activation energy for creep was found to be rather low ( $111 \pm 11 \text{ kJ}\cdot\text{mol}^{-1}$ ), indicating that the B2-to- $\text{Al}_{4-x}\text{Zr}_5$  transformation plays a major role on the creep behavior of the  $\text{AlMo}_{0.5}\text{NbTa}_{0.5}\text{TiZr}$  alloy.
- (5) The RSA demonstrates superior creep resistance compared to other B2 engineering alloys and rCCA with B2 matrix, under similar temperatures and stress conditions. However, the creep resistance of the RSA is lower than cast Ni-based alloys that are commonly used for structural applications.

In summary, while the  $\text{AlMo}_{0.5}\text{NbTa}_{0.5}\text{TiZr}$  RSA shows promising creep properties, it presents a poor microstructural stability, which can decrease its performance over time and increase its susceptibility to failure. Therefore, we believe that the design of more creep-resistant refractory RSAs should focus on increasing the stability of the A2/B2 nanostructure.

### **CRedit authorship contribution statement**

Patricia Suárez Ocano: Experimental Methodology, Formal analysis, Data curation, writing - original draft. R., Christian Gadelmeier: Experimental Methodology (creep testing), data curation, Writing - review & editing. Uwe Glatzel: Methodology, Writing - review & editing. Guillaume Laplanche: Conceptualization, Methodology, Writing - review & editing, Supervision. Leonardo Agudo Jácome: Conceptualization, Methodology, TEM measurements, Formal analysis, writing original draft - review & editing, Supervision, and Funding acquisition.

### **Declaration of Competing Interest**

The authors declare that they have no known competing financial interests or personal relationships that could have appeared to influence the work reported in this paper.

## Acknowledgments

LAJ and GL acknowledge support through the projects n°. 398838389 and B8 of the SFB TR103 funded by the Deutsche Forschungsgemeinschaft (DFG). The authors would like to thank Dr.-Ing. Stephan Laube, Dr.-Ing. Alexander Kaufmann, Prof. Martin Heilmaier (Karlsruher Institut für Technologie) for the fabrication of the alloy as well as Dr.-Ing. Benjamin Ruttert, Dr.-Ing. Inmaculada López Galilea and Prof. Theisen (Ruhr University Bochum) for HIP treatment. The authors acknowledge R. Schwidessen and M. Tovar for performing the X-ray diffraction experiments and the Helmholtz-Zentrum Berlin X-ray Core Lab. Parts of this work were performed at the electron microscopy center at the Bundesanstalt für Materialforschung und -prüfung. PSO and LAJ acknowledge Prof. Gert Nolze and Romeo Saliwan Neumann for the EBSD analysis, Dr. Reza Darvishi Kamachali for fruitful discussion, and Prof. Robert Maaß for the valuable review and comments on the manuscript.

## References

- [1] D.B. Miracle, O.N. Senkov, A critical review of high entropy alloys and related concepts, *Acta Materialia* 122 (2017) 448-511. doi: 10.1016/j.actamat.2016.08.081.
- [2] D.K. Yadav, Y. Shadangi, S.D. Yadav, S. Sinha, Development of a high strength, low density and corrosion resistant novel FeCrMoNb<sub>1.5</sub>Ti<sub>0.5</sub> complex concentrated alloy, *Materials Today Communications* 35 (2023) 105521. doi: 10.1016/j.mtcomm.2023.105521.
- [3] F.P. Wang, J.W. Wu, Y.X. Guo, X.J. Shang, J. Zhang, Q.B. Liu, A novel high-entropy alloy with desirable strength and ductility designed by multi-component substitution for traditional austenitic alloys, *J Alloy Compd* 937 (2023). doi: 10.1016/j.jallcom.2022.168266.
- [4] D. Kumar, Recent Advances in Tribology of High Entropy Alloys: A Critical Review, *Progress in Materials Science* (2023) 101106. doi: 10.1016/j.pmatsci.2023.101106.
- [5] J.S. Luo, W.T. Sun, D.S. Liang, K. Chan, X.S. Yang, F.Z. Ren, Superior wear resistance in a TaMoNb compositionally complex alloy film via in-situ formation of the amorphous-crystalline nanocomposite layer and gradient nanostructure, *Acta Materialia* 243 (2023). doi: 10.1016/j.actamat.2022.118503.
- [6] D.B. Miracle, M.H. Tsai, O.N. Senkov, V. Soni, R. Banerjee, Refractory high entropy superalloys (RSAs), *Scr. Mater* 187 (2020) 445-452. doi: 10.1016/j.scriptamat.2020.06.048.
- [7] O. Senkov, D. Isheim, D. Seidman, A. Pilchak, Development of a Refractory High Entropy Superalloy, *Entropy* 18(3) (2016) 102. doi: 10.3390/e18030102.
- [8] O.N. Senkov, C. Woodward, D.B. Miracle, Microstructure and Properties of Aluminum-Containing Refractory High-Entropy Alloys, *JOM* 66(10) (2014) 2030-2042. doi: 10.1007/s11837-014-1066-0.
- [9] Z.T. Kloenne, J.-P. Couzinié, M. Heczko, R. Gröger, G.B. Viswanathan, W.A.T. Clark, H.L. Fraser, On the bcc/B2 interface structure in a refractory high entropy alloy, *Scr. Mater* 223 (2023) 115071. doi: 10.1016/j.scriptamat.2022.115071.
- [10] T.E. Whitfield, H.J. Stone, C.N. Jones, N.G. Jones, Microstructural Degradation of the AlMo<sub>0.5</sub>NbTa<sub>0.5</sub>TiZr Refractory Metal High-Entropy Superalloy at Elevated Temperatures, *Entropy* 23(1) (2021) 80. doi: 10.3390/e23010080.
- [11] Z.T. Kloenne, K. Kadirvel, J.P. Couzinie, G.B. Viswanathan, Y.Z. Wang, H.L. Fraser, High temperature phase stability of the compositionally complex alloy AlMo<sub>0.5</sub>NbTa<sub>0.5</sub>TiZr, *Applied Physics Letters* 119(15) (2021). doi: 10.1063/5.0069497.
- [12] M. Premkumar, K.S. Prasad, A.K. Singh, Structure and stability of the B2 phase in Ti-25Al-25Zr alloy, *Intermetallics* 17(3) (2009) 142-145. doi: 10.1016/j.intermet.2008.10.009.



- [13] T.K. Tsao, A.C. Yeh, C.M. Kuo, K. Kakehi, H. Murakami, J.W. Yeh, S.R. Jian, The High Temperature Tensile and Creep Behaviors of High Entropy Superalloy, *Sci rep* 7(1) (2017) 12658. doi: 10.1038/s41598-017-13026-7.
- [14] P. Kral, W. Blum, J. Dvorak, N. Yurchenko, N. Stepanov, S. Zherebtsov, L. Kuncicka, M. Kvapilova, V. Sklenicka, Creep behavior of an AlTiVNbZr<sub>0.25</sub> high entropy alloy at 1073 K, *Mat Sci Eng a-Struct* 783 (2020). doi: 10.1016/j.msea.2020.139291.
- [15] C. Gadelmeier, Y. Yang, U. Glatzel, E.P. George, Creep strength of refractory high-entropy alloy TiZrHfNbTa and comparison with Ni-base superalloy CMSX-4, *Cell Rep Phys Sci* 3(8) (2022). doi: 10.1016/j.xcrp.2022.100991.
- [16] C.J. Liu, C. Gadelmeier, S.L. Lu, J.W. Yeh, H.W. Yen, S. Gorsse, U. Glatzel, A.C. Yeh, Tensile creep behavior of HfNbTaTiZr refractory high entropy alloy at elevated temperatures, *Acta Mater* 237 (2022). doi: 10.1016/j.actamat.2022.118188.
- [17] X. Shen, S.W. Xin, S.J. Ding, Y. He, W.G. Dong, B.R. Sun, X.C. Cai, T.D. Shen, Intermediate-temperature creep behaviors of an equiatomic VNbMoTaW refractory high-entropy alloy, *J Mater Res Technol* 24 (2023). doi: 10.1016/j.jmrt.2023.04.141.
- [18] M.E. Kassner, *Fundamentals of Creep in Metals and Alloys*, 2nd Edition, Fundamentals of Creep in Metals and Alloys, 2nd Edition (2009) 1-295. doi: 10.1016/C2012-0-06071-1.
- [19] P. Suárez Ocaño, S.G. Fries, I. Lopez-Galilea, R.D. Kamachali, J. Roik, L. Agudo Jácome, The AlMo<sub>0.5</sub>NbTa<sub>0.5</sub>TiZr refractory high entropy superalloy: Experimental findings and comparison with calculations using the CALPHAD method, *Mater Des* 217 (2022) 110593. doi: 10.1016/j.matdes.2022.110593.
- [20] C. Gadelmeier, S. Haas, T. Lienig, A. Manzoni, M. Feuerbacher, U. Glatzel, Temperature Dependent Solid Solution Strengthening in the High Entropy Alloy CrMnFeCoNi in Single Crystalline State, *Metals* 10(11) (2020). doi: 10.3390/met10111412.
- [21] U. Glatzel, F. Schleifer, C. Gadelmeier, F. Krieg, M. Muller, M. Mosbacher, R. Volkl, Quantification of Solid Solution Strengthening and Internal Stresses through Creep Testing of Ni-Containing Single Crystals at 980 °C, *Metals* 11(7) (2021). doi: 10.3390/met11071130.
- [22] P.M. Kellner, *Hochtemperaturkriecheigenschaften von pulver- und schmelzmetallurgisch hergestellten Mo-Si-B-Legierungen mit Zugaben von Aluminium und Germanium*, Lehrstuhl Metallische Werkstoffe, Universität Bayreuth, Bayreuth, 2018, p. 124.
- [23] R. Volkl, B. Fischer, M. Beschliesser, U. Glatzel, Evaluating strength at ultra-high temperatures - Methods and results, *Mat Sci Eng A* 483-84 (2008) 587-589. doi: 10.1016/j.msea.2006.09.171.
- [24] W. Kraus, G. Nolze, POWDER CELL - A program for the representation and manipulation of crystal structures and calculation of the resulting X-ray powder patterns, *J. Appl. Crystallogr.* 29 (1996) 301-303. doi: 10.1107/S0021889895014920.
- [25] Y. Meng, X.H. Ju, X.P. Yang, The measurement of the dislocation density using TEM, *Materials Characterization* 175 (2021). doi: 10.1016/j.matchar.2021.111065.
- [26] L. Agudo Jácome, G. Eggeler, A. Dlouhy, Advanced scanning transmission stereo electron microscopy of structural and functional engineering materials, *Ultramicroscopy* 122 (2012) 48-59. doi: 10.1016/j.ultramic.2012.06.017.
- [27] P.A. Stadelmann, Ems - a Software Package for Electron-Diffraction Analysis and Hrem Image Simulation in Materials Science, *Ultramicroscopy* 21(2) (1987) 131-145. doi: 10.1016/0304-3991(87)90080-5.
- [28] C.A. Schneider, W.S. Rasband, K.W. Eliceiri, NIH Image to ImageJ: 25 years of image analysis, *Nat Methods* 9(7) (2012) 671-675. doi: 10.1038/nmeth.2089.
- [29] O.D. Sherby, P.M. Burke, Mechanical Behavior of Crystalline Solids at Elevated Temperature, *Progress in Materials Science* 13(7) (1967) 323-+. doi: 10.1016/0079-6425(68)90024-8.
- [30] H.J. Frost, M.F. Ashby., *Deformation-mechanism maps : the plasticity and creep of metals and ceramics*, Pergamon Press, Oxford [Oxfordshire], New York 1982.
- [31] J.K. Jensen, Characterization of a High Strength, Refractory High Entropy Alloy, AlMo<sub>0.5</sub>NbTa<sub>0.5</sub>TiZr, *Materials Science and Engineering*, The Ohio State University, 2017, p. 227.
- [32] J.K. Jensen, B.A. Welk, R.E.A. Williams, J.M. Sosa, D.E. Huber, O.N. Senkov, G.B. Viswanathan, H.L. Fraser, Characterization of the microstructure of the compositionally complex alloy Al<sub>1</sub>Mo<sub>0.5</sub>Nb<sub>1</sub>Ta<sub>0.5</sub>Ti<sub>1</sub>Zr<sub>1</sub>, *Scr. Mater* 121 (2016) 1-4. doi: 10.1016/j.scriptamat.2016.04.017.

- [33] P. Suárez Ocaño, A. Manzoni, I. Lopez-Galilea, B. Rutttert, G. Laplanche, L. Agudo Jácome, Influence of cooling rate on the microstructure and room temperature mechanical properties in the refractory  $\text{AlMo}_{0.5}\text{NbTa}_{0.5}\text{TiZr}$  superalloy, *J. Alloys Compd* 949 (2023) 169871. doi: 10.1016/j.jallcom.2023.169871.
- [34] L. Agudo Jácome, G. Gobekli, G. Eggeler, Transmission electron microscopy study of the microstructural evolution during high-temperature and low-stress (011) [11] shear creep deformation of the superalloy single crystal LEK 94, *J. Mater. Res.* 32(24) (2017) 4491-4502. doi: 10.1557/jmr.2017.336.
- [35] Q. Wang, J.C. Han, Y.F. Liu, Z.W. Zhang, C. Dong, P.K. Liaw, Coherent precipitation and stability of cuboidal nanoparticles in body-centered-cubic  $\text{Al}_{0.4}\text{Nb}_{0.5}\text{Ta}_{0.5}\text{TiZr}_{0.8}$  refractory high entropy alloy, *Scr. Mater* 190 (2021) 40-45. doi: 10.1016/j.scriptamat.2020.08.029.
- [36] D. Hull, D.J. Bacon, Introduction to Dislocations, fifth edition ed., Butterworth-Heinemann 2011. doi: 10.1016/C2009-0-64358-0.
- [37] W. Blum, Versetzungsmodelle der Hochtemperaturplastizität metallischer Werkstoffe, *Z Metallkd* 68 (1977) 484. doi: 10.1515/ijmr-1977-680704.
- [38] A. Epishin, T. Link, U. Bruckner, P.D. Portella, Kinetics of the topological inversion of the gamma/gamma'-microstructure during creep of a nickel-based superalloy, *Acta Materialia* 49(19) (2001) 4017-4023. doi: 10.1016/S1359-6454(01)00290-7.
- [39] L. Agudo Jácome, P. Nortershauser, C. Somsen, A. Dlouhy, G. Eggeler, On the nature of  $\gamma'$  phase cutting and its effect on high temperature and low stress creep anisotropy of Ni-base single crystal superalloys, *Acta Materialia* 69 (2014) 246-264. doi: 10.1016/j.actamat.2014.01.021.
- [40] J. Weertman, Physical Metallurgy, 3rd ed., Eds. Elsevier, Amsterdam, 1983.
- [41] S. Chen, J. Qiao, H. Diao, T. Yang, J. Poplawsky, W. Li, F. Meng, Y. Tong, L. Jiang, P.K. Liaw, Y. Gao, Extraordinary creep resistance in a non-equiatomic high-entropy alloy from the optimum solid-solution strengthening and stress-assisted precipitation process, *Acta Mater* 244 (2023) 118600. doi: 10.1016/j.actamat.2022.118600.
- [42] K.R. Forbes, U. Glatzel, R. Darolia, W.D. Nix, High-Temperature Deformation Properties of NiAl Single Crystals *Metallurgical and Materials Transactions A* volume 27 (1996) 1229-1240. doi: 10.1007/BF02649860.
- [43] E. Arzt, P. Grahle, Creep of Particle-Reinforced NiAl Intermetallics - New Materials for up to 1400 °C, *Mater Res Soc Symp P* 364 (1995) 525-536. doi: 10.1557/PROC-364-525.
- [44] N.S. Stoloff, Iron aluminides: present status and future prospects, *Mat Sci Eng A* 258(1-2) (1998) 1-14. doi: 10.1016/S0921-5093(98)00909-5.
- [45] W.J. Zhang, R.S. Sundar, S.C. Deevi, Improvement of the creep resistance of FeAl-based alloys, *Intermetallics* 12(7-9) (2004) 893-897. doi: 10.1016/j.intermet.2004.02.020.
- [46] M. Ciesla, M. Manka, F. Binczyk, P. Gradon, Creep Behaviour of Modified Mar-247 Superalloy, *Arch Metall Mater* 61(2) (2016) 701-704. doi: 10.1515/amm-2016-0119.
- [47] M. Kvapilova, J. Dvorak, P. Kral, K. Hrbacek, V. Sklenicka, Creep behaviour and life assessment of a cast nickel - base superalloy MAR-M247, *High Temp Mat Pr-Isr* 38 (2019) 590-600. doi: 10.1515/htmp-2019-0006.
- [48] K. Chen, J.X. Dong, Z.H. Yao, Creep Failure and Damage Mechanism of Inconel 718 Alloy at 800-900 degrees C, *Met Mater Int* 27(5) (2021) 970-984. doi: 10.1007/s12540-019-00447-4.
- [49] Q.Z. Yue, L. Liu, W.C. Yang, C. He, D.J. Sun, T.W. Huang, J. Zhang, H.Z. Fu, Stress dependence of the creep behaviors and mechanisms of a third-generation Ni-based single crystal superalloy, *J Mater Sci Technol* 35(5) (2019) 752-763. doi: 10.1016/j.jmst.2018.11.015.
- [50] J. Hunfeld, H. Sommer, J. Kiese, H.C. Wang, A.R. Khorasgani, T. Li, C. Somsen, A. Kostka, G. Laplanche, Design of a new wrought CrCoNi-based medium-entropy superalloy C-264 for high-temperature applications, *Materials & Design* 211 (2021). doi: 10.1016/j.matdes.2021.110174.

**Supplementary Material related to the article entitled:  
“Creep degradation of the AlMo<sub>0.5</sub>NbTa<sub>0.5</sub>TiZr refractory  
high-entropy superalloy.”**

Patricia Suárez Ocaño <sup>a,\*</sup>, Guillaume Laplanche <sup>b</sup>, Christian Gadelmeier <sup>c</sup>,  
Uwe Glatzel <sup>c</sup>, Leonardo Agudo Jácome <sup>a</sup>

<sup>a</sup> Federal Institute for Materials Research and Testing (BAM), Department for Materials Engineering, Unter den Eichen 87, 12205 Berlin, Germany.

<sup>b</sup> Institute for Materials, Ruhr-University Bochum, Universitätsstr. 150, 44801 Bochum, Germany.

<sup>c</sup> Metals and Alloys, University of Bayreuth, 95447 Bayreuth, Germany.

\*Corresponding author: [patricia.suarez-ocano@bam.de](mailto:patricia.suarez-ocano@bam.de)

These supplementary materials provide additional information regarding the above-mentioned article. It is divided into five sections:

- a. Determination of TEM sample thickness in A2/Al<sub>4-x</sub>Zr<sub>5</sub> domains
- b. Microstructural characterization after annealing (head of creep samples,  $\sigma \approx 0$ )
- c. X-ray diffraction analyses
- d. Microstructural characterization after creep (gage of creep samples,  $\sigma \neq 0$ )
- e. Determination of a possible Moiré effect

### **a. Determination of TEM sample thickness in A2/Al<sub>4-x</sub>Zr<sub>5</sub> domains**

To evaluate dislocation densities, it is necessary to determine the thickness of the sample within the region where the dislocation density is evaluated. Since the electropolishing procedure induced a preferential etching in the A2/Al<sub>4-x</sub>Zr<sub>5</sub> regions, they were thinner than the surrounding A2/B2 regions. Thus, a method was implemented to account for this difference in thicknesses. To determine the thickness of the TEM sample within A2/Al<sub>4-x</sub>Zr<sub>5</sub> "domains", a procedure that involved taking a STEM-BF micrograph (Figure S1a) was conducted, considering the orientation determined from the diffraction pattern in Figure S1b and the geometry of the TEM sample represented in Figure S1c.

The dislocation contained in A2 phase (bcc1) has a projection whose trace is marked with the blue line in Figure S1a, and whose magnitude is  $O \approx 59$  nm. It has been described in literature that screw dislocations typically move in bcc phases [1]. Therefore, we assume that the dislocation in the A2 phase, marked by blue, is along the  $a(111)$ . A representation of the cubic unit cell oriented along the (111) plane is shown in Figure S1b, where the trace of the dislocation line in Figure S1a is also represented by the same blue line, shown as  $\vec{s}$  in Figure S1c. The (111) plane is approximately parallel to the sample plane, and therefore, the normal  $\vec{n}$  of the sample is parallel to the zone axis  $\vec{ZA}$ , as shown in Figure S1c. The angle between the  $\vec{ZA}$  and the  $\vec{s}$ , as shown in Figure S1c, can be determined using:

$$\cos \phi = \left| \frac{\vec{ZA} \cdot \vec{s}}{|\vec{ZA}| |\vec{s}|} \right|$$

where  $\vec{ZA} = [111]$  and the  $\vec{s} = [11\bar{1}]$ , and  $\phi$  is the angle between them.  $\phi \approx 70.53^\circ$ , which give  $\alpha \approx 19.47^\circ$  (cf. Figure S1c). After obtaining this angle, the tangent function was applied to calculate the opposite (the dashed line marked in red in the triangle in Figure S1c) and hence determine the thickness of the sample (“X”). Thus, the thickness of the sample was found to be  $X \approx 21$  nm in the domains.

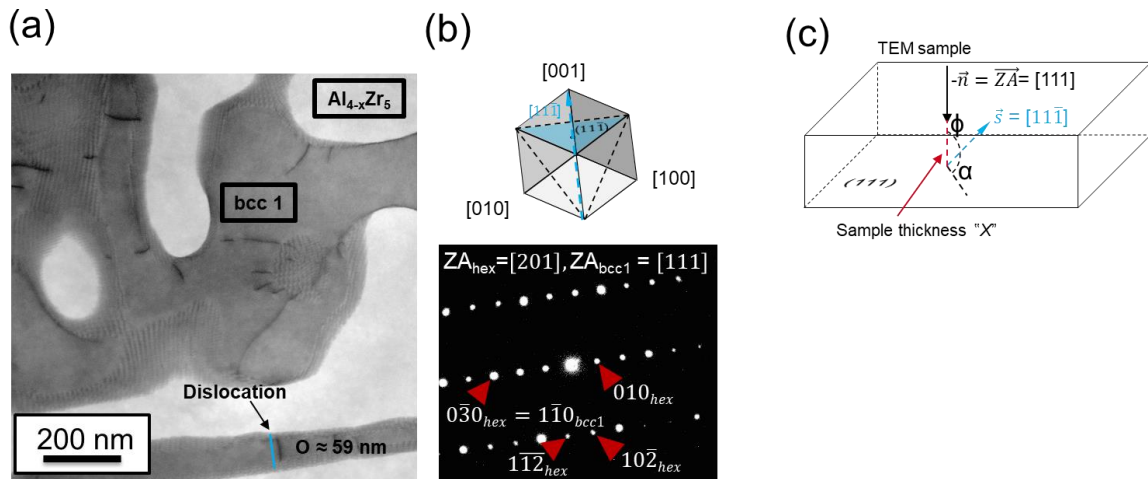


**Figure S1.** Representation of the procedure to determine the thickness of the TEM sample (a) STEM-HAADF micrograph of an  $\text{Al}_{4-x}\text{Zr}_5/\text{A2}$  domain showing a diffraction contrast, where dislocations in the A2 phase are visible. (b) Corresponding SADP where diffraction spots from the  $\text{Al}_4\text{Zr}_5$  phase ( $\text{P6}_3/\text{mcm}$  space group) are marked with red arrow heads (zone axis:  $[201]_{\text{Al}_{4-x}\text{Zr}_5}$ ) while the A2 phase is oriented along the  $[111]_{\text{A2}}$  zone axis. (c) Representation of the TEM sample. Trigonometric relation between the thickness of the sample “X” and the trace of dislocation line marked by the blue line in (a) and the blue arrow in the cube in (b).



## b. Microstructural characterization after annealing

*Determination of phase area fractions after annealing (head of creep samples,  $\sigma \approx 0$ )*

The microstructural evolution in the  $\text{AlMo}_{0.5}\text{NbTa}_{0.5}\text{TiZr}$  RSA after annealing at 900 °C for 142 h, 1000 °C for 116 h, and 1100 °C for 102 h, is shown in the BSE micrographs displayed in [Figures S2a-c](#), respectively. In these images, taken at a magnification of 8.000X, A2/Al<sub>4-x</sub>Zr<sub>5</sub> domains are visible. These domains were first marked in black (see [Figures S2d-f](#)) using the image analysis software FIJI. Then, [Figures S2d-f](#) were binarized and the area fraction of the black/white regions was measured from [Figures S2g-i](#), where the black regions represent the A2/Al<sub>4-x</sub>Zr<sub>5</sub> domains, and the white region represents the A2/B2 matrix, in [Figures S2g-i](#). A total of at least three images for each condition were binarized (not shown here) and analyzed to determine the total area fraction with the respective standard deviation. The results are summarized in [Table S1](#).

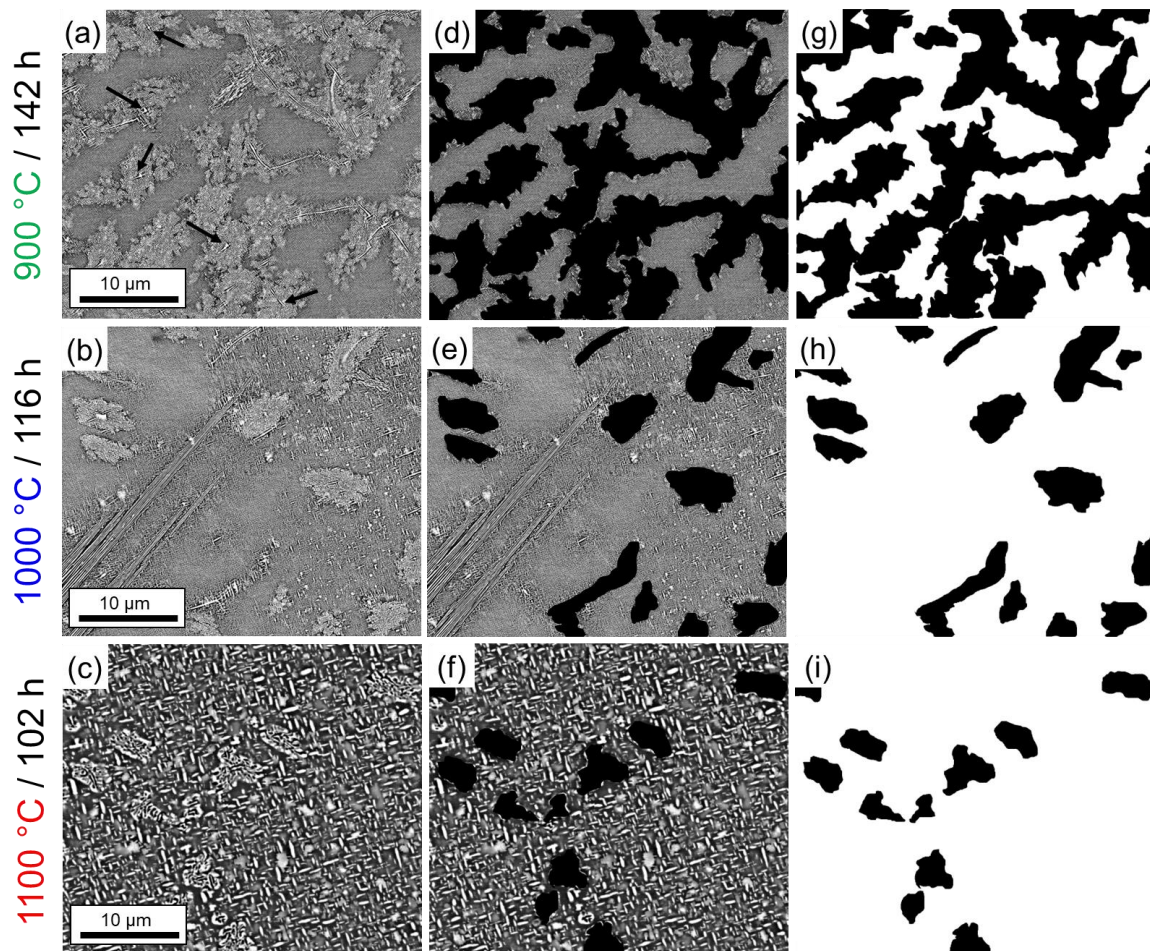


**Figure S2.** BSE micrographs of the  $\text{AlMo}_{0.5}\text{NbTa}_{0.5}\text{TiZr}$  RSA from the head of the miniaturized creep samples exposed to (a) 900 °C for 142 h, (b) 1000 °C for 116 h, and (c) 1100 °C for 102 h. (d-f) Same BSE micrographs as in (a-c) where A2/Al<sub>4-x</sub>Zr<sub>5</sub> domains are black. (g-i) Binarized images taken from (d-f), to quantify the area percentage of the domains (black) with respect to the A2/B2 matrix (white). Image analysis was performed with the FIJI software [2].

To determine the surface fraction of the  $A2+Al_{4-x}Zr_5$  phases at grain boundaries (GBs) and within needles (or plates), we used the same procedure as for the domains. [Figures S3a](#) and [d](#) show BSE micrographs of the RSA annealed at 900 °C for 142 h at low (300X) and medium magnifications (1000X), where structures at GBs and within needles (or plates) are visible, respectively. A total of at least three images for each condition were binarized (not shown here) and analyzed to determine the total area fraction with the respective standard deviation. Additionally, the same procedure was applied to the samples annealed at 1000 °C for 116 h and 1100 °C for 102 h (not shown here) to assess the surface fractions of the  $A2+Al_{4-x}Zr_5$  phases at GBs and within needles. All the obtained results are summarized in [Table S1](#).

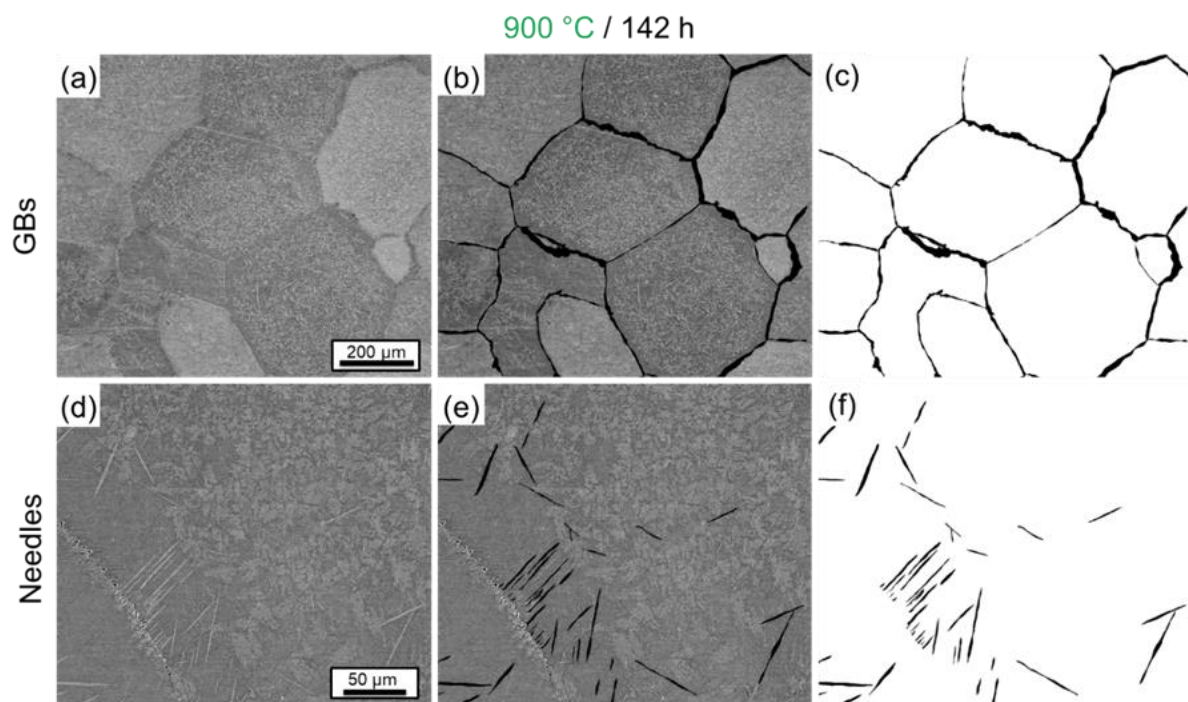


**Figure S3.** (a,d) BSE micrographs of the RSA from the head of creep samples exposed to 900 °C for 142 h (b) Same BSE micrograph as in (a) where  $A2/Al_{4-x}Zr_5$  regions at GBs are highlighted with a black color. (c) Binarized image, taken from (b), to quantify the area percentage of  $A2/Al_{4-x}Zr_5$  regions at GBs. (e) Same BSE micrograph as in (d) where  $A2/Al_{4-x}Zr_5$  needles (or plates) within grains are marked as black regions. (f) Binarized image, taken from (e), to quantify the area percentage of needles (or plates). Image analysis was performed with the FIJI software [2].

To quantify the  $Al_{4-x}Zr_5$  area fraction within  $A2/Al_{4-x}Zr_5$  domains, we analyzed the BSE micrographs in [Figures S4a-c](#) of specimens annealed at 900 °C for 142 h, 1000 °C for 116 h, and 1100 °C for 102h, respectively. The red-framed domains in [Figures S4a-c](#) are magnified in [Figures S4d-f](#). The latter were binarized and the results are shown in [Figures S4g-i](#), where the black and white regions represent the  $Al_{4-x}Zr_5$  and A2 phases, respectively. A total of at least three images



for each condition were binarized (not shown here) and analyzed to determine the average area percentages of the  $\text{Al}_{4-x}\text{Zr}_5$  and A2 phases within domains, see [Table S1](#).

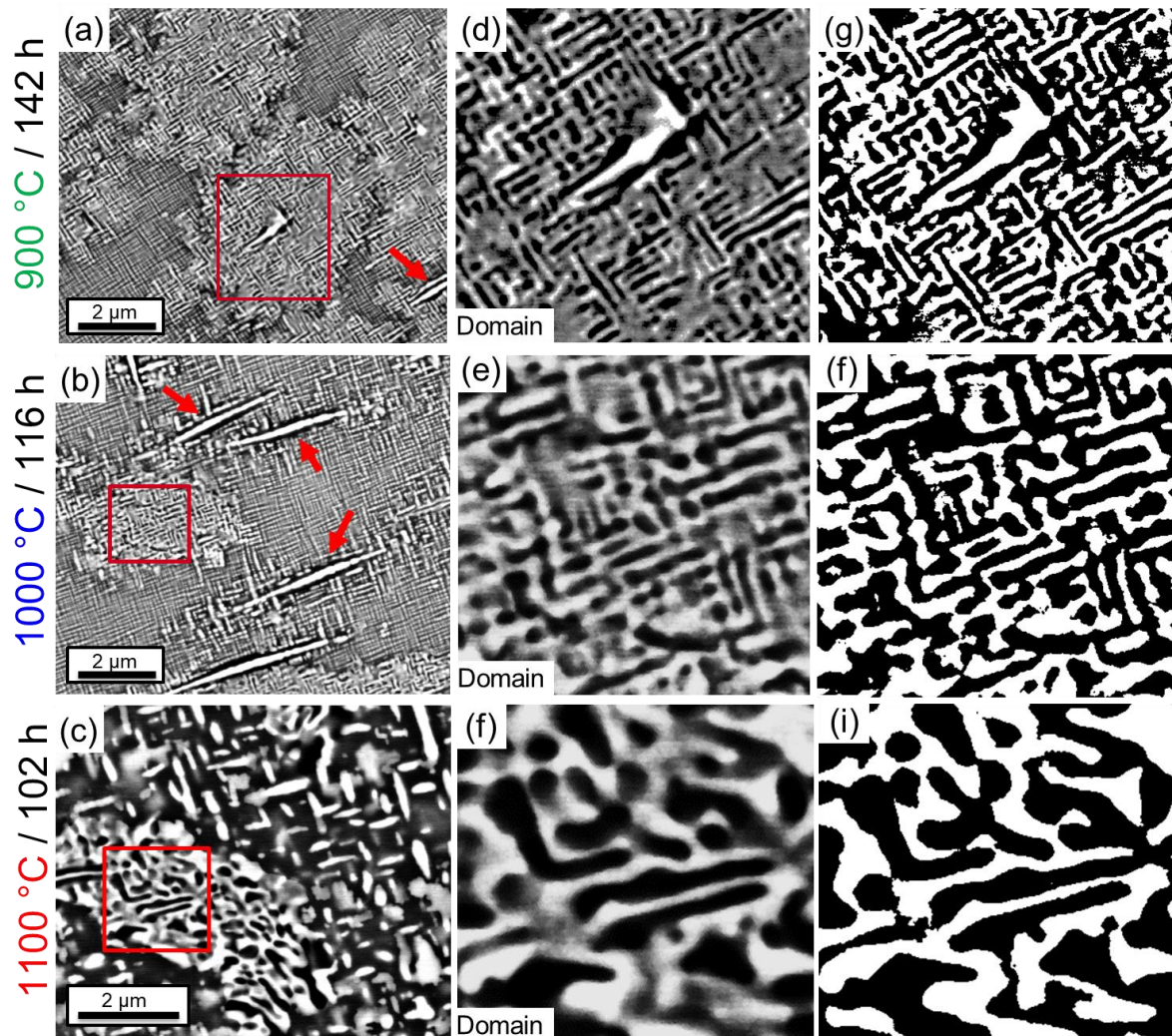


**Figure S4.** BSE micrographs of the  $\text{AlMo}_{0.5}\text{NbTa}_{0.5}\text{TiZr}$  RSA from the head of miniaturized creep samples exposed to (a) 900 °C for 142 h, (b) 1000 °C for 116 h, and (c) 1100 °C for 102 h. The red-framed regions showing  $\text{Al}_{4-x}\text{Zr}_5$ /A2 domains in (a-c) are magnified in (d-f), respectively. Using the image analysis software FIJI, the BSE micrographs in (d-f) were binarized and the results are shown in (g-i), respectively, where the  $\text{Al}_{4-x}\text{Zr}_5$  phase is black and the A2 phase white.

[Figure S5a](#) shows a BSE micrograph of the RSA at high magnification (30.000X), where an A2/B2 region in the head of a creep sample exposed to 1100 °C for 102 h can be observed. Using the same procedure as mentioned before, the surface percentages of the A2 and B2 phases and the corresponding standard deviations were determined, see [Table S1](#). Domain-free zones are seen close to GBs in the RSA annealed at ([Figure S6a](#)) 900 °C for 142 hours; ([b](#)) 1000 °C for 116 hours; and ([c](#)) 1100 °C for 102 hours. White double arrows were used in [Figures S6](#) to indicate the widths of these zones.

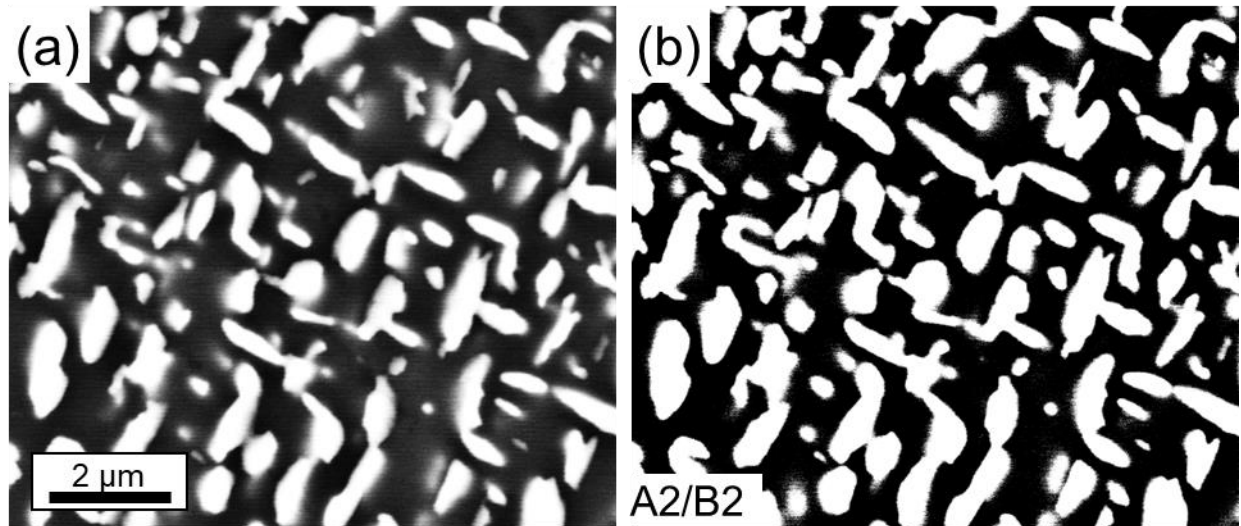


**Figure S5.** (a) BSE micrograph showing the A2/B2 matrix of the RSA after annealing at 1100 °C for 102 h (head of the creep specimen). (b) Binarized image from (a), using an image analysis software to determine the area fraction of the A2 and B2 phases. In (b), the A2 precipitates appear as white particles and the B2 channels as a black background.

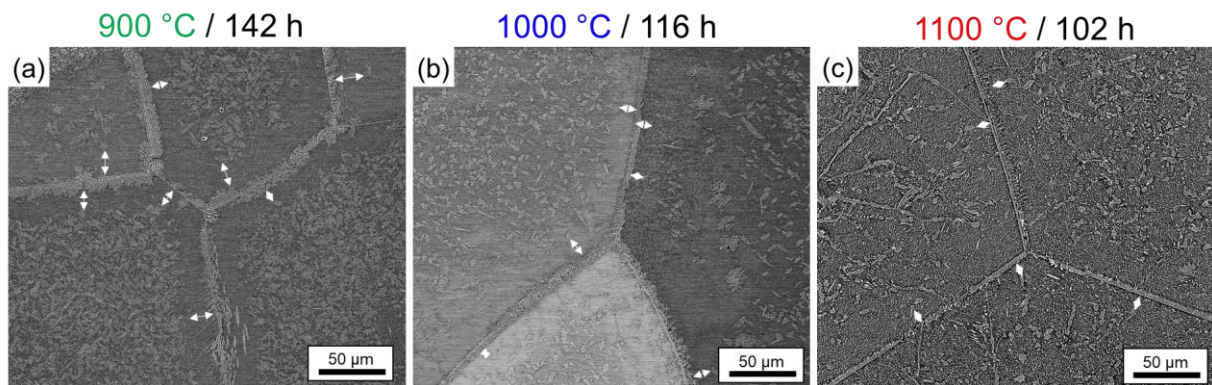


**Figure S6.** After annealing of the RSA, domain-free zones are observed near grain boundaries. The widths of these zones are marked with white double arrows. BSE micrographs of the RSA from the head of miniaturized creep samples exposed to (a) 900 °C for 142 h, (b) 1000 °C for 116 h, and (c) 1100 °C for 102 h.

The microstructural characteristics of the RSA annealed at 900 °C for 142 h, 1000 °C for 116 h, and (c) 1100 °C for 102 h are displayed in [Figures 7a-c](#), respectively. These include GBs covered with A2 and  $Al_{4-x}Zr_5$  phases, A2/ $Al_{4-x}Zr_5$  domains within grains, and A2/B2 zones in grain interiors.



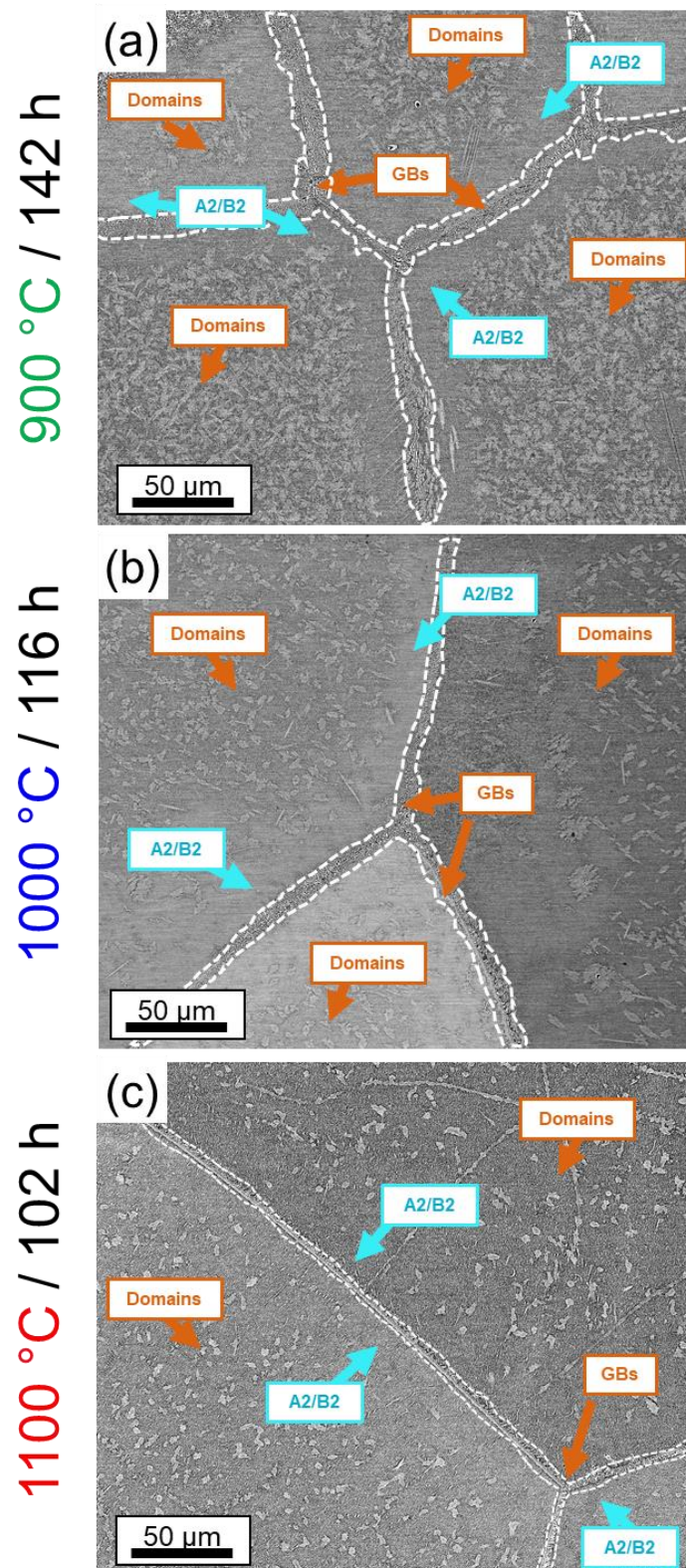


**Figure S7.** Overview of microstructural features in the RSA after annealing at (a) 900 °C for 142 h, (b) 1000 °C for 116 h, and (c) 1100 °C for 102 h. The low-magnification BSE micrographs, taken from the head of miniaturized creep samples, where grain boundaries (GBs) covered with Al<sub>4-x</sub>Zr<sub>5</sub>/A<sub>2</sub> regions, Al<sub>4-x</sub>Zr<sub>5</sub>/A<sub>2</sub> domains within grains and A<sub>2</sub>/B<sub>2</sub> zones in grain interiors are marked with arrows.

### c. X-ray diffraction analyses

Figure 8a shows the XRD pattern of the RSA in the as-received state (*i.e.*, homogenized at 1400 °C, HIPed at 170 MPa and 1370 °C for 2 h, and cooled at 10 °C/min). The pattern confirms the presence of the B2, A2, and hexagonal Al-Zr-rich phases. The latter is indexed as  $\text{Al}_4\text{Zr}_5$ . The lattice parameters of the phases are  $331.48 \pm 0.15$  pm and  $326.12 \pm 0.09$  pm for the B2 and A2 phases, respectively, and  $a = 805.65 \pm 0.63$  and  $c = 545.04 \pm 1.19$  pm for  $\text{Al}_{4-x}\text{Zr}_5$ ,  $0 \leq x \leq 1$ .

Figures 8b and c show XRD patterns recorded from the head of the creep specimen exposed to 900 °C for 142 h and 1100 °C for 11 h, respectively. Figure S8a-c confirms the presence of the A2, B2, and hexagonal  $\text{Al}_{4-x}\text{Zr}_5$  phases before and after annealing. Diffraction peaks corresponding to the hexagonal phase are more intense in the annealed samples than in the as-received sample. This is in good agreement with the increase in the area fraction of this phase following annealing. For the sample annealed at 900 °C and 142 h, the lattice parameters of the phases are  $331.19 \pm 0.11$  pm and  $325.68 \pm 0.02$  pm for the B2 and A2 phases, respectively, and  $a = 805.65 \pm 0.63$  pm and  $c = 545.04 \pm 1.19$  pm for  $\text{Al}_{4-x}\text{Zr}_5$ .

For the sample annealed at 1100 °C and 11 h, the lattice parameters of the  $\text{Al}_{4-x}\text{Zr}_5$  phase are similar to the sample annealed at 900 °C, and the lattice parameters of the A2 and B2 phases are 326.12 and 331.57 pm, respectively.

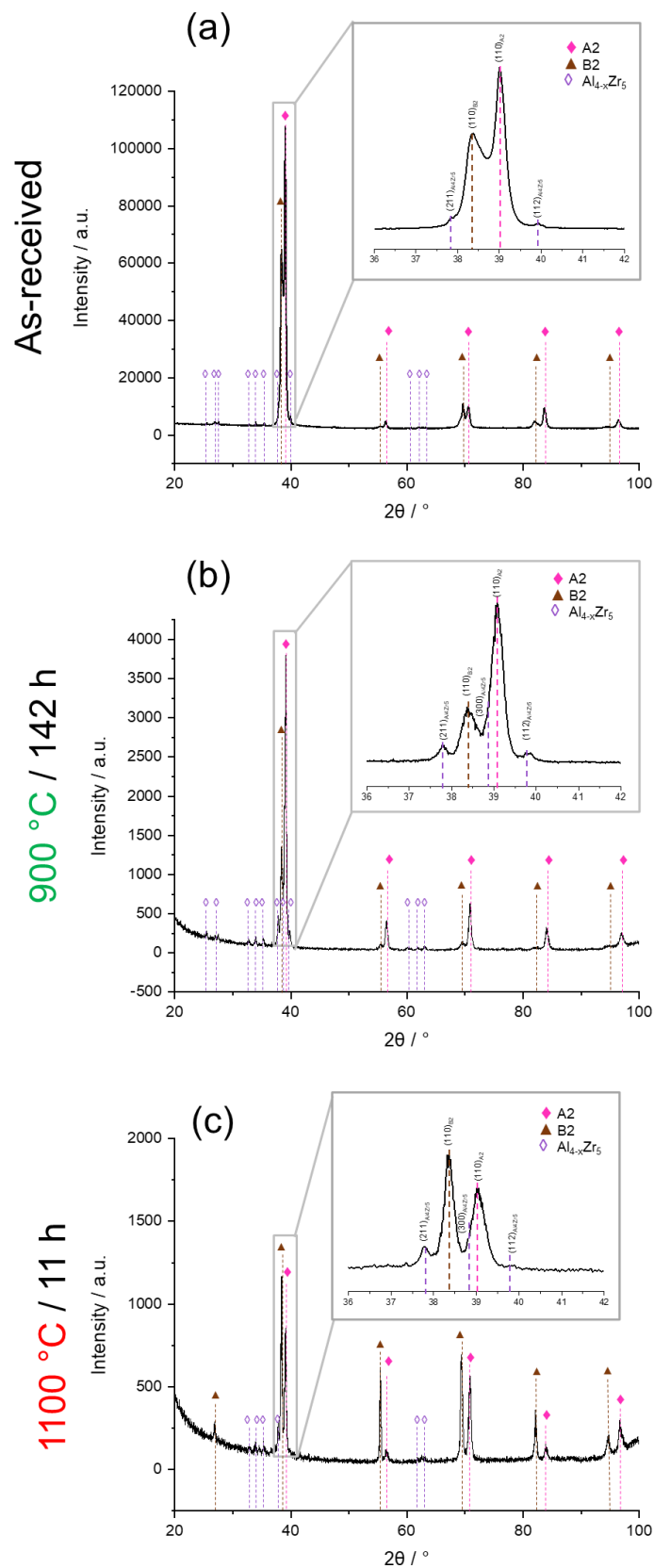


**Figure S8.** XRD of the RSA (a) before creep (as-received state) and after annealing at (b) 900 °C for 142 h, and (c) 1100 °C for 11 h.

**Table S1.** Comparison of area fractions and sizes of the different phases in the crept samples after exposure to different temperatures and plastic strains.

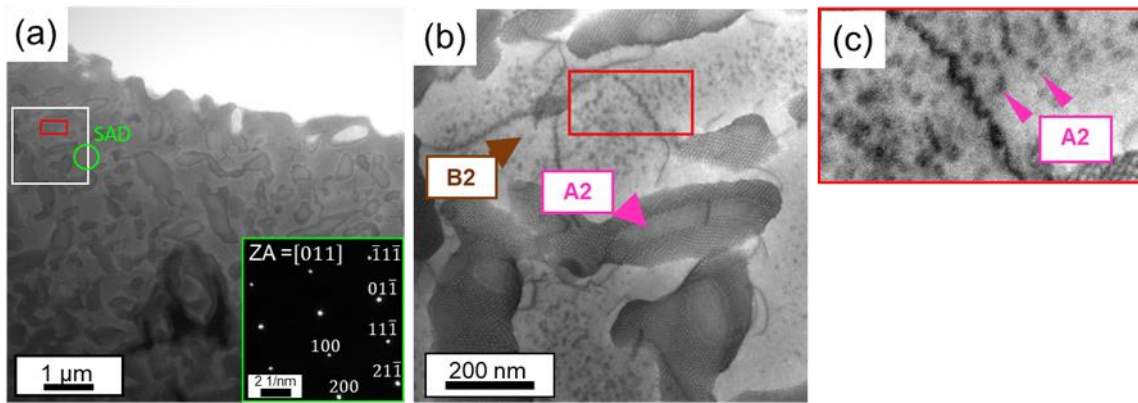
Sample	T / °C)	t / h	$\sigma$ / MPa	$\epsilon$ / %	Phase/region area fraction / %									Phase size			Minimum distance between domains and GBs ( $\mu\text{m}$ )
					Relative A2 fraction in the A2/B2	Al <sub>4-x</sub> Zr <sub>5</sub> /A2			Relative A2 fraction in domains/needles	Relative Al <sub>4-x</sub> Zr <sub>5</sub> fraction in domains/needles	Total Al <sub>4-x</sub> Zr <sub>5</sub> fraction*	Total A2 fraction*	Total B2 fraction*	A2 precipitates (nm)	Al <sub>4-x</sub> Zr <sub>5</sub> /A2		
						needles	domains	GBs							Needle length ( $\mu\text{m}$ )	Domain diameter ( $\mu\text{m}$ )	
As-received	-	-	-	-	38 ± 2	-	-	≤ 1	-	-	≤ 1	38 ± 2	62 ± 2	4.5-41.7	-	-	-
Head	900	142	≈ 0	≈ 0	38 ± 2**	2	51	5	42 ± 2	58 ± 2	34 ± 2	40 ± 2	26 ± 2	18 < x < 95***	34 ± 18	5 ± 1	18 ± 7
	1000	116	≈ 0	≈ 0	38 ± 2**	2	16	6	43 ± 3	57 ± 3	14 ± 3	39 ± 2	47 ± 2	18 < x < 105***	13 ± 5	5 ± 2	8 ± 3
	1100	102	≈ 0	≈ 0	35 ± 3	-	9	5	44 ± 3	56 ± 3	8 ± 3	36 ± 2	56 ± 2	217-747	-	4 ± 1	8 ± 2
Gage length	900	142	60	0.64	27 ± 6	2	54	5	44 ± 2	56 ± 2	34 ± 2	41 ± 6	24 ± 6	95-228	28 ± 12	5 ± 2	19 ± 6
	1000	116	30-60	0.47	31 ± 5	1	16	5	44 ± 3	56 ± 3	12 ± 3	41 ± 5	47 ± 5	105-250	15 ± 4	4 ± 1	7 ± 1
	1100	102	30	1.03	32 ± 4	-	12	5	44 ± 2	56 ± 2	10 ± 2	39 ± 4	51 ± 4	293-997	-	4 ± 1	8 ± 2

\*Total amount in the RSA

\*\* Due to the limited resolution of the SEM, we assume the same phase fraction as in the as-received state.

\*\*\*Due to the limited resolution of the SEM, we assume A2 precipitates size “x” to be larger than in the as-received state, and smaller than in the gage length.





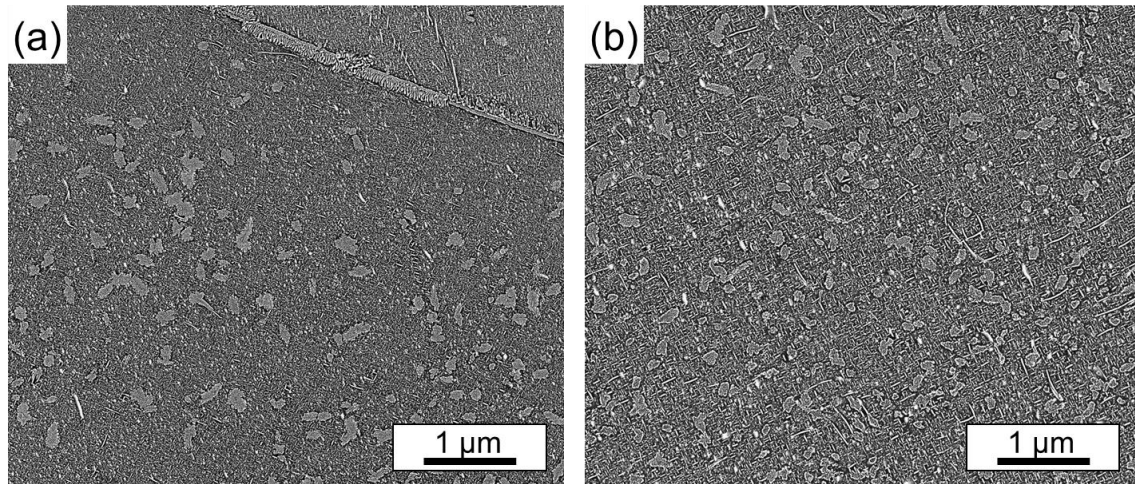
**Figure S9.** (a) STEM-BF micrograph of the A2/B2 substructure in the head of a miniaturized sample ( $\sigma \approx 0$ ) of the RSA after exposure at 1100 °C for  $\approx 200$  h at (a) low magnification showing the SADP from the region marked by the green circle oriented along  $ZA = [011]$ , (b) in the region marked by the white square in (a), (c) higher magnification of the red framed region in (b), showing within the B2 matrix reinforced by A2 nanoprecipitates.

Figure S9a shows a micrograph of the A2/B2 nanostructure in the head of a miniaturized sample of the RSA after exposure at 1100 °C for  $\approx 200$  h. The SADP from the region delimited by the green circle is oriented along  $ZA = [011]$ , as shown in the inset (*cf.* Figure S9a). In Figure S9b, we present the region marked by the white square in Figure S9a (also Figure 5 of the manuscript). The region marked in red and magnified in Figure S9c shows a region analogous to the previously mentioned SAD region marked in green within Figure S9a. Upon examination of the SADP, it becomes evident that both phases, *i.e.*, A2 and B2, are discernible. Notably, the region designated by the green circle exclusively aligns with the B2 matrix phase, and the diffraction pattern exclusively reveals the presence of the A2 and B2 phases. Based on this observation, we can conclude that the A2 phase precipitates are the secondary component within the B2 phase.

#### d. Microstructural characterization after creep

*Determination of phase area fractions after creep (gage of creep samples,  $\sigma \neq 0$ )*

Figure S10 shows BSE micrographs of the RSA after creep at 1100 °C for 11 h, where the head ( $\varepsilon \approx 0\%$ , Figure S10a), and the gage ( $\varepsilon \approx 0.66\%$ , Figure S10b) of the corresponding creep sample are compared. At this magnification, it is visible that the domains are distributed uniformly inside the grains.



**Figure S10.** Non-significant effect of applied load during annealing on microstructure of the RSA. (a) BSE micrographs of the material crept at 1100 °C and 60 MPa for 11 h: (a) head of the creep sample (no applied stress, no plastic deformation) and (b) gage of sample crept to  $\epsilon \approx 0.66\%$ .

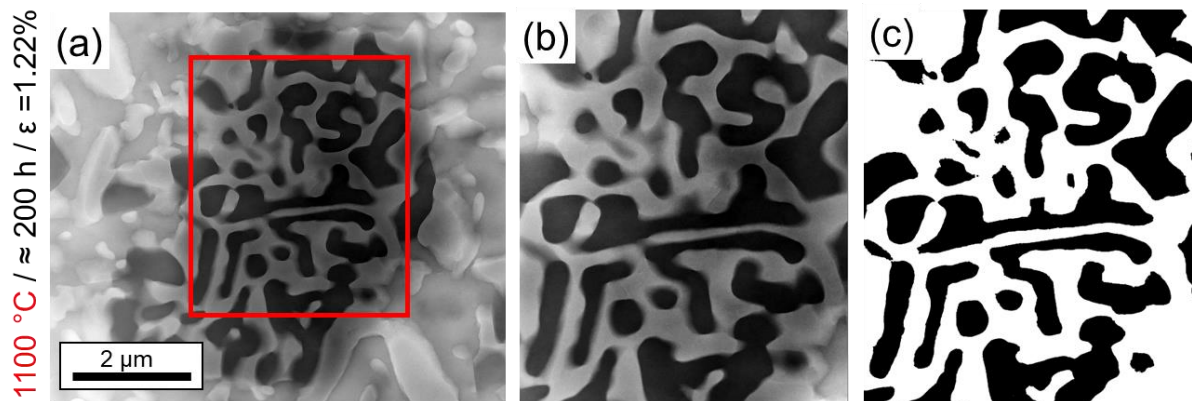


**Figure S11.** Determination of the surface fraction of phases in A2/Al<sub>4-x</sub>Zr<sub>5</sub> domains in the RSA crept at 1100 °C for 102 h up to  $\epsilon \approx 1.22\%$ . (a-b) STEM-HAADF micrographs taken from the gage of the miniaturized creep sample. The red-framed A2/Al<sub>4-x</sub>Zr<sub>5</sub> domain in (a) is magnified in (b), and binarized in (c) to quantify the area percentage (%) of the Al<sub>4-x</sub>Zr<sub>5</sub> phase. In the binarized image, the black and white regions correspond to the Al<sub>4-x</sub>Zr<sub>5</sub> and A2 phases, respectively.

[Figure S11a](#) shows a STEM-HAADF micrograph of the RSA after creep at 1100 °C for 102 h resulting in  $\epsilon \approx 1.3\%$ . The image was taken from the gage of the creep sample. To quantify the surface fraction of the Al<sub>4-x</sub>Zr<sub>5</sub> phase in domains, a region of the micrograph in [\(a\)](#) is marked with a red square and magnified in [\(Figure S11b\)](#) where there is a combination of Al<sub>4-x</sub>Zr<sub>5</sub>/A2 phases. [Figure S11b](#) was binarized [\(Figure S11c\)](#) to determine the area percentage of the black region, corresponding to the Al<sub>4-x</sub>Zr<sub>5</sub> phase and the white region, corresponding to the A2 phase. The obtained results are summarized in [Table S1](#).

### e. Determination of orientation relationship between the A2 and Al<sub>4-x</sub>Zr<sub>5</sub> needles-like regions

As a starting point, the morphology of the needles and was considered, since it they show a fine lamellar A2/Al<sub>4-x</sub>Zr<sub>5</sub> substructure that runs approximately parallel to the needle trace. These lamellae also run approximately parallel to {100}<sub>A2/B2</sub>, where the initially coherent A2/B2 interfaces are located. One of these planes is also approximately parallel to the *c* axis of the hexagonal lattice that in turn aligns approximately along the needle traces (*cf.* a1 and n3 in [Figure 8a](#) in the manuscript). As the thin A2/Al<sub>4-x</sub>Zr<sub>5</sub> lamellae could be due to a semicoherent substructure, the planes of the Al<sub>4-x</sub>Zr<sub>5</sub> phase with interplanar distances  $d_{hkl}$  were inspected using the software JEMS [3], which followed these orientation tendencies, and which would give a mismatch < 10 % with  $d_{h00}$  for the A2 phase. [Table S2](#) shows the list of for plane families and their hexagonal equivalents, their  $d_{hkl}$  and the calculated mismatch  $(1 - d_{h00_{A2}}/d_{hkl_{Al4-xZr5}}) \times 100$ .

**Table S2.** Interplanar distances  $d$  of  $hkl_{Al4-xZr5}$  that yield to a mismatch < 10 % with  $d_{h00_{A2}}$  ( $h$ : 1,2).

$h00_{A2}$	$d_{h00_{A2}} / \text{nm}$	$d_{hkl_{Al4-xZr5}} / \text{nm}$	Mismatch / %	$hkl_{Al4-xZr5}$
<b>100</b>	0.3232	0.34116	5.6	111, $\bar{1}\bar{1}0$ , $2\bar{1}1$ , $1\bar{2}1$ , $\bar{2}11$
		0.16763	3.7	230, $\bar{5}20$ , $\bar{2}50$ , $3\bar{5}0$
<b>200</b>	0.1616	0.16104	0.3	321, $\bar{5}21$ , $\bar{3}51$
		0.15944	1.3	$5\bar{1}0$ , 410, $4\bar{5}0$

Subsequently, the HKL 5 software was used to generate the pole figures of the Al<sub>4-x</sub>Zr<sub>5</sub> (hexagonal) phase for the needle region of the EBSD map in [Figure 8a](#). Comparing these pole figures with the pole figure of the A2/B2 phases, it was found that only one of the {321}<sub>Al<sub>4-x</sub>Zr<sub>5</sub></sub> reflections, with a mismatch of 0.3 % (*cf.* [Table S2](#)), coincides with one of the {010}<sub>A2</sub> (*cf.* a1 and n3 respectively marked in [Figure 8c](#) and [d](#) of the main manuscript). Therefore, a possible semicoherency OR is found, as described by [Equation 3](#) in the main manuscript.

## f. Determination of a possible Moiré effect

In the RSA, the cube-on-cube relationship of the A2/B2 substructure, with {100} interfaces, shows two sets of diffracting planes but different lattice parameters. When the transmitted electron beam passes through these two lattices one after another, a Moiré pattern may appear in the overlapping region of the resulting image, with interference fringes that arise from a superposition of the two original interplanar distances,  $d_1$ , and  $d_2$ .

As described in Ref. [4], bright and dark fringes or patterns with spacing  $D$  may thus form between these two periodicities, following the relationship:

$$D = \frac{d_1 d_2}{d_1 - d_2}$$

where  $d_1$ , and  $d_2$ , are the interplanar spacings of each phase for the respective operating reflection vector  $\mathbf{g}$ .

From the lattice parameters of the A2 and B2 phases determined by XRD ( $a_{A2}$  and  $a_{B2}$ ), the respective interplanar spacings ( $d_{hkl}$ ) that should be observed in TEM were determined. [Table S3](#) summarizes the measured  $a_{A2}$ ,  $a_{B2}$ ,  $d_{110}$ ,  $D_{\text{calc}}$  (calculated), and  $D_{\text{exp}}$  (experimental).  $D_{\text{calc}}$  was determined using  $d_{110}$  extracted from the XRD lattice parameters for each phase.  $D_{\text{exp}}$  was determined by measuring the average values for the pattern spacing along the blue line in the red square shown in [Figure S12](#).

**Table S3.** Lattice parameters ( $a$ ), Miller indices of the diffracting planes ( $hkl$  reflections), interplanar spacings ( $d_{hkl}$ ), calculated and experimental periodicity ( $D_{\text{calc}}$  and  $D_{\text{exp}}$ ), determined from the XRD patterns in [Figure S8](#).

Phase	$a$ / nm	Reflection			$d_{hkl}$ / nm	$D_{\text{calc}}$ / nm	$D_{\text{exp}}$ / nm
		h	k	l			
B2	0.3313	1	1	0	0.234264	12.92	10.74
A2	0.3254	1	1	0	0.230093		



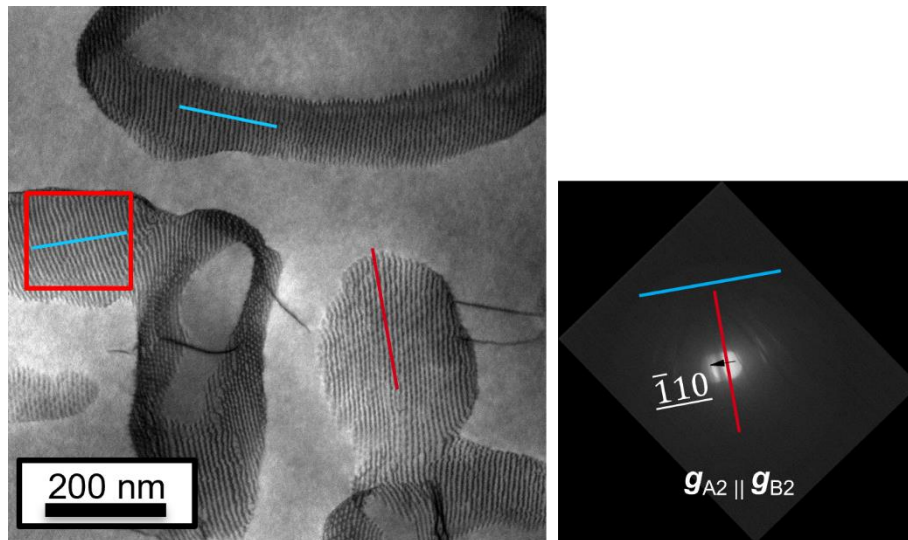


**Figure S12.** STEM-BF micrograph of the A2/B2 nanostructure oriented along the [111] zone axis after exposure of the RSA to 1100 °C for 200 h up to  $\epsilon \approx 1.22$  %. The image was taken from the gage of the creep specimen. The pattern spacing at the A2/B2 interface was measured along the blue line in (a) to determine a possible Moiré effect.

As  $D_{\text{calc}}$  and  $D_{\text{exp}}$  do not match (*cf.* Table S3), with a difference of  $\approx 20$  %, it can be concluded that the visible patterns at the A2/B2 interface are not related to the Moiré effect but correspond to dislocation networks. Furthermore, as Moiré fringes for our cube-on-cube A2/B2 orientation relationship would be parallel to the traces of the diffraction planes ( $\mathbf{g}_{\text{A2}} = \bar{1}10 \parallel \mathbf{g}_{\text{B2}} = \bar{1}10$ ) and perpendicular to  $\Delta\mathbf{g}$ , the pattern lines visible in Figure S12 do not match the plane traces of the diffraction planes that would contribute to the Moiré effect (see red line in Figure S12).

## References

- [1] D. Hull, D.J. Bacon, Introduction to Dislocations, fifth edition ed., Butterworth-Heinemann 2011. doi: 10.1016/C2009-0-64358-0.
- [2] C.A. Schneider, W.S. Rasband, K.W. Eliceiri, NIH Image to ImageJ: 25 years of image analysis, Nat Methods 9(7) (2012) 671-675. doi: 10.1038/nmeth.2089.
- [3] P.A. Stadelmann, Ems - a Software Package for Electron-Diffraction Analysis and Hrem Image Simulation in Materials Science, Ultramicroscopy 21(2) (1987) 131-145. doi: 10.1016/0304-3991(87)90080-5.
- [4] J.W. Edington, Practical Electron Microscopy in Materials Science, Van Nostrand Reinhold New York, 1977.

## 5. General conclusions and outlook

The work presented here comprises a comprehensive investigation of hitherto not addressed relevant aspects of the  $\text{AlMo}_{0.5}\text{NbTa}_{0.5}\text{TiZr}$  RSA, which include: 1) thermodynamic and microstructural stabilities at high temperatures through CALPHAD method, 2) microstructure analysis in both, as-cast (AC) and annealed state (AN), 3) microstructure, lattice misfit, and mechanical properties at room temperature (Vickers hardness and fracture toughness) as affected by cooling rates, and 4) creep behavior. The present study aimed to evaluate the potential of the RSA for high-temperature structural applications and explore opportunities to improve its room temperature mechanical properties, which have been described as a major concern for this alloy. To accomplish this, several materials states from different processing steps and routes, including as-cast, homogenized at 1400 °C for 24 hours, and different cooling rates after homogenization were explored. The alloy was analyzed in several ways, such as microstructural analysis, mechanical characterization at room temperature via nanohardness and microhardness-based fracture toughness, and at high temperature (from 900 to 1100 °C) *via* tensile creep testing. The key findings and conclusions from the analysis of the RSA are summarized as follows:

The as cast and homogenized states at 1400 °C for 24 h exhibit distinct microstructures. In the AC state, the dendritic structure comprised A2/B2 phases in both the dendritic and interdendritic regions. Additionally, A2 phase precipitates were embedded in a B2 phase matrix, with an edge length < 20 nm, which differs to the AN state. In the latter, a strong plate-like formation and channels (A2/B2 structure) with an edge length  $\approx$  10-fold larger is present. Furthermore, within the interdendritic structure in the AC state, a mostly amorphous phase was found, which was rich in Al and Zr ( $\approx$  8 % of phase, 5 % crystalline), with a  $\text{P6}_3/\text{mcm}$  space group and  $\text{Al}_{4-x}\text{Zr}_5$  stoichiometry. The AN crystallizes completely after annealing.

The phase stability of the RSA using equilibrium CALPHAD calculations with TCNI10 and TCHEA3 databases, showed a good agreement with the AN in the high temperature phase formation, anticipating the formation of two bcc phases, *i.e.*, Al-Zr-Ti-rich and Mo-Nb-Ta-rich phases, assumed to be respectively the A2 and B2 phases determined experimentally. However, in the non-equilibrium condition using the Scheil-Gulliver model equation, there are many discrepancies, indicating the formation of a single bcc phase, and phases such as Sigma and Laves, which were not identified in the AC experimental microstructure. These results highlight the need for additional research to refine the modeling in the used TC databases, in which accurate solidification paths and ordered phases formation are lacking due to the absence of key ternary diagrams (*e.g.*, Mo-Nb-Ta, Mo-Nb-Ti, Mo-Nb-Zr, Nb-Ta-Zr, Nb-Ta-Ti, Ta-Ti-Zr, Ti-Zr-Mo, Ti-Zr-Nb).

Through CALPHAD calculations, it was possible to anticipate the formation of a miscibility gap, which confirmed the hypothesized spinodal decomposition, as the mechanism of precipitation of the A2/B2 phase nanostructure observed experimentally. Furthermore, a proposed mechanism describes the formation of A2 precipitates, inspired in an earlier mechanism observed in alloys with miscibility gap regions and a large lattice misfit. Then, the development of the RSA microstructure appears to be a result of a dynamic process, characterized by a complex coarsening of the A2/B2 microstructure, which is notably influenced by the lattice misfit between the A2/B2 phases and varies with time and temperature.

When the cooling rate starting at the solutioning temperature is increased, it leads to the formation of a finer and more homogeneous A2/B2 substructure while inhibiting grain boundary precipitation of the hexagonal  $\text{Al}_{4-x}\text{Zr}_5$  intermetallic phase. The A2/B2 substructure refinement was also found in the as-cast state.

The finer A2/B2 substructure without  $\text{Al}_{4-x}\text{Zr}_5$  phase at GBs achieved at higher cooling rates enhances the room temperature hardness without affecting the fracture toughness, which remains poor. This hardness enhancement is highly influenced by the constrained phases (*i.e.*, A2/B2), resulting in reduced stresses and strain forces acting at the interface (and therefore reduced misfit), when the microstructure becomes smaller and more homogeneous. Thus, implementing this processing route enables the alloy to exhibit improved resistance, particularly at room temperature, which is highly desired in many technical applications. However, from a mechanical perspective, the similarity in fracture toughness between the RSA and other B2 intermetallics is as a limitation, as it makes the material more challenging to manage at room temperature.

DTA results proved that the liquid phase appears at a temperature higher than for Ni-based alloys, *e.g.*,  $\approx 200$  °C higher than for the SX CMX4 alloy, which points in the right direction for high temperature structural applications. Keeping this in mind, the high temperature stability and creep resistance in the 900–1100 °C and 30–160 MPa regime was evaluated in this work, in order to further assess the applicability of the RSA and related alloys for this kind of applications. Thus, a Norton exponent  $n \approx 2.7\text{--}3.4$  was found for the load range  $30 < \sigma < 90$  MPa, which verifies the three-power law as the mechanism at lower stresses. In the stress level  $90 < \sigma < 160$  MPa, the five-power law can be interpreted as valid at 1000 °C, where dislocation climb is expected to be rate controlling for creep plasticity.

Characteristic microstructural changes in the RSA play a crucial role in the mechanism of deformation during tensile creep. First, the effect of only high temperature exposure, *i.e.*,  $\varepsilon \approx 0$  %, promotes microstructural changes that include: 1) phase transformation from the B2 phase to the  $\text{Al}_{4-x}\text{Zr}_5$  hexagonal phase with two ORs and their associated domain and needle morphologies, 2) faceting of  $\text{Al}_{4-x}\text{Zr}_5$  hexagonal phase decorating the GBs, which elongate along the  $[0001]_{\text{Al}_{4-x}\text{Zr}_5}$  at

900 and 1000 °C and enhances needle formation, and 3) coarsening and coherency loss of the starting A2/B2 nanostructure.

The formation of domain and needle structures, in both of which a A2 /Al<sub>4-x</sub>Zr<sub>5</sub> lamellar substructure evolves from a as the transformation  $B2 \rightarrow A2 + Al_{4-x}Zr_5$  during the creep process, facilitates the dislocation movement within the ductile A2 phase. This phase transformation leads to a recovery process that is associated with a reduction in misfit stresses and a "topological phase inversion" that promotes plasticity. Therefore, the phase transformation is an important thermodynamically driven mechanism that contributes to creep around 900 °C. In this manner, the B2-to-Al<sub>4-x</sub>Zr<sub>5</sub>+A2 transformation could contribute to decrease the apparent activation energy for creep in the RSA, which was determined as  $111 \pm 11$  kJ/mol. Additionally, the low apparent activation energy can also be partly explained by its stronger elastic modulus dependence at low homologous temperatures (here,  $T/T_m < 0.65$ ). The value for the apparent activation energy found here is namely low compared to other B2-structured alloys and CCAs.

However, the  $\sigma$ -enhanced coarsening of the A2/B2 structure and its associated rafting also enhances dislocation movement during creep, especially around 1100 °C. Thus, at higher temperature, where the A2/B2 and domains coarsening is more dramatic,  $\dot{\epsilon}$  is higher at least partly due to a reduction of the Orowan stress in both A2 and B2 phases.

The misfit between the A2/B2 phase is  $\approx -1$ – $-2$  % when the RSA is cooled at different rates, *i.e.*, higher misfit ( $\approx -1.71$ ) when the cooling rate is lower (5 °C/min), and lower misfit ( $\approx -1.36$ ) when the cooling rate is higher (30 °C/min). Furthermore, as the temperature increases in a short-term experiment ( $\approx 30$  min), the coefficient of thermal expansion of the A2 phase induces a lattice parameter expansion that is faster than that of the B2 phase. Consequently, the lattice misfit becomes less negative, especially up to 900 °C.

However, the formation of dislocation networks between the former interfaces is promoted after long-term temperature exposure at 1100 °C and  $\approx 200$  h, which accommodate the coherency stresses between the A2 and B2 phases, which in turn increases lattice misfit to  $> 2\%$ .

In general, a comparison between the RSA and other equivalent microstructures of previous works showed that the RSA has a superior creep resistance than other B2-structure alloys, including other B2-structured CCAs. However, when comparing with well-established Ni-based superalloys that are designed for structural applications in the high temperature regime, the RSA still presents lower creep resistance, probably due to the poor microstructural stability, which can minimize the long-term high temperature performance and increase the tendency to failure.

Interestingly, the RSA with a nanostructure that resembles that of the Ni-based superalloys, was described to be a good prospect for high-temperature structural applications, with superior



compression properties than the former up to 1200 °C. Although the creep resistance of the RSA at evaluated temperatures is lower than for some Ni-based superalloys, the superior creep resistance compared to other B2-structure alloys is encouraging. However, grain boundary and B2-matrix instabilities, as well as lack of room temperature ductility require further improvement before considering this alloy for the intended applications. Furthermore, the mechanical properties have been evaluated so far under vacuum conditions (in order to separate the effect of the mechanical behavior and the degradation of the alloy by oxidation and/or corrosion). Evaluating the oxidation behavior at the intended application temperatures has received little considerations to date, despite its essential character for typical high-temperature applications. Thus, in terms of future prospects, additional research is needed in this respect.

Finally, the findings of this study have practical applications in the design and development of the RSA material class, where knowledge of microstructure, mechanical properties, and creep behavior are critical for achieving desired material properties. Therefore, this study advances the understanding of the RSA class and provides a foundation for future research in this area.

## References

- [1] J.-W. Yeh, S.-K. Chen, S.-J. Lin, J.-Y. Gan, T.-S. Chin, T.-T. Shun, C.-H. Tsau, S.-Y. Chang, Nanostructured High-Entropy Alloys with Multiple Principal Elements: Novel Alloy Design Concepts and Outcomes, *Adv Eng Mater* 5 (2004) 299-303. doi: 10.1002/adem.200300567 2004.
- [2] B. Cantor, I.T.H. Chang, P. Knight, A.J.B. Vincent, Microstructural development in equiatomic multicomponent alloys, *Mater. Sci. Eng. A* 375-377 (2004) 213-218. doi: 10.1016/j.msea.2003.10.257.
- [3] A. Asabre, A. Kostka, O. Stryzhyboroda, J. Pfetzinger-Micklich, U. Hecht, G. Laplanche, Effect of Al, Ti and C additions on Widmanstätten microstructures and mechanical properties of cast  $Al_{0.6}CoCrFeNi$  compositionally complex alloys, *Mater. Des.* 184 (2019) 108201. doi: 10.1016/j.matdes.2019.108201.
- [4] O.N. Senkov, S. Gorsse, D.B. Miracle, High temperature strength of refractory complex concentrated alloys, *Acta Mater* 175 (2019) 394-405. doi: 10.1016/j.actamat.2019.06.032.
- [5] M. Reiberg, C.Y. Duan, X.H. Li, E. Werner, High-temperature phase characterization of AlCrFeNiTi compositionally complex alloys, *Mater. Chem. Phys.* 275 (2022). doi: 10.1016/j.matchemphys.2021.125272.
- [6] N.Y. Yurchenko, N.D. Stepanov, S.V. Zherebtsov, M.A. Tikhonovsky, G.A. Salishchev, Structure and mechanical properties of B2 ordered refractory AlNbTiVZr<sub>x</sub> (x=0-1.5) high-entropy alloys, *Mat Sci Eng A* 704 (2017) 82-90. doi: 10.1016/j.msea.2017.08.019.
- [7] O.N. Senkov, C.F. Woodward, Microstructure and properties of a refractory NbCrMo<sub>0.5</sub>Ta<sub>0.5</sub>TiZr alloy, *Materials Science and Engineering: A* 529 (2011) 311-320. doi: 10.1016/j.msea.2011.09.033.
- [8] K.K. Tseng, C.C. Juan, S. Tso, H.C. Chen, C.W. Tsai, J.W. Yeh, Effects of Mo, Nb, Ta, Ti, and Zr on Mechanical Properties of Equiatomic Hf-Mo-Nb-Ta-Ti-Zr Alloys, *Entropy* 21(1) (2019). doi: 10.3390/e21010015.
- [9] Z.Q. Xu, Z.L. Ma, M. Wang, Y.W. Chen, Y.D. Tan, X.W. Cheng, Design of novel low-density refractory high entropy alloys for high-temperature applications, *Mat Sci Eng A* 755 (2019) 318-322. doi: 10.1016/j.msea.2019.03.054.
- [10] O.N. Senkov, G.B. Wilks, D.B. Miracle, C.P. Chuang, P.K. Liaw, Refractory high-entropy alloys, *Intermetallics* 18(9) (2010) 1758-1765. doi: 10.1016/j.intermet.2010.05.014.
- [11] V. Soni, B. Gwalani, O.N. Senkov, B. Viswanathan, T. Alam, D.B. Miracle, R. Banerjee, Phase stability as a function of temperature in a refractory high-entropy alloy, *J Mater Res* 33(19) (2018) 3235-3246. doi: 10.1557/jmr.2018.223.
- [12] O. Senkov, D. Isheim, D. Seidman, A. Pilchak, Development of a Refractory High Entropy Superalloy, *Entropy* 18(3) (2016) 102. doi: 10.3390/e18030102.
- [13] A. Iturbe, E. Giraud, E. Hormaetxe, A. Garay, G. Germain, K. Ostolaza, P.J. Arrazola, Mechanical characterization and modelling of Inconel 718 material behavior for machining process assessment, *Mat Sci Eng A* 682 (2017) 441-453. doi: 10.1016/j.msea.2016.11.054.
- [14] A.M.S. Costa, E.S.N. Lopes, R.J. Contieri, R. Caram, R. Baldan, G.E. Fuchs, C.A. Nunes, Microstructural and Mechanical Characterization of Directionally Solidified Conventional and Nb-Modified Mar-M247 Superalloy, *Journal of Materials Engineering and Performance* 28(4) (2019) 2427-2438. doi: 10.1007/s11665-019-04014-1.
- [15] Y. Liu, R. Hu, J.S. Li, H.C. Kou, H.W. Li, H. Chang, H.Z. Fu, Deformation characteristics of as-received Haynes230 nickel base superalloy, *Mat Sci Eng A* 497(1-2) (2008) 283-289. doi: 10.1016/j.msea.2008.07.052.
- [16] T.E. Whitfield, H.J. Stone, C.N. Jones, N.G. Jones, Microstructural Degradation of the AlMo<sub>0.5</sub>NbTa<sub>0.5</sub>TiZr Refractory Metal High-Entropy Superalloy at Elevated Temperatures, *Entropy* 23(1) (2021) 80. doi: 10.3390/e23010080.
- [17] R. Tewari, N.K. Sarkar, D. Harish, B. Vishwanadh, G.K. Dey, S. Banerjee, *Intermetallics and Alloys for High Temperature Applications, Materials under Extreme Conditions: Recent Trends and Future Prospects* (2017) 293-335. doi: 10.1016/B978-0-12-801300-7.00009-7.
- [18] A. Shirzadi, S. Jackson, *Structural Alloys for Power Plants Operational Challenges and High-temperature Materials: Operational Challenges and High-Temperature Materials*, Woodhead Publ Ser En (45) (2014) XXI-XXII.
- [19] S. Biswas, S. Ramachandra, P. Hans, S.P.S. Kumar, *Materials for Gas Turbine Engines: Present Status, Future Trends and Indigenous Efforts*, *J Indian I Sci* 102(1) (2022) 297-309. doi: 10.1007/s41745-022-00295-z.
- [20] A.P. Mouritz, *Superalloys for gas turbine engines*, Woodhead Publ Mater (2012) 251-267. doi: Book\_Doi 10.1533/9780857095152.

- [21] A. Misra, Composite materials for aerospace propulsion related to air and space transportation, 2016. doi: 10.1016/B978-1-78242-325-6.00012-8.
- [22] G.K. Salwan, R. Subbarao, S. Mondal, Comparison and selection of suitable materials applicable for gas turbine blades, *Mater Today-Proc* 46 (2021) 8864-8870. doi: 10.1016/j.matpr.2021.05.003.
- [23] C. Korner, M. Ramsperger, C. Meid, D. Burger, P. Wollgramm, M. Bartsch, G. Eggeler, Microstructure and Mechanical Properties of CMSX-4 Single Crystals Prepared by Additive Manufacturing, *Metall Mater Trans A* 49a(9) (2018) 3781-3792. doi: 10.1007/s11661-018-4762-5.
- [24] M. Palumbo, D. Baldissin, L. Battezzati, O. Tassa, R. Wunderlich, H.J. Fecht, R. Brooks, K. Mills, Thermodynamic properties of CMSX-4 superalloy: Results from the Thermolab project, *Mater Sci Forum* 508 (2006) 591-596. doi: 10.4028/www.scientific.net/MSF.508.591.
- [25] M.R. Condruz, G. Matache, A. Paraschiv, C. Puscasu, Homogenization heat treatment and segregation analysis of equiaxed CMSX-4 superalloy for gas turbine components, *J Therm Anal Calorim* 134(1) (2018) 443-453. doi: 10.1007/s10973-018-7085-2.
- [26] R.C. Reed, K.A. Green, P. Caron, T.P. Gabb, M.G. Fahrman, E.S. Huron, S.A. Woodard, *Superalloys 2008*, TMS, Warrendale PA 2008. doi: 10.1017/S0001924000087509.
- [27] A. Kracke, Superalloys, the most successful alloy system of modern times-past, present, and future, in: J.R.G. E.A. Ott, A. Banik, I. Dempster, T.P. Gabb, R. Helmink, X. Liu, A. Mitchell, G.P. Sjöberg, A. Wusatowska-Sarnek (Ed.) *Proc. 7th Int. Symp. on Superalloys 718 and derivatives*, TMS, Warrendale, 2010, p. 13.50.
- [28] D.V.V. Satyanarayana, N.E. Prasad, Nickel-Based Superalloys, *Ind Inst Met Ser* (2017) 199-228. doi: 10.1007/978-981-10-2134-3\_9.
- [29] P.W. Bridgman, Certain physical properties of single crystals of tungsten, antimony, bismuth, tellurium, cadmium, zinc, and tin., *P Am Acad Arts Sci* 60(1/14) (1925) 305-383. doi: 10.2307/25130058.
- [30] A.F. Giamei, Development of Single Crystal Superalloys: A Brief History, *Advances Materials and Processes* 171(9) (2013) 26-30. doi: 10.31399/asm.amp.2013-09.p026.
- [31] U. Unnikrishnan, V. Yang, A review of cooling technologies for high temperature rotating components in gas turbine, *Propulsion and Power Research* 11(3) (2022) 293-310.
- [32] V.V.S. Prasad, R.G. Baligidad, A.A. Gokhale, Niobium and Other High Temperature Refractory Metals for Aerospace Applications, *Ind Inst Met Ser* (2017) 267-288. doi: 10.1007/978-981-10-2134-3\_12.
- [33] J.A. Lemberg, R.O. Ritchie, Mo-Si-B Alloys for Ultrahigh-Temperature Structural Applications, *Adv Mater* 24(26) (2012) 3445-3480. doi: 10.1002/adma.201200764.
- [34] R.L. Fleischer, High-Temperature, High-Strength Materials — An Overview, *JOM* 37(12) (1985) 16-20. doi: 10.1007/BF03259961.
- [35] L. Agudo Jácome, J. Heyer, P. Nörtershäuser, C.Somsen, A. Dlouhý, G. Eggeler, High Temperature Dislocation Creep in Different Tensile Directions in LEK 94, in: F.A. K.Maruyama, M.Igarashi, K.Kishida, M.Suzuki, K.Yoshimi (Ed.) *Proceedings of the 12th International Conference on Creep and Fracture of Engineering Materials and Structures (JIMIS 11)*, The Japan Institute of MetalsThe Japan Institute of Metals, Kyoto, Japan, 2012.
- [36] R.A. Perkins, G.H. Meier, The oxidation behavior and protection of niobium, *JOM* 42(8) (1990) 17-21. doi: 10.1007/BF03221046.
- [37] J.R. Davis, *Refractory Metal Alloys*, ASM International2001. doi: 10.31399/asm.tb.aub.9781627082976.
- [38] S.N. Zhang, L.N. Jia, Y.L. Guo, B. Kong, C.G. Zhou, H. Zhang, Improvement in the oxidation resistance of Nb-Si-Ti based alloys containing zirconium, *Corros Sci* 163 (2020). doi: 10.1016/j.corsci.2019.108294.
- [39] L.A. Jacome, P. Nortershauser, J.K. Heyer, A. Lahni, J. Frenzel, A. Dlouhy, C. Somsen, G. Eggeler, High-temperature and low-stress creep anisotropy of single-crystal superalloys, *Acta Materialia* 61(8) (2013) 2926-2943. doi: 10.1016/j.actamat.2013.01.052.
- [40] H.M. Daoud, A.M. Manzoni, N. Wanderka, U. Glatzel, High-Temperature Tensile Strength of Al<sub>10</sub>Co<sub>25</sub>Cr<sub>8</sub>Fe<sub>15</sub>Ni<sub>36</sub>Ti<sub>6</sub> Compositionally Complex Alloy (High-Entropy Alloy), *Jom* 67(10) (2015) 2271-2277. doi: 10.1007/s11837-015-1484-7.
- [41] Y. Ikedaa, B. Grabowska, F. Körmanna, Ab initio phase stabilities and mechanical properties of multicomponent alloys: A comprehensive review for high entropy alloys and compositionally complex alloys, *Materials Characterization* 147 (2019) 464-511.
- [42] Z. Li, K.G. Pradeep, Y. Deng, D. Raabe, C.C. Tasan, Metastable high-entropy dual-phase alloys overcome the strength-ductility trade-off, *Nature* 534(7606) (2016) 227-30. doi: 10.1038/nature17981.

- [43] D.B. Miracle, O.N. Senkov, A critical review of high entropy alloys and related concepts, *Acta Materialia* 122 (2017) 448-511. doi: 10.1016/j.actamat.2016.08.081.
- [44] F. Otto, A. Dlouhý, C. Somsen, H. Bei, G. Eggeler, E.P. George, The influences of temperature and microstructure on the tensile properties of a CoCrFeMnNi high-entropy alloy, *Acta Materialia* 61(15) (2013) 5743-5755. doi: 10.1016/j.actamat.2013.06.018.
- [45] F. Otto, A. Dlouhý, K.G. Pradeep, M. Kuběnová, D. Raabe, G. Eggeler, E.P. George, Decomposition of the single-phase high-entropy alloy CrMnFeCoNi after prolonged anneals at intermediate temperatures, *Acta Mater.* 112 (2016) 40-52. doi: 10.1016/j.actamat.2016.04.005.
- [46] B. Gludovatz, A. Hohenwarter, D. Catoor, E.H. Chang, E.P. George, R.O. Ritchie, A fracture-resistant high-entropy alloy for cryogenic applications, *Science* 345(6201) (2014) 1153-1158. doi: 10.1126/science.1254581.
- [47] D. Miracle, J. Miller, O. Senkov, C. Woodward, M. Uchic, J. Tiley, Exploration and Development of High Entropy Alloys for Structural Applications, *Entropy* 16(1) (2014) 494-525. doi: 10.3390/e16010494.
- [48] O.N. Senkov, C. Woodward, D.B. Miracle, Microstructure and Properties of Aluminum-Containing Refractory High-Entropy Alloys, *JOM* 66(10) (2014) 2030-2042. doi: 10.1007/s11837-014-1066-0.
- [49] O.N. Senkov, S.V. Senkova, C. Woodward, Effect of aluminum on the microstructure and properties of two refractory high-entropy alloys, *Acta Materialia* 68 (2014) 214-228. doi: 10.1016/j.actamat.2014.01.029.
- [50] X.P. Tan, D. Mangelinck, C. Perrin-Pellegrino, L. Rougier, C.-A. Gandin, A. Jacot, D. Ponsen, V. Jaquet, Spinodal Decomposition Mechanism of  $\gamma'$  Precipitation in a Single Crystal Ni-Based Superalloy, *Metallurgical and Materials Transactions A* 45(A) (2014) 4725-4730. doi: 10.1016/j.matdes.2017.11.033.
- [51] O.N. Senkov, J.K. Jensen, A.L. Pilchak, D.B. Miracle, H.L. Fraser, Compositional variation effects on the microstructure and properties of a refractory high-entropy superalloy AlMo<sub>0.5</sub>NbTa<sub>0.5</sub>TiZr, *Mater Des* 139 (2018) 498-511. doi: 10.1016/j.matdes.2017.11.033.
- [52] P. Suárez Ocaño, S.G. Fries, I. Lopez-Galilea, R.D. Kamachali, J. Roik, L. Agudo Jácome, The AlMo<sub>0.5</sub>NbTa<sub>0.5</sub>TiZr refractory high entropy superalloy: Experimental findings and comparison with calculations using the CALPHAD method, *Mater Des* 217 (2022) 110593. doi: 10.1016/j.matdes.2022.110593.
- [53] X. Liu, K. Vecchio, Processing, microstructure evolution and mechanical property improvements of an Al-V-Cr-Mn-Fe-Ni CCA with an as-cast BCC/B2 coherent nanostructure, *Mat Sci Eng A* 852 (2022). doi: 10.1016/j.msea.2022.143698.
- [54] M. Wischi, K.N. Campo, L.F. Starck, E.B. da Fonseca, S.N. Lopes, R. Caram, Microstructure and mechanical behavior of the directionally solidified AlCoCrFeNi<sub>2.1</sub> eutectic high-entropy alloy, *J Mater Res Technol* 20 (2022) 811-820. doi: 10.1016/j.jmrt.2022.07.065.
- [55] H.L. Huang, Y. Sun, P.P. Cao, Y. Wu, X.J. Liu, S.H. Jiang, H. Wang, Z.P. Lu, On cooling rates dependence of microstructure and mechanical properties of refractory high-entropy alloys HfTaTiZr and HfNbTiZr, *Scr. Mater* 211 (2022). doi: 10.1016/j.scriptamat.2022.114506.
- [56] W. Lonski, M. Spilka, M. Kadziolka-Gawel, P. Gebara, A. Radon, T. Warski, K. Mlynarek-Zak, R. Babilas, The effect of cooling rate on the structure and selected properties of AlCoCrFeNiSi<sub>x</sub> (x=0; 0.25; 0.5; 0.75) high entropy alloys, *J Alloy Compd* 905 (2022). doi: 10.1016/j.jallcom.2022.164074.
- [57] O.N. Senkov, D.B. Miracle, K.J. Chaput, J.P. Couzinie, Development and exploration of refractory high entropy alloys-A review, *J Mater Res* 33(19) (2018) 3092-3128. doi: 10.1557/jmr.2018.153.
- [58] S. Naka, Development of intermetallic materials for structural applications: Toward designing multi-constituent and/or multi-phase alloys, *J. Phys. IV* 6(C2) (1996) 147-152. doi: 10.1051/jp4:1996220.
- [59] Z.D. Han, N. Chen, S.F. Zhao, L.W. Fan, G.N. Yang, Y. Shao, K.F. Yao, Effect of Ti additions on mechanical properties of NbMoTaW and VNbMoTaW refractory high entropy alloys, *Intermetallics* 84 (2017) 153-157. doi: 10.1016/j.intermet.2017.01.007.
- [60] O.N. Senkov, J.M. Scott, S.V. Senkova, D.B. Miracle, C.F. Woodward, Microstructure and room temperature properties of a high-entropy TaNbHfZrTi alloy, *Journal of Alloys and Compounds* 509(20) (2011) 6043-6048. doi: 10.1016/j.jallcom.2011.02.171.
- [61] O.N. Senkov, J.M. Scott, S.V. Senkova, F. Meisenkothen, D.B. Miracle, C.F. Woodward, Microstructure and elevated temperature properties of a refractory TaNbHfZrTi alloy, *Journal of Materials Science* 47(9) (2012) 4062-4074. doi: 10.1007/s10853-012-6260-2.
- [62] C.C. Juan, M.H. Tsai, C.W. Tsai, C.M. Lin, W.R. Wang, C.C. Yang, S.K. Chen, S.J. Lin, J.W. Yeh, Enhanced mechanical properties of HfMoTaTiZr and HfMoNbTaTiZr refractory high-entropy alloys, *Intermetallics* 62 (2015) 76-83. doi: 10.1016/j.intermet.2015.03.013.



- [63] V. Soni, B. Gwalani, T. Alam, S. Dasari, Y. Zheng, O.N. Senkov, D. Miracle, R. Banerjee, Phase inversion in a two-phase, BCC+B2, refractory high entropy alloy, *Acta Materialia* (2020). doi:
- [64] B.Q. Chen, L.C. Zhuo, Latest progress on refractory high entropy alloys: Composition, fabrication, post processing, performance, simulation and prospect, *Int J Refract Met H* 110 (2023). doi: 10.1016/j.ijrmhm.2022.105993.
- [65] H. Chen, T. Hanemann, S. Seils, D. Schliephake, A.S. Tirunilai, M. Heilmaier, K.P. Weiss, A. Kauffmann, Influence of Temperature and Plastic Strain on Deformation Mechanisms and Kink Band Formation in Homogenized HfNbTaTiZr, *Crystals* 11(2) (2021). doi: 10.3390/cryst11020081.
- [66] J.P. Couzinie, M. Heczko, V. Mazanova, O.N. Senkov, M. Ghazisaeidi, R. Banerjee, M.J. Mills, High-temperature deformation mechanisms in a BCC+B2 refractory complex concentrated alloy, *Acta Mater* 233 (2022). doi: 10.1016/j.actamat.2022.117995.
- [67] P. Kumar, S.J. Kim, Q. Yu, J. Ell, M. Zhang, Y. Yang, J.Y. Kim, H.-K. Park, A.M. Minor, E.S. Park, R.O. Ritchie, Compressive vs. tensile yield and fracture toughness behavior of a body-centered cubic refractory high-entropy superalloy Al<sub>0.5</sub>Nb<sub>1.25</sub>Ta<sub>1.25</sub>TiZr at temperatures from ambient to 1200°C, *Acta Mater* 245 (2023) 118620. doi: 10.1016/j.actamat.2022.118620.
- [68] W.R. Wang, W.L. Wang, S.C. Wang, Y.C. Tsai, C.H. Lai, J.W. Yeh, Effects of Al addition on the microstructure and mechanical property of AlxCoCrFeNi high-entropy alloys, *Intermetallics* 26 (2012) 44-51. doi: 10.1016/j.intermet.2012.03.005.
- [69] W.R. Wang, W.L. Wang, J.W. Yeh, Phases, microstructure and mechanical properties of AlxCoCrFeNi high-entropy alloys at elevated temperatures, *Journal of Alloys and Compounds* 589 (2014) 143-152. doi: 10.1016/j.jallcom.2013.11.084.
- [70] Y.J. Zhou, Y. Zhang, Y.L. Wang, G.L. Chen, Solid solution alloys of AlCoCrFeNiTix with excellent room-temperature mechanical properties, *Applied Physics Letters* 90(18) (2007). doi: 10.1063/1.2734517.
- [71] S. Laube, A. Kauffmann, S. Schellert, S. Seils, A.S. Tirunilai, C. Greiner, Y.M. Eggeler, B. Gorr, H.J. Christ, M. Heilmaier, Formation and thermal stability of two-phase microstructures in Al-containing refractory compositionally complex alloys, *Sci Technol Adv Mat* 23(1) (2022) 692-706. doi: 10.1080/14686996.2022.2132118.
- [72] J.W. Gibbs, The Scientific Papers of J. Willard Gibbs, *Nature* 75 (1907) 361–362. doi: 10.1038/075361a0.
- [73] D.A. Porter, K.E. Easterling, M.Y. Sherif, *Phase Transformations in Metals and Alloys*, CRC Press, 2009.
- [74] J.W. Cahn, Spinodal Decomposition in Cubic Crystals, *Acta Metallurgica* 10(Mar) (1962) 179-+. doi: Doi 10.1016/0001-6160(62)90114-1.
- [75] S.S. Brenner, P.P. Camus, M.K. Miller, W.A. Soffa, Phase-Separation and Coarsening in Fe-Cr-Co Alloys, *Acta Metallurgica* 32(8) (1984) 1217-1227. doi: Doi 10.1016/0001-6160(84)90128-7.
- [76] W.A. Soffa, D.E. Laughlin, Recent experimental studies of continuous transformations in alloys: An overview, *Proceedings of an International Conference on Solid - Solid Phase Transformations*, AIME, USA, 1981, pp. 159-183.
- [77] M.A. Ali, I. López-Galilea, S. Gao, B. Ruttart, W. Amin, O. Shchyglo, A. Hartmaier, W. Theisen, I. Steinbach, Effect of  $\gamma'$  precipitate size on hardness and creep properties of Ni-base single crystal superalloys: Experiment and simulation, *Materialia* 12 (2020) 100692. doi: 10.1016/j.mtla.2020.100692.
- [78] H. R. Abedi, O.A. Ojo, X. Cao, Effect of Cooling Rate on Precipitation Behavior of Gamma Prime in a Newly Developed Co-based Superalloy, *JOM* 72 (2020) 4054-4059. doi: 10.1007/s11837-020-04241-1.
- [79] A. Munitz, S. Salhov, G. Guttman, N. Derimow, M. Nahmany, Heat treatment influence on the microstructure and mechanical properties of AlCrFeNiTi<sub>0.5</sub> high entropy alloys, *Mat Sci Eng A* 742 (2019) 1-14. doi: 10.1016/j.msea.2018.10.114.
- [80] K. Xiong, L. Huang, X.F. Wang, L. Yu, W. Feng, Cooling-Rate Effect on Microstructure and Mechanical Properties of Al<sub>0.5</sub>CoCrFeNi High-Entropy Alloy, *Metals* 12(8) (2022). doi: 10.3390/met12081254.
- [81] G. Brunetti, A. Settefrati, A. Hazotte, S. Denis, J.J. Fundenberger, A. Tidu, E. Bouzy, Determination of  $\gamma$ - $\gamma'$  lattice misfit in a single-crystal nickel-based superalloy using convergent beam electron diffraction aided by finite element calculations, *Micron* 43(2-3) (2012) 396-406. doi: 10.1016/j.micron.2011.10.009.
- [82] Y. Wang, L.Q. Chen, A.G. Khachaturyan, Kinetics of Strain-Induced Morphological Transformation in Cubic Alloys with a Miscibility Gap, *Acta Metall. et Mater.* 41(1) (1993) 279-296. doi: 10.1016/0956-7151(93)90359-Z.

- [83] T. Miyazaki, H. Imamura, H. Mori, T. Kozakai, Theoretical and Experimental Investigations on Elastic Interactions between  $\gamma'$ -Precipitates in a Ni-Al Alloy, *Journal of Materials Science* 16(5) (1981) 1197-1203. doi: 10.1007/Bf01033832.
- [84] N. Saunders, A.P. Miodownik, CALPHAD (Calculation of Phase Diagrams): A Comprehensive Guide, Pergamon 1998.
- [85] J.J. Carroll, Phase diagrams, *Natural Gas Hydrates: A Guide for Engineers*, 2nd Edition (2009) 211-228. doi: 10.1016/B978-0-7506-8490-3.00009-4.
- [86] H.L. Lukas, S.G. Fries, B. Sundman, COMPUTATIONAL THERMODYNAMICS The Calphad Method, 2010.
- [87] H.L. Chen, H.H. Mao, Q. Chen, Database development and Calphad calculations for high entropy alloys: Challenges, strategies, and tips, *Mater. Chem. Phys.* 210 (2018) 279-290. doi: 10.1016/j.matchemphys.2017.07.082.
- [88] W. Cao, S.L. Chen, F. Zhang, K. Wu, Y. Yang, Y.A. Chang, R. Schmid-Fetzer, W.A. Oates, PANDAT software with PanEngine, PanOptimizer and PanPrecipitation for multi-component phase diagram calculation and materials property simulation, *Calphad-Computer Coupling of Phase Diagrams and Thermochemistry* 33(2) (2009) 328-342. doi: 10.1016/j.calphad.2008.08.004.
- [89] C.W. Bale, E. Belisle, P. Chartrand, S.A. Deckerov, G. Eriksson, A.E. Gheribi, K. Hack, I.H. Jung, Y.B. Kang, J. Melancon, A.D. Pelton, S. Petersen, C. Robelin, J. Sangster, P. Spencer, M.A. Van Ende, FactSage thermochemical software and databases, 2010-2016, *Calphad-Computer Coupling of Phase Diagrams and Thermochemistry* 54 (2016) 35-53. doi: 10.1016/j.calphad.2016.05.002.
- [90] O.N. Senkov, C. Zhang, A.L. Pilchak, E.J. Payton, C. Woodward, F. Zhang, CALPHAD-aided development of quaternary multi-principal element refractory alloys based on NbTiZr, *Journal of Alloys and Compounds* 783 (2019) 729-742. doi: 10.1016/j.jallcom.2018.12.325.
- [91] A.F. Andreoli, R.G. Mendes, V.T. Witusiewicz, O. Shuleshova, M.A. van Huis, K. Nielsch, I. Kaban, Phase constitution and microstructure of the NbTiVZr refractory high-entropy alloy solidified upon different processing, *Acta Mater* 221 (2021). doi: 10.1016/j.actamat.2021.117416.
- [92] T. Li, S. Wang, W. Fan, Y. Lu, T. Wang, T. Li, P.K. Liaw, CALPHAD-aided design for superior thermal stability and mechanical behavior in a TiZrHfNb refractory high-entropy alloy, *Acta Materialia* 246 (2023) 118728. doi: 10.1016/j.actamat.2023.118728.
- [93] B. Zhang, M.C. Gao, Y. Zhang, S.M. Guo, Senary refractory high-entropy alloy Cr x MoNbTaVW, *Calphad* 51 (2015) 193-201. doi: 10.1016/j.calphad.2015.09.007.
- [94] H.W. Yao, J.W. Qiao, M.C. Gao, J.A. Hawk, S.G. Ma, H.F. Zhou, Y. Zhang, NbTaV-(Ti,W) refractory high-entropy alloys: Experiments and modeling, *Mat Sci Eng A* 674 (2016) 203-211. doi: 10.1016/j.msea.2016.07.102.
- [95] E. Scheil, Bemerkungen zur Schichtkristallbildung, *International Journal of Materials Research* 34(3) (1942) 70-72. doi: 10.1515/ijmr-1942-340303.
- [96] G.H. Gulliver, The Quantitative Effect of Rapid Cooling Upon the Constitution of Binary Alloys, *J. Inst. Met.* 9 (1913) 120-157.
- [97] L. Agudo Jácome, G. Gobekli, G. Eggeler, Transmission electron microscopy study of the microstructural evolution during high-temperature and low-stress (011) [11] shear creep deformation of the superalloy single crystal LEK 94, *J. Mater. Res.* 32(24) (2017) 4491-4502. doi: 10.1557/jmr.2017.336.
- [98] H.B. Long, S.R. Bakhtiari, Y.N. Liu, S.C. Mao, H. Wei, Y.H. Chen, A. Li, D.L. Kong, L. Yan, L.Y. Yang, Z. Zhang, X.D. Han, A comparative study of rafting mechanisms of Ni-based single crystal superalloys, *Mater Des* 196 (2020). doi: 10.1016/j.matdes.2020.109097.
- [99] J.K. Jensen, B.A. Welk, R.E.A. Williams, J.M. Sosa, D.E. Huber, O.N. Senkov, G.B. Viswanathan, H.L. Fraser, Characterization of the microstructure of the compositionally complex alloy Al<sub>1</sub>Mo<sub>0.5</sub>Nb<sub>1</sub>Ta<sub>0.5</sub>Ti<sub>1</sub>Zr<sub>1</sub>, *Scr. Mater* 121 (2016) 1-4. doi: 10.1016/j.scriptamat.2016.04.017.
- [100] Z.T. Kloenne, J.-P. Couzinié, M. Heczko, R. Gröger, G.B. Viswanathan, W.A.T. Clark, H.L. Fraser, On the bcc/B2 interface structure in a refractory high entropy alloy, *Scr. Mater* 223 (2023) 115071. doi: 10.1016/j.scriptamat.2022.115071.
- [101] K. Kadirvel, Z. Kloenne, J.K. Jensen, H. Fraser, Y.Z. Wang, Phase-field modelling of transformation pathways and microstructural evolution in multi-principal element alloys, *Appl Phys Lett* 119(17) (2021) 171905. doi: 10.1063/5.0065522.
- [102] J.K. Jensen, Characterization of a High Strength, Refractory High Entropy Alloy, AlMo<sub>0.5</sub>NbTa<sub>0.5</sub>TiZr, *Materials Science and Engineering The Ohio State University*, 2017, p. 227.

- [103] Z.T. Kloenne, K. Kadirvel, J.P. Couzinie, G.B. Viswanathan, Y.Z. Wang, H.L. Fraser, High temperature phase stability of the compositionally complex alloy AlMo<sub>0.5</sub>NbTa<sub>0.5</sub>TiZr, *Applied Physics Letters* 119(15) (2021). doi: 10.1063/5.0069497.
- [104] H. Brooks, Metal interfaces, in: A.S.f. Metals (Ed.) Thirty-third National Metal Congress and Exposition, The Society Detroit, 1952, p. 20.
- [105] M.J. Mehl, D. Hicks, C. Toher, O. Levy, R.M. Hanson, G. Hart, S. Curtarolo, The AFLOW Library of Crystallographic Prototypes: Part 1, *Comp. Mater. Sci.* 136 (2017) S1-S828. doi: 10.1016/j.commatsci.2017.01.017.
- [106] P. Villars, L.D. Calvert, Pearson's handbook of crystallographic data for intermetallic phases, ASM International, Materials Park, Ohio, USA, 1991.
- [107] W. Kraus, G. Nolze, POWDER CELL - A program for the representation and manipulation of crystal structures and calculation of the resulting X-ray powder patterns, *J. Appl. Crystallogr.* 29 (1996) 301-303. doi: 10.1107/S0021889895014920.
- [108] G.V. Samsonov, Handbook of the Physicochemical Properties of the Elements, Springer New York, 1968. doi: 10.1007/978-1-4684-6066-7.
- [109] W. Steurer, Crystal Structures of Metallic Elements and Compounds, *Physical Metallurgy* 2014. doi: 10.1016/B978-0-444-53770-6.00001-0.
- [110] Z.B. Li, H. Zhang, G.H. Zhang, K.C. Chou, Fabrication and Characterization of Tungsten Heavy Alloys with High W Content by Powder Metallurgy, *Metall. Mater. Trans. A* 53(3) (2022) 1085-1098. doi: 10.1007/s11661-021-06579-w.
- [111] M. Faleschini, H. Kreuzer, D. Kiener, R. Pippan, Fracture toughness investigations of tungsten alloys and SPD tungsten alloys, *J. Nucl. Mater.* 367–370 (2007) 800-805. doi: 10.1016/j.jnucmat.2007.03.079.
- [112] M.A.M. Ghazali, M.A. Harimon, M.S. Mustapa, Mechanical Behavior and Microstructural Analysis of Molybdenum-TZM Alloy Subjected to Different Annealing Temperature, *JSE* 1 (2019) 31-35. doi: 10.30650/jse.v1i1.522.
- [113] B.V. Cockeram, The fracture toughness and toughening mechanisms of wrought low carbon arc cast, oxide dispersion strengthened, and molybdenum-0.5 pct titanium-0.1 pct zirconium molybdenum plate stock, *Metall. Mater. Trans. A* 36 (2005) 1777-1791. doi: 10.1007/s11661-005-0042-2.
- [114] C.C. Juan, M.H. Tsai, C.W. Tsai, W.L. Hsu, C.M. Lin, S.K. Chen, S.J. Lin, J.W. Yeh, Simultaneously increasing the strength and ductility of a refractory high-entropy alloy via grain refining, *Mater Lett* 184 (2016) 200-203. doi: 10.1016/j.matlet.2016.08.060.
- [115] S.M. Chen, Z.J. Ma, S. Qiu, L.J. Zhang, S.Z. Zhang, R. Yang, Q.M. Hu, Phase decomposition and strengthening in HfNbTaTiZr high entropy alloy from first-principles calculations, *Acta Mater* 225 (2022). doi: 10.1016/j.actamat.2021.117582.
- [116] Y.D. Wu, J.J. Si, D.Y. Lin, T. Wang, W.Y. Wang, Y.D. Wang, Z.K. Liu, X.D. Hui, Phase stability and mechanical properties of AlHfNbTiZr high-entropy alloys, *Mat Sci Eng a-Struct* 724 (2018) 249-259. doi: 10.1016/j.msea.2018.03.071.
- [117] F.G. Coury, T. Butler, K. Chaput, A. Saville, J. Copley, J. Foltz, P. Mason, K. Clarke, M. Kaufman, A. Clarke, Phase equilibria, mechanical properties and design of quaternary refractory high entropy alloys, *Materials & Design* 155 (2018) 244-256. doi: 10.1016/j.matdes.2018.06.003.
- [118] H. Dobbstein, E.L. Gurevich, E.P. George, A. Ostendorf, G. Laplanche, Laser metal deposition of a refractory TiZrNbHfTa high-entropy alloy, *Addit Manuf* 24 (2018) 386-390. doi: 10.1016/j.addma.2018.10.008.
- [119] O.N. Senkov, G.B. Wilks, J.M. Scott, D.B. Miracle, Mechanical properties of Nb<sub>25</sub>Mo<sub>25</sub>Ta<sub>25</sub>W<sub>25</sub> and V<sub>20</sub>Nb<sub>20</sub>Mo<sub>20</sub>Ta<sub>20</sub>W<sub>20</sub> refractory high entropy alloys, *Intermetallics* 19(5) (2011) 698-706. doi: 10.1016/j.intermet.2011.01.004.
- [120] M.E. Kassner, Fundamentals of Creep in Metals and Alloys, 2nd Edition, Fundamentals of Creep in Metals and Alloys, 2nd Edition (2009) 1-295. doi: 10.1016/C2012-0-06071-1.
- [121] F. Norton, The creep of steel at high temperatures, Mc Graw Hill, New York, USA, 1929.
- [122] S. Straub, W. Blum, H.J. Majer, T. Ungar, A. Borbely, H. Renner, Long-range internal stresses in cell and subgrain structures of copper during deformation at constant stress, *Acta Materialia* 44(11) (1996) 4337-4350. doi: 10.1016/1359-6454(96)00104-8.
- [123] R. Bürgel, H.J. Maier, T. Niendorf, Handbuch Hochtemperatur-Werkstofftechnik: Grundlagen, Werkstoffbeanspruchungen, hochtemperaturlwgerungen und -beschichtungen, Springer Vieweg 2011.

- [124] D. Caillard, J.L. Martin, New Trends in Creep Microstructural Models for Pure Metals, *Rev Phys Appl* 22(3) (1987) 169-183. doi: 10.1051/rphysap:01987002203016900.
- [125] C.J. Liu, C. Gadelmeier, S.L. Lu, J.W. Yeh, H.W. Yen, S. Gorsse, U. Glatzel, A.C. Yeh, Tensile creep behavior of HfNbTaTiZr refractory high entropy alloy at elevated temperatures, *Acta Mater* 237 (2022). doi: 10.1016/j.actamat.2022.118188.
- [126] T. Czeppe, S. Wierzbinski, Structure and mechanical properties of NiAl and Ni(3)Al-based alloys, *Int J Mech Sci* 42(8) (2000) 1499-1518. doi: 10.1016/S0020-7403(99)00087-9.
- [127] E.M. Schulson, D.R. Barker, A Brittle to Ductile Transition in NiAl of a Critical Grain-Size, *Scripta Metallurgica* 17(4) (1983) 519-522. doi: 10.1016/0036-9748(83)90344-7.
- [128] S.V. Raj, S.C. Farmer, Observation of a New Creep Regime in Polycrystalline Ni-50(at-Percent)Al Intermetallic Alloy, *Mat Res S C* 288 (1993) 647-652.
- [129] H.Y. Gao, Y.H. He, P.Z. Shen, J. Zou, N.P. Xu, Y. Jiang, B.Y. Huang, C.T. Liu, Porous FeAl intermetallics fabricated by elemental powder reactive synthesis, *Intermetallics* 17(12) (2009) 1041-1046. doi: 10.1016/j.intermet.2009.05.007.
- [130] N.S. Stoloff, Iron aluminides: present status and future prospects, *Mat Sci Eng a-Struct* 258(1-2) (1998) 1-14. doi: 10.1016/S0921-5093(98)00909-5.
- [131] T. Kim, K.T. Hong, K.S. Lee, The relationship between the fracture toughness and grain boundary character distribution in polycrystalline NiAl, *Intermetallics* 11 (2003) 33-39. doi: 10.1016/S0966-9795(02)00167-X.
- [132] T. Chen, J.M. Hampikian, N.N. Thadhani, Synthesis and characterization of mechanically alloyed and shock-consolidated nanocrystalline NiAl intermetallic, *Acta Mater.* 47(8) (1999) 2567-2579. doi: 10.1016/S1359-6454(99)00059-2.
- [133] J.M. Zhu, H.M. Fu, H.F. Zhang, A.M. Wang, H. Li, Z.Q. Hu, Microstructures and compressive properties of multicomponent AlCoCrFeNiMo<sub>x</sub> alloys, *Mat Sci Eng a-Struct* 527(26) (2010) 6975-6979. doi: 10.1016/j.msea.2010.07.028.
- [134] K.R. Forbes, U. Glatzel, R. Darolia, W.D. Nix, High-Temperature Deformation Properties of NiAl Single Crystals *Metallurgical and Materials Transactions A* volume 27 (1996) 1229–1240. doi: 10.1007/BF02649860.
- [135] W.J. Yang, R.A. Dodd, Steady-State Creep and Associated Microstructures in Stoichiometric and Non-Stoichiometric Polycrystalline NiAl, *Metal Science Journal* 7(1) (1973) 41-47. doi: 10.1179/030634573790445307.
- [136] J.D. Whittenberger, Effect of Composition and Grain-Size on Slow Plastic-Flow Properties of NiAl between 1200 and 1400 K, *Journal of Materials Science* 22(2) (1987) 394-402. doi: 10.1007/Bf01160744.
- [137] T. Khan, P. Caron, S. Naka, High Temperature Aluminides and Intermetallics, in: C.T.L. S.H. Whang, D.P. Pope, J.O. Stiegler (Ed.) *TMS*, Warrendale, PA, 1990, p. 219.
- [138] J.D. Whittenberger, R.K. Viswanadham, S.K. Mannan, B. Sprissler, Elevated temperature slow plastic deformation of NiAl-TiB<sub>2</sub> particulate composites at 1200 and 1300K, *Journal of Materials Science* 25 (1990) 35–44. doi: 10.1007/BF00544181.
- [139] R.R. Vandervoort, A.K. Mukherjee, J.E. Dorn., Elevated Temperature deformation mechanisms in beta prime-NiAl, *ASM TRANS QUART* 59 (1966) 930-944. doi:
- [140] J. Bevk, R.A. Dodd, P.R. Strutt, The orientation dependence of deformation mode and structure in stoichiometric NiAl single crystals deformed by high temperature steady-state creep, *Metall Mater Trans B* 4 (1973) 159–166 doi: 10.1007/BF02649615.
- [141] K.R. Forbes, U. Glatzel, R. Darolia, W.D. Nix, High-temperature deformation properties of NiAl single crystals, *Metall Mater Trans A* 27(5) (1996) 1229-1240. doi: 10.1007/Bf02649860.
- [142] S.V. Raj, S.C. Farmer, Observation of a New Creep Regime in Polycrystalline Ni-50(at.%) Al Intermetallic Alloy, *MRS Online Proceedings Library* 288 (1992) 647–652. doi: 10.1557/PROC-288-647.
- [143] S.V. Raj, S.C. Farmer, High temperature ordered intermetallic alloys V, *MRS Online Proceedings Library* 288 (1993) 647.
- [144] E. Arzt, P. Grahle, Creep of Particle-Reinforced NiAl Intermetallics - New Materials for up to 1400 °C, *Mater Res Soc Symp P* 364 (1995) 525-536. doi: 10.1557/PROC-364-525.
- [145] J.D. Whittenberger, E. Arzt, M.J. Luton, 1400-K and 1500-K Compressive Creep-Properties of an NiAl-Al<sub>n</sub> Composite, *Scripta Metall Mater* 26(12) (1992) 1925-1930. doi: 10.1016/0956-716x(92)90060-R.



- [146] E. Arzt, P. Grahle, High temperature creep behavior of oxide dispersion strengthened NiAl intermetallics, *Acta Materialia* 46(8) (1998) 2717-2727. doi: 10.1016/S1359-6454(97)00474-6.
- [147] W.J. Zhang, R.S. Sundar, S.C. Deevi, Improvement of the creep resistance of FeAl-based alloys, *Intermetallics* 12(7-9) (2004) 893-897. doi: 10.1016/j.intermet.2004.02.020.
- [148] J.D. Whittenberger, M.V. Nathal, D.J. Gaydos, Compressive and Tensile Creep in Fe-40Al-0.1Zr-0.4B at 1100-K, *Intermetallics* 2(3) (1994) 193-200. doi: 10.1016/0966-9795(94)90058-2.
- [149] P. Kral, W. Blum, J. Dvorak, N. Yurchenko, N. Stepanov, S. Zhrebtsov, L. Kuncicka, M. Kvapilova, V. Sklenicka, Creep behavior of an AlTiVNbZr<sub>0.25</sub> high entropy alloy at 1073 K, *Mat Sci Eng A* 783 (2020). doi: 10.1016/j.msea.2020.139291.
- [150] C.G. Mckamey, P.J. Maziasz, J.W. Jones, Effect of Addition of Molybdenum or Niobium on Creep-Rupture Properties of Fe<sub>3</sub>Al, *J Mater Res* 7(8) (1992) 2089-2106. doi: 10.1557/Jmr.1992.2089.
- [151] V.K. Sikka, B.G. Gieseke, R.H. Baldwin, Mechanical properties of Fe sub 3 Al-based alloys, 1. international conference on heat-resistant materials, Lake Geneva WI (United States), 1991, pp. 22-26.
- [152] J. Phillips, G. Eggeler, B. Ilchner, E. Batawi, On the influence of crystal structure on creep in a Fe<sub>3</sub>Al-based alloy, *Scripta Materialia* 36(6) (1997) 693-698. doi: 10.1016/S1359-6462(96)00439-3.
- [153] B. Voyzelle, J.D. Boyd, High-temperature deformation behaviour of Fe<sub>3</sub>Al, *Mat Sci Eng A* 258(1-2) (1998) 243-248. doi: Doi 10.1016/S0921-5093(98)00940-X.
- [154] M.A. Morris-Munoz, Creep deformation of oxide-dispersion-strengthened Fe-40Al intermetallic: thermal and athermal contributions, *Intermetallics* 7(6) (1999) 653-661. doi: 10.1016/S0966-9795(98)00079-X.
- [155] R.S. Sundar, T.R.G. Kutty, D.H. Sastry, Hot hardness and creep of Fe<sub>3</sub>Al-based alloys, *Intermetallics* 8(4) (2000) 427-437. doi: 10.1016/S0966-9795(99)00118-1.
- [156] J.D. Whittenberger, The influence of grain size and composition on slow plastic flow in FeAl between 1000 and 1400 K, *Mater Sci Eng* 77 (1986) 103-113. doi: 10.1016/0025-5416(86)90358-7.
- [157] J. Murray, A. Peruzzi, J.P. Abriata, The Al-Zr (Aluminum-Zirconium) System *J. Phase equilibria* 13 (1992) 277-291. doi: 10.1007/BF02667556.
- [158] J. She, Y.Z. Zhan, Z.H. Hu, C.L. Li, J. Hu, Y. Du, H.H. Xu, Experimental study of Al-Zr-Y system phase equilibria at 773 K, *Journal of Alloys and Compounds* 497(1-2) (2010) 118-120. doi: 10.1016/j.jallcom.2010.03.073.
- [159] J.L. Du, B. Wen, R. Melnik, Y. Kawazoe, Cluster characteristics and physical properties of binary Al-Zr intermetallic compounds from first principles studies, *Comp Mater Sci* 103 (2015) 170-178. doi: 10.1016/j.commatsci.2015.03.039.
- [160] G. Ghosh, M. Asta, First-principles calculation of structural energetics of Al-TM (TM = Ti, Zr, Hf) intermetallics, *Acta Materialia* 53(11) (2005) 3225-3252. doi: 10.1016/j.actamat.2005.03.028.
- [161] C.A. Schneider, W.S. Rasband, K.W. Eliceiri, NIH Image to ImageJ: 25 years of image analysis, *Nat Methods* 9(7) (2012) 671-675. doi: 10.1038/nmeth.2089.
- [162] D. Hull, D.J. Bacon, *Introduction to Dislocations*, fifth edition ed., Butterworth-Heinemann 2011. doi: 10.1016/C2009-0-64358-0.

## List of Publications

### *List of first-authored publications*

[I] **P. Suárez Ocaño**, S.G. Fries, I. Lopez-Galilea, R. Darvishi Kamachali, J. Roik, L. Agudo Jácome, *The AlMo<sub>0.5</sub>NbTa<sub>0.5</sub>TiZr refractory high entropy superalloy: Experimental findings and comparison with calculations using the CALPHAD method*. Mater. Des. 217 (2022) 110593. <https://doi.org/10.1016/j.matdes.2022.110593>.

[II] **P. Suárez Ocaño**, L. Agudo Jácome, I. Lopez-Galilea, R. Darvishi Kamachali, S.G. Fries, *Data regarding the experimental findings compared with CALPHAD calculations of the AlMo<sub>0.5</sub>NbTa<sub>0.5</sub>TiZr refractory high entropy superalloy*. Data in Brief (2023) 46, 108858. <https://doi.org/10.1016/j.dib.2022.108858>.

[III] **P. Suárez Ocaño**, A. M. Manzoni, I. Lopez-Galilea, B. Rutttert, G. Laplanche, L. Agudo Jácome, *Influence of cooling rate and lattice misfit on the microstructure and mechanical properties in the refractory AlMo<sub>0.5</sub>NbTa<sub>0.5</sub>TiZr high entropy superalloy*, Journal of Alloys and Compounds 949 (2023) 169871. <https://doi.org/10.1016/j.jallcom.2023.169871>.

[IV] **P. Suárez Ocaño**, G. Laplanche, C. Gadelmeier, U. Glatzel, L. Agudo Jácome, *Creep degradation of the AlMo<sub>0.5</sub>NbTa<sub>0.5</sub>TiZr refractory high entropy superalloy*, to be submitted.

### *List of co-authored publications*

[V] Y. Yesilcicek, S. Haas, **P. Suárez Ocaño**, E. Zaiser, R. Hesse, D. M. Többens, U. Glatzel, A. M. Manzoni, *Controlling Lattice Misfit and Creep Rate Through the  $\gamma'$  Cube Shapes in the Al<sub>10</sub>Co<sub>25</sub>Cr<sub>8</sub>Fe<sub>15</sub>Ni<sub>36</sub>Ti<sub>6</sub> Compositionally Complex Alloy with Hf and W Additions*, High Entropy Alloys & Materials (2022), <https://doi.org/10.1007/s44210-022-00009-1>.

## Curriculum vitae

### Personal Information

**Place and date of birth:** Caracas, November 25<sup>th</sup>, 1991

**Citizenship:** Uruguayan/Venezuelan

**Languages:** English (fluent)/ German (Basic)/ Spanish (native language)



## EDUCATION

- 2019 – Present**      **RUHR UNIVERSITÄT BOCHUM**, Bochum, Germany  
**FACULTY OF ENGINEERING DEPARTMENT OF MECHANICAL ^  
ENGINEERING** Doctoral research.
- 2009 – 2016**      **CENTRAL UNIVERSITY OF VENEZUELA**, Caracas, Venezuela  
**FACULTY OF ENGINEERING. SCHOOL FOR MATERIAL  
SCIENCES AND METALLURGICAL ENGINEERING**  
Metallurgical engineering degree (*with honors*)
- July – Sep. 2014**      **FOUNDATION ENGINEERING INSTITUTE**, Caracas, Venezuela  
**INSTITUTE OF MATERIALS SCIENCE AND TECHNOLOGY**  
Academic (research) internship. Laboratory of electrochemistry.

## WORK EXPERIENCE

- 2023 – Present**      **BUNDESANSTALT FÜR MATERIALFORSCHUNG UND -PRÜFUNG**,  
Berlin, Germany  
**DEPARTMENT 5: MATERIALS ENGINEERING**  
Position: Research Assistant  
Topic: Deformation and damage mechanisms in L-PBF fabricated 316L  
austenitic steel after high temperature fatigue loading.
- 2019 – 2023**      **BUNDESANSTALT FÜR MATERIALFORSCHUNG UND -PRÜFUNG**,  
Berlin, Germany  
**DEPARTMENT 5: MATERIALS ENGINEERING**  
Position: Research Assistant  
Topic: Incipient Oxidation and Deformation Mechanisms of the Complex  
Concentrated Alloy AlMo<sub>0.5</sub>NbTa<sub>0.5</sub>TiZr in the High Temperature Regime.
- 2016 – 2018**      **THERMOFISHER SCIENTIFIC**. Caracas, Venezuela  
**SUPPORT DEPARTMENT**  
Position: Product and application engineer
- 2016**      **CENTRAL UNIVERSITY OF VENEZUELA**, Caracas, Venezuela  
**FACULTY OF ENGINEERING**  
**Department Mechanical Metallurgy**  
Undergraduate researcher. Subject: *Microstructural characterization of a  
commercial Al-6063 alloy obtained by casted cylinders and homogenized at  
industrial level (Honorable Mention)*